frontiers | Research Topics

Heat transfer in data centers, volume II

Edited by
Chengbin Zhang, Matteo Fasano, Xiangdong Liu and Fang-Bao Tian

Published in
Frontiers in Energy Research

ISSN 1664-8714
ISBN 978-2-83250-748-3
DOI 10.3389/978-2-83250-748-3

About Frontiers

Frontiers is more than just an open access publisher of scholarly articles: it is a pioneering approach to the world of academia, radically improving the way scholarly research is managed. The grand vision of Frontiers is a world where all people have an equal opportunity to seek, share and generate knowledge. Frontiers provides immediate and permanent online open access to all its publications, but this alone is not enough to realize our grand goals.

Frontiers journal series

The Frontiers journal series is a multi-tier and interdisciplinary set of open-access, online journals, promising a paradigm shift from the current review, selection and dissemination processes in academic publishing. All Frontiers journals are driven by researchers for researchers; therefore, they constitute a service to the scholarly community. At the same time, the *Frontiers journal series* operates on a revolutionary invention, the tiered publishing system, initially addressing specific communities of scholars, and gradually climbing up to broader public understanding, thus serving the interests of the lay society, too.

Dedication to quality

Each Frontiers article is a landmark of the highest quality, thanks to genuinely collaborative interactions between authors and review editors, who include some of the world's best academicians. Research must be certified by peers before entering a stream of knowledge that may eventually reach the public - and shape society; therefore, Frontiers only applies the most rigorous and unbiased reviews. Frontiers revolutionizes research publishing by freely delivering the most outstanding research, evaluated with no bias from both the academic and social point of view. By applying the most advanced information technologies, Frontiers is catapulting scholarly publishing into a new generation.

What are Frontiers Research Topics?

Frontiers Research Topics are very popular trademarks of the *Frontiers journals series*: they are collections of at least ten articles, all centered on a particular subject. With their unique mix of varied contributions from Original Research to Review Articles, Frontiers Research Topics unify the most influential researchers, the latest key findings and historical advances in a hot research area.

Find out more on how to host your own Frontiers Research Topic or contribute to one as an author by contacting the Frontiers editorial office: frontiersin.org/about/contact

Heat transfer in data centers, volume II

Topic editors

Chengbin Zhang — Southeast University, China

Matteo Fasano — Polytechnic University of Turin, Italy

Xiangdong Liu — Yangzhou University, China

Fang-Bao Tian — University of New South Wales Canberra, Australia

Citation

Zhang, C., Fasano, M., Liu, X., Tian, F.-B., eds. (2023). *Heat transfer in data centers, volume II*. Lausanne: Frontiers Media SA. doi: 10.3389/978-2-83250-748-3

Table of contents

frontiers | Frontiers in Energy Research

OPINION
published: 19 May 2022
doi: 10.3389/fenrg.2022.928811

Bioinspired Fiber for Directional Droplet Self-Transportation and Its Potential for Enhanced Condensation

*Qianchen Rui and Wei Yu **

College of Electrical, Energy and Power Engineering, Yangzhou University, Yangzhou, China

Keywords: bioinspired fiber, surface wettability, droplet, microfluidics, electrospinning

INTRODUCTION

Phase-change heat transfer has attracted great attention in engineering disciplines in recent years due to the tremendous latent heat and significant efficiency for energy transfer involved in its process (Liu et al., 2013; Cho et al., 2016). As a typical process, vapor-liquid phase-change heat transfer has great potential in applications such as heat exchangers and electronic cooling (Zhang et al., 2011; Wen et al., 2018). When water vapor encounters solid surfaces at low temperature, a vapor to liquid phase-change process, i.e., condensation occurs, accompanied by the release of a large quantity of latent heat (Edalatpour et al., 2018). During this process, two types of condensation can occur, i.e., film condensation and dropwise condensation. In comparison with film condensation, the condensate in the dropwise condensation process exists in the form of droplets rather than a continuous film, which ensures good heat transfer between the vapor and surface (Goswami et al., 2021), shown in **Figure 1A**. Therefore, dropwise condensation has drawn growing research interest, especially on functional surfaces for enhanced dropwise condensation (Chu et al., 2017; Wang et al., 2018).

In nature, spider silk (Zheng et al., 2010), cactus (Ju et al., 2012), nepenthes alata (Gorb et al., 2013), etc., with functional surfaces are capable of directional droplet self-transportation, which sheds light on the functional surface for enhanced dropwise condensation. In this paper, the mechanisms for dropwise condensation and directional droplet self-transportation are introduced. Then, several methods for fabricating bioinspired microfibers are summarized to discuss their potential for enhanced condensation.

PRINCIPLES OF DROPLET CONDENSATION

Whether it is film condensation or dropwise condensation, the condensate formed acts as a thermal resistance carrier for heat exchange between the vapor and solid surface. Compared with film condensation, the shedding of droplets during droplet condensation leads to a much smaller thermal resistance. The removal of larger droplets will enable increased vapor condensation on the solid surface, which enhances the vapor-liquid phase change heat transfer (Lv et al., 2022).

DIRECTIONAL DROPLET SELF-TRANSPORTATION

Due to their unique structure, natural materials such as spider silk, cactus and nepenthes alata exhibit directional water transportation. Specifically, tiny droplets in fog can be captured and merged into larger droplets on the surface of these materials (Venkatesan et al., 2020). Spider silk will be taken as an example to describe its water collection principles and characteristics in detail, shown in **Figure 1B**.

OPEN ACCESS

Edited by:
Chengbin Zhang,
Southeast University, China

Reviewed by:
Leigang Zhang,
Zhengzhou University of Light Industry, China
Qiang Ma,
Jiangsu University, China

***Correspondence:**
Wei Yu
weiyu@yzu.edu.cnmailto:weiyu@yzu.edu.cn

Specialty section:
This article was submitted to Process and Energy Systems Engineering, a section of the journal Frontiers in Energy Research

Received: *26 April 2022*
Accepted: *03 May 2022*
Published: *19 May 2022*

Citation:
Rui Q and Yu W (2022) Bioinspired Fiber for Directional Droplet Self-Transportation and Its Potential for Enhanced Condensation. Front. Energy Res. 10:928811. doi: 10.3389/fenrg.2022.928811

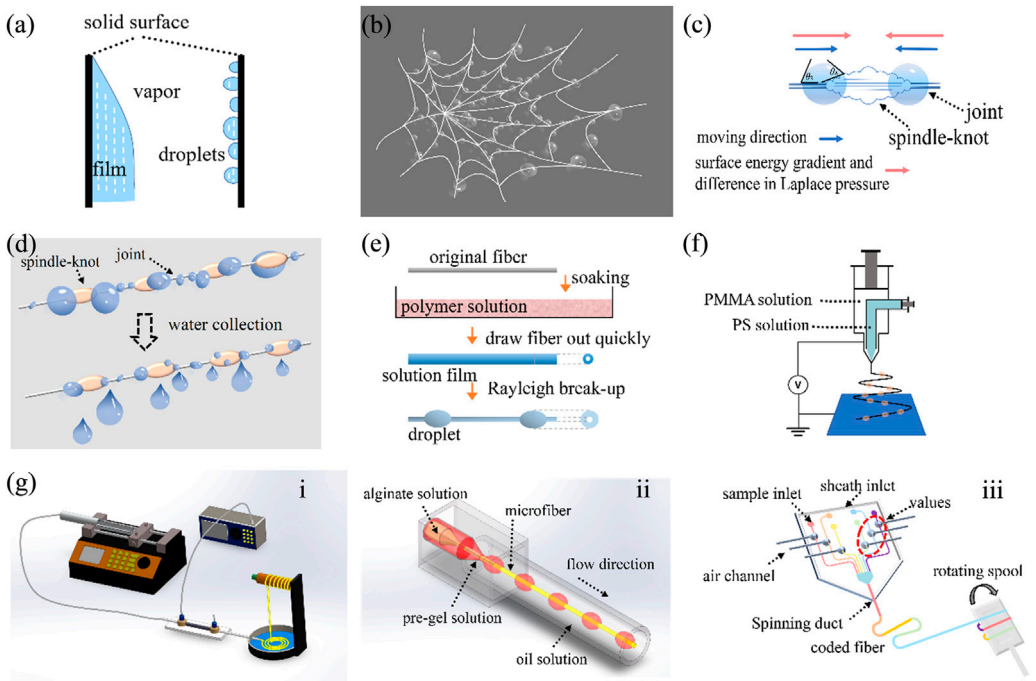

FIGURE 1 | Principles, fabrication and application of Bioinspired fiber for directional droplet self-transportation. **(A)** Two condensation modes; **(B)** Water collection on spider silks; **(C)** Mechanism of directional droplet self-transportation; **(D)** Water-harvesting behavior of bioinspired microfibers; **(E)** Dip-coating method; **(F)** Electrospinning, method; **(G)** Microfluidic method, i) Emulsion-based coaxial microfluidic method, ii)Integrative spinning-coating-emulsification coaxial capillary microfluidic method, iii) Pneumatic-valve microfluidic chip spinning method.

In a foggy morning, a spider web is usually covered with tiny water droplets. Zheng et al. investigated the directional water collection behavior on spider silk (Zheng et al., 2010). The silk shows a unique structure, including periodic spindle-knots composed of random nanofibrils and joints comprising aligned nanofibrils, resulting in an excellent ability to harvest water (Liu et al., 2022). Moreover, there exists a surface roughness gradient and surface wettability gradient between the periodic spindle knots and the joint. Functional surface with wettability gradient is a promising option for the self-propelled droplet motion, including super-slippery surface (Wang et al., 2017; Wang et al., 2018), textured surface (Wu et al., 2011; Zhang et al., 2016). Thus, the surface energy gradient, induced by the surface roughness gradient and surface wettability gradient, drives the tiny droplet from the smooth joint to the spindle knot, shown in **Figure 1C**. In addition, due to the curvature gradient of materials, the Laplace pressure gradient is also beneficial for directional droplet self-transportation.

BIOINSPIRED MICROFIBER FABRICATION

Inspired by spider silk, several attempts have been made to fabricate microfibers for directional droplet self-transportation (Haefner et al., 2015; Tian and Wang, 2018), shown in **Figure 1D**. At present, the fabrication methods for such bioinspired microfibers can be roughly divided into three categories, namely, the Rayleigh instability method, electrodynamics method and microfluidic methods (Chen and Guo, 2019; Li et al., 2019). Dip-coating (Tian et al., 2011), a widely used Rayleigh instability method, utilizes a nylon/carbon fiber and a polymer solution as materials, shown in **Figure 1E**. The fiber is first placed horizontally on the polymer solution. Then, the fiber is immersed in the polymer solution and pulled out. Therefore, a film of the polymer solution covers the fiber, which breaks up into droplets that hang onto the fiber due to Rayleigh instability. For the electrodynamics method, a necklace structure, which is similar to the spindle-knot, is generated over the nanofibers by the influence of an electrostatic force and surface tension (Ura et al., 2021), shown in **Figure 1F**. However, the above methods have difficulty precisely controlling the size and spacing of the spindle-knots.

The microfluidic methods are capable of precisely controlling the size and spacing of spindle-knots by adjusting the flow rate or pressure, showing superiority in the preparation of spider-silk-like microfibers (Chen et al., 2013; Chen et al., 2015; Liu et al., 2020; Gao et al., 2021), shown in **Figure 1G**. The oil-in-water emulsion or gas-in-water emulsion can be formed under the shear force by injecting immiscible liquid or gas phase into the continuous flow. The microfibers with spindle-knots will be fabricated until the continuous phase enclosing the heterogeneous core is solidified and dehydrated. The emulsion-based coaxial

microfluidic method is widely used in microfluidic spinning, especially for oil-in-water emulsions (Ji et al., 2015) and air-in-water emulsions (Liu et al., 2016; Tian et al., 2017). The injected air is formed as tiny bubbles with the same size and equal distance. The shell phase using sodium alginate solution will be solidified in the $CaCl_2$ solution due to the cross-linked reaction between alginate solutions and Ca^{2+} ions. Thus, bioinspired water-harvesting microfibers with periodic spindle-knots can be successfully fabricated.

PERFORMANCE OF BIOINSPIRED MICROFIBERS

According to previous investigations, such bioinspired microfibers demonstrate excellent properties for droplet directional collection, with potential for enhanced condensation (Zhang et al., 2017; Majidi et al., 2021). Zhu et al. found three different condensation morphologies for droplets on microfibers both experimentally and numerically (Zhu et al., 2020). The difference in the condensation morphologies is contributed by the relationship between the thermal conduction resistance within the fiber and condensation heat transfer resistance on the microfiber surface. The water collection capacity of microfibers can be influenced by their own structure and environmental humidity. A test of the water-collecting capacity on different spindle knots for microfibers was conducted by Hou et al. Three types of 1 mm long bioinspired fibers with nearly the same knots (110 μm in length and 200 μm in height) were used (Hou et al., 2012). It can be observed that the fiber with one spindle knot has the ability to collect 1.71 μL water droplets in 160 s, and the fiber with two knots takes over 205 s to collect 3.38 μL droplets. The droplet moves on the artificial spider silk with nearly 0.2–0.3 mm/s (Zheng et al., 2010; Bai et al., 2011).

CONCLUSION AND OUTLOOK

In this paper, we briefly describe the mechanisms for dropwise condensation heat transfer and the importance of droplet removal for enhanced dropwise condensation. Two key factors that dominate droplet self-transportation: the surface energy gradient and Laplace pressure are summarized. Inspired by natural water-harvesting behavior, the enhancement of heat transfer can be realized by accelerating the merging and shedding of droplets on microfibers. Several fabrication methods for bioinspired microfibers and the performance of bioinspired microfibers are introduced. These microfibers are beneficial for achieving enhanced heat exchange, and their capacity to harvest water and save resources is of great significance. So far, the water collection capacity of most microfibers is extremely dependent on high humidity environments and the performance is not good at low humidity conditions. In addition, the effect of extrinsic factors such as temperature, wind and magnetic force on the water collection capacity of microfibers is not clear. Therefore, the performance of the bioinspired fiber in external environment should be improve to extend the application in enhanced condensation.

AUTHOR CONTRIBUTIONS

WY contributed to the conception of the study. QR wrote the first draft of the manuscript. All authors contributed to manuscript revision and read and approved the submitted version.

FUNDING

This work is supported by Natural Science Foundation of the Jiangsu Higher Education Institutions of China (20KJB470006).

REFERENCES

Bai, H., Sun, R., Ju, J., Yao, X., Zheng, Y., and Jiang, L. (2011). Large-Scale Fabrication of Bioinspired Fibers for Directional Water Collection. *Small* 7 (24), 3429–3433. doi:10.1002/smll.201101408

Chen, W., and Guo, Z. (2019). Hierarchical Fibers for Water Collection Inspired by Spider Silk. *Nanoscale* 11 (33), 15448–15463. doi:10.1039/C9NR04065J

Chen, Y., Liu, X., and Shi, M. (2013). Hydrodynamics of Double Emulsion Droplet in Shear Flow. *Appl. Phys. Lett.* 102 (5), 051609. doi:10.1063/1.4789865

Chen, Y., Wu, L., and Zhang, L. (2015). Dynamic Behaviors of Double Emulsion Formation in a Flow-Focusing Device. *Int. J. Heat Mass Transf.* 82, 42–50. doi:10.1016/j.ijheatmasstransfer.2014.11.027

Cho, H. J., Preston, D. J., Zhu, Y., and Wang, E. N. (2016). Nanoengineered Materials for Liquid-Vapour Phase-Change Heat Transfer. *Nat. Rev. Mater* 2 (2), 16092. doi:10.1038/natrevmats.2016.92

Chu, F., Wu, X., Zhu, Y., and Yuan, Z. (2017). Relationship between Condensed Droplet Coalescence and Surface Wettability. *Int. J. Heat Mass Transf.* 111, 836–841. doi:10.1016/j.ijheatmasstransfer.2017.04.052

Edalatpour, M., Liu, L., Jacobi, A. M., Eid, K. F., and Sommers, A. D. (2018). Managing Water on Heat Transfer Surfaces: A Critical Review of Techniques to Modify Surface Wettability for Applications with Condensation or Evaporation. *Appl. Energy* 222, 967–992. doi:10.1016/j.apenergy.2018.03.178

Gao, W., Lei, Z., Liu, X., and Chen, Y. (2021). Dynamic Liquid Gating Artificially Spinning System for Self-Evolving Topographies and Microstructures. *Langmuir* 37 (4), 1438–1445. doi:10.1021/acs.langmuir.0c02910

Gorb, E. V., Baum, M. J., and Gorb, S. N. (2013). Development and Regeneration Ability of the Wax Coverage in Nepenthes Alata Pitchers: A Cryo-SEM Approach. *Sci. Rep.* 3, 3078. doi:10.1038/srep03078

Goswami, A., Pillai, S. C., and McGranaghan, G. (2021). Surface Modifications to Enhance Dropwise Condensation. *Surfaces Interfaces* 25, 101143. doi:10.1016/j.surfin.2021.101143

Haefner, S., Benzaquen, M., Bäumchen, O., Salez, T., Peters, R., McGraw, J. D., et al. (2015). Influence of Slip on the Plateau-Rayleigh Instability on a Fibre. *Nat. Commun.* 6 (1), 7409. doi:10.1038/ncomms8409

Hou, Y., Chen, Y., Xue, Y., Wang, L., Zheng, Y., and Jiang, L. (2012). Stronger Water Hanging Ability and Higher Water Collection Efficiency of Bioinspired Fiber with Multi-Gradient and Multi-Scale Spindle Knots. *Soft Matter* 8 (44), 11236. doi:10.1039/c2sm26421h

Ji, X., Guo, S., Zeng, C., Wang, C., and Zhang, L. (2015). Continuous Generation of Alginate Microfibers with Spindle-Knots by Using a Simple Microfluidic Device. *RSC Adv.* 5 (4), 2517–2522. doi:10.1039/c4ra10389k

Ju, J., Bai, H., Zheng, Y., Zhao, T., Fang, R., and Jiang, L. (2012). A Multi-Structural and Multi-Functional Integrated Fog Collection System in Cactus. *Nat. Commun.* 3, 1247. doi:10.1038/ncomms2253

Li, C., Liu, Y., Gao, C., Li, X., Xing, Y., and Zheng, Y. (2019). Fog Harvesting of a Bioinspired Nanocone-Decorated 3D Fiber Network. *ACS Appl. Mat. Interfaces* 11 (4), 4507–4513. doi:10.1021/acsami.8b15901

Liu, H., Wang, Y., Yin, W., Yuan, H., Guo, T., and Meng, T. (2022). Highly Efficient Water Harvesting of Bioinspired Spindle-Knotted Microfibers with Continuous Hollow Channels. *J. Mat. Chem. A* 10 (13), 7130–7137. doi:10.1039/D2TA00242F

Liu, X., Chen, Y., and Shi, M. (2013). Dynamic Performance Analysis on Start-Up of Closed-Loop Pulsating Heat Pipes (CLPHPs). *Int. J. Therm. Sci.* 65, 224–233. doi:10.1016/j.ijthermalsci.2012.10.012

Liu, X., Zhang, C., Yu, W., Deng, Z., and Chen, Y. (2016). Bubble Breakup in a Microfluidic T-Junction. *Sci. Bull.* 61 (10), 811–824. doi:10.1007/s11434-016-1067-1

Liu, Y., Yang, N., Li, X., Li, J., Pei, W., Xu, Y., et al. (2020). Water Harvesting of Bioinspired Microfibers with Rough Spindle-Knots from Microfluidics. *Small* 16 (9), 1901819. doi:10.1002/smll.201901819

Lv, F., Zhao, F., Cheng, D., Dong, Z., Jia, H., Xiao, X., et al. (2022). Bioinspired Functional SLIPSs and Wettability Gradient Surfaces and Their Synergistic Cooperation and Opportunities for Enhanced Condensate and Fluid Transport. *Adv. Colloid Interface Sci.* 299, 102564. doi:10.1016/j.cis.2021.102564

Majidi, S. S., Su, Y., Jørgensen, M. L., Müller, C., Forooghi, P., Nie, G., et al. (2021). Rayleigh Instability-Driven Coaxial Spinning of Knotted Cell-Laden Alginate Fibers as Artificial Lymph Vessels. *ACS Appl. Mat. Interfaces* 13 (19), 22142–22149. doi:10.1021/acsami.1c00798

Tian, X., Chen, Y., Zheng, Y., Bai, H., and Jiang, L. (2011). Controlling Water Capture of Bioinspired Fibers with Hump Structures. *Adv. Mat.* 23 (46), 5486–5491. doi:10.1002/adma.201103111

Tian, Y., and Wang, L. (2018). Bioinspired Microfibers for Water Collection. *J. Mat. Chem. A* 6 (39), 18766–18781. doi:10.1039/C8TA08104B

Tian, Y., Zhu, P., Tang, X., Zhou, C., Wang, J., Kong, T., et al. (2017). Large-scale Water Collection of Bioinspired Cavity-Microfibers. *Nat. Commun.* 8 (1), 1080. doi:10.1038/s41467-017-01157-4

Ura, D. P., Knapczyk-Korczak, J., Szewczyk, P. K., Sroczyk, E. A., Busolo, T., Marzec, M. M., et al. (2021). Surface Potential Driven Water Harvesting from Fog. *ACS Nano* 15 (5), 8848–8859. doi:10.1021/acsnano.1c01437

Venkatesan, H., Chen, J., Liu, H., Liu, W., and Hu, J. (2020). A Spider-Capture-Silk-Like Fiber with Extremely High-Volume Directional Water Collection. *Adv. Funct. Mat.* 30 (30), 2002437. doi:10.1002/adfm.202002437

Wang, J., Gao, W., Zhang, H., Zou, M., Chen, Y., and Zhao, Y. (2018). Programmable Wettability on Photocontrolled Graphene Film. *Sci. Adv.* 4 (9), eaat7392. doi:10.1126/sciadv.aat7392

Wang, J., Sun, L., Zou, M., Gao, W., Liu, C., Shang, L., et al. (2017). Bioinspired Shape-Memory Graphene Film with Tunable Wettability. *Sci. Adv.* 3 (6), e1700004. doi:10.1126/sciadv.1700004

Wen, R., Ma, X., Lee, Y.-C., and Yang, R. (2018). Liquid-vapor Phase-Change Heat Transfer on Functionalized Nanowired Surfaces and beyond. *Joule* 2 (11), 2307–2347. doi:10.1016/j.joule.2018.08.014

Wu, J., Ma, R., Wang, Z., and Yao, S. (2011). Do droplets Always Move Following the Wettability Gradient? *Appl. Phys. Lett.* 98 (20), 204104. doi:10.1063/1.3592997

Zhang, B., Lei, Q., Wang, Z., and Zhang, X. (2016). Droplets Can Rebound toward Both Directions on Textured Surfaces with a Wettability Gradient. *Langmuir* 32 (1), 346–351. doi:10.1021/acs.langmuir.5b04365

Zhang, C., Chen, Y., Wu, R., and Shi, M. (2011). Flow Boiling in Constructal Tree-Shaped Minichannel Network. *Int. J. Heat Mass Transf.* 54 (1), 202–209. doi:10.1016/j.ijheatmasstransfer.2010.09.051

Zhang, S., Huang, J., Chen, Z., and Lai, Y. (2017). Bioinspired Special Wettability Surfaces: From Fundamental Research to Water Harvesting Applications. *Small* 13 (3), 1602992. doi:10.1002/smll.201602992

Zheng, Y., Bai, H., Huang, Z., Tian, X., Nie, F.-Q., Zhao, Y., et al. (2010). Directional Water Collection on Wetted Spider Silk. *Nature* 463 (7281), 640–643. doi:10.1038/nature08729

Zhu, F., Fang, W.-Z., Zhang, H., Zhu, Z., New, T. H., Zhao, Y., et al. (2020). Water Condensate Morphologies on a Cantilevered Microfiber. *J. Appl. Phys.* 127 (24), 244902. doi:10.1063/5.0007474

Conflict of Interest: The authors declare that the research was conducted in the absence of any commercial or financial relationships that could be construed as a potential conflict of interest.

Publisher's Note: All claims expressed in this article are solely those of the authors and do not necessarily represent those of their affiliated organizations, or those of the publisher, the editors and the reviewers. Any product that may be evaluated in this article, or claim that may be made by its manufacturer, is not guaranteed or endorsed by the publisher.

frontiers | Frontiers in Energy Research

ORIGINAL RESEARCH
published: 19 May 2022
doi: 10.3389/fenrg.2022.911458

Simultaneous Impact of Hollow Droplet and Continuous Dense Droplet on Liquid Film

Dashu Li[1], *Gangtao Liang*[2] *and Dan Hua*[3]*

[1]CNOOC Research Institute Co. Ltd., Beijing, China, [2]Key Laboratory of Ocean Energy Utilization and Energy Conservation of Ministry of Education, School of Energy and Power Engineering, Dalian University of Technology, Dalian, China, [3]Jiangsu Key Laboratory of Micro and Nano Heat Fluid Flow Technology and Energy Application, School of Environmental Science and Engineering, Suzhou University of Science and Technology, Suzhou, China

The Simultaneous impact of a hollow droplet and a continuous dense droplet on a liquid film was investigated using the coupled level set and volume of fluid (CLSVOF) method. Analyses included fluid dynamics and heat transfer characteristics in impact. Results showed that the interfacial phenomena after impact incorporates spreading, central jet between droplets, edge liquid sheet, and counter jet inside the hollow droplet. The pressure gradient is the major cause for the above phenomena. The significant parameter of impact velocity is closely related to the dynamics and heat transfer for droplets impacting on a liquid film. Droplets with higher impact velocity exhibit a greater spreading factor, central jet height, edge jet height, and counter jet height. Besides, wall heat flux increases more notably for droplets with a higher impact velocity. Compared with the continuous droplet, the hollow droplet shows a smaller spreading factor and edge jet height, a higher wall heat flux, but a narrow thermally affected region. This study provides a fundamental understanding for the application of high-pressure spray combustion.

Keywords: droplet impact, hollow droplet, continuous dense droplet, central jet, counter jet

OPEN ACCESS

Edited by:
Chengbin Zhang,
Southeast University, China

Reviewed by:
Cheng Yu,
University of Hawaii at Manoa, United States
Wei Gao,
Harvard University, United States

***Correspondence:**
Dan Hua
huadan@usts.edu.cn

Specialty section:
This article was submitted to Process and Energy Systems Engineering, a section of the journal Frontiers in Energy Research

Received: *02 April 2022*
Accepted: *12 April 2022*
Published: *19 May 2022*

Citation:
Li D, Liang G and Hua D (2022) Simultaneous Impact of Hollow Droplet and Continuous Dense Droplet on Liquid Film. Front. Energy Res. 10:911458. doi: 10.3389/fenrg.2022.911458

INTRODUCTION

Droplet impact on a liquid film has been witnessed in many industrial applications, such as spray cooling, falling-film evaporation, ink jet printing, internal combustion, and plasma spraying (Yarin, 2006; Liu et al., 2013; Liang and Mudawar, 2016; Wang et al., 2017; Wang et al., 2018; Li and Duan, 2019). Recently, a mass of experimental and numerical studies had been conducted on this phenomenon (Li et al., 2017; Liang and Mudawar, 2017a, b; Liang and Mudawar, 2017c; Wang et al., 2018). Compared with investigations on the impact of a single continuous dense droplet, multi-droplet impact received far less attention (Roisman and Tropea, 2002; Sivakumar and Tropea, 2002; Zhang et al., 2016), which, however, is encountered frequently in applications involving droplet impact. On the other hand, microbubbles usually form randomly inside droplets in high-pressure spray combustion (Gulyaev et al., 2009; Kumar et al., 2013; Lu et al., 2015), which indicates that the simultaneous impact of a hollow droplet and a continuous dense droplet is a common occurrence under this context. Also, in a practical condition, a thin liquid film will be builtup on the solid surface upon impact in the initial stage. This implies that the subsequent droplet will interact with the liquid film instead of with the solid surface (Liu et al., 2016). Inspired by the abovementioned information, this study will focus on the dynamics and heat transfer characteristics involved during a hollow droplet and a continuous dense droplet impinging on a liquid film simultaneously.

In recent years, many experimental and numerical efforts have been dedicated to single continuous dense droplet impact (Liang and Mudawar, 2016). From the experimental viewpoint, a high-speed camera was mainly used to investigate the transient dynamic behavior during impact (Oguz and Prosperetti, 1989; Peck and Sigurdson, 1994; Alghoul et al., 2011; Negeed et al., 2013; Negeed et al., 2014; Stevens, 2014). While in numerical studies, typical CFD methods such as marker and cell (MAC) (Harlow and Welch, 1965), level set (Lee et al., 2011), volume of fluid (VOF) (Rocco et al., 2010; Chen et al., 2013; Chen et al., 2015), lattice Boltzmann method (LBM) (Lee and Liu, 2010; Chen and Deng, 2017; Pravinraj and Patrikar, 2017), and coupled level set and volume of fluid (CLSVOF) method (Liang et al., 2014) have been employed. The interfacial phenomena during impact such as spreading, edge liquid sheet, and splashing, with their corresponding underlying mechanisms were comprehensively investigated (Sivakumar and Tropea, 2002; Guo et al., 2010). The effects of impact velocity, droplet initial diameter, impact angle, and the initial thickness of the liquid film were mainly considered. Also, the heat transfer during droplet impact was studied (Liang and Mudawar, 2017c).

When compared with a continuous dense droplet, quite a limited number of studies on hollow droplet impact are found. Due to the effects of cavitation bubbles, hollow droplets have more complex effects on both liquid flow and heat transfer than a continuous dense droplet does alone. Gulyaev and Solonenko (2013) experimentally studied a hollow droplet impact on a flat surface. The central counter jet was analyzed at different operating conditions. Kumar et al. (2012) numerically studied the hollow droplet impact on a flat surface using the VOF method. Hollow droplet impacting was compared with the impact of continuous dense droplets. The influence of the hollow droplet initial impact velocity and shell thickness on the impact dynamics was also analyzed. Li et al. (2018, 2019) used the CLSVOF method to investigate the dynamics and heat transfer associated with a hollow droplet impact on a dry flat surface and a liquid film, respectively. The differences between the hollow droplet impact and continuous dense droplet impact are mainly discussed.

As stated in a previous paragraph, the multi-droplet impact has received far less attention than the single droplet impact. Most of the work is focused on the impact on a solid wall (Park et al., 2012; Qiu et al., 2017). Quite a limited amount of research has focused on multiple droplets' impact on a liquid film. Cossali et al. (2004) were the first to experimentally investigate multiple droplets' impact on a liquid film. The effects of impacting velocity and film thickness were mainly analyzed. Soriano et al. (2014) experimentally investigated the hydrodynamics and heat transfer behaviors of multiple droplets' impact on a liquid film. Droplet spacing between adjacent impinging droplets plays an important role in heat transfer behavior. Raman et al. (2015) used the LBM to numerically study the dynamic behavior of two droplets impacting on a liquid film. The results showed that a larger separation gap between the droplets led to a delay in formation of a central jet, while the spread length increased. Liang et al. (2019) numerically investigated multiple droplets successively impacting on a liquid film using the CLSVOF method. It was revealed that successive impacts of multiple droplets increased the splashing thresholds for trailing droplets. Liang et al.(2018) also conducted numerical simulations on multiple droplets simultaneously impacting on the liquid film. A geometric model was established to explain the impact region that contained two semicircular regions and a series of rectangular regions during simultaneous impact. The variations in residual film thickness in each region as well as the total area and average film thickness were analyzed.

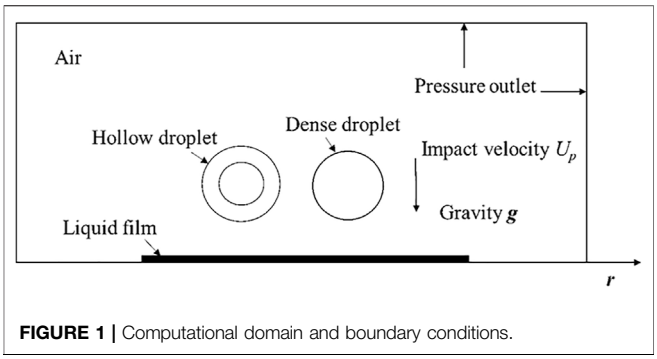

FIGURE 1 | Computational domain and boundary conditions.

However, there are a few studies on the case of the hollow droplet and continuous dense droplets simultaneously impacting on a liquid film. In high-pressure combustion and spay cooling, there are multiple droplets, namely, hollow droplets and continuous dense droplets, impacting on a liquid film. The investigations on a single droplet impacting on a liquid film could not reveal the effects of interaction of the droplets on the hydrodynamics and heat transfer mechanism of the multiple droplets impacting on a liquid film. Thus, it is significantly important and very necessary to deepen the understanding of this case. In this study, a numerical model was developed using the CLSVOF method to simulate droplet dynamics and heat transfer behaviors of a hollow droplet and a continuous dense droplet simultaneously impacting on the liquid film. The interface evolution and associated heat transfer characteristics of the droplets are mainly discussed. The governing mechanisms behind the dynamics and heat transfer behaviors are also analyzed. It is believed that this study will provide a fundamental understanding of high-pressure spray combustion and its associated applications involving hollow droplet impact.

METHODOLOGY

Problem Description

Figure 1 shows the geometric model of a hollow droplet and a dense droplet impinging on a liquid film. The two droplets share the same impacting velocity U_p. The initial diameter of the droplets D_0 is 2.091 mm with a dimensionless shell thickness δ_p^* of 0.25; the latter is defined as $\delta_p^* = \delta_p/D_p$, where δ_p is the shell thickness. The initial diameter of the continuous dense droplet D_0 is 2 mm, which has the same mass as the hollow droplet to ensure the same initial kinetic energy. The droplets horizontal spacing S is 3.2 mm. The initial thickness of the liquid film h_0 is 0.2091 mm. The droplets' temperature is 323 K, and the temperature of the

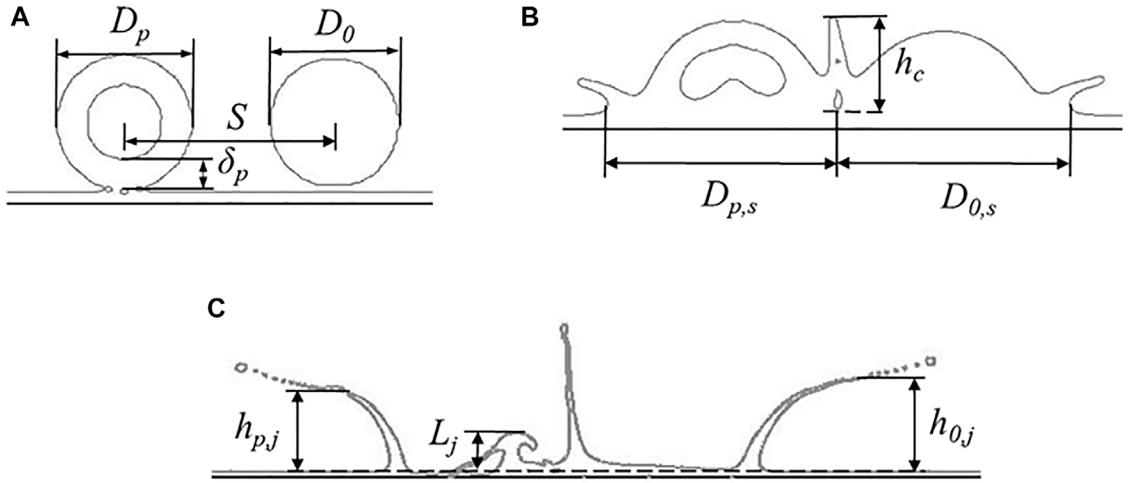

FIGURE 2 | Typical evolution stages in the impact of hollow droplet and continuous dense droplet on the liquid film: **(A)** droplets contact with liquid film, **(B)** central jet between droplets, and **(C)** counter jet inside the hollow droplet.

wall, liquid film, and surrounding air is 300 K. The physical properties and other parameters include liquid density ρ_l = 835 kg m^{-3}, air density ρ_g = 1.225 kg m^{-3}, surface tension coefficient σ = 0.039 N·m^{-1}, liquid viscosity μ_l = 2.745 × 10^{-3} Pa s^{-1}, air viscosity μ_g = 1.789 × 10^{-5} Pa s^{-1}, equilibrium contact angle θ = 30°, and gravity = 9.8 m s^{-2}.

Representative evolution stages prior to and after the droplets' impingement are presented in **Figures 2A–C**. The spreading diameters of the hollow and continuous dense droplets are $D_{p,s}$ and $D_{0,s}$, respectively. The height of the central jet between the droplets is h_c, and the heights of the edge jet of the hollow droplet and continuous dense droplet are $h_{p,j}$ and $h_{0,j}$, respectively. The height of the counter jet inside the hollow droplet is L_j. For convenience and being consistent with previous works, the spreading factor of a hollow droplet, the spreading factor of a dense droplet, the edge jet height of the hollow droplet, the edge jet height of the dense droplet, and the counter jet height were normalized based on the droplet diameters for analysis, i.e., $f_p = D_{p,s}/D_p$, $f_0 = D_{0,s}/D_0$, $h^*_{p,j} = h_{p,j}/D_p$, $h^*_{0,j} = h_{0,j}/D_0$, and $L^*_j = L_j/D_p$.

Numerical Method and Mode

In this study, the CLSVOF method (Sussman and Puckett, 2000) is employed to perform the simulations with the aid of the commercial software FLUENT. Continuity, momentum, and energy equations used throughout the domain include

$$\nabla \cdot \vec{V} = 0, \tag{1}$$

$$\frac{\partial}{\partial t}\left(\rho(\phi)\vec{V}\right) + \nabla \cdot \left[\rho(\phi)\vec{V}\vec{V}\right] = -\nabla p + \nabla \cdot \left[\mu(\phi)\left(\nabla\vec{V} + \nabla\vec{V}^T\right)\right] + \rho(\phi)\vec{g} - \vec{F}, \tag{2}$$

$$\frac{\partial}{\partial t}\left[\rho(\varphi)c_pT\right] + \nabla \cdot \left[\rho(\varphi)c_p\vec{V}T\right] = \nabla \cdot (\lambda\nabla T), \tag{3}$$

where $\vec{V}$, $\vec{g}$, and p represent velocity vector, gravitational acceleration, and pressure, respectively; $\mu(\varphi)$ and $\rho(\varphi)$ signify dynamic viscosity and density, respectively, and φ is the level set function; c_p, T, and λ are specific heat, temperature, and thermal conductivity, respectively, and $\vec{F}$ is the surface tension solved by the continuum surface force (CSF) model by Brackbill et al. (1992), expressed as

$$\vec{F} = \sigma\kappa(\varphi)\nabla H(\varphi), \tag{4}$$

$$H(\varphi) = \begin{cases} 0 & \varphi < -\delta_{tr} \\ \frac{1}{2} + \frac{\varphi}{2a} + \frac{1}{2\pi}\sin\left(\frac{\pi\varphi}{a}\right) & |\varphi| \le \delta_{tr} \\ 1 & \varphi > \delta_{tr} \end{cases} \tag{5}$$

where $\kappa(\varphi)$ and σ are interface curvature and surface tension coefficient, respectively; δ_{tr} denotes thickness of the transition region at the interface, and $\delta_{tr} = 1.5a$ is adopted in this study, where a is the minimum size of the computational cell. The smoothed $\rho(\varphi)$ and $\mu(\varphi)$ are respectively expressed as

$$\rho(\varphi) = \rho_g + \left(\rho_l - \rho_g\right)H(\varphi), \tag{6}$$

$$\mu(\varphi) = \mu_g + \left(\mu_l - \mu_g\right)H(\varphi), \tag{7}$$

where subscripts g and l represent gas and liquid phases, respectively.

Notice that the numerical method above is only briefly introduced, and more details about this method, in particular the solving schemes for the numerical method, can be found in the authors' previous studies (Li et al., 2018; Li et al., 2019).

In this work, a two-dimensional model that is shown in **Figure 1** is used, with a computational domain of 15 × 30 mm. For the purpose of accurately capturing the complex evolution of the central jet between droplets and the counter jet inside droplets, intensified adaptive meshes are used. Numerical

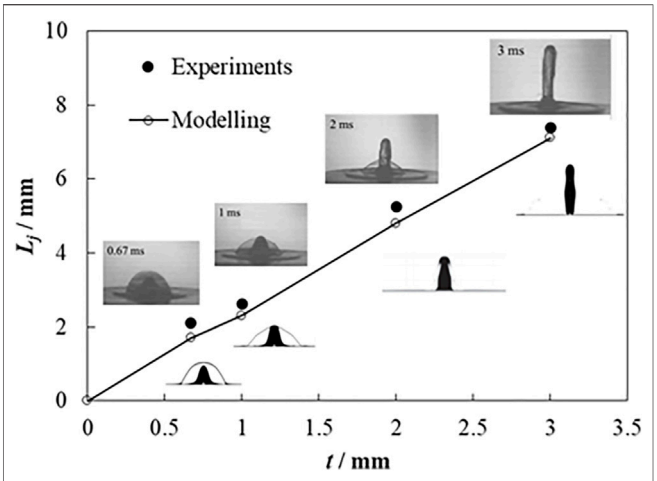

FIGURE 3 | Comparison of the experiment (Gulyaev and Solonenko, 2013) and simulation results for hollow droplet impact.

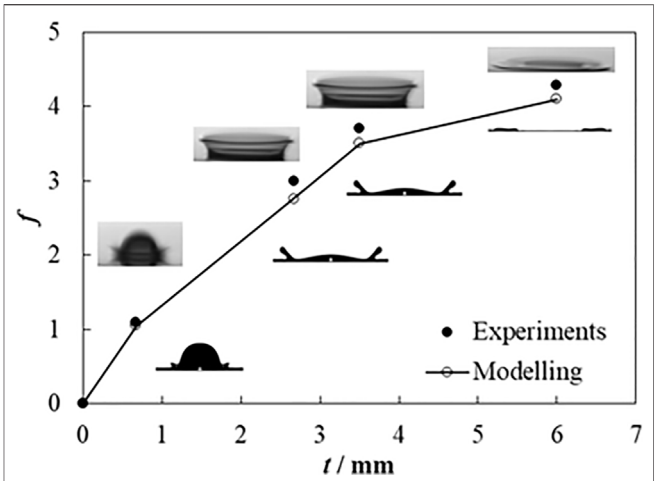

FIGURE 4 | Comparison of the experiment (Li et al., 2017) and simulation results for the continuous dense droplet.

results from the structured meshes with total grid numbers of 150,000, 186,000, and 252,000 are compared to check mesh independence. The numerical conditions include D_p = 2.091 mm, δ_p^* = 0.25, S = 3.2 mm, U_p = 6 m s^{-1}, and h_0 = 0.2091 mm. The spreading factor is set as the comparing criterion, and the results show that the spreading factors with grid numbers of 1,86,000 and 2,52,000 are very close to each other, but the result with the grid number of 1,50,000 has a large difference with the former two. Thus, the grid number of 1,86,000 is used to guarantee the calculation accuracy and also to save the computation resource. It needs to be pointed out that the two-dimensional model in this work has its limitation in simulating the genuine phenomenon of droplets interaction, but it will pave the way for further extension of a three-dimensional model including phase transition.

Model Validation

For the model validation, it will be a good choice to compare the numerical results with closely related experiments. Unfortunately, the experiments of a hollow droplet and a continuous dense droplet simultaneously impacting on a liquid film are not available at present. To warrant the effectiveness of the model, the cases of a hollow droplet impact, and a continuous dense droplet impact are validated, respectively. For the hollow droplet, only experimental results of the hollow droplet impact on a dry substrate are available (Gulyaev and Solonenko, 2013). The conditions are expressed as follows: a glycerin hollow droplet with an initial diameter D_p = 5.25 mm and dimensionless shell thickness δ_p^* = 0.082 at 5.94 m s^{-1} velocity impacting on a dry flat surface vertically. The droplet temperature is the same as ambient air. The comparison between the numerical results and experimental data is shown in **Figure 3**. It is found that they coincide much well with each other, in both the morphology of the impacting droplet and height of the central jet (L_j).

For the dense droplet, experimental observation and measurement from a previous study (Li et al., 2017) are used to validate the numerical result of a continuous dense droplet impact on a liquid film. The conditions are expressed as follows: a continuous dense droplet with an initial diameter D_0 = 2.378 mm at 2.1 m s^{-1} velocity vertically impacting on a liquid film with an initial thickness of 0.2 mm. The droplet temperature is the same as ambient air. The comparison is exhibited in **Figure 4**, which shows a very good agreement in droplet qualitative evolution and quantitative spreading factor.

RESULTS AND DISCUSSIONS

Morphology of Impacting Droplets

Figure 5 shows the interface evolution of a hollow droplet and a dense droplet simultaneously impacting on a liquid film, with the impact velocity of 6 m s^{-1}. The time when the droplets make contact with the liquid film is set as 0 ms.

As can be observed in **Figure 5**, the droplets spread after making contact with the liquid film. At 0.15 ms, the hollow droplet and continuous dense droplet collide, where the central jet can be found at the colliding point. Also, an entrapped air bubble emerges inside the central jet. At the outside spreading edge, a liquid sheet resulting from the effects of spreading potential, viscous dissipation, and surface tension is observed. At 0.35 ms, the central jet presents an oblique movement toward the hollow droplet. This is mainly due to the effect of the larger spreading potential of the continuous dense droplet, which produces larger colliding energy upon droplets' collision, causing an oblique central jet. Liquid at the top of the central jet ruptures, which produces secondary tiny droplets. Concomitantly, the fluid inside the hollow droplet converges at the impact center, where the counter jet is enveloped. At 0.45 ms, for the hollow droplet impact, the counter jet moves across the liquid shell, resulting in the rupture of the liquid shell. For the continuous dense droplet impact, fluid inside the liquid sheet deforms greatly as a groove, without the counter jet that appears inside the hollow droplet. It is also found that the liquid at the rim of the edge liquid sheet for continuous dense droplet breaks into secondary droplets, which cannot be found for the edge liquid sheet from the hollow

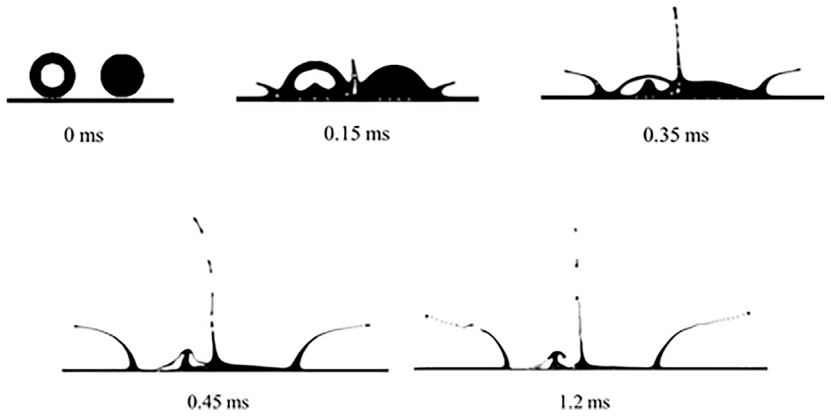

FIGURE 5 | Morphology of droplets impact on liquid film at 6 m s^{-1}.

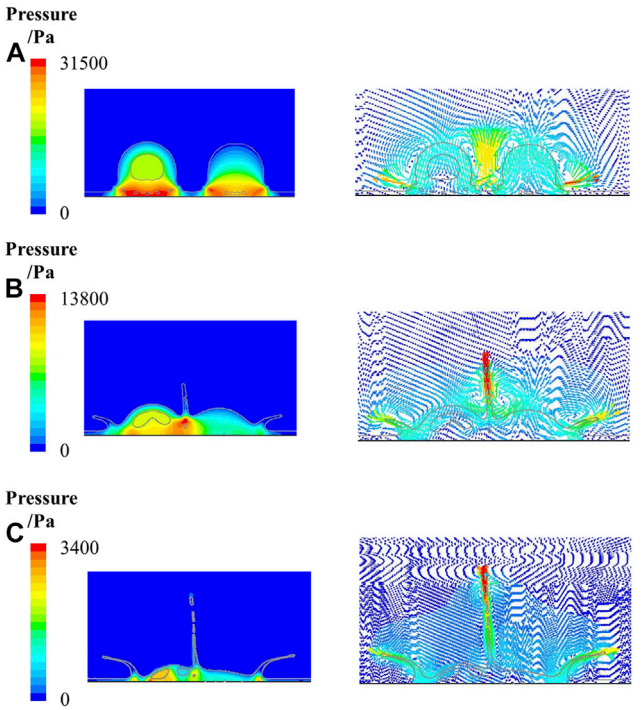

FIGURE 6 | Pressure and velocity distribution of droplets impact at different time instants: **(A)** 0.05 ms, **(B)** 0.2 ms, and **(C)** 0.5 ms.

droplet. At 1.2 ms, the liquid at the edge liquid sheet shows a more obvious splashing process for both the hollow droplet and the continuous dense droplet. Thus, the obliquely moving central jet and the counter jet are the unique features for the simultaneous impingement of a hollow droplet and a continuous dense droplet.

Fluid Dynamics Analysis

Figure 6 shows pressure and velocity distributions during a hollow droplet and a continuous dense droplet impacting on a liquid film simultaneously, where the conditions are the same to those shown in **Figure 5**.

As can be found in **Figure 6A**, at 0.05 ms, when the droplets make contact with the liquid film, pressures at the spreading edge for both the hollow droplet (31,453 Pa) and continuous dense droplet (29,864 Pa) are greater than the main part of the droplets, which causes the spreading of the droplets. The spreading velocities for the hollow droplet and continuous dense droplet are 13.9 and 14.769 m s^{-1}, respectively.

In **Figure 6B** at 0.2 ms, the maximum pressure is at the bottom of the central droplets (20,834 Pa). A large pressure gradient can be found within the central jet, which is the main cause for the formation of the central jet. Besides, pressures at the root of the edge liquid sheet for the hollow droplet and the continuous dense droplet are 7,877 and 8,957 Pa, respectively, which are the maximum in the edge liquid sheet area. The pressure gradient causes the formation of an edge jet. Also, the pressure gradient inside the counter jet within a hollow droplet decreases from the bottom (10,264 Pa) to the top (8,839 Pa), which is the main cause for the formation of the counter jet. As can been observed in the velocity distribution, the maximum velocity (14.48 m s^{-1}) of the central jet is at the top, which is larger than the spreading velocities of the hollow droplet (5 m s^{-1}) and continuous dense droplet (5.36 m s^{-1}), as well as the edge jet velocities of the hollow droplet (10 m s^{-1}) and continuous dense droplet (11.43 m s^{-1}). The maximum velocity at the top of the counter jet inside the hollow droplet is 1.525 m s^{-1}.

It can be seen from **Figure 6C** that at 0.5 ms, the pressure at the bottom of the central jet reduces to 2,173 Pa. The pressure gradient inside the central jet is not sufficient to sustain the development of the central jet. A breakup can be seen at the top of the central liquid jet, where the secondary droplets show significant kinetic splashing under fluid instabilities. Also, the pressures at the spreading edge (2,874 Pa) and the root of the edge jet (1,823 Pa) are larger than those of their surrounding areas, which means that the pressure gradient keeps resulting in spreading and edge jetting. The pressure gradient inside the counter jet within the hollow droplet is also large enough to keep forming the counter jet. As can be found in the velocity

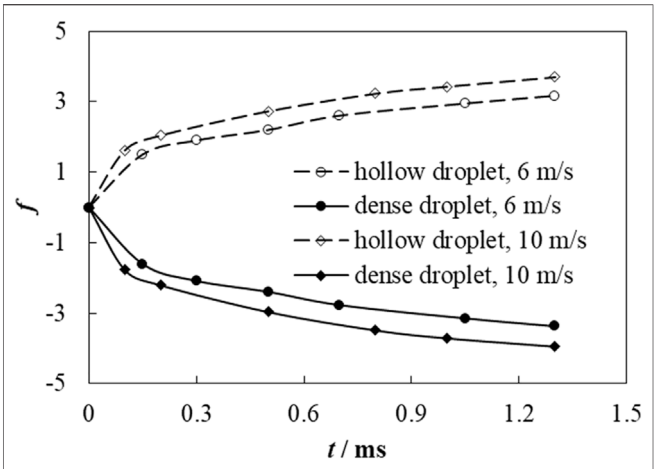

FIGURE 7 | Spreading factor of a hollow droplet and continuous dense droplet at impact velocities of 6 and 10 m s^{-1}.

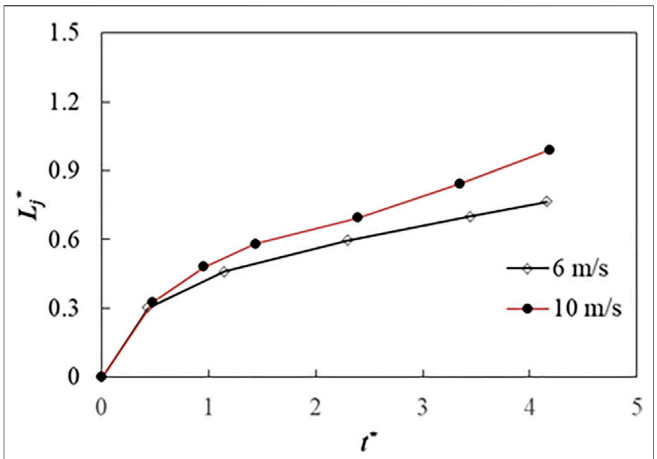

FIGURE 9 | Dimensionless counter jet height of hollow droplet at impact velocities of 6 and 10 m s^{-1}.

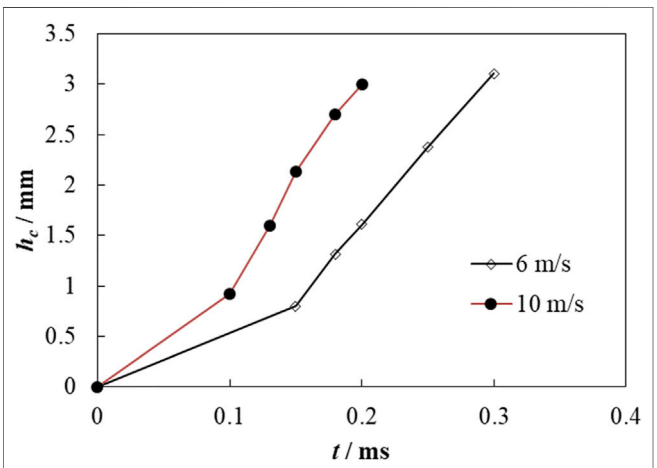

FIGURE 8 | Central jet height of droplets at impact velocities of 6 and 10 m s^{-1}.

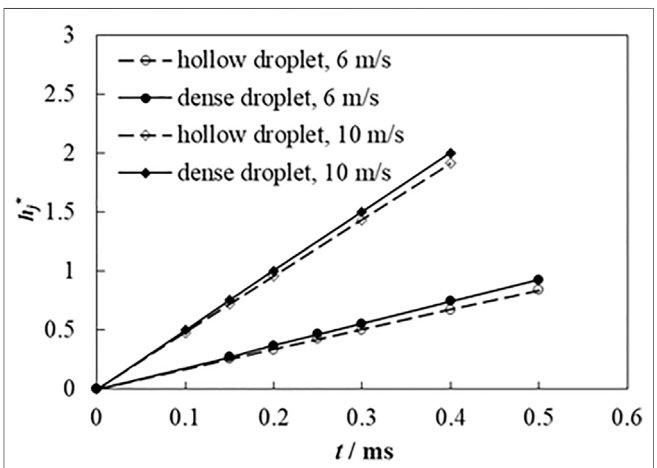

FIGURE 10 | Dimensionless edge jet height of hollow droplet and continuous dense droplet at impact velocities of 6 and 10 m s^{-1}.

distribution at the same instant, the velocity at the top of the central jet reduces to 5.21 m s^{-1}, while the velocity of the secondary droplets is 14.8 m s^{-1}. Also, the spreading velocities of the hollow droplet and continuous dense droplet reduce to 4.5 and 5.2 m s^{-1}, respectively, but the edge jet velocities of the hollow droplet and continuous dense droplet increase to 9.7 and 10.4 m s^{-1}, respectively. The velocities at the bottom of the central jet and counter jet are 0.7 and 0.7439 m s^{-1}, respectively, with an almost existing flow stagnation near this point. Note that it is more difficult to transfer the heat from the droplets to wall surface because of such an existence of flow stagnation.

Effects of Impact Velocity on Flow Characteristics

Figure 7 shows the spreading factor f of two droplets impacting on a liquid film, where S = 3.2 mm and U_p = 6 and 10 m s^{-1}. The spreading factors for the different droplets increase with time. Droplets with a higher impact velocity have larger spreading factors. The maximum spreading factors for the hollow droplet at 6 and 10 m s^{-1} are 3.17 and 3.7, respectively, while the maximum spreading factors for a continuous dense droplet at 6 and 10 m s^{-1} are 3.37 and 4.0, respectively. The spreading factor of a continuous dense droplet is always larger than that of a hollow droplet at different impact velocities.

Figure 8 shows the height of the central jet for droplets' impaction at different time instants and impact velocities. Droplets with different impact velocities have the same trend for the height of the central jet. At the initial stage of impact, the height of the central jet increases gently, while after t = 0.1 and 0.15 ms, the increasing trend is accelerated. Also, as can be seen in **Figure 6B**, an upward-moving flow is observed at the colliding point between the droplets caused by a high pressure at that point, which forms the central jet between the droplets. Due to this, the droplets with a higher impact velocity have greater spreading

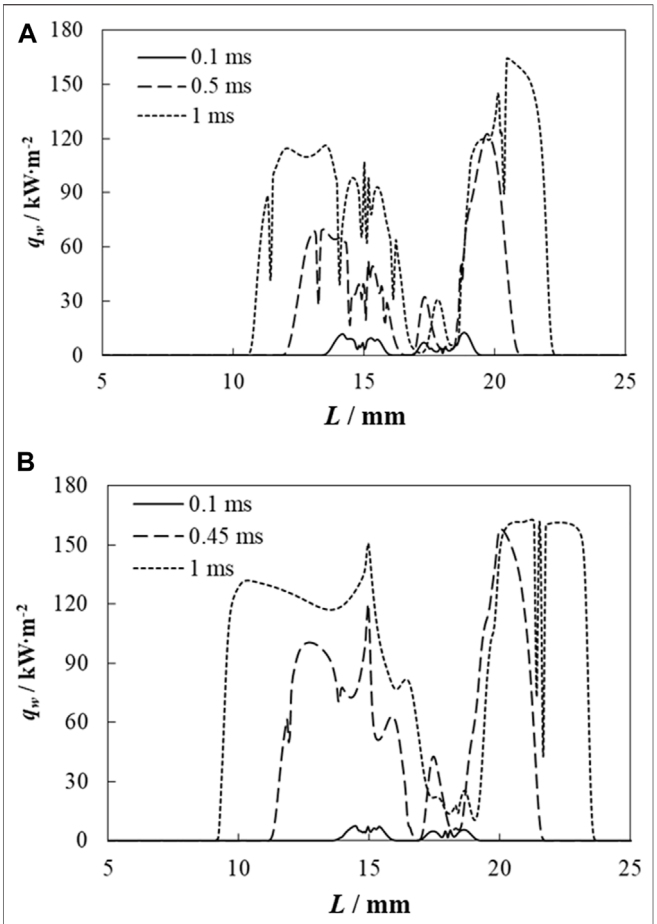

FIGURE 11 | Wall heat flux distribution at impact velocities of 6 and 10 m s^{-1}: **(A)** 6 m s^{-1} and **(B)** 10 m s^{-1}.

kinetic energy, which can be converted to a larger pressure at the colliding point between the droplets; consequently, a greater jetting potential can be formed in droplets' colliding. Therefore, the droplets with a higher impact velocity have a larger central jet height.

Figure 9 shows the dimensionless height of the counter jet inside a hollow droplet during droplets' impaction at the different velocities, where t*= tU_p/D_p. As can be seen in **Figure 9**, the dimensionless height of the counter jet is close to each other at different velocities at the initial stages of its formation. When t^* = 0.5, L_j^* at 6 m s^{-1} becomes smaller than at 10 m s^{-1}. With increasing time, the gap of L_j^* between the different velocities is enlarged significantly.

Figure 10 exhibits the dimensionless height of the edge jet during the droplets' impact on the liquid film at different impact velocities. It is found that the droplets with higher impact velocity have larger dimensionless heights of the edge jet. The dimensionless height of the edge jet for a continuous dense droplet is slightly larger than that for a hollow droplet. This means that the edge jet for a continuous dense droplet is easier to break up due to the effect of hydrodynamic instabilities, which is corresponding to the morphology of droplet impact shown in **Figure 5**.

Effects of Impact Velocity on Heat Transfer Characteristics

Figure 11 shows the distribution of wall heat flux (qw) when a hollow droplet and a continuous dense droplet impinge on a liquid film at several time instants under the impact velocities of 6 and 10 m s^{-1}, in which S = 3.2 mm. The wall heat flux qw can be expressed as

$$q_w = h_f (T_l - T_w), \tag{8}$$

where h_f is fluid-side local heat transfer coefficient, determined by

$$h_f = -\frac{\lambda}{\Delta T} \left.\frac{\partial T}{\partial y}\right|_{y=0}, \tag{9}$$

where λ is the thermal conductivity, ΔT is the temperature difference, and $\left.\frac{\partial T}{\partial y}\right|_{y=0}$ is the normal ratio of liquid temperature variation at the wall, and T_l and T_w are the local fluid temperature and wall surface temperature, respectively.

In **Figure 11A** at 0.1 ms, the wall heat flux is relatively low because the liquid film prohibits the thermal effect of the impacting droplets on the wall surface. As droplets spread, the interaction between the droplets and wall is enhanced remarkably. At 0.5 ms, the wall heat flux increases sharply, and the maximum wall heat flux reaches 126 kW m^{-2}. Due to the vortex flow near the wall surface, wall heat flux fluctuates at the droplets' impacting the area. When t = 1 ms, the maximum wall heat flux increases to 165.2 kW m^{-2}. It needs to be pointed that the wall heat flux at the hollow droplet–impacting area is larger than at the continuous dense droplet–impacting area. This is because the hollow droplet disturbance is more violent than the continuous dense droplets' due to the formation of a counter jet inside the hollow droplet. Also, it can be found that the thermally affected distances of the hollow droplet ($r_{h,p}$) are 4.8 and 6 mm at t = 0.5 and 1 ms, respectively, while the thermally affected distances of the continuous dense droplet ($r_{h,0}$) are 4.9 and 6.196 mm at t = 0.5 and 1 ms, respectively; the latter of these being slightly larger than those for the hollow droplet. It can be concluded that the dynamics of the impacting droplets affects heat transfer during impaction significantly. It is also found that at instants of 0.5 and 1 ms, when R = 16.5 and 17 mm, respectively, the wall heat flux almost decreases to zero. This is because of flow stagnation (as shown in **Figure 6C**) at this point due to the formation of the central jet that greatly inhibits heat transfer. This phenomenon should be considered and addressed in particular droplet spray applications.

In **Figure 11B**, when the impact velocity increases to 10 m s^{-1}, the wall heat flux distribution has almost the same trend as that of impacting at 6 m s^{-1}. At 0.45 ms, the maximum wall heat flux reaches 160.4 kW m^{-2}, which is very close to that at t = 1 ms for an impact velocity of 6 m s^{-1}. The thermally affected region of the continuous dense droplet is also larger than that of the hollow droplet at 0.45 and 1 ms, where $r_{h,0}$ = 5.6452 and 7.6452 mm, and $r_{h,p}$ = 5.512 and 7.315 mm, respectively. It can also be found that

$r_{h,0}$ and $r_{h,p}$ of the droplets impacting at 10 m s^{-1} are larger than those impacting at 6 m s^{-1}. This means that increasing the impact velocity can enhance heat transfer when the droplets impinge on a liquid film due to the intensified interaction between the droplets and wall surface at higher impact velocities.

CONCLUSION

With the aid of the CLSVOF method, a hollow droplet and a continuous dense droplet simultaneously impacting on a liquid film are numerically studied in this research. Spreading, central jet between droplets, and edge liquid sheet can be observed after droplets' impingement. Counter jet can be found inside a hollow droplet after impact, which is the main differential feature when compared with a continuous dense droplet. A pressure gradient is the main cause for spreading, central jet, edge liquid sheet, and counter jet formation. The impact velocity is closely related to the dynamics and heat transfer for droplets' impacting on liquid film. Droplets with a higher velocity have a larger spreading factor, central jet height, edge jet height, and counter jet height. The spreading factor and edge jet height for continuous dense droplets are larger than those for hollow droplets. Wall heat flux increases more notably for droplets with a higher impact velocity. A hollow droplet has a larger wall heat flux but a smaller thermally affected region than a continuous droplet. This study could provide guidelines for chip-level electronics cooling, internal combustion design, and surface coating.

DATA AVAILABILITY STATEMENT

The original contributions presented in the study are included in the article/Supplementary Material, further inquiries can be directed to the corresponding author.

AUTHOR CONTRIBUTIONS

GL and DH contributed to the conception and design of the study, and DL performed the simulations and wrote the first draft of the manuscript. All authors contributed to manuscript revision, and read and approved the submitted version.

FUNDING

Support of the National Natural Science Foundation of China under Grant No. 51876025 and NSAF Joint Fund under U2030112 is gratefully acknowledged.

REFERENCES

Alghoul, S. K., Eastwick, C. N., and Hann, D. B. (2011). Normal Droplet Impact on Horizontal Moving Films: an Investigation of Impact Behaviour and Regimes. *Exp. Fluids* 50 (5), 1305–1316. doi:10.1007/s00348-010-0991-0

Brackbill, J. U., Kothe, D. B., and Zemach, C. (1992). A Continuum Method for Modeling Surface Tension. *J. Comput. Phys.* 100 (2), 335–354. doi:10.1016/0021-9991(92)90240-y

Chen, Y., and Deng, Z. (2017). Hydrodynamics of a Droplet Passing through a Microfluidic T-junction. *J. Fluid Mech.* 819, 401–434. doi:10.1017/jfm.2017.181

Chen, Y., Liu, X., and Shi, M. (2013). Hydrodynamics of Double Emulsion Droplet in Shear Flow. *Appl. Phys. Lett.* 102 (5), 051609. doi:10.1063/1.4789865

Chen, Y., Wu, L., and Zhang, L. (2015). Dynamic Behaviors of Double Emulsion Formation in a Flow-Focusing Device. *Int. J. Heat Mass Transfer* 82, 42–50. doi:10.1016/j.ijheatmasstransfer.2014.11.027

Cossali, G., Marengo, M., and Santini, M. (2004). "Impact of Single and Multiple Drop Array on a Liquid Film," in *19th Annual Meeting of ILASS* (Nottingham, UK: ILASS Europe), 1–8. 06-08/09/2004.

Gulyaev, I. P., Solonenko, O. P., Gulyaev, P. Y., and Smirnov, A. V. (2009). Hydrodynamic Features of the Impact of a Hollow Spherical Drop on a Flat Surface. *Tech. Phys. Lett.* 35 (10), 885–888. doi:10.1134/S1063785009100034

Gulyaev, I. P., and Solonenko, O. P. (2013). Hollow Droplets Impacting onto a Solid Surface. *Experiments in Fluids* 54 (1), 1432. doi:10.1007/s00348-012-1432-z

Guo Jia-Hong, J. H., Dai Shi-Qiang, S. Q., and Dai Qin, Q. (2010). Experimental Research on the Droplet Impacting on the Liquid Film. *Acta Phys. Sin.* 59 (4), 2601–2609. doi:10.7498/aps.59.2601

Harlow, F. H., and Welch, J. E. (1965). Numerical Calculation of Time-dependent Viscous Incompressible Flow of Fluid with Free Surface. *Phys. Fluids* 8 (12), 2182–2189. doi:10.1063/1.1761178

Kumar, A., Gu, S., and Kamnis, S. (2012). Simulation of Impact of a Hollow Droplet on a Flat Surface. *Appl. Phys. A.* 109 (1), 101–109. doi:10.1007/s00339-012-7043-y

Kumar, A., Gu, S., Tabbara, H., and Kamnis, S. (2013). Study of Impingement of Hollow ZrO2 Droplets onto a Substrate. *Surf. Coat. Technology* 220, 164–169. doi:10.1016/j.surfcoat.2012.08.061

Lee, S. H., Hur, N., and Kang, S. (2011). A Numerical Analysis of Drop Impact on Liquid Film by Using a Level Set Method. *J. Mech. Sci. Technol.* 25 (10), 2567–2572. doi:10.1007/s12206-011-0613-7

Lee, T., and Liu, L. (2010). Lattice Boltzmann Simulations of Micron-Scale Drop Impact on Dry Surfaces. *J. Comput. Phys.* 229 (20), 8045–8063. doi:10.1016/j.jcp.2010.07.007

Li, D., and Duan, X. (2019). Numerical Analysis of Droplet Impact and Heat Transfer on an Inclined Wet Surface. *Int. J. Heat Mass Transfer* 128, 459–468. doi:10.1016/j.ijheatmasstransfer.2018.09.025

Li, D., Duan, X., Zheng, Z., and Liu, Y. (2018). Dynamics and Heat Transfer of a Hollow Droplet Impact on a Wetted Solid Surface. *Int. J. Heat Mass Transfer* 122, 1014–1023. doi:10.1016/j.ijheatmasstransfer.2018.02.017

Li, D. S., Qiu, X. Q., Zheng, Z. W., and Zhang, D. (2017a). Numerical Analysis of a Coupled Level Set-VOF Method for the Study of Droplet Impact on Wetted Surface. *J. Chem. Eng. Chin. Universities* 31 (3), 570–578.

Li, D., Zhang, D., and Zheng, Z. (2019). Numerical Analysis of Hollow Droplet Impacts on a Dry Flat Surface. *Int. J. Heat Mass Transfer* 129, 753–763. doi:10.1016/j.ijheatmasstransfer.2018.09.063

Li, D., Zhang, D., Zheng, Z., and Tian, X. (2017b). Numerical Analysis on Air Entrapment during a Droplet Impacts on a Dry Flat Surface. *Int. J. Heat Mass Transfer* 115, 186–193. doi:10.1016/j.ijheatmasstransfer.2017.08.023

Liang, G., Guo, Y., and Shen, S. (2014). Gas Properties on Crown Behavior and Drop Coalescence. *Numer. Heat Transfer, B: Fundamentals* 65 (6), 537–553. doi:10.1080/10407790.2014.884834

Liang, G., and Mudawar, I. (2017c). Review of Drop Impact on Heated walls. *Int. J. Heat Mass Transfer* 106, 103–126. doi:10.1016/j.ijheatmasstransfer.2016.10.031

Liang, G., and Mudawar, I. (2016). Review of Mass and Momentum Interactions during Drop Impact on a Liquid Film. *Int. J. Heat Mass Transfer* 101, 577–599. doi:10.1016/j.ijheatmasstransfer.2016.05.062

Liang, G., and Mudawar, I. (2017a). Review of spray Cooling - Part 1: Single-phase and Nucleate Boiling Regimes, and Critical Heat Flux. *Int. J. Heat Mass Transfer* 115, 1174–1205. doi:10.1016/j.ijheatmasstransfer.2017.06.029

Liang, G., and Mudawar, I. (2017b). Review of spray Cooling - Part 2: High Temperature Boiling Regimes and Quenching Applications. *Int. J. Heat Mass Transfer* 115, 1206–1222. doi:10.1016/j.ijheatmasstransfer.2017.06.022

Liang, G., Zhang, T., Chen, H., Yu, H., and Shen, S. (2019). Successive Impact of Multiple Droplets on Liquid Film. *Eur. J. Mech. - B/Fluids* 74, 389–398. doi:10.1016/j.euromechflu.2018.09.011

Liang, G., Zhang, T., Yu, H., Chen, H., and Shen, S. (2018). Simultaneous Impact of Multiple Droplets on Liquid Film. *J. Ind. Eng. Chem.* 65, 51–61. doi:10.1016/j.jiec.2018.04.011

Liu, X., Chen, Y., and Shi, M. (2013). Dynamic Performance Analysis on Start-Up of Closed-Loop Pulsating Heat Pipes (CLPHPs). *Int. J. Therm. Sci.* 65, 224–233. doi:10.1016/j.ijthermalsci.2012.10.012

Liu, X., Zhang, C., Yu, W., Deng, Z., and Chen, Y. (2016). Bubble Breakup in a Microfluidic T-junction. *Sci. Bull.* 61 (10), 811–824. doi:10.1007/s11434-016-1067-1

Lü, M., Ning, Z., Yan, K., Fu, J., and Sun, C. (2015). Instability and Breakup of Cavitation Bubbles within Diesel Drops. *Chin. J. Chem. Eng.* 23 (1), 262–267. doi:10.1016/j.cjche.2014.10.009

Negeed, E.-S. R., Albeirutty, M., and Takata, Y. (2014). Dynamic Behavior of Micrometric Single Water Droplets Impacting onto Heated Surfaces with TiO2 Hydrophilic Coating. *Int. J. Therm. Sci.* 79, 1–17. doi:10.1016/j.ijthermalsci.2013.12.011

Negeed, E.-S. R., Hidaka, S., Kohno, M., and Takata, Y. (2013). High Speed Camera Investigation of the Impingement of Single Water Droplets on Oxidized High Temperature Surfaces. *Int. J. Therm. Sci.* 63, 1–14. doi:10.1016/j.ijthermalsci.2012.07.014

Oguz, H. N., and Prosperetti, A. (1989). Surface-tension Effects in the Contact of Liquid Surfaces. *J. Fluid Mech.* 203, 149–171. doi:10.1017/s0022112089001412

Park, J. Y., Min, C. K., Granick, S., and Cahill, D. G. (2012). Residence Time and Heat Transfer when Water Droplets Hit a Scalding Surface. *J. Heat Transfer-Transactions Asme* 134 (10), 101503. doi:10.1115/1.4006802

Peck, B., and Sigurdson, L. (1994). The Three-dimensional Vortex Structure of an Impacting Water Drop. *Phys. Fluids* 6 (2), 564–576. doi:10.1063/1.868352

Pravinraj, T., and Patrikar, R. (2017). Modelling and Investigation of Partial Wetting Surfaces for Drop Dynamics Using Lattice Boltzmann Method. *Appl. Surf. Sci.* 409, 214–222. doi:10.1016/j.apsusc.2017.02.242

Qiu, L., Dubey, S., Choo, F. H., and Duan, F. (2017). The Statistical Analysis of Droplet Train Splashing after Impinging on a Superheated Surface. *J. Heat Transfer-Transactions Asme* 139 (5), 052201. doi:10.1115/1.4035661

Raman, K. A., Jaiman, R. K., Lee, T. S., and Low, H. T. (2015). On the Dynamics of crown Structure in Simultaneous Two Droplets Impact onto Stationary and Moving Liquid Film. *Comput. Fluids* 107, 285–300. doi:10.1016/j.compfluid.2014.11.007

Rocco, G., Coppola, G., and De Luca, L. (2010). Simulation of Drop Impact on a Thin Liquid Film by Means of the VOF Method. *Aerotecnica* 89 (1), 25–35.

Roisman, I. V., and Tropea, C. (2002). Impact of a Drop onto a Wetted wall: Description of crown Formation and Propagation. *J. Fluid Mech.* 472, 373–397. doi:10.1017/S0022112002002434

Sivakumar, D., and Tropea, C. (2002). Splashing Impact of a spray onto a Liquid Film. *Phys. Fluids* 14 (12), L85–L88. doi:10.1063/1.1521418

Soriano, G. E., Zhang, T., and Alvarado, J. L. (2014). Study of the Effects of Single and Multiple Periodic Droplet Impingements on Liquid Film Heat Transfer. *Int. J. Heat Mass Transfer* 77, 449–463. doi:10.1016/j.ijheatmasstransfer.2014.04.075

Stevens, C. S. (2014). Scaling of the Splash Threshold for Low-Viscosity Fluids. *Epl* 106 (2), 24001. doi:10.1209/0295-5075/106/24001

Sussman, M., and Puckett, E. G. (2000). A Coupled Level Set and Volume-Of-Fluid Method for Computing 3D and Axisymmetric Incompressible Two-phase Flows. *J. Comput. Phys.* 162 (2), 301–337. doi:10.1006/jcph.2000.6537

Wang, H., Zhao, Z., Liu, Y., Shao, C., Bian, F., and Zhao, Y. (2018a). Biomimetic Enzyme cascade Reaction System in Microfluidic Electrospray Microcapsules. *Sci. Adv.* 4 (6). doi:10.1126/sciadv.aat2816

Wang, J., Gao, W., Zhang, H., Zou, M., Chen, Y., and Zhao, Y. (2018b). Programmable Wettability on Photocontrolled Graphene Film. *Sci. Adv.* 4 (9), eaat7392. doi:10.1126/sciadv.aat7392

Wang, J., Sun, L., Zou, M., Gao, W., Liu, C., Shang, L., et al. (2017). Bioinspired Shape-Memory Graphene Film with Tunable Wettability. *Sci. Adv.* 3 (6), e1700004. doi:10.1126/sciadv.1700004

Yarin, A. L. (2006). DROP IMPACT DYNAMICS: Splashing, Spreading, Receding, Bouncing. *Annu. Rev. Fluid Mech.* 38, 159–192. doi:10.1146/annurev.fluid.38.050304.092144

Zhang, T., Muthusamy, J. P., Alvarado, J. L., Kanjirakat, A., and Sadr, R. (2016). Numerical and Experimental Investigations of crown Propagation Dynamics Induced by Droplet Train Impingement. *Int. J. Heat Fluid Flow* 57, 24–33. doi:10.1016/j.ijheatfluidflow.2015.10.003

Conflict of Interest: The author DL is employed by CNOOC Research Institute Co. Ltd.

The remaining authors declare that the research was conducted in the absence of any commercial or financial relationships that could be construed as a potential conflict of interest.

Publisher's Note: All claims expressed in this article are solely those of the authors and do not necessarily represent those of their affiliated organizations, or those of the publisher, the editors, and the reviewers. Any product that may be evaluated in this article, or claim that may be made by its manufacturer, is not guaranteed or endorsed by the publisher.

NOMENCLATURE

a Minimum size of computational cell

c_p Specific heat

D_p Initial diameter of hollow droplet

$D_{p,s}$ Spreading diameter of hollow droplet

D_0 Initial diameter of continuous dense droplet

$D_{0,s}$ Spreading diameter of continuous dense droplet

f Spreading factor

$\vec{F}$ Source term of surface tension

$\vec{g}$ Gravity vector

h Heat transfer coefficient

h_c Central jet height

$h_{p,j}$ Edge jet height of hollow droplet

$h_{0,j}$ Edge jet height of continuous dense droplet

H Heaviside function

L Radius coordinate

L_j Height of counter jet

$\hat{n}_w$ Unit vector normal to wall

p Pressure

q_w Wall heat flux

$r_{h,p}$ Thermally affected distance of hollow droplet

$r_{h,p}$ Thermally affected distance of hollow droplet

S Droplets horizontal interval

t Time

U_p Impact velocity

$\vec{V}$ Velocity vector

y Direction normal to wall

Greek symbols

δ_p Shell thickness

θ Equilibrium contact angle

$\kappa\ (\phi)$ Interface curvature

λ Thermal conductivity

μ Viscosity

ρ Density

σ Surface tension coefficient

$\hat{\tau}_w$ Unit vector tangential to wall

ϕ Level set function

Superscript

* Dimensionless

Subscripts

g Gas phase

l Liquid phase.

frontiers | Frontiers in Energy Research

BRIEF RESEARCH REPORT
published: 30 May 2022
doi: 10.3389/fenrg.2022.918161

Application of Monodisperse Encapsulated Phase Change Materials in Building Thermal Energy Storage

Zhenya Li[1], Chuanliang Liu[1], Yingying Chen[2,3]*, Ning Hao[1], Li Jiang[1] and Wenjie Bian[1]*

[1]Shanghai Power Equipment Research Institute Co. Ltd, Shanghai, China, [2]Ningbo Water Meter(Group) Co. Ltd., Ningbo, China, [3]College of Electrical, Energy and Power Engineering, Yangzhou University, Yangzhou, China

Monodisperse encapsulated phase change materials (PCMs) are fabricated *via* microfluidic technology. To evaluate the thermoregulation ability of PCM capsules applied in building thermal energy storage, a gypsum model house with PCM capsules embedded is prepared. The temperature revolutions outside and inside the gypsum model house with different PCM capsules filling ratios are investigated. The effect of the filling ratio of the PCM on the thermoregulation performance is discussed. The potential application of monodisperse encapsulated PCMs in building thermal energy storage is verified. Attributing to the PCM capsules, the thermal response of the gypsum model house to the varying environmental temperature is retarded. As the filling ratios increase, the thermoregulation performance of the gypsum model house is better.

Keywords: phase change materials, thermal energy storage, encapsulation, droplet microfluidics, thermoregulation

OPEN ACCESS

Edited by:
Chengbin Zhang,
Southeast University, China

Reviewed by:
Feng Yao,
Suzhou University of Science and Technology, China
Jiayi Zheng,
Nanjing University of Science and Technology, China

****Correspondence:***
Chuanliang Liu
liuchuanliang@speri.com.cn
Yingying Chen
18362825932@163.com

Specialty section:
This article was submitted to Process and Energy Systems Engineering, a section of the journal Frontiers in Energy Research

Received: *12 April 2022*
Accepted: *26 April 2022*
Published: *30 May 2022*

Citation:
Li Z, Liu C, Chen Y, Hao N, Jiang L and Bian W (2022) Application of Monodisperse Encapsulated Phase Change Materials in Building Thermal Energy Storage. Front. Energy Res. 10:918161. doi: 10.3389/fenrg.2022.918161

INTRODUCTION

Phase change materials (PCMs), which can absorb or release heat during the melting or solidification process, can be applied to indoor thermal comfort (Deng et al., 2021; Lamrani et al., 2021), personal thermal management (Shi et al., 2021; Li et al., 2021), electronic cooling (Wang et al., 2021; Kothari et al., 2021), photothermal functional surface (Wang et al., 2018; Wang et al., 2017), and solar energy storage (Zhang et al., 2020; Javadi et al., 2020; Kumar et al., 2020), as shown in **Figure 1**. However, the leakage of PCMs may lead to corrosion or fire risk (Hu, 2020). Hence, it is important to encapsulate the PCMs with a shell or supporting matrix (Su et al., 2015).

There are several approaches for the encapsulation of PCMs (Milián et al., 2017), which are usually categorized into physical methods and chemical methods, including spray drying (Borreguero et al., 2011), interfacial polycondensation (Zhang and Rochefort, 2012), suspension polymerization (Sánchez-Silva et al., 2010), and emulsion polymerization (Zhang et al., 2019). However, traditional encapsulation approaches suffer from low encapsulation efficiency and poor monodispersity, which makes it hard to obtain encapsulated PCMs with stable thermal properties (Cárdenas-Ramírez et al., 2020). Recently, droplet microfluidics technology shed light on the encapsulation of PCMs, for the precise control of a single droplet (Chen et al., 2015) and high encapsulation efficiency (Liang et al., 2014; Chen and Deng, 2017; Zhang et al., 2018; Akamatsu et al., 2019). Wen et al. prepared the phase change microfibers with core–shell structure by a facile and controllable microfluidic strategy (Wen et al., 2015). Shi et al. prepared polyurea microcapsules containing paraffin *via* a microfluidic device, with an encapsulation efficiency of 96.5% (Shi et al., 2020). Han et al. achieved the precisely microfluidic encapsulation of PCMs with high

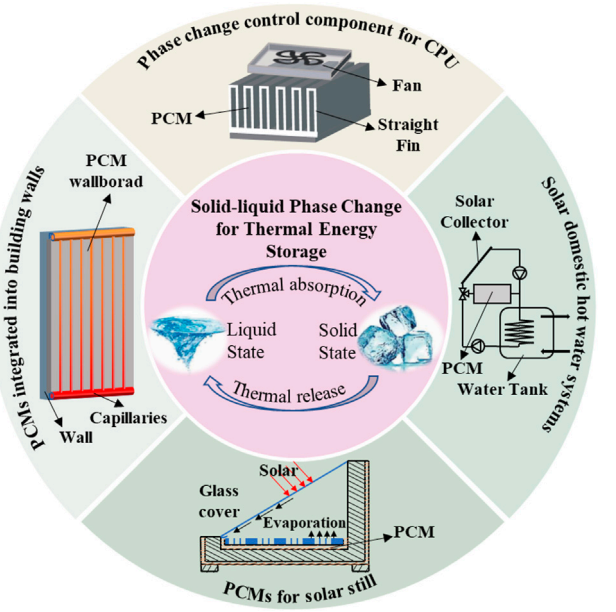

FIGURE 1 | Applications of the PCMs.

monodispersity (Han et al., 2020). Hao et al. introduced multilayer graphene to the preparation of encapsulated PCMs *via* microfluidic technology (Hao et al., 2022). The thermoregulation ability of the PCM capsules is enhanced while the degeneration of energy storage capacity is negligible. However, there are few studies on the thermoregulation capacity of monodisperse encapsulated PCMs *via* microfluidic technology for building thermal energy storage.

In this study, PCM capsules are generated *via* microfluidic technology. A thermoregulation experiment system is built to test the thermal performance of the gypsum model house embedded with the PCM capsules. The temperature distributions inside the gypsum model house and outside the gypsum model house are investigated. The effect of the filling ratio of the PCM on the thermoregulation performance is discussed. The potential application of monodisperse encapsulated PCMs in building thermal energy storage is verified.

EXPERIMENTAL SETUP AND METHODS

Preparation of PCM Capsules

In this study, the PCM capsule emulsion template is obtained by a microfluidic chip made of two capillaries in this paper (Chen et al., 2013). The details about the fabrication and structure of the microfluidic chip can be found in our previous study (Hao et al., 2022). The inner phase fluid is paraffin RT25 with a phase change temperature of 22–27°C, and the outer phase fluid is low viscosity sodium alginate ($C_6H_7O_6Na$) aqueous solution with a mass fraction of 3 wt%. The emulsion template is introduced into the collection unit, and then the shell is solidified by chemical reaction to prepare the wet PCM capsules. The calcium chloride ($CaCl_2$) aqueous solution with a mass fraction of 5 wt% is filled in the collection unit. Subsequently, the dry PCM capsules are obtained after putting the wet PCM capsules into an oven at 30°C. The coefficient of variation of the PCM capsules prepared in this study is less than 2%, indicating that the PCM capsules have good monodispersity. The dimensional parameter M is defined as the mass ratio between the core material RT25 of the PCM capsules and the shell calcium alginate to characterize the core–shell structure of PCM capsules. The PCM capsules with M = 11.2 are used in this study. The melting enthalpy and solidification enthalpy of PCM capsules are $\triangle H_m$ = 165.9 (J/g) and $\triangle H_c$ = 166.1 J/g.

Experimental System for Characterization of Thermoregulation

In order to systematically characterize the thermal regulation ability, a gypsum model house filled with PCM capsules (radius of 1.5-mm) is designed and built, and then the temperature changes on the surface and inside the model house with different filling ratios (*FR*s) of PCM capsules under the condition of infrared radiation heating are observed experimentally. The dimension of the gypsum model house is 50 mm in length, 25 mm in width, and 30 mm in height. The experimental system diagram of thermal regulation characterization of PCM capsules is shown in **Figure 2**. The gypsum model house is heated by radiant heat, and the surface and internal temperatures of the model house are measured and recorded using an infrared thermal imager (TH9260, Japan Electric Co., Ltd., Japan) and a thermocouple thermometer (K type, Omega Co., Ltd., United States), The temperature measuring points inside the gypsum model house are arranged as T_{I1}, T_{I2}, and T_{I3} successively from the heat source side (as shown in **Figure 1**).

In this experiment, the *FR* of PCM capsules in the gypsum board is adjusted by changing the number of filled PCM capsules of the same size. The number of PCM capsules filled in a single gypsum board is 0, 20, 35, and 60, respectively, and the *FR* of PCM capsules is 0%, 11.91%, 20.85%, and 35.74%, respectively, according to **Eq. 1**.

$$FR(\%) = \frac{N_{capsule} V_{capsule}}{V_{gb}}. \quad (1)$$

Here, $V_{capsule}$ and V_{gb} represent the volume of PCM capsules and gypsum board, respectively, and $N_{capsule}$ indicates the number of PCM capsules inside the gypsum board.

RESULTS AND DISCUSSION

During the heating process, the initial temperature of the model house with filling rates of 0%, 11.91%, 20.85%, and 35.74% is the same as the ambient temperature (15.5°C). **Figure 3** presents the comparison of infrared thermal images of the model house surface during the heating and cooling stages under infrared light source thermal radiation with different *FR*s of PCM capsules. As expected, the surface temperature of the gypsum model house increases significantly after the infrared light source is turned on. At the initial stage of the heating process (before 4.5 min), there is no clear

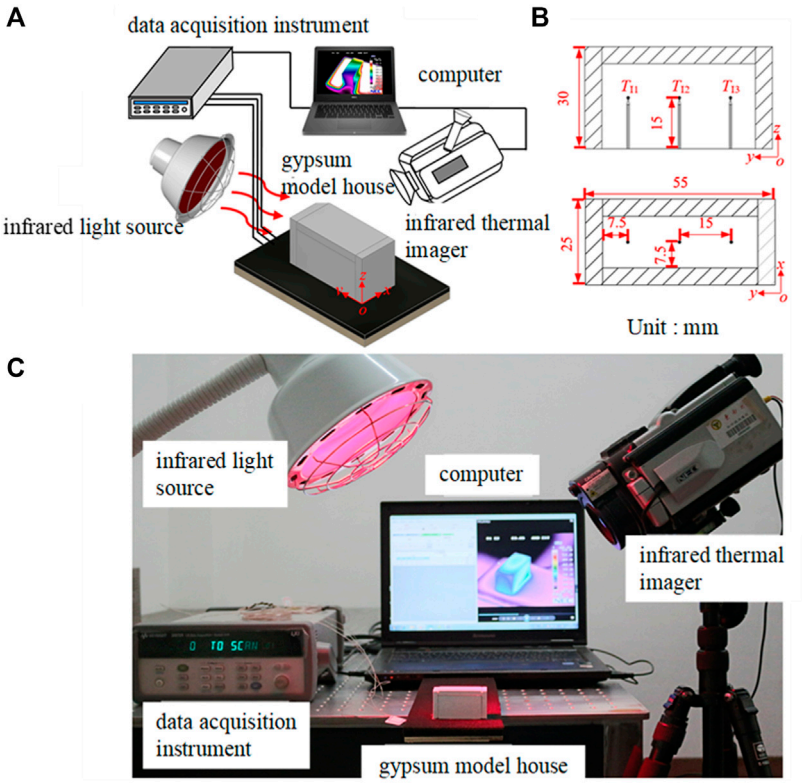

FIGURE 2 | Thermal regulation characterization experiment of PCM capsules: **(A)** schematic diagram; **(B)** structure of the model house; **(C)** photograph of the experimental system.

difference between the infrared thermal images on the gypsum model house surface with different *FR*s. It can be explained that the change of the surface temperature mainly depends on the radiation heat of the infrared light source. As time goes on, the surface temperature of the gypsum model house further rises and reaches the melting point of RT25. At this time, the surface temperature of the gypsum model house begins to be affected by the PCM capsules filled inside. Since the PCM contained in the capsules absorb part of the energy from the external environment in the melting process, the rising surface temperature of the gypsum model house can be effectively reduced. Therefore, it can be seen that the surface temperature of the gypsum model house filled with PCM capsules is significantly lower than that without PCM capsules at the same time. In addition, with the increase in heating time, the continuous endothermic melting process of the internal PCM further slows down the rise of the surface temperature. Therefore, it can be seen that as heating time goes on, the difference in the surface temperature between the gypsum model house with $FR > 0\%$ and that with $FR = 0\%$ becomes more obvious. In addition, for the gypsum model house with higher *FR*, the volume of PCM inside the model house is higher, so more heat can be absorbed from the surrounding environment. Thus, the thermal response of the gypsum model house to the rising environmental temperature is retarded.

Under the thermal radiation of an infrared light source, three thermocouples (T_{I1}, T_{I2}, and T_{I3}) are used to measure the inside temperature of the gypsum model house with different *FR*s, and T_{avg} is the arithmetical average of the temperature measured by the three thermocouples. As seen in **Figure 4A**, at the initial heating stage, there is little difference in the internal temperature of the gypsum model house with different *FR*s, because the melting point of most PCMs has not been reached at this time, and the rising temperature mainly depends on sensible heat of gypsum board and PCM capsules. In addition, when the environment temperature rises to the melting point of PCM, the PCM begins to melt and absorbs heat from the environment, thus reducing the rising rate of the temperature inside the model house. Compared with the gypsum model house filled with PCM capsules, the overall temperature variations of the gypsum model house filled with PCM capsules are significantly less. As *FR* increases, there are more PCMs in the gypsum model house, so more heat can be absorbed by PCM during the melting process. The retarded thermal response of the gypsum model house to the rising environmental temperature is more obvious. Therefore, the curve of the inside temperature of the gypsum model house is gentler with the increasing *FR*.

As seen in **Figure 3**, during the heating stage, before the melting of the PCMs, the surface temperature of the gypsum model house is not affected by *FR*. So, the initial temperature of the cooling stage is set at 30°C. First, the gypsum model house is heated by infrared thermal radiation till its internal temperature reaches 30°C. The gypsum model house with different *FR*s is cooled by natural convection at ambient temperature (18°C). It

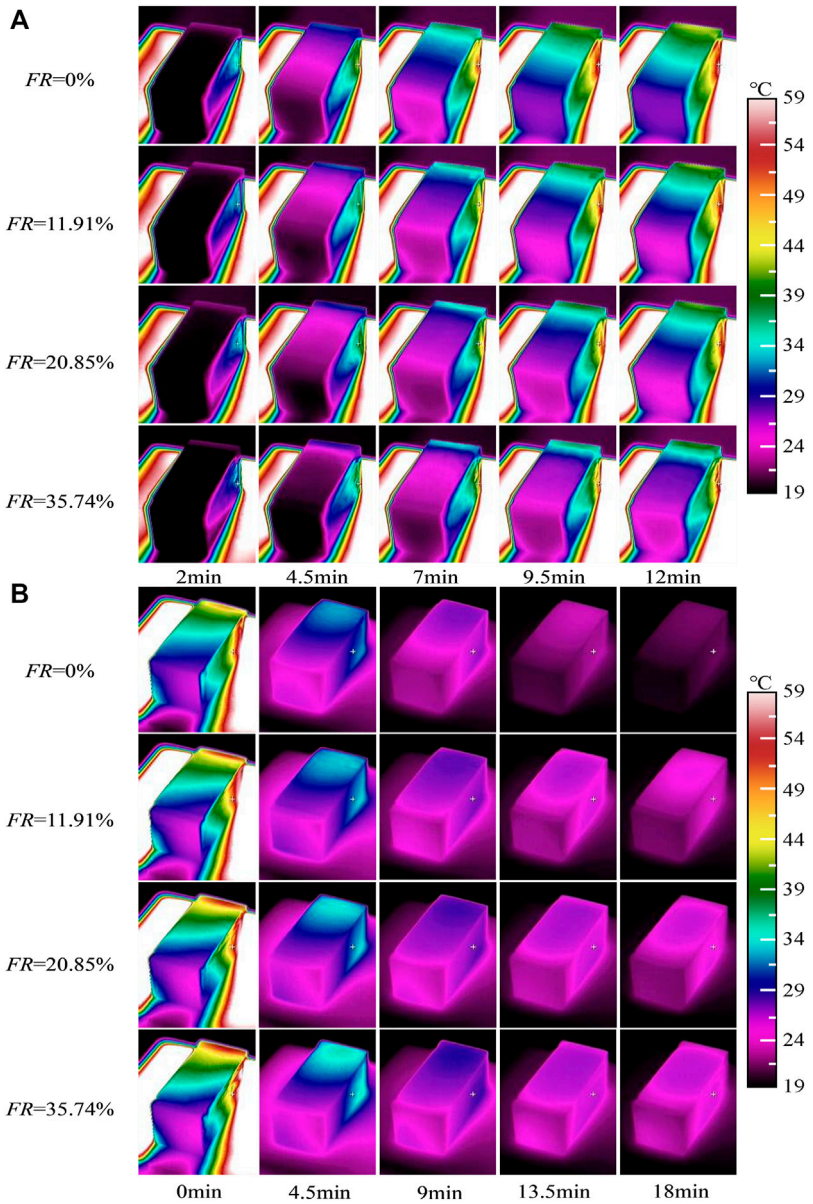

FIGURE 3 | Surface temperature distribution of model house with different *FRs*: **(A)** heating stage; **(B)** cooling stage.

can be seen from the variations of the infrared thermal image of the gypsum model house (shown in **Figure 3B**) that the gypsum model house surface temperature drops rapidly when the infrared light source is turned off. As it reaches the solidification range of RT25 (22–27°C), PCM solidifies and releases heat which can offset part of the heat in the environment released by the gypsum model house and slow down the drop in surface temperature of the house. As a result, it can be seen that the gypsum model house surface temperature filled with PCM capsules is significantly higher than that without PCM capsules. In addition, when *FR* increases, the heat released during solidification also increases, and the gypsum model house surface temperature is higher at the same time. Combined with what is presented in **Figure 3B**, at the initial cooling stage, there is basically no difference in the internal temperature of the gypsum model house with different filling rates. This is because the temperature of PCM has not reached the solidification point, and the drop in the temperature is mainly caused by the sensible heat decrease of the gypsum board and PCM under natural convection. When the ambient temperature drops to the solidification temperature of PCM, the PCM releases heat to the surrounding environment under the action of latent heat, thus slowing down the decrease of the internal temperature of the gypsum model house. It can also be seen that when the *FR* increases, the declining trend of the internal temperature of the gypsum model house filled with more PCM capsules will be slower.

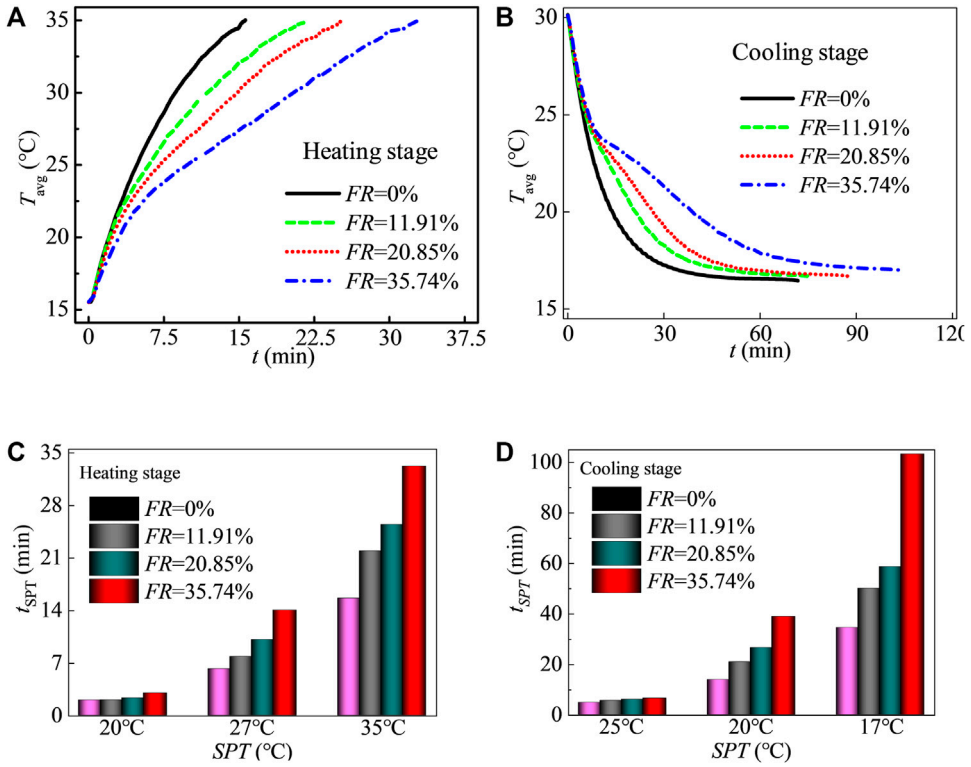

FIGURE 4 | Thermal performance of the model house with different *FRs*: **(A)** temperature distributions inside the model house during the heating stage; **(B)** temperature distributions inside the model house during the cooling stage; **(C)** time required for the model house to reach SPTs during the heating stage; **(D)** heating stage; **(B)** time required for the model house to reach SPTs during the cooling stage.

In order to more intuitively characterize the thermoregulation ability of PCM capsules, the time required for the temperature of the gypsum model house to reach the three set point temperatures (SPTs) of 20°C, 27°C, and 35°C in the heating stage are calculated, respectively. In addition, the time required for the temperature of the gypsum model house to reach 25°C, 20°C, and 17°C in the cooling stage are also calculated. As seen in **Figures 4C,D**, both during the heating and cooling stage, the time required to reach the three SPTs increases with the increasing *FR*, and the difference in the required time is most obvious at 30°C and 17°C. At this temperature, the PCM filled inside the capsules has completely absorbed or released all its latent heat through the melting or solidification process. For the filling ratio of 11.91%, 20.85%, and 35.74%, the time required to reach the SPT of 17°C during the cooling stage increases by 44.8%, 69.9%, and 198.8%, respectively. So, the thermoregulation effect of the PCM on the gypsum model house is strongest at this temperature.

CONCLUSION

In this study, the PCM capsules with good monodispersity are generated *via* microfluidic technology. The potential application of monodisperse encapsulated PCMs in building thermal energy storage is tested by the thermoregulation experiment of the gypsum model house embedded by the PCM capsules. The results indicate that the variation of the inside and outside surface temperatures of the model house decreases due to the heat capacity of the PCM capsules. Attributing to the PCM capsules, the thermal response of the gypsum model house to the varying environmental temperature is retarded. As the filling ratios increase, the thermoregulation performance of the gypsum model house is better. For the filling ratio of 11.91%, 20.85%, and 35.74%, the time required to reach the SPT of 17°C during the cooling stage increases by 44.8%, 69.9%, and 198.8%, respectively. Hence, the application of the monodisperse encapsulated PCMs in building thermal energy storage is verified.

DATA AVAILABILITY STATEMENT

The raw data supporting the conclusions of this article will be made available by the authors, without undue reservation.

AUTHOR CONTRIBUTIONS

CL and YC contributed to the conception and design of the study. ZL performed the statistical analysis and wrote the first draft of the manuscript. NH, LJ, and WB wrote sections of the manuscript. All authors contributed to manuscript revision, read, and approved the submitted version.

REFERENCES

Akamatsu, K., Ogawa, M., Katayama, R., Yonemura, K., and Nakao, S.-I. (2019). A Facile Microencapsulation of Phase Change Materials within Silicone-Based Shells by Using Glass Capillary Devices. *Colloids Surfaces A Physicochem. Eng. Aspects* 567, 297–303. doi:10.1016/j.colsurfa.2019.01.076

Borreguero, A. M., Valverde, J. L., Rodríguez, J. F., Barber, A. H., Cubillo, J. J., and Carmona, M. (2011). Synthesis and Characterization of Microcapsules Containing RubithermRT27 Obtained by Spray Drying. *Chem. Eng. J.* 166, 384–390. doi:10.1016/j.cej.2010.10.055

Cardenas-Ram, C., Jaramillo, F., and G Mez, M. (2020). Systematic Review of Encapsulation and Shape-Stabilization of Phase Change Materials. *J. Energy Storage* 30, 101495. doi:10.1016/j.est.2020.101495

Chen, Y., and Deng, Z. (2017). Hydrodynamics of a Droplet Passing through a Microfluidic T-Junction. *J. Fluid Mech.* 819, 401–434. doi:10.1017/jfm.2017.181

Chen, Y., Liu, X., and Shi, M. (2013). Hydrodynamics of Double Emulsion Droplet in Shear Flow. *Appl. Phys. Lett.* 102, 051609. doi:10.1063/1.4789865

Chen, Y., Wu, L., and Zhang, L. (2015). Dynamic Behaviors of Double Emulsion Formation in a Flow-Focusing Device. *Int. J. Heat Mass Transf.* 82, 42–50. doi:10.1016/j.ijheatmasstransfer.2014.11.027

Deng, Z., Zhang, X., Zhang, Y., Jiang, S., and Yu, C. (2021). Thermal Energy Charging Improvement of a Latent Thermal Energy Storage System Via Fractal-Branched Fins. *Fractals* 29, 2150007. doi:10.1142/s0218348x21500079

Han, X., Kong, T., Zhu, P., and Wang, L. (2020). Microfluidic Encapsulation of Phase-Change Materials for High Thermal Performance. *Langmuir* 36, 8165–8173. doi:10.1021/acs.langmuir.0c01171

Hao, G., Yu, C., Chen, Y., Liu, X., and Chen, Y. (2022). Controlled Microfluidic Encapsulation of Phase Change Material for Thermo-Regulation. *Int. J. Heat Mass Transf.* 190, 122738. doi:10.1016/j.ijheatmasstransfer.2022.122738

Hu, H. (2020). Recent Advances of Polymeric Phase Change Composites for Flexible Electronics and Thermal Energy Storage System. *Compos. Part B Eng.* 195, 108094. doi:10.1016/j.compositesb.2020.108094

Javadi, F. S., Metselaar, H. S. C., and Ganesan, P. (2020). Performance Improvement of Solar Thermal Systems Integrated with Phase Change Materials (PCM), a Review. *Sol. Energy* 206, 330–352. doi:10.1016/j.solener.2020.05.106

Kothari, R., Sahu, S. K., Kundalwal, S. I., and Mahalkar, P. (2021). Thermal Performance of Phase Change Material-Based Heat Sink for Passive Cooling of Electronic Components: An Experimental Study. *Int. J. Energy Res.* 45, 5939–5963. doi:10.1002/er.6215

Kumar, A., Singh, A. P., and Singh, O. (2020). Effect of Novel PCM Encapsulation Designs on Electrical and Thermal Performance of a Hybrid Photovoltaic Solar Panel. *Sol. Energy* 205, 320. doi:10.1016/j.solener.2020.05.062

Lamrani, B., Johannes, K., and Kuznik, F. (2021). Phase Change Materials Integrated into Building Walls: An Updated Review. *Renew. Sustain. Energy Rev.* 140, 110751. doi:10.1016/j.rser.2021.110751

Li, J., Zhu, X., Wang, H., Lin, P., Jia, L., Li, L., et al. (2021). Synthesis and Properties of Multifunctional Microencapsulated Phase Change Material for Intelligent Textiles. *J. Mater Sci.* 56, 2176–2191. doi:10.1007/s10853-020-05399-4

Liang, W.-G., Yang, C., Wen, G.-Q., Wang, W., Ju, X.-J., Xie, R., et al. (2014). A Facile and Controllable Method to Encapsulate Phase Change Materials with Non-toxic and Biocompatible Chemicals. *Appl. Therm. Eng.* 70, 817–826. doi:10.1016/j.applthermaleng.2014.06.006

Milian, Y. E., Gutierrez, A., Grageda, M., and Ushak, S. (2017). A Review on Encapsulation Techniques for Inorganic Phase Change Materials and the Influence on Their Thermophysical Properties. *Renew. Sustain. Energy Rev.* 73, 983. doi:10.1016/j.rser.2017.01.159

Sanchez-Silva, L., Rodr Guez, J. F., Romero, A., Borreguero, A. M., Carmona, M., and S Nchez, P. (2010). Microencapsulation of PCMs with a Styrene-Methyl Methacrylate Copolymer Shell by Suspension-like Polymerisation. *Chem. Eng. J.* 157, 216. doi:10.1016/j.cej.2009.12.013

Shi, J., Qin, M., Aftab, W., and Zou, R. (2021). Flexible Phase Change Materials for Thermal Energy Storage. *Energy Storage Mater.* 41, 321–342. doi:10.1016/j.ensm.2021.05.048

Shi, T., Hu, P., and Wang, J. (2020). Preparation of Polyurea Microcapsules Containing Phase Change Materials Using Microfluidics. *ChemistrySelect* 5, 2342–2347. doi:10.1002/slct.201904570

Su, W., Darkwa, J., and Kokogiannakis, G. (2015). Review of Solid-Liquid Phase Change Materials and Their Encapsulation Technologies. *Renew. Sustain. Energy Rev.* 48, 373–391. doi:10.1016/j.rser.2015.04.044

Wang, J., Gao, W., Zhang, H., Zou, M., Chen, Y., and Zhao, Y. (2018). Programmable Wettability on Photocontrolled Graphene Film. *Sci. Adv.* 4, eaat7392. doi:10.1126/sciadv.aat7392

Wang, J., Sun, L., Zou, M., Gao, W., Liu, C., Shang, L., et al. (2017). Bioinspired Shape-Memory Graphene Film with Tunable Wettability. *Sci. Adv.* 3, e1700004. doi:10.1126/sciadv.1700004

Wang, J., Yu, K., Duan, R., Xie, G., and Sund N, B. (2021). Enhanced Thermal Management by Introducing Nanoparticle Composite Phase Change Materials for Cooling Multiple Heat Sources Systems. *Energy* 227, 120495.

Wen, G.-Q., Xie, R., Liang, W.-G., He, X.-H., Wang, W., Ju, X.-J., et al. (2015). Microfluidic Fabrication and Thermal Characteristics of Core-Shell Phase Change Microfibers with High Paraffin Content. *Appl. Therm. Eng.* 87, 471–480. doi:10.1016/j.applthermaleng.2015.05.036

Zhang, B., Zhang, Z., Kapar, S., Ataeian, P., Da Silva Bernardes, J., Berry, R., et al. (2019). Microencapsulation of Phase Change Materials with Polystyrene/cellulose Nanocrystal Hybrid Shell via Pickering Emulsion Polymerization. *ACS Sustain. Chem. Eng.* 7, 17756–17767. doi:10.1021/acssuschemeng.9b04134

Zhang, C., Li, J., and Chen, Y. (2020). Improving the Energy Discharging Performance of a Latent Heat Storage (LHS) Unit Using Fractal-Tree-Shaped Fins. *Appl. Energy* 259, 114102. doi:10.1016/j.apenergy.2019.114102

Zhang, X., Xie, R., Hu, W.-X., Faraj, Y., Zhao, Q., Fan, X.-X., et al. (2018). Microfluidic Fabrication of Core-Sheath Composite Phase Change Microfibers with Enhanced Thermal Conductive Property. *J. Mater Sci.* 53, 15769–15783. doi:10.1007/s10853-018-2677-6

Zhang, Y., and Rochefort, D. (2012). Characterisation and Applications of Microcapsules Obtained by Interfacial Polycondensation. *J. Microencapsul.* 29, 636–649. doi:10.3109/02652048.2012.676092

Conflict of Interest: Authors ZL, CL, NH, LJ and WB were employed by Shanghai Power Equipment Research Institute Co. Ltd. Author YC was employed by Ningbo Water Meter (Group) Co. Ltd.

frontiers | Frontiers in Energy Research

OPINION
published: 02 June 2022
doi: 10.3389/fenrg.2022.923454

Opportunities and Challenges for the Development of Ultra-Thin Heat Pipe

*Taocheng Zhao and Zheng Hu**

Key Laboratory of Energy Thermal Conversion and Control of Ministry of Education, School of Energy and Environment, Southeast University, Nanjing, China

Keywords: ultra-thin heat pipe, wick structure, heat dissipation, portable electronic device, thermal management

INTRODUCTION

The continuous progress of the internet and microelectronics, especially portable devices such as smartphones, tablet computers, and smartwatches, has resulted in compact, integrated, and miniaturized tools, consuming high power. The 11th and 12th generation CPUs are the main CPUs used in laptops in the past 2 years. The operating power consumption has reached 180 W with a size of 50 × 25 mm. The surface heat flux can be up to 14.4 W/cm^2 (Liu et al., 2013). The miniaturization of electronic devices has greatly reduced the effective area of heat dissipation. With the continuous upgrading of the power consumption of electronic devices, the surface heat flux will inevitably increase rapidly, bringing tough challenges against the safe cooling limits of portable electronics due to the limited space (Micheli et al., 2013; Tang et al., 2018).

The reliability of electronic devices is apparently sensitive to temperature that should be reserved within safe operational limits. Therefore, developing the advanced heat dissipation technology is continuously required to avoid damage and failure of electronic devices due to overheating. As a passive cooling technology, heat pipe has become an effective approach for electronic cooling, considering high thermal conductivity, simple structure, and no external driving force (Su et al., 2018). However, traditional heat pipes, such as loop heat, pulsating heat, and oscillating heat pipes, can no longer satisfy high heat dissipation in a limited space for portable electronic devices, which are lighter and thinner (Dai et al., 2020). Therefore, ultra-thin heat pipes (UTHP) have been widely investigated and used in high heat flux portable electronic cooling due to their compact size, high stability, and effective temperature uniformity. This study summarizes the recent development of UTHP technology and wick structures and analyzes the challenges and future prospects (Zhong et al., 2020).

CURRENT RESEARCH STATUS OF UTHP

Types of UTHP

UTHP is defined as a flat heat pipe with a thickness of less than 2 mm. UTHP can effectively remove the heat generated by electronic devices because of its thin thickness, high equivalent thermal conductivity, and being closely attached to the electronic devices. The thickness of UTHP for laptops, tablets, and smartphones/watches is 1–2, 0.8–1.2, and 0.4–0.6 mm, respectively (Hong et al., 2017).

Compared with the conventional heat pipe, the structure and wick of the UTHP are quite different due to the miniaturization of the size. At present, UTHP can be divided into flattened heat pipe (FHP), vapor chamber (VC), and ultra-thin loop heat pipe (UTLHP) (Li and Lv, 2016), as shown in **Figures 1A–C**.

As demonstrated in **Figure 1A**, the FHP usually is composed of the evaporation section, the insulation section, and the condensation section along the axial direction, which are similar to those of the conventional heat pipe (Cui et al., 2022). The liquid working medium absorbs heat,

OPEN ACCESS

Edited by:
Xiangdong Liu,
Yangzhou University, China

Reviewed by:
Feng Yao,
Suzhou University of Science and Technology, China
Dong Li,
Nanjing Normal University, China

****Correspondence:***
Zheng Hu
zhu@microflows.net

Specialty section:
This article was submitted to Process and Energy Systems Engineering, a section of the journal Frontiers in Energy Research

Received: *19 April 2022*
Accepted: *02 May 2022*
Published: *02 June 2022*

Citation:
Zhao T and Hu Z (2022) Opportunities and Challenges for the Development of Ultra-Thin Heat Pipe. Front. Energy Res. 10:923454. doi: 10.3389/fenrg.2022.923454

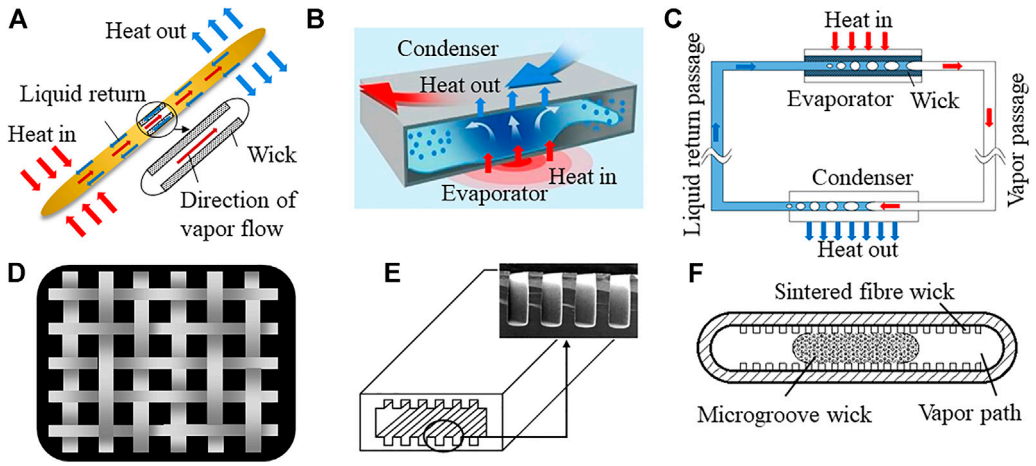

FIGURE 1 | Schematic diagram of UTHP: **(A)** FHP, **(B)** VC, **(C)** UTLHP, **(D)** sintered wick structure, **(E)** microgrooved wick structure (Gillot et al., 2003), and **(F)** composite wick structure (Li et al., 2016)

evaporates in the evaporation section, and condenses into liquid in the condensation section. The liquid working medium flows back from the condensation section end to the evaporation section by capillary force in the wick. The long flat structure manufactured by flatting cylindrical copper pipes enables the FHP to achieve multiple heat sources and long-distance heat transfer. The FHP is widely applied in small mobile devices such as smartphones and tablet computers. However, FHP has the defects of small surface area, single shape, and poor adaptability. The VC consists of a closed container with a plate-like structure (Li et al., 2021). The evaporation and condensation sections are located on both sides of the container while the inner wall is covered with a wick structure, as shown in **Figure 1B**. The VC has the advantages of lighter weight, larger condensation area, and more flexible structure, which makes the VC widely applied in electronic cooling with high heat flux. The UTLHP is deemed to be more adaptive, and it usually consists of an evaporator, vapor passage, condenser, and liquid return passage, which is in a ring structure as a whole, as illustrated in **Figure 1C**. All components of the UTLHP are made of smooth walls because of the lower resistance of the working fluid flow, except for the wick structure (Hong et al., 2016). The smooth-walled tube is conducive to the long-distance heat transfer of the UTLHP. In addition, different from other UTHP, separate evaporators and condensers of UTLHP cannot only eliminate possible entrainment effects but also remove more heat generated by electronic devices.

Wick Structure of UTHP

As a core part of the UTHP, wick supplies capillary force through the gas-liquid interface to actuate the working fluid circulation. The heat transfer characteristic of UTHP primarily depends on the wick capillary flow phase transition behavior. At present, the wick structure of UTHP mainly includes the sintered wick, microgrooved wick, and composite wick, as demonstrated in **Figures 1D–F**.

Currently, most UTHP uses sintered wick structures because of their excellent capability and low cost. The sintered wick can be divided into sintered powder wick, sintered mesh wick, and sintered fiber wick, as shown in **Figure 1D** for sintered mesh wick (Zu et al., 2021). The most widely used sintered powder wick in the traditional heat pipe has almost been substituted for sintered mesh/fiber wick that is employed to fabricate ultra-high temperature polymers due to thicker powder layers and cracks caused by leveling in UTHP. Using sintered mesh/fiber as wick, thinner, more flexible flat heat pipe can be obtained. The microgrooved wick structure has gradually become the preferred option for UTHP because of unique advantages such as high permeability and low thermal resistance, as shown in **Figure 1E** (Zeng et al., 2017). The shells of UTHP with the microgrooved wick structure are usually made of non-metallic materials. Moreover, the microgrooved wick structure is mostly fabricated by laser micromachining and plasma etching. Although the micromachining process can obtain thinner UTHP with higher heat transfer characteristics, its high cost, unstable quality, and complicated process limit the applications. The wick of UTHP with good thermal performance should ensure high permeability and large capillary force. The sintered wick structure has higher capillary pump force with lower liquid permeability, while the microgrooved wick structure has the opposite performance. Therefore, composite wick structures that combine two or more types of single wick structures have been investigated to equilibrate the contradiction between high permeability and large capillary force (Jiang et al., 2014). At present, the most used composite wick in UTHP are the sintered mesh-groove composite wick and sintered powder-groove composite wick, as shown in **Figure 1F**. However, owing to the complicated manufacturing procedure, high cost of manufacture, and low production efficiency, the application of composite wick structure is limited in ultra-thin electronic cooling.

OPPORTUNITIES AND CHALLENGES

Recently, increasing heat dissipation demands in portable electronic devices with high heat flux has unveiled opportunities and challenges that can affect the progress and applications of UTHP. Considering the research actuality and application requirements of UTHP, the following aspects need to be further studied:

1) Develop more accurate and reliable machining technology and packaging technology for UTHP. Traditional machining methods such as cylindrical heat pipe flattening technology have certain defects, which will cause deformation of the shell, poor sealing performance, and low manufacturing yield. It greatly increases the manufacturing cost and restricts its large-scale development and applications of UTHP.
2) Due to the increasing integration of portable electronic devices, the operating environment of UTHP is becoming continuously complex. It is indispensable to design UTHP with different cross-sectional shapes suitable for the surface structure of the heat source according to the specific operating environment. In addition, the research on the reliability and stability of the UTHP in intermittent operation under the location and conditions of variable heat fluxes and variable heat sources should be carried out, which lays a scientific foundation for further development and applications of UTHP.

AUTHOR CONTRIBUTIONS

ZH contributed to guiding the study. TZ wrote the draft of the manuscript and revised it.

FUNDING

Natural Science Foundation of Jiangsu Province (no. BK20210239).

REFERENCES

Cui, Z., Jia, L., Wang, Z., Dang, C., and Yin, L. (2022). Thermal Performance of an Ultra-thin Flat Heat Pipe with Striped Super-hydrophilic Wick Structure. *Appl. Therm. Eng.* 208, 118249. doi:10.1016/J.APPLTHERMALENG.2022.118249

Dai, X., Tang, Y., Liu, T., and Wang, S. (2020). Experimental Investigation on the Thermal Characteristics of Ultra-thin Flattened Heat Pipes with Bending Angles. *Appl. Therm. Eng.* 172, 115150. doi:10.1016/J.APPLTHERMALENG.2020.115150

Gillot, C., Avenas, Y., Cezac, N., Poupon, G., Schaeffer, C., and Fournier, E. (2003). Silicon Heat Pipes Used as Thermal Spreaders. *IEEE Trans. Comp. Packag. Technol.* 26, 332–339. doi:10.1109/TCAPT.2003.815092

Hong, S., Wang, S., and Zhang, L. (2017). Effect of Groove Configuration on Two-phase Flow Instability for Ultra-thin Looped Heat Pipes in Thermal Management System. *Int. J. Therm. Sci.* 121, 369–380. doi:10.1016/J.IJTHERMALSCI.2017.07.024

Hong, S., Wang, S., and Zhang, Z. (2016). Multiple Orientations Research on Heat Transfer Performances of Ultra-thin Loop Heat Pipes with Different Evaporator Structures. *Int. J. Heat Mass Transf.* 98, 415–425. doi:10.1016/J.IJHEATMASSTRANSFER.2016.03.049

Liu, X., Chen, Y., and Shi, M. (2013). Dynamic performance analysis on start-up of closed-loop pulsating heat pipes (CLPHPs). *Int. J. Therm. Sci.* 65, 224–233. doi:10.1016/J.IJTHERMALSCI.2012.10.012

Jiang, L., Ling, J., Jiang, L., Tang, Y., Li, Y., Zhou, W., et al. (2014). Thermal Performance of a Novel Porous Crack Composite Wick Heat Pipe. *Energy Convers. Manag.* 81, 10–18. doi:10.1016/J.ENCONMAN.2014.01.044

Li, D., Huang, Z., Zhao, J., Jian, Q., and Chen, Y. (2021). Analysis of Heat Transfer Performance and Vapor-Liquid Meniscus Shape of Ultra-thin Vapor Chamber with Supporting Columns. *Appl. Therm. Eng.* 193, 117001. doi:10.1016/J.APPLTHERMALENG.2021.117001

Li, J., and Lv, L. (2016). Experimental Studies on a Novel Thin Flat Heat Pipe Heat Spreader. *Appl. Therm. Eng.* 93, 139–146. doi:10.1016/J.APPLTHERMALENG.2015.09.038

Li, Y., Zhou, W., He, J., Yan, Y., Li, B., and Zeng, Z. (2016). Thermal Performance of Ultra-thin Flattened Heat Pipes with Composite Wick Structure. *Appl. Therm. Eng.* 102, 487–499. doi:10.1016/J.APPLTHERMALENG.2016.03.097

Micheli, L., Sarmah, N., Luo, X., Reddy, K. S., and Mallick, T. K. (2013). Opportunities and Challenges in Micro- and Nano-Technologies for Concentrating Photovoltaic Cooling: A Review. *Renew. Sustain. Energy Rev.* 20, 595–610. doi:10.1016/J.RSER.2012.11.051

Su, Q., Chang, S., Zhao, Y., Zheng, H., and Dang, C. (2018). A Review of Loop Heat Pipes for Aircraft Anti-icing Applications. *Appl. Therm. Eng.* 130, 528–540. doi:10.1016/J.APPLTHERMALENG.2017.11.030

Tang, H., Tang, Y., Wan, Z., Li, J., Yuan, W., Lu, L., et al. (2018). Review of Applications and Developments of Ultra-thin Micro Heat Pipes for Electronic Cooling. *Appl. Energy* 223, 383–400. doi:10.1016/J.APENERGY.2018.04.072

Zeng, J., Lin, L., Tang, Y., Sun, Y., and Yuan, W. (2017). Fabrication and Capillary Characterization of Micro-grooved Wicks with Reentrant Cavity Array. *Int. J. Heat Mass Transf.* 104, 918–929. doi:10.1016/J.IJHEATMASSTRANSFER.2016.09.007

Zhong, G., Tang, Y., Ding, X., Rao, L., Chen, G., Tang, K., et al. (2020). Experimental Study of a Large-Area Ultra-thin Flat Heat Pipe for Solar Collectors under Different Cooling Conditions. *Renew. Energy* 149, 1032–1039. doi:10.1016/J.RENENE.2019.10.093

Zu, S., Liao, X., Huang, Z., Li, D., and Jian, Q. (2021). Visualization Study on Boiling Heat Transfer of Ultra-thin Flat Heat Pipe with Single Layer Wire Mesh Wick. *Int. J. Heat Mass Transf.* 173, 121239. doi:10.1016/J.IJHEATMASSTRANSFER.2021.121239

Conflict of Interest: The authors declare that the research was conducted in the absence of any commercial or financial relationships that could be construed as a potential conflict of interest.

frontiers | Frontiers in Energy Research

OPINION
published: 14 June 2022
doi: 10.3389/fenrg.2022.939932

Perspectives on Bioinspired Functional Surfaces for Heat Transfer Enhancement *via* Dropwise Condensation

*Ze Xu and Raza Gulfam**

Key Laboratory of Energy Thermal Conversion and Control of Ministry of Education, School of Energy and Environment, Southeast University, Nanjing, China

Keywords: bioinspired, functional surfaces, dropwise condensation, wettability, heat transfer

INTRODUCTION

Condensation is a ubiquitous gas–liquid phase change process and is widely applied in industrial fields, including chemical industry, heat transfer and exchange (Zhang et al., 2017), water collection, seawater desalination, thermal management (Liu et al., 2013), etc. There are fundamentally two modes of condensation, that is, filmwise and dropwise, whereas the dropwise condensation is supposed to be superior as it can provide greater nucleation density, faster droplet departure, and efficient surface renewal capability induced by faster droplet shedding. With the rising energy crisis across the globe, conceiving the dropwise condensation is highly necessary, which is deemed to be conducive in controlling and improving the energy utilization efficiency particularly in applications of heat transfer. Regarding this, advanced surface science has played a great role, leading to bioinspired functional surfaces (i.e., prepared by mimicking the surface structures, morphology, and chemistry of the lotus leaf, pitcher plant, desert beetle, and bamboo leaf) that have served as the competitive alternatives compared with the pristine surfaces (e.g., copper, aluminum, steel, and glass). In brief, various bioinspired functional surfaces have been recently proposed and investigated to realize the dropwise condensation, such as superhydrophobic surfaces that can promote droplet jumping; slippery liquid-infused porous surfaces (SLIPSs) that have self-healing ability and can lessen the adhesion force between the liquid and surfaces; wettability gradient surfaces that can promote droplet self-propulsion even on the horizontally positioned substrates and bi-philic surfaces that combine the advantages of both hydrophilic and hydrophobic characteristics. This review summarizes the fundamental factors affecting condensation, and provides the recent progress on bioinspired functional surfaces for dropwise condensation heat transfer enhancement.

Factors Affecting the Condensation

Wettability

Wettability is a significant factor influencing the condensation characteristics to the greatest extent, based on which the whole life cycle of the droplets, including nucleation, growth, and shedding, is decided. Wettability is further affected by the types of surfaces involved (flat or rough) and four surface regimes, encompassing the superhydrophobic, hydrophobic, hydrophilic, and superhydrophilic. According to the classical nucleation theory, nucleation prefers to take place on hydrophilic regions compared with hydrophobic regions because of the higher energy barrier on the hydrophobic regions (Varanasi et al., 2009). While droplets on hydrophobic regions can slide faster because of the less adhesion force than those on hydrophilic regions. Thus, wettability of pristine surfaces needs to be modified by adopting the bioinspired technology, ensuring that the droplet dynamics is efficient which is necessarily required even during dropwise condensation

OPEN ACCESS

Edited by:
Xiangdong Liu,
Yangzhou University, China

Reviewed by:
Wei Gao,
Harvard University, United States

****Correspondence:***
Raza Gulfam
gulfam@seu.edu.cn
gulfamrazahaidery@hotmail.com

Specialty section:
This article was submitted to Process and Energy Systems Engineering, a section of the journal Frontiers in Energy Research

Received: *09 May 2022*
Accepted: *12 May 2022*
Published: *14 June 2022*

Citation:
Xu Z and Gulfam R (2022) Perspectives on Bioinspired Functional Surfaces for Heat Transfer Enhancement via Dropwise Condensation. Front. Energy Res. 10:939932. doi: 10.3389/fenrg.2022.939932

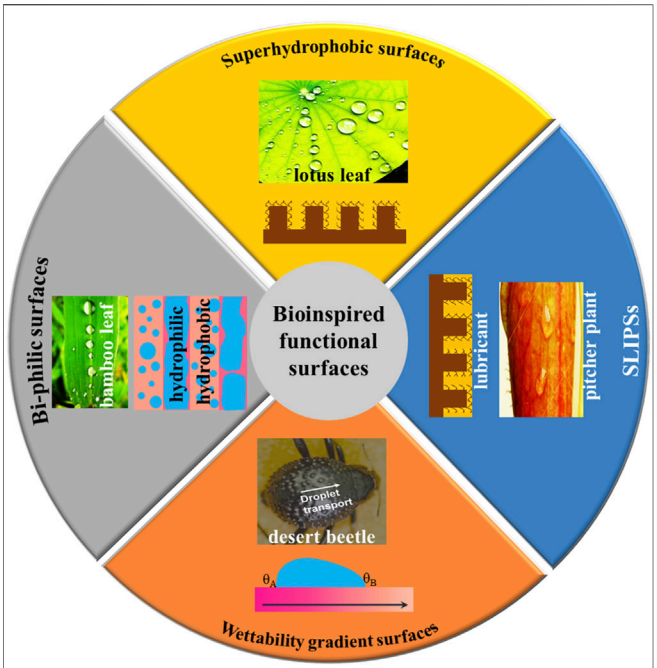

FIGURE 1 | Bioinspired functional surfaces for dropwise condensation heat transfer enhancement.

(Gulfam et al., 2022). Briefly, controlling the wetting behaviors of the droplets through rationally designed surfaces that can promote the droplet nucleation and detachment help enhance the dropwise condensation heat transfer.

Non-Condensable Gases

Non-condensable gases (existing between the surface and vapors) are one of the main external factors influencing the condensation heat transfer, increasing the diffusion resistance of steam, and forming the additional thermal resistance at the interface. The quantitative study has demonstrated that even 1% of non-condensable gases can result in approximately 50% reduction in dropwise condensation heat transfer (Ma et al., 2008). Increasing the velocity (Ji et al., 2020), turbulence (Eimann et al., 2018) of the vapor, and promoting the droplet jumping (Zhang et al., 2020) can weaken the adverse effect of non-condensable gases. Besides, several studies have shown that superhydrophobic surfaces with hierarchical structures have better condensation heat transfer than hydrophobic surfaces in the presence of a tiny amount of non-condensable gases. This is due to the more stable Cassie state of droplets formed by the gases trapped in the cavities of micro-nano structures of superhydrophobic surfaces (Ma et al., 2012; Hu et al., 2015).

Surface Subcooling

Surface subcooling provides the necessary driving force for condensation, which is defined as the temperature difference between the steam and surface. The droplet nucleation rate improves with the increasing subcooling degree, resulting in higher condensation heat flux. However, at higher subcooling degrees particularly for bioinspired functional surfaces, the heat transfer efficiency is underperformed due to overflow of condensate (Gulfam et al., 2022), for example, a decline in the condensation heat transfer coefficient has been experimentally reported (Lee et al., 2013). Therefore, it is a challenge to explore further ways aiming to improve dropwise condensation heat transfer under high subcooling degree for bioinspired functional surfaces (Wen et al., 2018).

BIOINSPIRED FUNCTIONAL SURFACES

Superhydrophobic Surfaces

Superhydrophobic slippery surfaces (e.g., lotus leaf) have the largest contact angle and lower sliding angle compared with other surfaces, provided that the droplets maintain a more stable Cassie state. During condensation, droplet jumping triggered by direct shedding or coalescence-induced shedding is an exclusive phenomenon on the superhydrophobic surfaces, promoting the efficient droplet removal and accelerating the refreshment of the surfaces (Donati et al., 2020). Boreyko et al. (Boreyko and Chen, 2009) first observed the droplet jumping caused by coalescence on the superhydrophobic surfaces with hierarchical structures. They demonstrated that this phenomenon was induced by the discharge of surplus surface energy during the coalescence process. Miljkovic et al. (2013b) experimentally proved that droplet jumping could advance the heat transfer coefficient by 30%. In addition, the return of the jumping droplets driven by gravity also influences the dropwise condensation heat transfer. In that case, Miljkovic et al. (2013a) further strengthened the condensation heat transfer performance by 50% enhancement by applying the electric field, with which the droplets could jump in a specific direction and suppress the return of the jumping droplets. Nevertheless, the superhydrophobic surfaces are not durable for longer condensation operations due to the emergence of the Wenzel state, resulting in the enhanced adhesion force, greater droplet pinning, and flooding on the surface.

Slippery Liquid-Infused Porous Surfaces

Slippery liquid-infused porous surfaces (SLIPSs) are composed of the porous substrate and injected lubricant that is immiscible with the condensate (e.g., pitcher plant) (Wang et al., 2017; Wang et al., 2018). The porous substrate functions as the carrier of lubricant with low surface energy (Gulfam et al., 2020). SLIPSs have self-healing ability because the lubricant can spread evenly on the substrate driven by capillary flow (Gao et al., 2020). Different from the superhydrophobic surfaces, the lubricant infused in SLIPSs replaces the air entrapped in the micro-nano structures. In general, SLIPSs have lower adhesion and smaller contact angle hysteresis (Dai et al., 2018), which can prevent the droplet pinning and accelerate the faster removal of the droplets. Park et al. (2016) proposed asymmetric-bump–like SLIPSs, reporting the enhanced condensation heat transfer. Xiao et al. (2013) proved that SLIPSs can heighten the condensation heat transfer by 100% compared with pristine surfaces. Furthermore, the rational selection of the lubricant can implement the condensation heat transfer enhancement of the low surface tension liquids. For instance, ethanol and hexane can realize the firm dropwise condensation on SLIPSs (Sett et al., 2019), achieving 100% enhancement in heat transfer. However, loss of the lubricant is the major challenge for the application of SLIPSs that degrade their performance (Gulfam et al., 2022). Therefore, improving the operational and shelf-life durability of

SLIPSs deserves further investigations, in which the lubricant loss via evaporation, physical shearing, and cloaking need to be avoided.

Wettability Gradient Surface

The bioinspired functional surfaces consisting of different wetting regimes, spanning between superhydrophobic, hydrophobic, hydrophilic, and superhydrophilic regimes, where the contact angle is changed as the spatial derivative (e.g., desert beetle), are called wettability gradient surfaces (WGS). They are widely known to provide directional self-propulsion of droplets, which, however, strongly depends on the sticky or slippery dynamics. For example, the directional self-driven motion of droplets from a hydrophobic regime to a hydrophilic regime has been achieved on WGS (Liu et al., 2017; Sommers et al., 2020), which has the great potential to further expedite droplet removal and enhance the condensation heat transfer (Tokunaga and Tsuruta, 2020; Deng et al., 2022) The mobility of droplets on the surface with radial wettability gradient was investigated experimentally in the pure steam (Daniel et al., 2001), where the droplets demonstrated coalescence with other droplets during the motion from a hydrophobic regime to a hydrophilic regime, resulting in the increased droplet velocity. Consequently, the surface promoted the droplet removal and heightened the dropwise condensation. Macner et al. (2014) further studied the droplet size distribution on a radial gradient surface during condensation, and results revealed that droplets would grow through direct condensation as well as *via* coalescence and then detach from the surface spontaneously, making room for new nucleation sites. Therefore, the gradient surface was occupied by small droplets, which guaranteed sufficient heat exchange area instead of developing into the liquid film and increasing the thermal resistance. However, more efforts are still indispensable to resolve the challenges encountered by WGS, including surface fabrication complexities, increasing the droplet velocity, achieving the longer droplet transport range, avoiding the droplet spreading, and pinning in the hydrophilic/superhydrophilic regimes, amongst others.

Bi-philic Surfaces

The bioinspired functional surfaces combining the bonus of both hydrophilic and hydrophobic regimes are called bi-philic surfaces (e.g., bamboo leaf). Indeed, droplets can shed swiftly on the slippery hydrophobic surface; however, the high-energy barrier of the hydrophobic regime is still a challenge, rendering the droplet nucleation more difficult (Shang et al., 2018). To overcome such deficiencies, various bi-philic surfaces have been investigated (Wilke et al., 2020), which can simultaneously enhance nucleation and remove the droplets. The design of bi-philic surfaces can include various structures, that is, stripes, grooves, patches, and fins. Peng et al. (2015) carried out an experimental study in pure steam, mainly exploring the influence of the size of hydrophilic stripes on condensation heat transfer. Results revealed that with the optimal size of hydrophilic stripe, heat flux of the hybrid bi-philic surface was 23% higher than that of the entire hydrophobic surface. Besides, hydrophilic groove structure can help reduce thickness of the condensate and transport it efficiently in the groove by surface tension (Peng et al., 2020; Chen et al., 2021), reducing the thermal resistance and improving the heat transfer performance (Ji et al., 2020). A 3D hybrid surface with a superhydrophobic ridge and hydrophilic microgrooves was prepared by Lo et al. (2019). The droplets on the superhydrophobic ridge moved spontaneously into the hydrophilic grooves, and the liquid bridges shed through the grooves, which increased the droplet detachment frequency at high subcooling and resulted in higher condensation hear transfer. Also, theoretical models have been recently presented (Xie et al., 2020), addressing the condensation heat transfer on the bi-philic surfaces. In addition to the aforementioned works, further efforts are recommended to establish theoretical models on the microgroove-based bi-philic surfaces.

CONCLUSION

Bioinspired functional surfaces have great potential to improve the condensation heat transfer by switching the filmwise mode into dropwise mode. The main factors affecting dropwise condensation were discussed. During dropwise condensation, the droplet nucleation, growth, and shedding are highly influenced by the surface wettability and droplet dynamics, which should indeed ensure slippery characteristics for efficient heat transfer. Non-condensable gases should be avoided in order to achieve faster condensation process. Subcooling degree should be controlled depending on the application demands because bioinspired functional surfaces normally lead to the best results at low subcooling as reported until now. Bioinspired functional surfaces, including superhydrophobic surfaces, slippery liquid-infused porous surfaces, wettability gradient surfaces, and bi-philic surfaces, need further efforts addressing the challenges such as durability enhancement, reducing the fabrication complexities, and subjecting them abundantly in condensation heat transfer applications at industrial scales.

AUTHOR CONTRIBUTIONS

ZX and RG developed the concept of the study. All authors revised the manuscript and read and approved the submitted version.

REFERENCES

Boreyko, J. B., and Chen, C.-H. (2009). Self-Propelled Dropwise Condensate on Superhydrophobic Surfaces. *Phys. Rev. Lett.* 103 (18), 184501. doi:10.1103/PhysRevLett.103.184501

Chen, S., Wang, R., Wu, F., Zhang, H., Gao, X., and Jiang, L. (2021). Copper-based High-Efficiency Condensation Heat Transfer Interface Consisting of Superhydrophobic Hierarchical Microgroove and Nanocone Structure. *Mater. Today Phys.* 19, 100407. doi:10.1016/j.mtphys.2021.100407

Dai, X., Sun, N., Nielsen, S. O., Stogin, B. B., Wang, J., Yang, S., et al. (2018). Hydrophilic Directional Slippery Rough Surfaces for Water Harvesting. *Sci. Adv.* 4 (3), 0919. doi:10.1126/sciadv.aaq0919

Daniel, S., Chaudhury, M. K., and Chen, J. C. (2001). Fast Drop Movements Resulting from the Phase Change on a Gradient Surface. *Science* 291 (5504), 633–636. doi:10.1126/science.291.5504.633

Deng, Z., Gao, S., Wang, H., Liu, X., and Zhang, C. (2022). Visualization Study on the Condensation Heat Transfer on Vertical Surfaces with a Wettability Gradient. *Int. J. Heat Mass Transf.* 184, 122331. doi:10.1016/j.ijheatmasstransfer.2021.122331

Donati, M., Lam, C. W. E., Milionis, A., Sharma, C. S., Tripathy, A., Zendeli, A., et al. (2020). Sprayable Thin and Robust Carbon Nanofiber Composite Coating for Extreme Jumping Dropwise Condensation Performance. *Adv. Mat. Interfaces* 8 (1), 2001176. doi:10.1002/admi.202001176

Eimann, F., Zheng, S., Philipp, C., Fieback, T., and Gross, U. (2018). Convective Dropwise Condensation Out of Humid Air inside a Horizontal Channel - Experimental Investigation of the Condensate Heat Transfer Resistance. *Int. J. Heat Mass Transf.* 127, 448–464. doi:10.1016/j.ijheatmasstransfer.2018.08.015

Gao, W., Wang, J., Zhang, X., Sun, L., Chen, Y., and Zhao, Y. (2020). Electric-tunable Wettability on a Paraffin-Infused Slippery Pattern Surface. *Chem. Eng. J.* 381, 122612. doi:10.1016/j.cej.2019.122612

Gulfam, R., Huang, T.-e., Lv, C., Orejon, D., and Zhang, P. (2022). Condensation Heat Transfer on Phase Change Slippery Liquid-Infused Porous Surfaces. *Int. J. Heat Mass Transf.* 185, 122384. doi:10.1016/j.ijheatmasstransfer.2021.122384

Gulfam, R., Orejon, D., Choi, C.-H., and Zhang, P. (2020). Phase-Change Slippery Liquid-Infused Porous Surfaces with Thermo-Responsive Wetting and Shedding States. *ACS Appl. Mat. Interfaces* 12 (30), 34306–34316. doi:10.1021/acsami.0c06441

Hu, H. W., Tang, G. H., and Niu, D. (2015). Experimental Investigation of Condensation Heat Transfer on Hybrid Wettability Finned Tube with Large Amount of Noncondensable Gas. *Int. J. Heat Mass Transf.* 85, 513–523. doi:10.1016/j.ijheatmasstransfer.2015.02.006

Ji, D.-Y., Lee, J.-W., Kim, D., Hwang, W., and Lee, K.-Y. (2020). Effective Reduction of Non-condensable Gas Effects on Condensation Heat Transfer: Surface Modification and Steam Jet Injection. *Appl. Therm. Eng.* 174, 115264. doi:10.1016/j.applthermaleng.2020.115264

Lee, S., Cheng, K., Palmre, V., Bhuiya, M. M. H., Kim, K. J., Zhang, B. J., et al. (2013). Heat Transfer Measurement during Dropwise Condensation Using Micro/nano-Scale Porous Surface. *Int. J. Heat Mass Transf.* 65, 619–626. doi:10.1016/j.ijheatmasstransfer.2013.06.016

Liu, C., Sun, J., Li, J., Xiang, C., Che, L., Wang, Z., et al. (2017). Long-range Spontaneous Droplet Self-Propulsion on Wettability Gradient Surfaces. *Sci. Rep.* 7 (1), 7552. doi:10.1038/s41598-017-07867-5

Liu, X., Chen, Y., and Shi, M. (2013). Dynamic Performance Analysis on Start-Up of Closed-Loop Pulsating Heat Pipes (CLPHPs). *Int. J. Therm. Sci.* 65, 224–233. doi:10.1016/j.ijthermalsci.2012.10.012

Lo, C.-W., Chu, Y.-C., Yen, M.-H., and Lu, M.-C. (2019). Enhancing Condensation Heat Transfer on Three-Dimensional Hybrid Surfaces. *Joule* 3 (11), 2806–2823. doi:10.1016/j.joule.2019.08.005

Ma, X.-H., Zhou, X.-D., Lan, Z., Li, Y.-M., and Zhang, Y. (2008). Condensation Heat Transfer Enhancement in the Presence of Non-condensable Gas Using the Interfacial Effect of Dropwise Condensation. *Int. J. Heat Mass Transf.* 51 (7-8), 1728–1737. doi:10.1016/j.ijheatmasstransfer.2007.07.021

Ma, X., Wang, S., Lan, Z., Peng, B., Ma, H. B., and Cheng, P. (2012). Wetting Mode Evolution of Steam Dropwise Condensation on Superhydrophobic Surface in the Presence of Noncondensable Gas. *J. Heat Transfer-Transactions Asme* 134 (2), 021501. doi:10.1115/1.4005094

Macner, A. M., Daniel, S., and Steen, P. H. (2014). Condensation on Surface Energy Gradient Shifts Drop Size Distribution toward Small Drops. *Langmuir* 30 (7), 1788–1798. doi:10.1021/la404057g

Miljkovic, N., Enright, R., Nam, Y., Lopez, K., Dou, N., Sack, J., et al. (2013a). Jumping-droplet-enhanced Condensation on Scalable Superhydrophobic Nanostructured Surfaces. *Nano Lett.* 13 (1), 179–187. doi:10.1021/nl303835d

Miljkovic, N., Preston, D. J., Enright, R., and Wang, E. N. (2013b). Electric-field-enhanced Condensation on Superhydrophobic Nanostructured Surfaces. *ACS Nano* 7 (12), 11043–11054. doi:10.1021/nn404707j

Park, K.-C., Kim, P., Grinthal, A., He, N., Fox, D., Weaver, J. C., et al. (2016). Condensation on Slippery Asymmetric Bumps. *Nature* 531 (7592), 78–82. doi:10.1038/nature16956

Peng, B., Ma, X., Lan, Z., Xu, W., and Wen, R. (2015). Experimental Investigation on Steam Condensation Heat Transfer Enhancement with Vertically Patterned Hydrophobic-Hydrophilic Hybrid Surfaces. *Int. J. Heat Mass Transf.* 83, 27–38. doi:10.1016/j.ijheatmasstransfer.2014.11.069

Peng, Q., Jia, L., Ding, Y., Dang, C., Yin, L., and Yan, X. (2020). Influence of Groove Orientation on Dropwise Condensation on Hydrophobic and Hierarchical Superhydrophobic Surfaces with Microgroove Arrays. *Int. Commun. Heat Mass Transf.* 112, 104492. doi:10.1016/j.icheatmasstransfer.2020.104492

Sett, S., Sokalski, P., Boyina, K., Li, L., Rabbi, K. F., Auby, H., et al. (2019). Stable Dropwise Condensation of Ethanol and Hexane on Rationally Designed Ultrascalable Nanostructured Lubricant-Infused Surfaces. *Nano Lett.* 19 (8), 5287–5296. doi:10.1021/acs.nanolett.9b01754

Shang, Y., Hou, Y., Yu, M., and Yao, S. (2018). Modeling and Optimization of Condensation Heat Transfer at Biphilic Interface. *Int. J. Heat Mass Transf.* 122, 117–127. doi:10.1016/j.ijheatmasstransfer.2018.01.108

Sommers, A. D., Panth, M., and Eid, K. F. (2020). Self-propelled Water Droplet Movement on a Laser-Etched Radial Gradient Copper Surface. *Appl. Therm. Eng.* 173, 115226. doi:10.1016/j.applthermaleng.2020.115226

Tokunaga, A., and Tsuruta, T. (2020). Enhancement of Condensation Heat Transfer on a Microstructured Surface with Wettability Gradient. *Int. J. Heat Mass Transf.* 156, 119839. doi:10.1016/j.ijheatmasstransfer.2020.119839

Varanasi, K. K., Hsu, M., Bhate, N., Yang, W., and Deng, T. (2009). Spatial Control in the Heterogeneous Nucleation of Water. *Appl. Phys. Lett.* 95 (9), 094101. doi:10.1063/1.3200951

Wang, J., Gao, W., Zhang, H., Zou, M., Chen, Y., and Zhao, Y. (2018). Programmable Wettability on Photocontrolled Graphene Film. *Sci. Adv.* 4 (9), eaat7392. doi:10.1126/sciadv.aat7392

Wang, J., Sun, L., Zou, M., Gao, W., Liu, C., Shang, L., et al. (2017). Bioinspired Shape-Memory Graphene Film with Tunable Wettability. *Sci. Adv.* 3 (6), e1700004. doi:10.1126/sciadv.1700004

Wen, R., Xu, S., Zhao, D., Yang, L., Ma, X., Liu, W., et al. (2018). Sustaining Enhanced Condensation on Hierarchical Mesh-Covered Surfaces. *Natl. Sci. Rev.* 5 (6), 878–887. doi:10.1093/nsr/nwy098

Wilke, K. L., Antao, D. S., Cruz, S., Iwata, R., Zhao, Y., Leroy, A., et al. (2020). Polymer Infused Porous Surfaces for Robust, Thermally Conductive, Self-Healing Coatings for Dropwise Condensation. *ACS Nano* 14 (11), 14878–14886. doi:10.1021/acsnano.0c03961

Xiao, R., Miljkovic, N., Enright, R., and Wang, E. N. (2013). Immersion Condensation on Oil-Infused Heterogeneous Surfaces for Enhanced Heat Transfer. *Sci. Rep.* 3, 1988. doi:10.1038/srep01988

Xie, J., She, Q., Xu, J., Liang, C., and Li, W. (2020). Mixed Dropwise-Filmwise Condensation Heat Transfer on Biphilic Surface. *Int. J. Heat Mass Transf.* 150, 119273. doi:10.1016/j.ijheatmasstransfer.2019.119273

Zhang, C., Shen, C., and Chen, Y. (2017). Experimental Study on Flow Condensation of Mixture in a Hydrophobic Microchannel. *Int. J. Heat Mass Transf.* 104, 1135–1144. doi:10.1016/j.ijheatmasstransfer.2016.09.029

Zhang, T.-Y., Mou, L.-W., Zhang, J.-Y., Fan, L.-W., and Li, J.-Q. (2020). A Visualized Study of Enhanced Steam Condensation Heat Transfer on a Honeycomb-like Microporous Superhydrophobic Surface in the Presence of a Non-condensable Gas. *Int. J. Heat Mass Transf.* 150, 119352. doi:10.1016/j.ijheatmasstransfer.2020.119352

Conflict of Interest: The authors declare that the research was conducted in the absence of any commercial or financial relationships that could be construed as a potential conflict of interest.

Publisher's Note: All claims expressed in this article are solely those of the authors and do not necessarily represent those of their affiliated organizations, or those of the publisher, the editors, and the reviewers. Any product that may be evaluated in this article, or claim that may be made by its manufacturer, is not guaranteed or endorsed by the publisher.

frontiers | Frontiers in Energy Research

OPINION
published: 14 June 2022
doi: 10.3389/fenrg.2022.928187

Viewpoints on the Refrigeration by Renewable Energy

Yue Lu[1] *and Erguang Huo*[1,2]*

[1]Key Laboratory of Energy Thermal Conversion and Control of Ministry of Education, School of Energy and Environment, Southeast University, Nanjing, China, [2]Jiangsu Key Laboratory of Micro and Nano Heat Fluid Flow Technology and Energy Application, School of Physical Science and Technology, Suzhou University of Science and Technology, Suzhou, China

Keywords: absorption refrigeration, adsorption refrigeration, solar energy, geothermal energy, multi-energy complementarity

INTRODUCTION

The increasing greenhouse gas emissions rates are drawing the attention of the world (Chapman et al., 2022). Carbon neutrality is proposed to guide economical construction within energy conservation and environmental protection. For now, various efforts have been taken to realize a low-carbon economy, for example, the developments of cold chain logistics based on the application of liquefied gas (Dong et al., 2021), thermal environment control of buildings based on energy storage using phase change material (Wang et al., 2012; Zhang et al., 2020), and renewable energy supply of vehicles based on hydrogen fuel cells (Tsuchiya, 2008). With the explosively increasing requirements of data processing, the power density of a data center can reach up to 400–3,000 W/m^2, which induces high heat dissipation demand (Zhang et al., 2011; Liu et al., 2013). Thus, the CO_2 emission for data center refrigeration is increasing rapidly (Deymi-Dashtebayaz and Valipour-Namanlo, 2019). It is urgent to develop refrigeration and cold-storage technologies based on zero-carbon energy. Since the extensively existed renewable energy (such as solar energy and geothermal energy) provides heat instead of electricity, the refrigeration methods driven by the heat source is optimal. We introduce the thermal-driven refrigeration methods and the renewable energy that can be utilized to provide insights for optimizing of low-carbon refrigeration for data centers.

OPEN ACCESS

Edited by:
Xiangdong Liu,
Yangzhou University, China

Reviewed by:
Guangping Lei,
North University of China, China
Chuang Wu,
Chongqing University, China

***Correspondence:**
Erguang Huo
huoerguang@126.com

Specialty section:
This article was submitted to Process and Energy Systems Engineering, a section of the journal Frontiers in Energy Research

Received: *25 April 2022*
Accepted: *09 May 2022*
Published: *14 June 2022*

Citation:
Lu Y and Huo E (2022) Viewpoints on the Refrigeration by Renewable Energy. Front. Energy Res. 10:928187. doi: 10.3389/fenrg.2022.928187

THERMAL-DRIVEN REFRIGERATION

Absorption Refrigeration

As illustrated in **Figure 1A**, in an absorption refrigeration cycle, the refrigerant absorbs heat from the heat source in the evaporator and turns from liquid into gas, producing a cooling effect. The gaseous refrigerant is absorbed in the absorber and then pumped to the generator to be pressurized. In the condenser, the gaseous refrigerant condenses into liquid and then expands through the valve and returns to the evaporator for cycling (Best and Rivera, 2015).

The most efficient and common working pairs are water–lithium bromide and ammonia–water. The former is used where moderate temperatures are required while the latter is generally used in large-capacity industrial applications requiring low temperatures. Water–lithium bromide absorption systems are disadvantageous when working at a condensation temperature higher than 40°C due to crystallization (Izquierdo, 2004). The binary ammonia–salt solutions of NH_3-NaSCN and NH_3-$LiNO_3$ are regarded as a viable alternative for ammonia–water. The Rankine cycle, including single-loop cogeneration cycle, Goswami cycle, and dual-loop cogeneration cycle, is applied in the co- and tri-generation system. The energy efficiency of a trigeneration system can reach more than 80% and meanwhile reduce CO_2 emission.

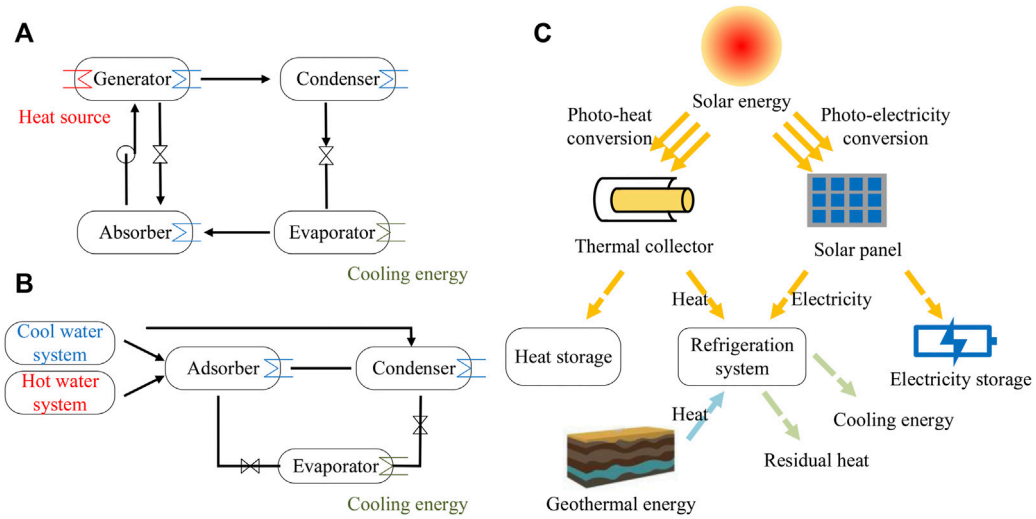

FIGURE 1 | Schematic diagram of refrigeration: **(A)** absorption refrigeration, **(B)** adsorption refrigeration, and **(C)** multi-energy complementarity.

Adsorption Refrigeration

The earliest adsorption refrigeration, single-bed intermittent cycle, is simple and reliable, but the efficiency is very low and the cooling output is discrete, as shown in **Figure 1B**. So recovery cycles are designed to improve the efficiency and practicability of adsorption refrigeration. Enhancing the adsorbent and optimizing the design of the adsorber are two common ways to improve the heat and mass transfer in adsorption systems. The adsorbent is improved by adding materials with high thermal conductivity. For example, the thermal conductivity of calcium chloride is only 0.1–0.2 W/(m ˚C) which can be increased by ten times by adding graphite powder (Eltom and Sayigh, 1994). Fins and heat pipes are optimal in increasing the effective heat transfer area of adsorbers (Vasiliev et al., 1996). The effects of fin geometries, spatial positions, and volume fractions of the filled adsorbent in a parallel-flow aluminum flat tube adsorption bed were compared on the heat transfer performance (Chen et al., 2020).

In summary, adsorbent refrigeration has a lower efficiency and is more robust than absorption refrigeration. Some improvements have been made to enhance the efficiencies of adsorbent refrigeration. However, it seems that it does not work for applications below freezing temperature.

RENEWABLE ENERGY REFRIGERATION

Among various renewable energy, such as wind energy, biomass energy, solar energy, and geothermal energy (Himri et al., 2009), the last two are the most applicated and easy to access. Hence, refrigeration of data centers based on solar energy and geothermal energy is most feasible.

Solar Energy

The single-effect lithium bromide absorption refrigerators with solar energy as a heat source are superior due to their excellent temperature match and economy. Categories, types, and volumes of solar energy collectors are pivotal in determining energy efficiency of the system (Gao et al., 2021; Yu et al., 2021). The average coefficient of performance (COP) of an absorption air conditioner with solar energy in summer was 0.6, with an average cooling capacity of 40 kW (Ebrahimi and Ahookhosh, 2016). Through TRNSYS software, a solar energy–driven lithium bromide absorption refrigeration system with a capacity of 11 kW was analyzed. The results prove that this system was economically competitive and the effect of global warming was lower than that for conventional refrigeration systems (Balghouthi et al., 2008).

The intensity of solar irradiation meets the duration for refrigeration demand. However, the low power density of solar energy restricts its application. The spotlighting device was proposed to promote the power density of solar energy (Rabl et al., 1978). A composite parabolic concentrator (CPC) combined with a fin-tube adsorber was applied to the adsorption refrigeration, in which the temperature of the adsorption bed rose from 26 to 124˚C in 120 min (Wang et al., 2018). Both numerical and experimental studies show that fins enhance the performance of the CPC adsorption bed (Zhao et al., 2019).

Overall, the absorption refrigeration of solar energy is superior to the adsorption refrigeration. However, the inherent instability of solar energy restricts constant and sustainable cooling. Solar-driven refrigeration assisted by energy storage is viable in situations that require unintermittent refrigeration.

Geothermal Energy

A large amount of geothermal energy is contained in the earth's interior, which offers a stable heat source. It is usually divided into shallow geothermal energy, hydrothermal geothermal energy, and hot dry rock geothermal energy.

The COP of an absorption cycle driven by geothermal energy was expected to reach 0.5654 at the mass flow rate of geothermal energy of 12 kg/s, and the relationship between COP and mass flow rate was positively correlated (Keçeciler et al., 2000). A combination of photovoltaic, solar chimney, and geothermal air

tubes was proposed for the refrigeration and ventilation of a room (Rania Elghamry, 2020). It turned out that the room temperature decreased by 3.4°C and the maximum power output of the photovoltaic panel increased by 30%.

Multi-Energy Complementarity

The combination of solar energy and geothermal energy can achieve better performance for refrigeration, as demonstrated in **Figure 1C**. The geothermal energy with medium and high temperatures is stable and sustainable, which contributes to the stable operation and high cooling efficiency. However, the natural recovery of soil temperature is difficult. Consequently, multi-energy complementarity, which combines the superiorities of geothermal energy and solar energy, is a solution for zero-carbon refrigeration. The solar–geothermal hybrid system showed a 5.5% boost in annual power generation and a 3.4% increment in maximum second efficiency compared to separate systems (Ghasemi et al., 2014). Integrating the CO_2-based Enhanced Geothermal Systems (EGS) into the solar power plant can achieve equal or higher efficiency than the sum of the two original systems (Jiang et al., 2017). Moreover, the cost of the system installation and maintenance could be reduced due to the decreased operating pressure and removal of the compressor.

CONCLUSION

Zero-carbon refrigeration technology based on renewable energy is significant in putting forward the carbon-neutral technical evolution. Multi-energy complementarity is a promising approach to realizing zero-carbon refrigeration for data centers. The high efficiency and sustainable operation of a zero-carbon refrigeration system depends on the efficient utilization of photovoltaic–photothermal energy, energy storage, step utilization of energy, and irreversible losses reduction.

AUTHOR CONTRIBUTIONS

EH contributed to conception of the study. YL wrote the first draft of the manuscript. All authors contributed to manuscript revision and read and approved the submitted version.

FUNDING

This work is supported by the National Natural Science Foundation of China (No. 52106023).

REFERENCES

Balghouthi, M., Chahbani, M. H., and Guizani, A. (2008). Feasibility of Solar Absorption Air Conditioning in Tunisia. *Build. Environ.* 43 (9), 1459–1470. doi:10.1016/j.buildenv.2007.08.003

Best, R., and Rivera, W. (2015). A Review of Thermal Cooling Systems. *Appl. Therm. Eng.* 75, 1162–1175. doi:10.1016/j.applthermaleng.2014.08.018

Chapman, A., Ertekin, E., Kubota, M., Nagao, A., Bertsch, K., Macadre, A., et al. (2022). Achieving a Carbon Neutral Future through Advanced Functional Materials and Technologies. *Bull. Chem. Soc. Jpn.* 95 (1), 73–103. doi:10.1246/bcsj.20210323

Chen, R., Quan, Z., Zhao, Y., and Tang, S. (2020). Performance Analysis of Adsorption Refrigeration System Based on Parallel Flow Flat Tube. *J. Eng. Thermophys.* 41 (4), 981–988.

Deymi-Dashtebayaz, M., and Valipour-Namanlo, S. (2019). Thermoeconomic and Environmental Feasibility of Waste Heat Recovery of a Data Center Using Air Source Heat Pump. *J. Clean. Prod.* 219, 117–126. doi:10.1016/j.jclepro.2019.02.061

Dong, Y., Xu, M., and Miller, S. A. (2021). Overview of Cold Chain Development in China and Methods of Studying its Environmental Impacts. *Environ. Res. Commun.* 2 (12), 122002. doi:10.1088/2515-7620/abd622

Ebrahimi, M., and Ahookhosh, K. (2016). Integrated Energy-Exergy Optimization of a Novel Micro-CCHP Cycle Based on MGT-ORC and Steam Ejector Refrigerator. *Appl. Therm. Eng.* 102, 1206–1218. doi:10.1016/j.applthermaleng.2016.04.015

Elghamry, R., and Hassan, H. (2020). An Experimental Work on the Impact of New Combinations of Solar Chimney, Photovoltaic and Geothermal Air Tube on Building Cooling and Ventilation. *Sol. Energy* 205, 142–153. doi:10.1016/j.solener.2020.05.049

Eltom, O. M. M., and Sayigh, A. A. M. (1994). A Simple Method to Enhance Thermal Conductivity of Charcoal Using Some Additives. *Renew. Energy* 4 (1), 113–118. doi:10.1016/0960-1481(94)90072-8

Gao, W., Lei, Z., Wu, K., and Chen, Y. (2021). Reconfigurable and Renewable Nano-Micro-Structured Plastics for Radiative Cooling. *Adv. Funct. Mat.* 31 (21), 2100535. doi:10.1002/adfm.202100535

Ghasemi, H., Sheu, E., Tizzanini, A., Paci, M., and Mitsos, A. (2014). Hybrid Solar-Geothermal Power Generation: Optimal Retrofitting. *Appl. Energy* 131, 158–170. doi:10.1016/j.apenergy.2014.06.010

Himri, Y., Malik, A. S., Boudghene Stambouli, A., Himri, S., and Draoui, B. (2009). Review and Use of the Algerian Renewable Energy for Sustainable Development. *Renew. Sustain. Energy Rev.* 13 (6-7), 1584–1591. doi:10.1016/j.rser.2008.09.007

Izquierdo, M. (2004). Crystallization as a Limit to Develop Solar Air-Cooled LiBr-H_2o Absorption Systems Using Low-Grade Heat. *Sol. Energy Mater. Sol. Cells* 81 (2), 205–216. doi:10.1016/j.solmat.2003.11.002

Jiang, P.-X., Zhang, F.-Z., and Xu, R.-N. (2017). Thermodynamic Analysis of a Solar-Enhanced Geothermal Hybrid Power Plant Using CO 2 as Working Fluid. *Appl. Therm. Eng.* 116, 463–472. doi:10.1016/j.applthermaleng.2016.12.086

Keçeciler, A., Acar, H. I., and Doğan, A. (2000). Thermodynamic Analysis of the Absorption Refrigeration System with Geothermal Energy: an Experimental Study. *Energy Convers. Manag.* 41, 37–48. doi:10.1016/S0196-8904(99)00091-6

Liu, X., Chen, Y., and Shi, M. (2013). Dynamic Performance Analysis on Start-Up of Closed-Loop Pulsating Heat Pipes (CLPHPs). *Int. J. Therm. Sci.* 65, 224–233. doi:10.1016/j.ijthermalsci.2012.10.012

Rabl, A., Goodman, N. B., and Winston, R. (1978). Practal Design Considerations for CPC Solar Collectors. *Sol. Energy* 22, 373–381. doi:10.1016/0038-092X(79)90192-0

Tsuchiya, H. (2008). Innovative Renewable Energy Solutions for Hydrogen Vehicles. *Int. J. Energy Res.* 32 (5), 427–435. doi:10.1002/er.1374

Vasiliev, L. L., Kanonchik, L. E., Antuh, A. A., and Kulakov, A. G. (1996). NaX Zeolite, Carbon Fibre and CaCl2 Ammonia Reactors for Heat Pumps and Refrigerators. *Adsorption* 2, 311–316. doi:10.1007/bf00879546

Wang, Y. J., Tao, H. G., and Zhang, Z. P. (2012). Experimental Study of Binary Composite Phase Change Material for Building. *Amm* 253-255, 354–357. doi:10.4028/www.scientific.net/AMM.253-255.354

Wang, Y., Li, M., Du, W., Yu, Q., Ji, X., and Ma, X. (2018). Performance Comparative Study of a Solar-Powered Adsorption Refrigerator with a CPC Collector/adsorbent Bed. *Energy Convers. Manag.* 173, 499–507. doi:10.1016/j.enconman.2018.07.080

Yu, C., Li, H., Chen, J., Qiu, S., Yao, F., and Liu, X. (2021). Investigation of the Thermal Performance Enhancement of a Photovoltaic Thermal (PV/T) Collector with Periodically Grooved Channels. *J. Energy Storage* 40, 102792. doi:10.1016/j.est.2021.102792

Zhang, C., Chen, Y., Wu, R., and Shi, M. (2011). Flow Boiling in Constructal Tree-Shaped Minichannel Network. *Int. J. Heat Mass Transf.* 54 (1), 202–209. doi:10.1016/j.ijheatmasstransfer.2010.09.051

Zhang, C., Li, J., and Chen, Y. (2020). Improving the Energy Discharging Performance of a Latent Heat Storage (LHS) Unit Using Fractal-Tree-Shaped Fins. *Appl. Energy* 259, 114102. doi:10.1016/j.apenergy.2019.114102

Zhao, C., Wang, Y., Li, M., and Du, W. (2019). Heat Transfer Performance Investigation on a Finned Tube Adsorbent Bed with a Compound Parabolic Concentrator (CPC) for Solar Adsorption Refrigeration. *Appl. Therm. Eng.* 152, 391–401. doi:10.1016/j.applthermaleng.2019.02.063

Conflict of Interest: The authors declare that the research was conducted in the absence of any commercial or financial relationships that could be construed as a potential conflict of interest.

Publisher's Note: All claims expressed in this article are solely those of the authors and do not necessarily represent those of their affiliated organizations, or those of the publisher, the editors, and the reviewers. Any product that may be evaluated in this article, or claim that may be made by its manufacturer, is not guaranteed or endorsed by the publisher.

frontiers | Frontiers in Energy Research

OPINION
published: 20 June 2022
doi: 10.3389/fenrg.2022.960537

Opportunities and Challenges of Seawater Desalination Technology

Jiangang Wang[1] *and Erguang Huo*[1,2]*

[1]Key Laboratory of Energy Thermal Conversion and Control of Ministry of Education, School of Energy and Environment, Southeast University, Nanjing, China, [2]Jiangsu Key Laboratory of Micro and Nano Heat Fluid Flow Technology and Energy Application, School of Physical Science and Technology, Suzhfou University of Science and Technology, Suzhou, China

Keywords: seawater desalination, multiple effect distillation, multi-stage flash, reverse osmosis, ocean thermal energy

INTRODUCTION

70% of the earth's surface is covered by water, but fresh water only accounts for 2.7% of total water in the world, and only 0.3% of freshwater can be directly used by humans (Zapata-Sierra et al., 2021). With the development of the world economy, population growth, and consumption of freshwater resources, the global per capita average of freshwater resources has dropped by half in the past 50 years, and the developed cities, island areas, and ships have more urgent demands for freshwater resources (Jones et al., 2019). It is predicted that three-quarters of the population in the world will suffer from freshwater shortages by 2050. In addition, the pollution of freshwater resources is more serious due to the impact of COVID-19, which has also accelerated research progress in the fields of freshwater protection and seawater desalination (Zhang et al., 2022).

Desalination technology, which produces freshwater by removing salt and other mineral components from seawater, has become one of the most important solutions for water treatment and drinking water production in the world (Lin et al., 2021). At present, there are 19,000 existing desalination plants, which can produce more than 1×10^8 m^3/day of freshwater (Alrowais et al., 2022). Most desalination plants are located in countries with a shortage of freshwater resources but rich in energy, such as the United States and Gulf states. In addition, China and India have developed rapidly in the field of seawater desalination and carried out a great deal of seawater desalination research (Liu et al., 2019; Eke et al., 2020). An overview of the major desalination technologies in the world and the desalination technology based on ocean thermal energy is introduced in this paper, and the possible challenges and future development prospects of seawater desalination technology in the future application are discussed to provide a reference for the subsequent development of the seawater desalination industry (Rey and Lauro, 1981).

DEVELOPMENT STATUS OF SEAWATER DESALINATION TECHNOLOGY

Desalination technologies can be classified according to the driving energy required in the desalination process, namely thermally-driven, mechanically-driven, and electrically-driven desalination methods (Nassrullah et al., 2020). Thermally-driven desalination technologies mainly include multiple effect distillation (MED) and multi-stage flash (MSF) (Aly et al., 2021). Mechanically-driven desalination technology mainly refers to membrane processes, among which reverse osmosis (RO) has been widely used due to its lower energy consumption and flexible installed capacity (Qasim et al., 2019). Electrically driven desalination technology allows ions to pass through selectivity exchange membranes under a direct-current electric field to obtain fresh water. Due to this technology's high consumption of direct electrical energy, it only accounts for 2% of the desalination capacity in the world (Subramani and Jacangelo, 2015). Additionally, emerging desalination

OPEN ACCESS

Edited by:
Xiangdong Liu,
Yangzhou University, China

Reviewed by:
Mengbing Cao,
Zhejiang University, China

***Correspondence:**
Erguang Huo
huoerguang@126.com

Specialty section:
This article was submitted to Process and Energy Systems Engineering, a section of the journal Frontiers in Energy Research

Received: *03 June 2022*
Accepted: *06 June 2022*
Published: *20 June 2022*

Citation:
Wang J and Huo E (2022) Opportunities and Challenges of Seawater Desalination Technology. Front. Energy Res. 10:960537. doi: 10.3389/fenrg.2022.960537

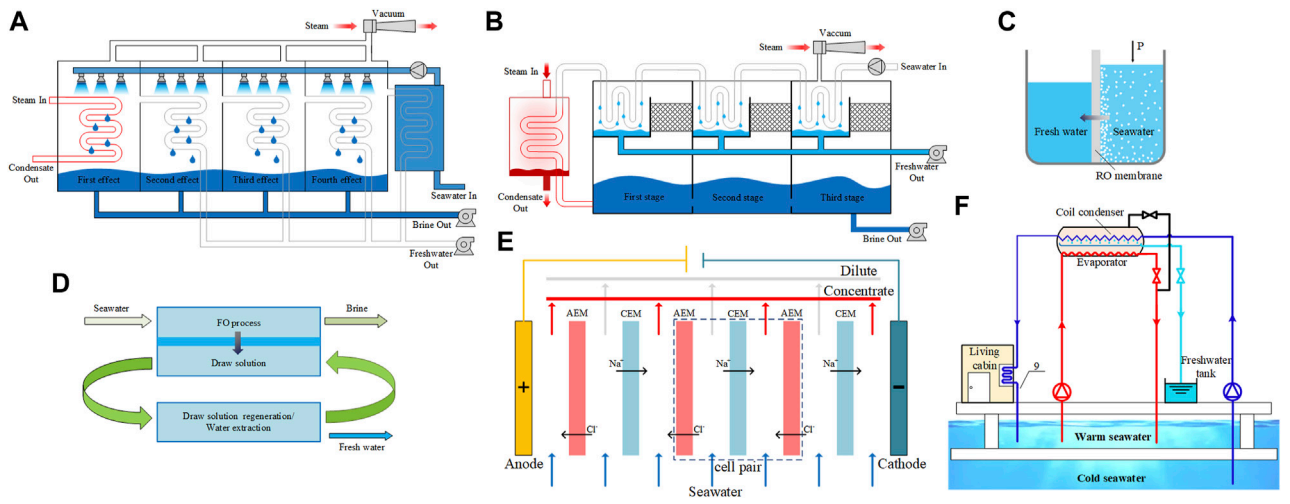

FIGURE 1 | Schematic of the seawater desalination process: **(A)** MED, **(B)** MSF, **(C)** RO, **(D)** FO, **(E)** ED/EDR, **(F)** low-pressure flash evaporation system powered by ocean thermal energy.

technologies, such as membrane distillation (MD) combining thermal energy and membrane separation, can be driven by low-grade heat rather than electricity. They are promising although currently being investigated at laboratory.

Figure 1A shows the schematic of the MED system (Alhotmani et al., 2020), the steam enters the first effect to heat the seawater as the heating medium. The seawater is heated to boiling temperature and then a part is evaporated. Condensation occurs once the generated vapor has flowed into the next effect, and the process repeats for all the effects. In the final condenser, the vapor produced in the last effect is condensed while the seawater is preheated (Wang et al., 2011). In the late 1970s, the technology of low-temperature multiple effect distillation (LT-MED) that utilizes low-grade steam at temperatures of 50–70°C is developed by IDE company, which reduces desalination costs, mitigates corrosion and scaling issues, resulting in the cost of producing fresh water is reduced to $0.738 per ton (Liu et al., 2021). The MSF is based on the flash evaporation principle, and the MSF process is shown in **Figure 1B** (Zhao et al., 2018). The seawater is heated by the steam and flows into the flash evaporator, and the hot seawater is rapidly vaporized due to the lower pressure in the flash evaporator than the saturation pressure. The generated vapor is condensed into fresh water while heating the front seawater, and the remaining seawater is sent to the next flash evaporator and vaporized at lower pressure (Khawaji et al., 2008). MSF technology is highly reliable and is easy to be scaled up, but it is often combined with thermal power plants to achieve "co-generation of fresh water and power" due to its large heat requirements, and the cost per ton of water production in this combined system is about $1.023 (Semiat, 2008).

As the most widely used seawater desalination technology in the world, RO is used in 84% of desalination plants (Ng et al., 2021). The principle of RO is as follows (**Figure 1C**): when the pressure applied to the seawater is greater than the osmotic pressure, the water molecules in the seawater will enter the freshwater side through the RO membrane, and the solute is isolated in the seawater side by the membrane. The research of RO technology mainly focuses on the improvement of membrane performance. The ideal RO membrane should have good mechanical properties, thermal stability, high desalination rate, low cost, and less impact on pH and temperature. RO technology has been substantially improved over the past few decades, resulting in the energy consumption per ton of fresh water produced has been significantly reduced to $0.749 (Patel et al., 2022). Nanomaterials, such as SiO_2 nanoparticles (Nguyen et al., 2021), carbon nanotubes (Ghanbari et al., 2015), and metal-organic frameworks (Ji et al., 2019), are receiving increasing attention for the preparation of RO membranes based on thin-film nanocomposite (TFN). This TFN membrane has the advantages of high chemical, thermal stability, and water permeability. Forward osmosis (FO) technology is different from RO technology. In the FO process, water is permeated from seawater to the draw solution through the FO membrane because of the higher osmotic pressure than the seawater. The main problem with this technology is that the fresh water in the draw solution is difficult to separate, the principle of FO is shown in **Figure 1D**.

The scheme of electrodialysis and electrodialysis reversal (ED/EDR) driven by electricity is shown in **Figure 1E**. The ED/EDR system consists of repeated unit pairs, each unit pair includes a desalination chamber and a concentration chamber. When seawater is introduced and energized, the Na^+ in the desalination chamber is migrated to the cathode through the cation exchange membrane (CEM), and the Cl^- is migrated to the anode through the anion exchange membrane (AEM), thus the fresh water is generated from the seawater in the desalination chamber and the concentrated seawater is formed in the concentration chamber. The scaling of EDR is reduced by periodically switching the polarity of the electrodes. ED/EDR has the advantages such as simple pretreatment of feedwater because only the charged ions are affected by the electric potential during the desalination process, thus ED/EDR technology is suitable for treating feed water with high suspended solids and

achieving high recovery rates. However, the capacity of seawater desalination plants using ED/EDR technology is generally small due to the high electricity consumption. In a study by Liu et al., the desalination rate of brackish water in ED/EDR reached 90% with electricity consumption of 1 kWh/m^3 (Liu and Wang, 2017).

The traditional seawater desalination technologies have the problems such as high investment, high energy consumption, and environmental pollution, the seawater desalination technology based on renewable energy is an effective way to solve the above problems (Chen et al., 2014). As marine renewable energy, ocean thermal energy is considered to have great development potential due to its huge reserves and stable energy supply (Gao et al., 2021). The seawater desalination technology based on ocean thermal energy is suitable for low latitude regions with the most effective method of flash evaporation technology (Gao et al., 2019). In this flash evaporation system, the surface warm seawater is flash evaporated by a vacuum pump at a low temperature, and the vapor produced is exchanged with the deep cold seawater and condensed into fresh water (Jin et al., 2017). However, the non-condensable gas (NCG) dissolved in the seawater is gradually released during the flashing process, and then the condensation process is hindered by the NCG, resulting in the yield of fresh water being reduced (Zhang et al., 2017). Therefore, a part of the electric energy must be consumed to ensure the operation of the vacuum pump to extract the NCG in the desalination process. To reduce electricity consumption, natural vacuum technology can be used in the flash tank (Al-Kharabsheh and Goswami, 2003). The natural vacuum technology is based on the Torricelli phenomenon, which makes the warm seawater at 30°C vaporize at a 10.33 m-high water column under natural conditions (**Figure 1F**). The electricity consumption and recovery rate achieved by this technology are 0.126 kWh/kg and 1.5%, respectively (Wang et al., 2022). It can be seen that the cost of ocean thermal energy only used for seawater desalination is higher than that of traditional desalination technologies such as RO due to the difficulty in extracting deep cold seawater. Therefore, this desalination technology is usually used as a supplement to ocean thermal energy conversion (OTEC) to improve the utilization efficiency of ocean thermal energy.

OPPORTUNITIES AND CHALLENGES

With the economic development and population growth, human demand for freshwater resources will continue to increase (Deng et al., 2017). This brings opportunities and challenges to the application and development of desalination technology, especially seawater desalination. This paper introduces the traditional seawater desalination technologies and the desalination technology based on ocean thermal energy with great development potential. Considering the research status and practical application requirements of seawater desalination technology, the following aspects need to be further studied in the future:

1) High cost is the worst problem for the development of the desalination industry, thus, more attention should be paid to the development of low-grade energy utilization for thermally-driven desalination processes. In addition, the performance of the membrane and the stability of membrane-based desalination processes should be improved.
2) Develop new technologies for desalination technology using renewable energy. Although renewable energy has abundant reserves and is environmentally friendly, it is generally inefficient and uneconomical. Therefore, a new desalination technology using renewable energy sources such as wind, solar, marine, and nuclear should be introduced to reduce traditional energy consumption and carbon emissions.

AUTHOR CONTRIBUTIONS

EH contributed to conception of the study. JW wrote the first draft of the manuscript. All authors contributed to manuscript revision, read, and approved the submitted version.

FUNDING

This work is supported by National Natural Science Foundation of China (No. 52106023).

REFERENCES

Al-hotmani, O. M. A., Al-Obaidi, M. A., Filippini, G., Manenti, F., Patel, R., and Mujtaba, I. M. (2020). Optimisation of Multi Effect Distillation Based Desalination System for Minimum Production Cost for Freshwater via Repetitive Simulation. *Comput. Chem. Eng.* 135, 106710. doi:10.1016/j.compchemeng.2019.106710

Al-Kharabsheh, S., and Goswami, D. Y. (2003). Analysis of an Innovative Water Desalination System Using Low-Grade Solar Heat. *Desalination* 156, 323–332. doi:10.1016/S0011-9164(03)00363-1

Alrowais, R., Shahzad, M. W., Burhan, M., Bashir, M. T., Chen, Q., Xu, B. B., et al. (2022). A Thermally-Driven Seawater Desalination System: Proof of Concept and Vision for Future Sustainability. *Case Stud. Therm. Eng.* 35, 102084. doi:10.1016/j.csite.2022.102084

Aly, S., Manzoor, H., Simson, S., Abotaleb, A., Lawler, J., and Mabrouk, A. N. (2021). Pilot Testing of a Novel Multi Effect Distillation (MED) Technology for Seawater Desalination. *Desalination* 519, 115221. doi:10.1016/j.desal.2021.115221

Chen, Y., Shen, C., Shi, M., and Peterson, G. P. (2014). Visualization Study of Flow Condensation in Hydrophobic Microchannels. *AICHE J.* 60, 1182–1192. doi:10.1002/aic.14319

Deng, Z., Zhang, C., Shen, C., Cao, J., and Chen, Y. (2017). Self-propelled Dropwise Condensation on a Gradient Surface. *Int. J. Heat Mass Transf.* 114, 419–429. doi:10.1016/j.ijheatmasstransfer.2017.06.065

Eke, J., Yusuf, A., Giwa, A., and Sodiq, A. (2020). The Global Status of Desalination: An Assessment of Current Desalination Technologies, Plants and Capacity. *Desalination* 495, 114633. doi:10.1016/j.desal.2020.114633

Gao, W., Qi, J., Zhang, J., Chen, G., and Wu, D. (2019). An Experimental Study on Explosive Boiling of Superheated Droplets in Vacuum Spray Flash Evaporation. *Int. J. Heat Mass Transf.* 144, 118552. doi:10.1016/j.ijheatmasstransfer.2019.118552

Gao, W., Lei, Z., Liu, X., and Chen, Y. (2021). Dynamic Liquid Gating Artificially Spinning System for Self-Evolving Topographies and Microstructures. *Langmuir* 37, 1438–1445. doi:10.1021/acs.langmuir.0c02910

Ghanbari, M., Emadzadeh, D., Lau, W. J., Lai, S. O., Matsuura, T., and Ismail, A. F. (2015). Synthesis and Characterization of Novel Thin Film Nanocomposite

(TFN) Membranes Embedded with Halloysite Nanotubes (HNTs) for Water Desalination. *Desalination* 358, 33–41. doi:10.1016/j.desal.2014.11.035

Ji, C., Xue, S., Tang, Y.-J., Ma, X.-H., and Xu, Z.-L. (2019). Polyamide Membranes with Net-like Nanostructures Induced by Different Charged MOFs for Elevated Nanofiltration. *ACS Appl. Polym. Mat.* 2, 585–593. doi:10.1021/acsapm.9b00973

Jin, Z.-j., Ye, H., Wang, H., Li, H., and Qian, J.-y. (2017). Thermodynamic Analysis of Siphon Flash Evaporation Desalination System Using Ocean Thermal Energy. *Energy Convers. Manag.* 136, 66–77. doi:10.1016/j.enconman.2017.01.002

Jones, E., Qadir, M., van Vliet, M. T. H., Smakhtin, V., and Kang, S.-m. (2019). The State of Desalination and Brine Production: A Global Outlook. *Sci. Total Environ.* 657, 1343–1356. doi:10.1016/j.scitotenv.2018.12.076

Khawaji, A. D., Kutubkhanah, I. K., and Wie, J.-M. (2008). Advances in Seawater Desalination Technologies. *Desalination* 221, 47–69. doi:10.1016/j.desal.2007.01.067

Lin, S., Zhao, H., Zhu, L., He, T., Chen, S., Gao, C., et al. (2021). Seawater Desalination Technology and Engineering in China: A Review. *Desalination* 498, 114728. doi:10.1016/j.desal.2020.114728

Liu, Y., and Wang, J. (2017). Energy-saving "NF/EDR" Integrated Membrane Process for Seawater Desalination. Part II. The Optimization of ED Process. *Desalination* 422, 142–152. doi:10.1016/j.desal.2017.07.010

Liu, S. Y., Zhang, G. X., Han, M. Y., Wu, X. D., Li, Y. L., Chen, K., et al. (2019). Freshwater Costs of Seawater Desalination: Systems Process Analysis for the Case Plant in China. *J. Clean. Prod.* 212, 677–686. doi:10.1016/j.jclepro.2018.12.012

Liu, S., Wang, Z., Han, M., and Zhang, J. (2021). Embodied Water Consumption between Typical Desalination Projects: Reverse Osmosis versus Low-Temperature Multi-Effect Distillation. *J. Clean. Prod.* 295, 126340. doi:10.1016/j.jclepro.2021.126340

Nassrullah, H., Anis, S. F., Hashaikeh, R., and Hilal, N. (2020). Energy for Desalination: A State-Of-The-Art Review. *Desalination* 491, 114569. doi:10.1016/j.desal.2020.114569

Ng, Z. C., Lau, W. J., Matsuura, T., and Ismail, A. F. (2021). Thin Film Nanocomposite RO Membranes: Review on Fabrication Techniques and Impacts of Nanofiller Characteristics on Membrane Properties. *Chem. Eng. Res. Des.* 165, 81–105. doi:10.1016/j.cherd.2020.10.003

Nguyen, T.-Q., Tung, K.-L., Lin, Y.-L., Dong, C.-D., Chen, C.-W., and Wu, C.-H. (2021). Modifying Thin-Film Composite Forward Osmosis Membranes Using Various SiO2 Nanoparticles for Aquaculture Wastewater Recovery. *Chemosphere* 281, 130796. doi:10.1016/j.chemosphere.2021.130796

Patel, C. G., Barad, D., and Swaminathan, J. (2022). Desalination Using Pressure or Electric Field? A Fundamental Comparison of RO and Electrodialysis. *Desalination* 530, 115620. doi:10.1016/j.desal.2022.115620

Qasim, M., Badrelzaman, M., Darwish, N. N., Darwish, N. A., and Hilal, N. (2019). Reverse Osmosis Desalination: A State-Of-The-Art Review. *Desalination* 459, 59–104. doi:10.1016/j.desal.2019.02.008

Rey, M., and Lauro, F. (1981). Ocean Thermal Energy and Desalination. *Desalination* 39, 159–168. doi:10.1016/S0011-9164(00)86118-4

Semiat, R. (2008). Energy Issues in Desalination Processes. *Environ. Sci. Technol.* 42, 8193–8201. doi:10.1021/es801330u

Subramani, A., and Jacangelo, J. G. (2015). Emerging Desalination Technologies for Water Treatment: A Critical Review. *Water Res.* 75, 164–187. doi:10.1016/j.watres.2015.02.032

Wang, X., Christ, A., Regenauer-Lieb, K., Hooman, K., and Chua, H. T. (2011). Low Grade Heat Driven Multi-Effect Distillation Technology. *Int. J. Heat Mass Transf.* 54, 5497–5503. doi:10.1016/j.ijheatmasstransfer.2011.07.041

Wang, L., Ma, X., Kong, H., Jin, R., and Zheng, H. (2022). Investigation of a Low-Pressure Flash Evaporation Desalination System Powered by Ocean Thermal Energy. *Appl. Therm. Eng.* 212, 118523. doi:10.1016/j.applthermaleng.2022.118523

Zapata-Sierra, A., Cascajares, M., Alcayde, A., and Manzano-Agugliaro, F. (2021). Worldwide Research Trends on Desalination. *Desalination* 519, 115305. doi:10.1016/j.desal.2021.115305

Zhang, C., Shen, C., and Chen, Y. (2017). Experimental Study on Flow Condensation of Mixture in a Hydrophobic Microchannel. *Int. J. Heat Mass Transf.* 104, 1135–1144. doi:10.1016/j.ijheatmasstransfer.2016.09.029

Zhang, X., Jiang, J., Yuan, F., Song, W., Li, J., Xing, D., et al. (2022). Estimation of Water Footprint in Seawater Desalination with Reverse Osmosis Process. *Environ. Res.* 204, 112374. doi:10.1016/j.envres.2021.112374

Zhao, J., Wang, M., Lababidi, H. M. S., Al-Adwani, H., and Gleason, K. K. (2018). A Review of Heterogeneous Nucleation of Calcium Carbonate and Control Strategies for Scale Formation in Multi-Stage Flash (MSF) Desalination Plants. *Desalination* 442, 75–88. doi:10.1016/j.desal.2018.05.008

Conflict of Interest: The authors declare that the research was conducted in the absence of any commercial or financial relationships that could be construed as a potential conflict of interest.

Publisher's Note: All claims expressed in this article are solely those of the authors and do not necessarily represent those of their affiliated organizations, or those of the publisher, the editors and the reviewers. Any product that may be evaluated in this article, or claim that may be made by its manufacturer, is not guaranteed or endorsed by the publisher.

frontiers | Frontiers in Energy Research

OPINION
published: 20 June 2022
doi: 10.3389/fenrg.2022.954718

Discussions of Cold Plate Liquid Cooling Technology and Its Applications in Data Center Thermal Management

*Yufeng Zhang, Chengcheng Fan and Guanru Li**

Key Laboratory of Energy Thermal Conversion and Control of Ministry of Education, Southeast University, Nanjing, China

Keywords: data center, cold plate liquid cooling, heat dissipation of electronic devices, PUE, thermal management

INTRODUCTION

With the rapid development of information technology such as 5G mobile communication, big data and cloud computing, the size and capacity of data centers are increasing at a rapid pace. To achieve high-performance computing, the electronic devices of data centers are increasingly high-integrated, which leads to an increase in heat generation power and heat flow density (Dong et al., 2017). For example, a traditional data center consumes about 7 kW per rack, while a new high-performance server consumes 50 kW per rack and is expected to reach over 100 kW within 5 years (Garimella et al., 2012). The increase in power density of high-performance servers makes the data center heat dissipation problem more obvious (Zhang et al., 2021). How the cooling system timely and efficiently removes the heat generated by the electronic devices to meet the temperature requirements of their normal work has become the main bottleneck restricting the green development of data centers.

Over 40% of the data center's energy consumption is generated by the cooling system which is one of the highest energy consumption parts of the data centers (Habibi Khalaj and Halgamuge, 2017). Therefore, choosing efficient cooling technology is an effective means to avoid overheating failure of electronics and reduce energy consumption in data centers (Liu et al., 2013). Onefold air-cooled technology has been proved to be dissatisfied with the heat cooling requirements of high-power data centers with the problems such as local hot spots and high energy consumption (Moazamigoodarzi et al., 2020). The specific heat capacity of liquid is 1,000–3,500 times the specific heat capacity of air, and the thermal conductivity of the liquid is 15–25 times the thermal conductivity of air (Haywood et al., 2015). With the benefits of high reliability and low energy consumption, the liquid cooling technology better meets the cooling needs of new high-density data centers (Deng et al., 2022). Among the liquid cooling technologies, cooling plate-based liquid refrigeration technology is the earliest applied and the most popular, and its cooling effect is significantly better than air-cooled technology In engineering applications, the cold plate liquid cooling technology combined with air cooling technology can remove the heat of the server more quickly and reduce the power usage effectiveness (PUE) of the data center effectively. It is considered the main technical approach to solving the high heat flow and high power consumption problems of data center cooling systems (Habibi Khalaj et al., 2015).

This paper gives an outline of the development status of cooling plate-based liquid refrigeration technology and discusses the possible problems and challenges in its future application, providing a basis for the subsequent construction of green and high-efficiency data centers.

OPEN ACCESS

Edited by:
Xiangdong Liu,
Yangzhou University, China

Reviewed by:
Conghui Gu,
Jiangsu University of Science and Technology, China

****Correspondence:***
Guanru Li
liguanru@seu.edu.cn

Specialty section:
This article was submitted to Process and Energy Systems Engineering, a section of the journal Frontiers in Energy Research

Received: *27 May 2022*
Accepted: *06 June 2022*
Published: *20 June 2022*

Citation:
Zhang Y, Fan C and Li G (2022) Discussions of Cold Plate Liquid Cooling Technology and Its Applications in Data Center Thermal Management. Front. Energy Res. 10:954718. doi: 10.3389/fenrg.2022.954718

DEVELOPMENT STATUS OF COLD PLATE LIQUID COOLING TECHNOLOGY

The standard cooling plate-based liquid refrigeration system consists mainly of a cold plate, a cooling distribution unit, a circulating pump, and a chiller (Kheirabadi and Groulx, 2016). The cooling plate-based liquid refrigeration technology transports the heat from the electronic device to the coolant in the circulating pipe *via* the cold plate, and then the coolant transports the heat to the chiller, where it is eventually dissipated to the external environment or recycled (**Figure 1**).

In the cooling system based on cooling plate-based liquid refrigeration technology, the coolant has no direct contact with the server, which is an indirect liquid cooling technology. According to whether the evaporation of coolant occurs in the cold plate, can be categorized into single-phase cooling plate-based liquid refrigeration technology and two-phase cooling plate-based liquid refrigeration technology (Rani and Garg, 2021). Water-cooled backplanes are often used in cold plate cooling technology, distinguished as open water-cooled backplanes and closed water-cooled backplanes. Open water-cooled backplanes can reach a cooling power of 8–12 kW, while closed water-cooled backplanes use air to circulate inside the closed cabinet, which has high cooling utilization and its cooling power can reach 12–35 kW (Cecchinato et al., 2010). Compared with the backplane based on traditional air-cooled methods, data center cabinets with enclosed water-cooled backplanes can save nearly 35% of annual energy consumption and allow for precise cooling (Nadjahi et al., 2018). Therefore, the closed water-cooled backplane technology can be used to optimize the existing open cabinet, improve the cooling capabilities of the cooling system, reduce the data center power consumption, and lower the data center's PUE. The cabinet based on the closed water-cooled backplane designed by IBM successfully meets the heat dissipation requirements of the high heat flux server, and its heat cooling efficiency is 80% higher than that of onefold air-cooled technology (Zimmermann et al., 2012). The above solutions can realize precise cooling for specific cabinets and tackle the heat cooling dilemma of high-heat flux cabinets, however, there are also defects such as high customization cost and difficult maintenance.

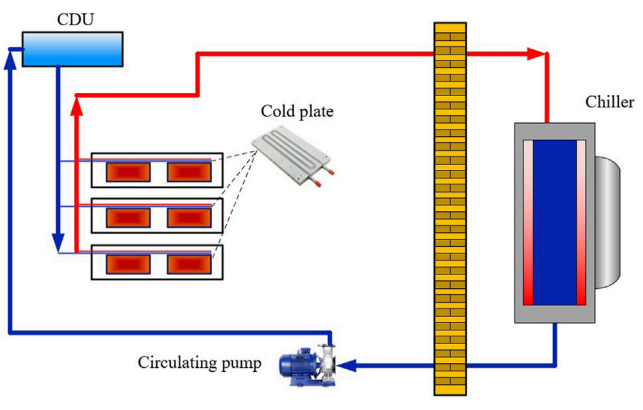

FIGURE 1 | Principle diagram of cooling plate-based liquid refrigeration technology in data centers.

The cold plate liquid cooling technology solution combined with air-cooled technology can be better utilized in the cooling system of the data center and enhance the refrigeration ability. The cold plate liquid cooling bears the main thermal load (e.g., CPU), and the air-cooled method undertakes the remaining dispersed portion of the heat load (e.g., Hard drive, interface cards) (Amalfi et al., 2022). The average annual PUE of a data center using this technical solution can be controlled below 1.2 (Cho et al., 2012). Customizing the cooling plates based on the configurational differences and thermal requirements of different electronic devices, such as CPUs, ASICs, graphics processors, accelerators, and hard disk drives, can further improve the system's thermal capacity (Zhang et al., 2011). In other words, matching the heat-generating parts of the server with the corresponding cooling plate can expand the application ratio of cold plate-liquid refrigeration, thus promoting the comprehensive use of cold plate liquid cooling technology in data centers and advancing the process of efficient as well as green development of data centers. The CPU and memory in the server are all cooled by cold plate-liquid refrigeration increasing the proportion of cooling plate-based liquid refrigeration technology to 90%, which can reduce the energy consumption by up to 50% compared to traditional air-cooled data centers (Zimmermann et al., 2012).

On one hand, the cooling capacity of cooling plate-based liquid refrigeration technology depends on the structural layout of the cooling system, and on the other hand, the coolant parameters also significantly affect its cooling performance. The requirements of different cold plate liquid cooling forms for the coolant are quite different (Li et al., 2020). The single-phase cold plate liquid uses the coolant to absorb heat in the cooling plate for removing the heat of the chip, without allowing vaporization (Ebrahimi et al., 2014; Wang et al., 2018). Compared with ordinary insulating liquid and refrigerant, due to the high boiling point and good heat transfer performance of water, it becomes an ideal cooling medium for single-phase plate cooling liquid. However, the existence of leakage hazards limits the application and demand of water as a medium (Ellsworth and Iyengar, 2009; Hao et al., 2022) The thermal oil has good electrical insulation, thermal conductivity, and heat recovery value, which can replace water as the cooling agent for cooling plate-based liquid refrigeration technology in data centers. The cabinet with the oil-cooled backplane can effectively lower the energy usage of the refrigeration system, compared to the air-cooled cabinet cooling efficiency increased by 48.16% (Yang et al., 2019). Two-phase cold plate liquid cooling removes the heat generated by electronic devices by evaporation phase change of coolant (Gess et al., 2015). Many low boiling point insulating liquids and refrigerants can be used as the coolant of two-phase cold plate liquid cooling technology, which will not be discussed here.

Cold plate liquid cooling technology has both benefits of lowering the cooling energy usage in data centers and providing good heat recovery benefits. The higher temperature of the coolant in the circulation pipe of the cold plate liquid

cooling system made it practical to efficiently leverage the waste heat, further improving the utilization of energy in data centers (Shia et al., 2021). Using this waste heat can realize district heating, absorption cooling, direct power generation, seawater desalination, and other heat recovery technologies (Cecchinato et al., 2010; Gullbrand et al., 2019). The district heating can directly use heat without conversion loss between different grades of energy, which has high economic value and is currently a more mature strategy for recovering waste heat from data centers. The CO_2 emission can be reduced by 4,102 tons per year by recovering the heat of the 3.5 MW data center as a thermal supply of district heating (Davies et al., 2016). About 1,620.87 tons of standard coal can be saved in each heating season by using cold plate liquid cooling technology to recover data center heating to implement district heating, and the power consumption efficiency of heat recovery (Ratio of total heat recovery amount to total heat recovery consumption power in a data center) is 1.4 times that of air-cooled thermal recovery (Marcinichen et al., 2012). In addition, if the waste heat from the data center is recycled in the power plant, the plant's efficiency can be increased by up to 2.2 percent. As a result, if a 500 MW power plant uses waste heat from a data center to generate electricity, it can save 1,95,000 tons of CO_2 emissions annually (Marcinichen et al., 2012). With the full coupling of cold plate liquid cooling technology and waste heat utilization of data centers, district heating technology will further expand the scale of application, and heat recovery technologies such as waste heat absorption refrigeration and direct power generation are also becoming increasingly sophisticated, energy-saving and carbon reduction will be achieved in a broader sense in the future.

PROBLEMS AND CHALLENGES OF COLD PLATE LIQUID COOLING TECHNOLOGY

The number of large and ultra-large data centers continues to increase globally. The traditional air-cooled technology cannot meet the thermal cooling demand of high-power and high-heat flux in the data centers. The tendency of high-efficiency data center construction makes the air-cooled technology face a great dilemma. More efficient and energy-saving cooling plate-based liquid refrigeration technology in future data center development is promising. Considering its research status and practical application requirements of heat dissipation in data centers, the cold plate liquid cooling technology still faces many challenges:

1) Low utilization of the core server room. The deployment environment for cold plate liquid cooling technology is different from traditional data centers. The data center retrofitting requires cold plate liquid cooling technology to match traditional air-cooled servers, which are costly to deploy and expensive to operate and maintain. The cold plate liquid cooling technology needs further optimization in terms of architecture, operation, and maintenance.
2) Leakage and corrosion prevention of coolant. The use of coolant involves the problem of leakage and corrosion prevention of the cooling system in the data centers. Higher requirements are needed for the composition of coolant and the packaging of auxiliary devices. Further research on raw materials and accessories is also needed to reduce the cost of large-scale applications.
3) Waste heat utilization of data centers. The higher the coolant temperature is, the easier the heat recovery will be. However, the increase in coolant temperature will widen the difference in temperature with the environment, resulting in additional heat loss and useless power consumption in the data center, which in turn affects the PUE. It is necessary to further study the coupling relationship among cooling temperature, energy-saving efficiency, and heat recovery performance to further enhance the efficiency of energy utilization in the data center.

AUTHOR CONTRIBUTIONS

Writing the original draft and editing, YZ; Conceptualization, CF; Formal analysis, GL. All authors contributed to manuscript revision, read, and approved the submitted version.

FUNDING

This work is supported by the National Key R&D Program of China (No. 2021YFB3803203).

REFERENCES

Amalfi, R. L., Salamon, T., Cataldo, F., Marcinichen, J. B., and Thome, J. R. (2022). Ultra-Compact Microscale Heat Exchanger for Advanced Thermal Management in Data Centers. *J. Electron. Packag.* 144 (2), 8. doi:10.1115/1.4052767

Cecchinato, L., Chiarello, M., and Corradi, M. (2010). A Simplified Method to Evaluate the Seasonal Energy Performance of Water Chillers. *Int. J. Therm. Sci.* 49, 1776–1786. doi:10.1016/j.ijthermalsci.2010.04.010

Cho, J., Lim, T., and Kim, B. S. (2012). Viability of Datacenter Cooling Systems for Energy Efficiency in Temperate or Subtropical Regions: Case Study. *Energy Build.* 55, 189–197. doi:10.1016/j.enbuild.2012.08.012

Davies, G. F., Maidment, G. G., and Tozer, R. M. (2016). Using Data Centres for Combined Heating and Cooling: An Investigation for London. *Appl. Therm. Eng.* 94, 296–304. doi:10.1016/j.applthermaleng.2015.09.111

Deng, Z., Gao, S., Wang, H., Liu, X., and Zhang, C. (2022). Visualization Study on the Condensation Heat Transfer on Vertical Surfaces with a Wettability Gradient. *Int. J. Heat Mass Transf.* 184, 122331. doi:10.1016/j.ijheatmasstransfer.2021.122331

Dong, J., Lin, Y., Deng, S., Shen, C., and Zhang, Z. (2017). Experimental Investigation of an Integrated Cooling System Driven by Both Liquid Refrigerant Pump and Vapor Compressor. *Energy Build.* 154, 560–568. doi:10.1016/j.enbuild.2017.08.038

Ebrahimi, K., Jones, G. F., and Fleischer, A. S. (2014). A Review of Data Center Cooling Technology, Operating Conditions and the Corresponding Low-Grade Waste Heat Recovery Opportunities. *Renew. Sustain. Energy Rev.* 31, 622–638. doi:10.1016/j.rser.2013.12.007

Ellsworth, M. J., and Iyengar, M. K. (2009). *Energy Efficiency Analyses and Comparison of Air and Water Cooled High Performance Servers.* San Francisco, California, USA: ASME, 907–914. http://asmedigitalcollection.

asme.org/InterPACK/proceedings-pdf/InterPACK2009/43604/907/2742018/907_1.pdf.

Garimella, S. v., Yeh, L.-T., and Persoons, T. (2012). Thermal Management Challenges in Telecommunication Systems and Data Centers. *IEEE Trans. Compon. Packag. Manufact. Technol.* 2, 1307–1316. doi:10.1109/TCPMT.2012.2185797

Gess, J. L., Bhavnani, S. H., and Johnson, R. W. (2015). Experimental Investigation of a Direct Liquid Immersion Cooled Prototype for High Performance Electronic Systems. *IEEE Trans. Compon. Packag. Manufact. Technol.* 5, 1451–1464. doi:10.1109/TCPMT.2015.2453273

Gullbrand, J., Luckeroth, M. J., Sprenger, M. E., and Winkel, C. (2019). Liquid Cooling of Compute System. *J. Electron. Packag. Trans. ASME* 141 (1), 10. doi:10.1115/1.4042802

Habibi Khalaj, A., and Halgamuge, S. K. (2017). A Review on Efficient Thermal Management of Air- and Liquid-Cooled Data Centers: From Chip to the Cooling System. *Appl. Energy* 205, 1165–1188. doi:10.1016/j.apenergy.2017.08.037

Habibi Khalaj, A., Scherer, T., Siriwardana, J., and Halgamuge, S. K. (2015). Multi-objective Efficiency Enhancement Using Workload Spreading in an Operational Data Center. *Appl. Energy* 138, 432–444. doi:10.1016/j.apenergy.2014.10.083

Hao, G., Yu, C., Chen, Y., Liu, X., and Chen, Y. (2022). Controlled Microfluidic Encapsulation of Phase Change Material for Thermo-Regulation. *Int. J. Heat Mass Transf.* 190, 122738. doi:10.1016/j.ijheatmasstransfer.2022.122738

Haywood, A. M., Sherbeck, J., Phelan, P., Varsamopoulos, G., and Gupta, S. K. S. (2015). The Relationship Among CPU Utilization, Temperature, and Thermal Power for Waste Heat Utilization. *Energy Convers. Manag.* 95, 297–303. doi:10.1016/j.enconman.2015.01.088

Kheirabadi, A. C., and Groulx, D. (2016). Cooling of Server Electronics: A Design Review of Existing Technology. *Appl. Therm. Eng.* 105, 622–638. doi:10.1016/j.applthermaleng.2016.03.056

Li, Y., Wen, Y., Tao, D., and Guan, K. (2020). Transforming Cooling Optimization for Green Data Center via Deep Reinforcement Learning. *IEEE Trans. Cybern.* 50 (5), 2002–2013. doi:10.1109/TCYB.2019.2927410

Liu, X., Chen, Y., and Shi, M. (2013). Dynamic Performance Analysis on Start-Up of Closed-Loop Pulsating Heat Pipes (CLPHPs). *Int. J. Therm. Sci.* 65, 224–233. doi:10.1016/j.ijthermalsci.2012.10.012

Marcinichen, J. B., Olivier, J. A., and Thome, J. R. (2012). On-chip Two-phase Cooling of Datacenters: Cooling System and Energy Recovery Evaluation. *Appl. Therm. Eng.* 41, 36–51. doi:10.1016/j.applthermaleng.2011.12.008

Moazamigoodarzi, H., Gupta, R., Pal, S., Tsai, P. J., Ghosh, S., and Puri, I. K. (2020). Modeling Temperature Distribution and Power Consumption in IT Server Enclosures with Row-Based Cooling Architectures. *Appl. Energy* 261, 114355. doi:10.1016/j.apenergy.2019.114355

Nadjahi, C., Louahlia, H., and Lemasson, S. (2018). A Review of Thermal Management and Innovative Cooling Strategies for Data Center. *Sustain. Comput. Inf. Syst.* 19, 14–28. doi:10.1016/j.suscom.2018.05.002

Rani, R., and Garg, R. (2021). A Survey of Thermal Management in Cloud Data Centre: Techniques and Open Issues. *Wirel. Pers. Commun.* 118 (1), 679–713. doi:10.1007/s11277-020-08039-x

Shia, D., Yang, J., Sivapalan, S., Soeung, R., and Amoah-Kusi, C. (2021). Corrosion Study on Single-phase Liquid Cooling Cold Plates with Inhibited Propylene Glycol/Water Coolant for Data Centers. *J. Manuf. Sci. Eng.* 143 (11), 7. doi:10.1115/1.4051059

Wang, J., Gao, W., Zhang, H., Zou, M., Chen, Y., and Zhao, Y. (2018). Programmable Wettability on Photocontrolled Graphene Film. *Sci. Adv.* 4. doi:10.1126/sciadv.aat7392

Yang, W., Yang, L., Ou, J., Lin, Z., and Zhao, X. (2019). Investigation of Heat Management in High Thermal Density Communication Cabinet by a Rear Door Liquid Cooling System. *Energies* 12, 4385. doi:10.3390/en12224385

Zhang, C., Chen, Y., Wu, R., and Shi, M. (2011). Flow Boiling in Constructal Tree-Shaped Minichannel Network. *Int. J. Heat Mass Transf.* 54, 202–209. doi:10.1016/j.ijheatmasstransfer.2010.09.051

Zhang, C., Li, G., Sun, L., and Chen, Y. (2021). Experimental Study on Active Disturbance Rejection Temperature Control of a Mechanically Pumped Two-phase Loop. *Int. J. Refrig.* 129, 1–10. doi:10.1016/j.ijrefrig.2021.04.038

Zimmermann, S., Meijer, I., Tiwari, M. K., Paredes, S., Michel, B., and Poulikakos, D. (2012). Aquasar: A Hot Water Cooled Data Center with Direct Energy Reuse. *Energy* 43, 237–245. doi:10.1016/j.energy.2012.04.037

Conflict of Interest: The authors declare that the research was conducted in the absence of any commercial or financial relationships that could be construed as a potential conflict of interest.

Publisher's Note: All claims expressed in this article are solely those of the authors and do not necessarily represent those of their affiliated organizations, or those of the publisher, the editors and the reviewers. Any product that may be evaluated in this article, or claim that may be made by its manufacturer, is not guaranteed or endorsed by the publisher.

frontiers | Frontiers in Energy Research

ORIGINAL RESEARCH
published: 04 July 2022
doi: 10.3389/fenrg.2022.922542

Supercritical Carbon Dioxide Turbine Design and Arrangement Optimization

Zhenya Li, Wenjie Bian, Li Jiang, Chuanliang Liu, Jinyuan Shi and Ning Hao*

Shanghai Power Equipment Research Institute Co. Ltd, Shanghai, China

To achieve a supercritical CO_2 cycle power generation system, a 25 MW supercritical CO_2 turbine rotor and cylinder were designed. Then, two compact arrangement schemes were proposed in this paper for the optimization of a supercritical CO_2 turbine rotor. In Scheme 1, the balance piston was arranged in the cooling gas section, which was more conducive to the arrangement of the dry gas seal. In Scheme II, the oil bearing was replaced by the gas bearing, and the dry gas seals at both ends of the turbine were installed outside the gas bearing, which was combined with the cooling gas section. The results suggest that the length of the rotor is reduced by 9% and 17% based on the above two schemes. The compact arrangement of the supercritical CO_2 turbine can well reduce the shaft length of the turbine, which is beneficial to the structural design and operation of the supercritical CO_2 turbine.

Keywords: supercritical carbon dioxide, turbomachinery, rotor design, compact arrangement, arrangement optimization

OPEN ACCESS

Edited by:
Chengbin Zhang,
Southeast University, China

Reviewed by:
Chaoqun Shen,
Yangzhou University, China
Liangyu Wu,
Yangzhou University, China

****Correspondence:***
Chuanliang Liu
liuchuanliang@speri.com.cn

Specialty section:
This article was submitted to Process and Energy Systems Engineering, a section of the journal Frontiers in Energy Research

Received: *18 April 2022*
Accepted: *27 May 2022*
Published: *04 July 2022*

Citation:
Li Z, Bian W, Jiang L, Liu C, Shi J and Hao N (2022) Supercritical Carbon Dioxide Turbine Design and Arrangement Optimization. Front. Energy Res. 10:922542. doi: 10.3389/fenrg.2022.922542

1 INTRODUCTION

Carbon dioxide has been widely used in supercritical carbon dioxide (sCO_2) Brayton cycle and transcritical carbon dioxide refrigeration cycle as working fluid (Yu et al., 2020). The combined system coupling sCO_2 Brayton cycle and refrigeration cycle could simultaneously produce power and cooling, exhibits great potential in green buildings, waste heat recovery, and industrial power supply (Wu C. et al., 2020; Khanmohammadi et al., 2020; Du et al., 2022). The sCO_2 cycle power generation system has high efficiency in a certain temperature range (Crespi et al., 2017; Li et al., 2020) and has advantages such as a small size, compact structure and so on (Ahn et al., 2015; Liao et al., 2019; Wu P. et al., 2020). It is a novel power generation technology that is currently a crucial research topic worldwide. It has broad application prospects in solar thermal power generation, small nuclear power, industrial waste heat and ship power (Qi et al., 2018; Mohammed et al., 2020; Guo et al., 2022).

Turbines are one of the core components of the sCO_2 power generation cycle. Due to its requests of high temperature, high pressure, high speed, and frequent start-and-stop, the design of turbine structures has become an important research field for scientific researchers and designers (Crespi et al., 2017; Luo et al., 2017). The rotor is the key component of the sCO_2 turbine unit. A reasonable arrangement of the rotor structure affects the overall shaft length and the design of the inner and outer cylinder structure, which is extremely important for the safety and reliability of the turbine. To ensure the efficient and smooth operation of the turbine, it is crucial for designers to study the reasonable arrangement of the sCO_2 turbine rotor.

For many years, researchers in various countries have performed much research on sCO_2 turbines and obtained many research results. For example, some institutes, such as Sandia Laboratories in the United States, Tokyo Institute of Technology in Japan, and the Korea Advanced Institute of Science and Technology, have designed the rotor of sCO_2 turbines and have put them into operation in the

laboratory. Odabaee et al.(Odabaee et al., 2016) used a 100 kW sCO_2 radial turbine with an inlet temperature of 560°C as the research focus and carried out an aerodynamic design on the turbine. In this study, the physical property data obtained by numerical calculation were compared with the NIST database, but the results showed that it was difficult to obtain accurate physical property data by fitting the gas state equation. In addition, Lee et al. considered the effects of the nonlinear physical property variation of the sCO_2 near the critical point in the traditional design method (Lee et al., 2012). The selection of an sCO_2 turbine was proposed by comparing important parameters such as the power and efficiency of sCO_2 turbines. In addition, Kim et al. conducted aerodynamic analysis on the sCO_2 turbine designed by the Korea Advanced Institute of Science and Technology and optimized the blades to improve the aerodynamic efficiency of the turbine (Kim et al., 2006; Kim et al., 2008). Schmitt et al. designed a 6-stage sCO_2 turbine with a power of 100 MW and an inlet temperature of 1,077°C (Schmitt et al., 2014). In this study, the parameters of the speed triangle were optimized, and the total power and efficiency of the turbine met the design requirements. Marion et al. developed a sCO_2 turbine applied to sCO_2-based power cycling to realize concentrated solar energy conversion in the SunShot project (Marion et al., 2019). In addition, Kalra et al. also jointly designed a 16 MW sCO_2 turbine conceptual diagram in the STEP (Supercritical Transformational Electric Power) project (Kalra et al., 2014). It indicated that the aerodynamic performance was improved by shearing rings instead of bolts. Feng et al. carried out aerodynamic analysis on 15 MW axial-flow sCO_2 turbines and 1.5 MW radial turbines based on the design of two different structural forms of sCO_2 turbines (Zhang et al., 2015). Xie et al. determined the shape of the nozzle and impeller by thermal design and linear design of a 200 kW sCO_2 radial turbine (Shi et al., 2015). They found that increasing the inlet height of the turbine impeller can reduce the manufacturing difficulty and the loss of secondary flow. The team also proposed a sCO_2 turbine that can adapt to a wide range of pressures and flow rates (Wang et al., 2016). The results show that the designed turbine can adaptively adjust the installation angle of the nozzle to correspond to different flow areas and adapt to different flow conditions.

Based on the above studies, it found that foreign countries have not only conducted in-depth research on the physical properties of sCO_2 and the aerodynamic design of turbines but have also made great progress in the overall layout and structural design of turbines. However, domestic research is still limited to sCO_2 aerodynamic design and flow arrangement. There are few studies on the compact overall arrangement of turbine rotors. Therefore, it is of great significance to improve the in-depth study of the compact arrangement of sCO_2 turbine rotors. With the purpose of creating a sCO_2 cycle power generation system, a 25 MW sCO_2 turbine rotor and cylinder were designed in this paper. Then, two compact arrangement schemes were proposed for the optimization of the sCO_2 turbine rotor in this paper. Finally, the advantages of the compact arrangement were analyzed by comparison with the traditional scheme.

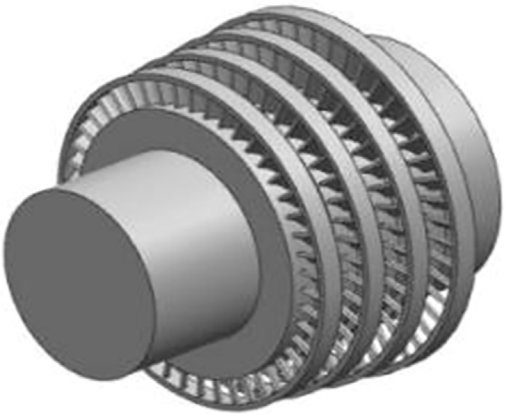

FIGURE 1 | 4-stage blade flow design of a 25 MW sCO_2 turbine.

TABLE 1 | Basic properties of CO_2.

Physical Property	Value
Molar mass M/kg·kmol^{-1}	44.01
Critical temperature T_c/K	304.21
Critical pressure P_c/MPa	7.38
Critical density ρ/kg·m^{-3}	383.98

TABLE 2 | Design parameters.

Design Parameters	Value
Inlet pressure P_0/MPa	24
Inlet temperature T_0/K	873
Outlet pressure P_2/MPa	8.5
Mass flow m/kg·s^{-1}	180
Isentropic efficiency η/%	90
Generation power N/MW	25
Rotating speed r/min	30,000

2 SCO2 TURBINE ROTOR DESIGN

In the design, a variety of rotational speed, flow diameter, blade stages, and turbine efficiency schemes were considered. According to results of the aerodynamic design a 4-stage turbine with a rotational speed of 30,000 r/min was finally determined. The design scheme is shown in **Figure 1**.

In addition, according to the actual demand, the generation power was set at 25 MW. The basic physical properties of CO_2 are listed in **Table 1**, and the design parameters of the turbine are listed in **Table 2**.

Based on the through-flow design, the preliminary design of the sCO_2 turbine rotor is completed. The layout is as follows: The turbine shafting adopts the form of a single-shaft double support, and the balance piston on the intake side is arranged opposite to the through-flow.

The gas flowing in the dry gas seal is discharged through the cooling sections at both ends, and the exhaust ports at both ends

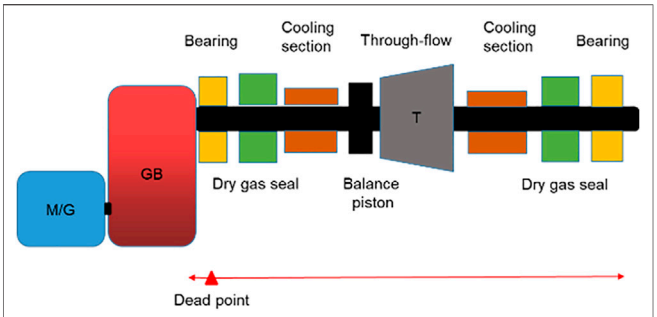

FIGURE 2 | Layout of 20 MW sCO_2 turbine rotor.

TABLE 3 | Rotor size of each part.

Shaft Position	Length(mm)	Diameter(mm)
Balance piston	480	260
Cooling section	220 × 2	180
Dry gas seal	200 × 2	180
Through flow + exhaust	480	192
Intake section	140	160
Length of shaft box	300 × 2	140

TABLE 4 | Key parameters of rotor.

Turbine rotor parameters	Value
Weight (kg)	850
Minimum shaft diameter (mm)	140
Maximum shaft diameter (mm)	260
Total span (mm)	2,540
Torsional stress (MPa)	44.5 (< 290)

are connected through the interlayer of the inner and outer cylinders. The intake side of the main gas is a thrust radial joint bearing, and the exhaust side is a supporting bearing. The bearing adopts tilting pad oil pressure sliding the bearing, and the rotor is connected to the transmission gearbox and the generator through a flexible coupling at the intake end. With the thrust bearing as the dead center, the rotor expands mainly to the right. The balance piston and the rotor are processed in the whole section, and the blades are installed in the circumferential direction. Since the shaft end needs to be arranged with dry gas seals and conventional dry gas seals have requirements on the temperature and pressure of the working environment, it is necessary to design a cooling gas for the shaft seal that reduces temperature and pressure. The system layout is shown in **Figure 2**.

The key parameters are calculated by setting the 3D model, and a preliminary torque check is carried out. The results are shown in **Table 4**.

According to the idea of the basic layout of the rotor, the size of the shaft section of the turbine rotor is preliminarily estimated, and the size design of the turbine rotor is completed for thermal

TABLE 5 | Materials of key components.

Components	Material
Rotor	GH 4169
Outer cylinder	ZG15Cr1Mo1 V
Inner cylinder	Alloy 625 cast
Blade	GH 4169
End seal body	Alloy 625 cast
Faceted bolts in inner cylinder	GH 4169
Faceted bolts in outer cylinder	20Cr1Mo1VNbTiB

TABLE 6 | Wall thickness summary comparison.

Minimum Wall Thickness of Inlet Volute/mm	50
Minimum wall Thickness of balance piston/mm	60
Minimum wall thickness of through-flow cylinder/mm	50
Minimum wall thickness of gas inlet/mm	50

stress analysis and expansion calculation. The calculation results are then provided back to the rotor designer to rerevise the rotor size and finally determine the size of each key part of the rotor. The detailed parameters are shown in **Table 4**.

Torsional Stress Check Formula

$$\tau = \frac{T}{W_p} = \frac{9.55 \times 10^6 \frac{P}{n}}{0.2d^3} \leq [\tau] \quad (1)$$

P- the power transmitted by the shaft, kW.
[τ]- the allowable torsional shear stress, MPa.
T-the torque received by the shaft, mm.
W- the torsional section coefficient of the shaft, $mm^3N\cdot$
n-the rotational speed of the shaft, r/min
d-the diameter of the shaft at the calculated section, mm.

3 DESIGN OF THE SCO_2 TURBINE CYLINDER

3.1 Main Material

The main gas parameters are 24 MPa and 600°C, while the turbine speed reaches 30,000 r/min. The strength requirements are strict, so the rotor material is selected to be GH4169 as indicated in **Table 5**. To avoid t friction between the rotor and inner cylinder, the same type of nickel-based alloy material needs to be used to ensure consistent the linear expansion coefficient. The material selection scheme is shown in **Table 5**. The inner cylinder, rotor and blades are made of nickel-based materials, and the outer cylinder is made of ferrite material 9–12Cr steel. The selected materials are all mature materials that have been widely used in the field of ultra-supercritical steam turbines worldwide.

3.2 Inner and Outer Cylinder Design

The 25 MW sCO_2 turbine adopts a double-ground bearing support form, an efficient single-process reaction through-flow and a direct-connected tangential gas intake. To overcome the

difficulties of a high-density sCO_2 and large aerodynamic and centrifugal loads on the rotor blades, a 3D modeling of the T-shaped, pre-twisted rotor blades was completed. For the high-parameter, high-pressure inner cylinder, a shrink ring seal with low thermal stress constraints was developed. Key dimensions and parameters, such as interference, are determined through finite element analysis. Because of the high critical pressure of CO_2, dry gas seals at the ends are required, and a unique end gas seal and its cooling system are designed for this purpose. Flow-solid coupling calculations were selected to evaluate the influence on the temperature and stress field of the dynamic and static components. Finally, the main layout and structure plan of the preliminary design stage are planned.

The 3D design diagram of the turbine cylinder is drawn according to the rotor structure dimensions in **Table 3** and **Table 4** and the overall layout of the turbine in **Figures 1**, **2** (see **Figure 3**).

The turbine cylinder is designed with a double-layer cylinder structure, and the inner and outer cylinders are sealed with a horizontal mid-section and flange bolt seal. The thickness of the inner cylinder is 50 mm and that of the outer cylinder is 60 mm. The inner diameter of the intake port is 120 mm and that of the exhaust port is 260 mm. The inner cylinder is supported by the horizontal mid-section of the outer cylinder. The top and bottom are positioned and guided by positioning pins to ensure that the inner and outer cylinders can freely shrink and expand. The single-flow design is adopted, and the balanced piston gas seal is designed on the intake side to reduce the entire through-flow thrust. The stator blades of all stages are directly installed on the overall inner cylinder, and cooling flow is introduced at the gas seals at the ends of the outer cylinder on both sides to cool the shaft section, preventing the high-temperature failure of the dry gas seal.

The wall thickness is determined by **Eqs. 2**, **3**.

According to the thin-walled cylinder bearing stress formula:

$$\sigma = \frac{\Delta PD}{2\delta} \leq [\sigma] \tag{2}$$

and we have:

$$\delta \geq \frac{\Delta PD}{2[\sigma]} \tag{3}$$

where:

σ—Stress.

△P—Pressure difference between the inside and outside cylinder walls.

D—Inner diameter of the pressure cylinder wall (without opening).

δ—Wall thickness of equal-walled cylinder.

According to the pressure difference between the inlet and the exhaust gas, it is estimated that the minimum wall thickness of the inlet volute is 50 mm, and the average stress is 40 MPa. To find the minimum wall thickness of the balance piston cylinder, the following discussion is used: According to the pressure difference between the inlet and exhaust gas of the first gear gas seal, as shown in **Table 6**, the minimum wall thickness is estimated to be 60 mm, and the average stress is 20 MPa: According to the pressure difference between the inlet and exhaust gas of the first stage vane, the minimum wall thickness of the through-flow cylinder is estimated to be 50 mm, and the average stress is 26 MPa. The minimum wall thickness of the gas inlet should also be assessed according to the pressure difference there. Due to the small diameter, the design wall thickness can be very thin; however, considering that it would be matched with the cannula, the preliminary design should be considered as 50 mm.

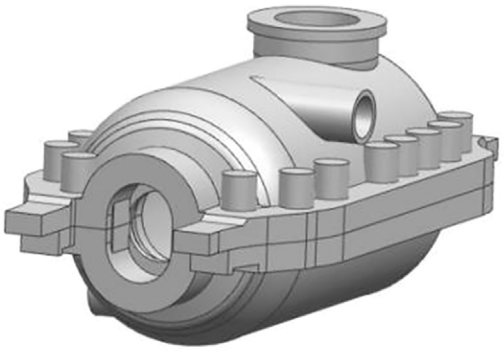

FIGURE 3 | Schematic diagram of the layout of the outer cylinder of the 20 MW sCO_2 Turbine.

The intake cylinder module of the turbine is supported on the front and rear bearing seats through cat claws, where the front cat claws simultaneously serve as the absolute center of the cylinder expansion, and the cylinder and the rotor expand in the same direction. The main control valve of the turbine is arranged on the left and right sides of the cylinder. The intake valve is directly connected to the outer cylinder through flanges and bolts. No gas guide pipe is required in the design. Laminated seals prevent leaks. The gas intake of the cylinder is adopted by the horizontal high and low tangential gas intake on both sides, the circulation part is implemented by the whole circumference gas intake, and the balance piston and the rotor are processed in the whole section. The cylinder exhaust is an upper exhaust port, which is connected to the exhaust pipe through a flange. The dry gas seal is designed so that the cylinder module is set on the outer cylinder, fixed by pins and expands at the same time as the outer cylinder. The influence of the expansion difference should be considered when designing the dry gas seal gap.

3.3 Analysis of Rotor Temperature Field

In the cooling gas design, when a large amount of cooling gas is used to lower the temperature of the rotating parts by forced convection cooling, it will cause greater thermal stress and thermal deformation, which will affect the safety of the components. However, when a small amount of gas is used, with the cooling scheme that isolates the outward tendency of the heat source, it can not only ensure the temperature limit of the contact surface between the shaft end and the dry gas seal but also, at most, limit the radial thermal stress gradient and thermal deformation. Therefore, when designing the cooling gas, it is necessary to fully ensure that the shaft end is not overheated and

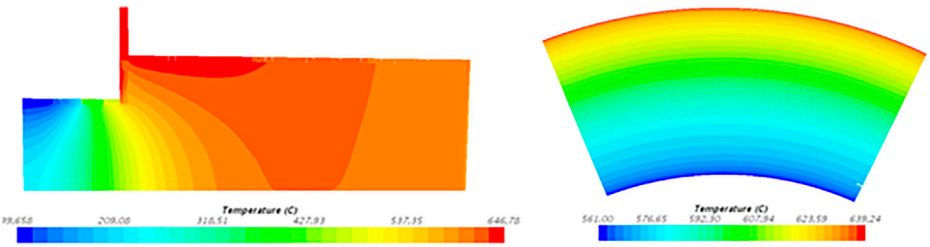

FIGURE 4 | CHT Calculate the temperature distribution.

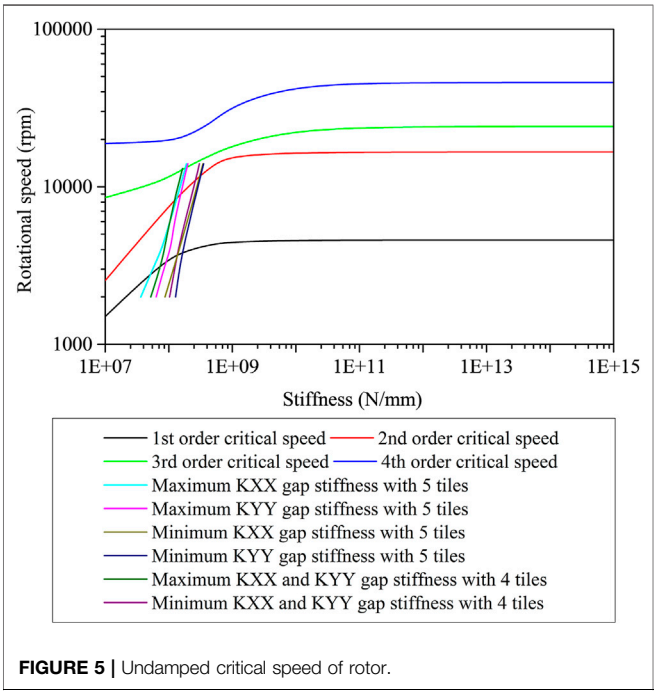

FIGURE 5 | Undamped critical speed of rotor.

to control the temperature by inputting a cooling source; on the other hand, it is also necessary to reduce the thermal stress and thermal deformation on the surface of the rotor and to control the temperature difference by reducing the gas flow through the part's surface. After analyzing the temperature field, it is most suitable to use a 120°C cooling gas. The temperature field change at the end of the rotor is shown in **Figure 4**, and the maximum temperature reaches 646.76°C.

After the dynamic analysis of the shafting, its response peak-to-peak value, critical speed avoidance rate and Class I stability can all meet the requirements of API 684. The analysis of the undamped critical speed shows that the critical speed of the first-order rigid support of the rotor is 4,649 r/min, and the rotor operates as a flexible rotor. The undamped critical speeds are 3,924 r/min, 9,630 r/min, and 13,200 r/min, respectively, as shown in **Figure 5**. The first and second types of unbalanced responses are calculated for the rotor, and the damped critical speeds are 4,133 r/min and 16,200 r/min, respectively (according to API 684, 10867 r/min is not judged as a critical speed), and its avoidance rate satisfies the API 684 request. The damped unbalanced response analysis shows that at the rated speed, the peak-to-peak response (maximum 7.7 μm) at the rotor front and rear axle inclinations meet the API 684 requirement of 25.4 μm. Under the condition of one time impeller cross-coupling stiffness, the logarithmic decay rate at the rated speed is greater than 0.1 regardless of whether it is supported by four-tiles or five-tiles bearings, and the rotor stability meets the requirements of API 684. The dynamic characteristics of the rotor supported by the 5-W and 4-W bearings are similar, and the logarithmic decay rate is larger while the stability is better at the rated speed of the 4-W bearing.

4 OPTIMIZATION OF SCO_2 TURBINE ARRANGEMENT

This design results in a large amount of leakage due to the large balance between piston length and diameter. The increase in the overall arrangement length of the rotor will lead to many problems in the structural design of the sCO_2 turbine rotor, such as endurance strength checks and creep stress assessments. Therefore, two schemes to optimize the arrangement of sCO_2 turbines are proposed.

4.1 Optimization Scheme I

To ensure that the shaft seal is cooled, with the exhaust pressure and balance thrust at the shaft end being reduced, the length of the balance piston being reduced, and the leakage of the high-temperature medium being reduced, which is conducive to the operation of the dry gas seal, the rotor structure and system of the turbine is optimized to balance the axial force, and the arrangement of the turbine rotor balance piston and the cooling position of the cooling gas are changed, shown in **Figure 6**.

The balance piston is arranged in the cooling gas section. Due to the low temperature of the turbine cooling gas section, the carbon ring seal can be arranged. Compared with the clearance of 0.5 mm of the ordinary seal, the carbon ring seal can achieve a clearance of 0.1 mm. However, the carbon ring seal has certain requirements for the ambient temperature and cannot be arranged in the high-temperature area. This arrangement can greatly reduce the length of the balance piston and the length of the high-temperature section of the rotor during turbine operation, which can decreases the thermal stress, thus

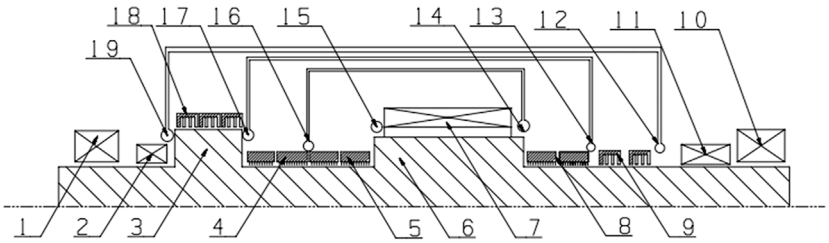

1-bearing, 2-dry gas seal, 3-balance piston, 4,5-labyrinth seal, 6-working substance, 7-blade, 8-labyrinth seal, 9-carbon ring seal, 10-bearing, 11-dry gas seal, 12-outlet, 13-inlet, 14-outlet, 15-inlet, 16-outlet, 17-inlet, 18-carbon ring seal, 19-outlet

FIGURE 6 | Improved sCO_2 turbine rotor in Arrangement I.

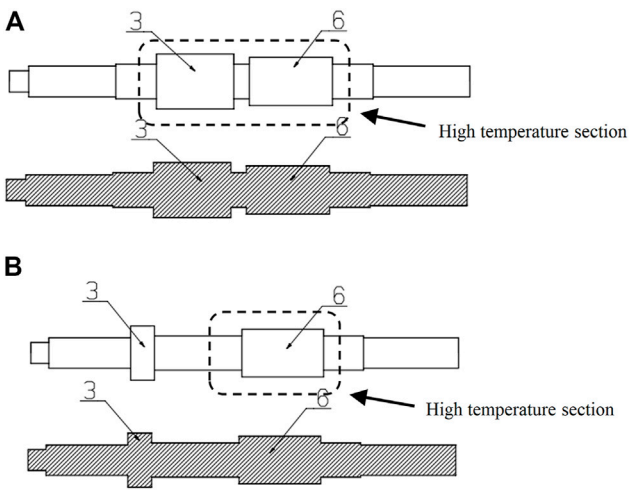

FIGURE 7 | sCO_2 turbine rotor structure design: **(A)** before optimization; **(B)** after optimization.

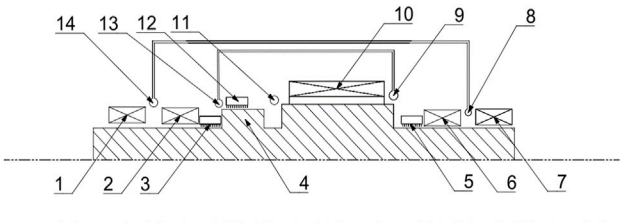

1-dry gas seal，2- bearing，3- labyrinth seal，4- balance piston，5- labyrinth seal，6- bearing，7- dry gas seal，8- inlet，9- outlet，10-through-flow，11- inlet，12- labyrinth seal，13- outlet，14- inlet

FIGURE 8 | Improved sCO_2 turbine rotor in Arrangement II.

improves the safety performance of the unit and reduces the leakage of mainstream gas to improve the operation efficiency. The leakage of mainstream gas is reduced by 0.5%. The inlet and exhaust of the cooling gas are independent, and the gas source is stable. The inlet and exhaust pressures of the cooling gas can be adjusted according to the requirements. The balance piston is used to balance the axial thrust of the flow passage of the rotor and sealing teeth. In this design, the size and length of the balance piston can be adjusted by modifying the inlet and exhaust pressure of the cooling gas, which can effectively control the size of the balance piston.

The arrangement of the cooling gas system enables the pressure to be reduced to a controllable pressure, which is the allowable design value of the dry gas seal. By applying cooling and pressure reduction designs in the system arrangement, the dry gas seal can operate normally, and the thermal stress of the rotor can be reduced by adjusting the temperature of the cooling gas.

The improvement of the turbine rotor arrangement and system can greatly shorten the overall span of the rotor. As shown in **Figure 7**, by improving the arrangement of the rotor, the length of the high-temperature section is reduced from 1,100 mm to 750 mm, which is a reduction of 32%; the length of the balance piston is reduced from 480 mm to 220 mm, which is a reduction of 54%; and the overall length of the rotor is reduced from 2,540 mm to 2,310 mm, which is a reduction of 9%.

4.2 Optimization Scheme II

This scheme is conducive to the overall structural design of the rotor, improves the safety performance of the rotor and can appropriately reduce the shaft diameter to improve the economic performance of the turbine unit.

The oil bearing is arranged outside the dry gas seal in the previous scheme, so the isolation gas needs to be set to prevent the oil gas of the oil bearing from entering the dry gas seal. The dry gas seal must be disassembled horizontally in the primary scheme. The disassembly of the dry gas seal is more troublesome if the oil bearing is arranged outside. In addition, a separate cooling system should be designed for the cooling gas in the shaft seal cooling section; otherwise, the excessive temperature could lead to the leakage of the working medium in the inner cylinder. These factors lead to the complexity of the arrangement of the rotor system and the large span of the rotor, which is not conducive to rotor dynamics design, safety verification and turbine operation.

A scheme is proposed in which the gas bearing replaces the oil bearing and combines with the cooling section to improve the

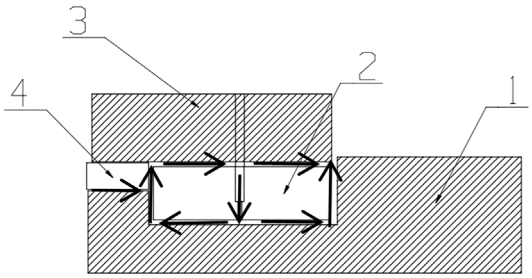

FIGURE 9 | sCO_2 turbine gas bearing arrangement diagram.

previously discussed shortcomings, as shown in **Figure 8**. The dry gas seals at both ends of the turbine are installed outside the gas bearing, which is combined with the original cooling section. This design has three advantages. First, by arranging the gas bearing inside the dry gas seal, the gas from the gas bearing can play the role of cooling gas at the same time, so a separate cooling section does not need to be arranged. The rotor and outer cylinder are cooled by the flow of the gas bearing, which can greatly reduce the overall length of the shaft, compact the overall structure and greatly improve the safety of the system. Second, the cooling gas system does not need to be designed separately, and no lubricating oil system is needed, so the isolation gas to prevent the oil gas from leaking into the dry gas seal is not needed. This design effectively reduces the complexity of the system. In addition, the arrangement of gas bearings can improve the service life of the bearing components of the turbine unit, reduce the mechanical loss of turbine rotation and improve the turbine efficiency. The flow direction design and specific structure of the cooling gas are shown in **Figure 9**.

By improving the rotor arrangement and system, compared to the original design, the length of the balance piston remains unchanged from the original 480 mm, and the length of the high-temperature section remains 1,100 mm. However, the mechanical loss is reduced by 0.3%. In this scheme, no additional cooling system is needed, so 440 mm of the cooling section is reduced to 0 mm, and the overall rotor length is reduced from 2,540 mm to 2,100 mm, which is a reduction of approximately 17%. This is conducive to rotor structural design and reduces the mechanical loss of rotor rotation.

In consideration of the requirements of gas bearings for rotor speed, weight and load, Scheme II is more suitable for sCO_2 turbine rotor arrangements with high speed (speed >3,000 r/min), low weight (weight less than 300 kg) and low load (load <10 MW).

5 CONCLUSION

In summary, to achieve a sCO_2 cycle power generation system, a 25 MW sCO_2 turbine rotor and cylinder were designed. In addition, two optimized design schemes of a sCO_2 turbine rotor were proposed. Finally, the advantages of the compact arrangement were analyzed by comparison with the traditional scheme. The main conclusions from this study are presented as follows:

(1) The improvement of turbine rotor arrangement can greatly shorten the overall span of the rotor. In Scheme I, the length of the high-temperature section is reduced by 32%, from 1,100 mm to 750 mm, and the length of the rotor is reduced by 9%, from 2,540 mm to 2,310 mm. In Scheme II, the length of the rotor is reduced by 17%, from 2,540 mm to 2,100 mm.
(2) The compact arrangement increases the efficiency of the turbine. The gas leakage loss of the system is reduced by 0.5% in Scheme I, and the mechanical loss is reduced by 0.3% in Scheme II.
(3) Compared with the traditional turbine scheme, the length of the balance piston is reduced in the schemes proposed in this paper, which is more conducive to the arrangement and operation of dry gas seals.
(4) Considering the requirements of gas bearings for rotor speed, weight and load, the arrangement in Scheme II is more suitable for the arrangement of sCO_2 turbine rotors with low load and low weight.

DATA AVAILABILITY STATEMENT

The raw data supporting the conclusion of this article will be made available by the authors, without undue reservation.

AUTHOR CONTRIBUTIONS

CL and JS contributed to conception and design of the study. ZL, WB, LJ and NH conducted the investigation and wrote the first draft of the manuscript. All authors contributed to manuscript revision, read, and approved the submitted version.

REFERENCES

Ahn, Y., Bae, S. J., Kim, M., Cho, S. K., Baik, S., Lee, J. I., et al. (2015). Review of Supercritical CO2 Power Cycle Technology and Current Status of Research and Development. *Nucl. Eng. Technol.* 47 (6), 647–661. doi:10.1016/j.net.2015.06.009

Crespi, F., Gavagnin, G., Sánchez, D., and Martínez, G. S. (2017). Supercritical Carbon Dioxide Cycles for Power Generation: A Review. *Appl. energy* 195, 152–183. doi:10.1016/j.apenergy.2017.02.048

Du, Y., Tian, G., and Pekris, M. (2022). A Comprehensive Review of Micro-scale Expanders for Carbon Dioxide Related Power and Refrigeration Cycles. *Appl. Therm. Eng.* 201, 117722. doi:10.1016/j.applthermaleng.2021.117722

Guo, J.-Q., Li, M.-J., He, Y.-L., Jiang, T., Ma, T., Xu, J.-L., et al. (2022). A Systematic Review of Supercritical Carbon dioxide(S-CO2) Power Cycle for Energy Industries: Technologies, Key Issues, and Potential Prospects. *Energy Convers. Manag.* 258, 115437. doi:10.1016/j.enconman.2022.115437

Kalra, C., Hofer, D., Sevincer, E., Moore, J., and Brun, K. (2014). "Development of High Efficiency Hot Gas Turbo-Expander for Optimized CSP Supercritical CO2 Power Block Operation," in *The Fourth International Symposium—Supercritical CO2 Power Cycles (sCO2): Citeseer)* (Southwest Research Institute), 1–11.

Khanmohammadi, S., Kizilkan, O., and Ahmed, F. W. (2020). Tri-objective Optimization of a Hybrid Solar-Assisted Power-Refrigeration System Working with Supercritical Carbon Dioxide. *Renew. Energy* 156, 1348–1360. doi:10.1016/j.renene.2019.11.155

Kim, T. W., Jeong, W. S., and Suh, K. Y. (2008). Numerical Modeling and Analysis of Supercritical Carbon Dioxide Turbine. *Trans. Am. Nucl. Soc.* 98 (1), 449–450. doi:10.1016/j.nucengdes.2015.08.016

Kim, T. W., Kim, N. H., and Suh, K. Y. (2006). Computational Fluid Dynamics Analysis for an Optimal Supercritical Carbon Dioxide Turbine Blade. *Trans. Am. Nucl. Soc.* 95, 790–791. doi:10.1115/ICONE16-48240

Lee, J., Lee, J. I., Ahn, Y., and Yoon, H. (2012). "Design Methodology of Supercritical CO2 Brayton Cycle Turbomachineries," in Turbo Expo: Power for Land, Sea, and Air, June 11–15, 2012 (Copenhagen, Denmark: American Society of Mechanical Engineers (ASME)), 975–983. doi:10.1115/GT2012-68933

Li, Z., Liu, X., Shao, Y., and Zhong, W. (2020). Research and Development of Supercritical Carbon Dioxide Coal-Fired Power Systems. *J. Therm. Sci.* 29 (3), 546–575. doi:10.1007/s11630-020-1282-6

Liao, G., Liu, L., E, J., Zhang, F., Chen, J., Deng, Y., et al. (2019). Effects of Technical Progress on Performance and Application of Supercritical Carbon Dioxide Power Cycle: A Review. *Energy Convers. Manag.* 199, 111986. doi:10.1016/j.enconman.2019.111986

Luo, D., Liu, Y., Sun, X., and Huang, D. (2017). The Design and Analysis of Supercritical Carbon Dioxide Centrifugal Turbine. *Appl. Therm. Eng.* 127, 527–535. doi:10.1016/j.applthermaleng.2017.08.039

Marion, J., Kutin, M., McClung, A., Mortzheim, J., and Ames, R. (2019). "The STEP 10 MWe sCO2 Pilot Plant Demonstration," in Turbo Expo: Power for Land, Sea, and Air, June 17–21, 2019 (Phoenix, Arizona, USA: American Society of Mechanical Engineers (ASME)). doi:10.1115/GT2019-91917

Mohammed, R. H., Alsagri, A. S., and Wang, X. (2020). Performance Improvement of Supercritical Carbon Dioxide Power Cycles through its Integration with Bottoming Heat Recovery Cycles and Advanced Heat Exchanger Design: a Review. *Int. J. Energy Res.* 44 (9), 7108–7135. doi:10.1002/er.5319

Odabaee, M., Sauret, E., and Hooman, K. (2016). CFD Simulation of a Supercritical Carbon Dioxide Radial-Inflow Turbine, Comparing the Results of Using Real Gas Equation of Estate and Real Gas Property File. *Appl. Mech. Mater.* 846, 85–90. doi:10.4028/www.scientific.net/AMM.846.85

Qi, H., Gui, N., Yang, X., Tu, J., and Jiang, S. (2018). The Application of Supercritical CO2 in Nuclear Engineering: A Review. *J. Comput. Multiph. Flows* 10 (4), 149–158. doi:10.1177/1757482x18765377

Schmitt, J., Willis, R., Amos, D., Kapat, J., and Custer, C. (2014). "Study of a Supercritical Co2 Turbine with Tit of 1350 K for Brayton Cycle with 100 Mw Class Output: Aerodynamic Analysis of Stage 1 Vane," in Turbo Expo: Power for Land, Sea, and Air, June 16–20, 2014 (Düsseldorf, Germany: American Society of Mechanical Engineers (ASME)). doi:10.1115/GT2014-27214

Shi, D., Li, L., Zhang, Y., and Xie, Y. (2015). "Thermodynamic Design and Aerodynamic Analysis of Supercritical Carbon Dioxide Turbine," in Proceedings of the 2015 International Conference on Electromechanical Control Technology and Transportation (Zhuhai, China): Advances in Engineering Research). doi:10.2991/icectt-15.2015.9

Wang, Y.Q., Shi, D. B., Zhang, D., and Xie, Y. H. (2016). Study on Aerodynamic Performance of a Partial-Admission Supercritical Carbon Dioxide Radial-Inflow Turbine. *Therm. Turbine* 45, 184–195.

Wu, C., Xu, X., Li, Q., Li, J., Wang, S., and Liu, C. (2020a). Proposal and Assessment of a Combined Cooling and Power System Based on the Regenerative Supercritical Carbon Dioxide Brayton Cycle Integrated with an Absorption Refrigeration Cycle for Engine Waste Heat Recovery. *Energy Convers. Manag.* 207, 112527. doi:10.1016/j.enconman.2020.112527

Wu, P., Ma, Y., Gao, C., Liu, W., Shan, J., Huang, Y., et al. (2020b). A Review of Research and Development of Supercritical Carbon Dioxide Brayton Cycle Technology in Nuclear Engineering Applications. *Nucl. Eng. Des.* 368, 110767. doi:10.1016/j.nucengdes.2020.110767

Yu, A., Su, W., Lin, X., Zhou, N., and Zhao, L. (2020). Thermodynamic Analysis on the Combination of Supercritical Carbon Dioxide Power Cycle and Transcritical Carbon Dioxide Refrigeration Cycle for the Waste Heat Recovery of Shipboard. *Energy Convers. Manag.* 221, 113214. doi:10.1016/j.enconman.2020.113214

Zhang, H., Zhao, H., Deng, Q., and Feng, Z. (2015). "Aerothermodynamic Design and Numerical Investigation of Supercritical Carbon Dioxide Turbine" in Turbo Expo: Power for Land, Sea, and Air, June 15–19, 2015 (Montreal, Quebec, Canada: American Society of Mechanical Engineers (ASME)). doi:10.1115/GT2015-42619

Conflict of Interest: ZL, WB, LJ, CL, JS, and NH were employed by Shanghai Power Equipment Research Institute Co. Ltd.

Publisher's Note: All claims expressed in this article are solely those of the authors and do not necessarily represent those of their affiliated organizations, or those of the publisher, the editors, and the reviewers. Any product that may be evaluated in this article, or claim that may be made by its manufacturer, is not guaranteed or endorsed by the publisher.

frontiers | Frontiers in Energy Research

OPINION
published: 05 July 2022
doi: 10.3389/fenrg.2022.952680

Current Status and Challenges for Liquid-Cooled Data Centers

*Hongwei Chen and Dong Li**

School of Energy and Mechanical Engineering, Nanjing Normal University, Nanjing, China

Keywords: data center, liquid cooling, immersion, cold plate, spray

1 INTRODUCTION

Data centers (DCs) are computing structures housing a large number of information and communications technology devices installed for processing, storing, and transmitting information (Khalaj and Halgamuge, 2017). In recent years, the size and number of DCs have been growing dramatically (Zhang, et al., 2018). According to statistics, as of the end of 2017, there were 285,000 DCs in use in China, and the equipment in DCs consumed more than 120 billion kWh of electricity annually, accounting for 2% of China's total electricity consumption. Based on this trend, it is predicted that by 2022, China's DCs will consume more than 250 billion kWh of electricity (Gong et al., 2022). Cooling systems consume 30–50% of the total DC energy consumption (Zhang et al., 2014), and failure to reduce cooling system energy consumption will undoubtedly result in a huge energy waste for the growing DC demand.

In the meantime, with the rapid development of new high-performance chips, the heat flux of the servers is increasing. If the heat of the servers cannot be released in time, the computing efficiency and stability of the chip will be affected and even cause the failure of electronic equipment (Murshed and Castro, 2017). Traditional air cooling can no longer meet the cooling needs of DCs; thus, it is necessary to adopt efficient cooling technology to ensure the safe operation of electronic equipment. Liquid cooling technology uses liquid as a refrigerant to transfer heat through direct or indirect contact with the heating element. Compared with air, the volumetric heat capacity of water is about 3500 times higher and the thermal conductivity is 25 times higher (Zimmermann et al., 2012), so for high-density servers, liquid cooling has become the obvious choice for DCs.

2 Current Research Status of Liquid-Cooled DCs

2.1 Classification of Liquid Cooling Technology

At present, the liquid cooling technology for the servers in DCs mainly includes immersion liquid cooling, cold plate liquid cooling, and spray liquid cooling. The difference lies mainly in the different ways of heat dissipation. Immersion liquid cooling is to completely soak the server in the cooling liquid and take away the heat of the heating element by single- or two-phase cooling. The cold plate liquid cooling is to connect the liquid cooling plate with the high-power heating element of the server, and other low-power heating elements are assisted by air cooling to achieve the overall cooling of the server. The spray liquid cooling is used to spray the cooling liquid on the surface of the heating element for heat dissipation. There are three main types of liquid cooling solutions that are discussed in the following subsections.

2.1.1 Immersion Liquid Cooling

According to whether the coolant undergoes phase change, the immersion liquid cooling is generally divided into single- and two-phase immersion liquid cooling. As shown in **Figure 1A** for single-phase immersion liquid cooling, the low-temperature coolant is sent to the heat exchanger by the circulation pump after absorbing the heat from the heating elements of the server using sensible heat. Then, it re-enters the liquid cooling tank to cool the server when the coolant is cooled by warm water

OPEN ACCESS

Edited by:
Chengbin Zhang,
Southeast University, China

Reviewed by:
Lingzi Wang,
Xi'an Jiaotong University, China

***Correspondence:**
Dong Li
62084@njnu.edu.cn

Specialty section:
This article was submitted to Process and Energy Systems Engineering, a section of the journal Frontiers in Energy Research

Received: *25 May 2022*
Accepted: *03 June 2022*
Published: *05 July 2022*

Citation:
Chen H and Li D (2022) Current Status and Challenges for Liquid-Cooled Data Centers. Front. Energy Res. 10:952680. doi: 10.3389/fenrg.2022.952680

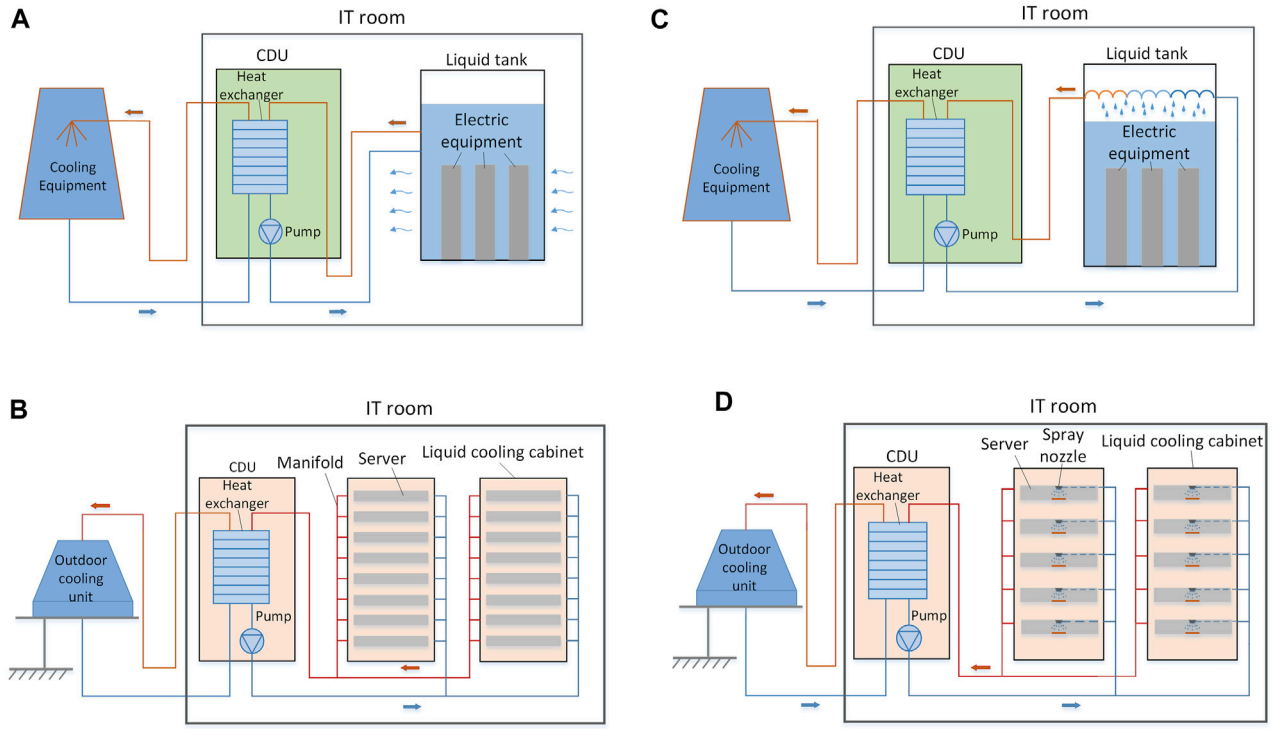

FIGURE 1 | Schematic diagram of liquid cooling technology for DCs: **(A)** single-phase immersion liquid cooling, **(B)** two-phase immersion liquid cooling, **(C)** cold plate liquid cooling, and **(D)** spray liquid cooling.

in the heat exchanger. Coolant control is relatively simple in single-phase liquid cooling, and coolant loss is low with good sealing, thereby eliminating the demand for frequent coolant replenishment. In the two-phase immersion liquid cooling system, the server is immersed in a liquid cooling tank containing low-boiling-point cooling liquid. As shown in **Figure 1B**, when the ambient heat reaches certain conditions, the cooling liquid will use latent heat to absorb the heat and produce a boiling phase change to cool down the equipment. The cooling liquid vapor is condensed by the condenser tube to the liquid state and then returned to the liquid cooling tank (Xie et al., 2022).

2.1.2 Cold Plate Liquid Cooling

Generally speaking, the cold plate liquid cooling mostly solves the heat dissipation of the devices with high heat generation in the server, such as the central processing unit (CPU), while other devices with low heat generation, such as hard disks and main memory, still rely on air cooling. The cold plate liquid cooling mainly transfers the heat from the heating element of the server to the circulating coolant indirectly through the liquid cooling plate. The circulation process is shown in **Figure 1C**. First, a manifold is arranged on the liquid cooling cabinet to convey the coolant to each liquid cooling computing node. Second, the inlet and outlet are connected with quick connectors, and the main connector is connected to the built-in or external coolant distribution unit (CDU). Third, the CDU is connected with the outdoor cooling unit, thus completing the liquid cooling cycle of the whole cabinet. Compared with traditional air-cooled servers, this technology significantly improves the energy utilization efficiency of DCs, with lower noise, and the installation and maintenance are basically the same as that of air-cooled servers (Kheirabadi and Groulx, 2016).

2.1.3 Spray Liquid Cooling

Spray liquid cooling is a liquid cooling technology in which the server is modified to deploy the corresponding spray device, and the coolant is directly sprayed on the surface of the heating element through the nozzle to absorb heat and is then discharged. Because it is a targeted cooling technology, compared with immersion liquid cooling, the required dose of coolant is lower, and the implementation is more economical. As shown in **Figure 1D**, the sprayed liquid cooling system mainly includes a liquid cooling cabinet, heat exchanger, circulation pump, and outdoor cooling unit. The liquid cooling cabinet is connected to the heat exchanger through piping, i.e., the heat of the heat-generating components of the server in the cabinet is absorbed by the coolant and cooled down in the heat exchanger. Sprayed liquid cooling has the features of high device integration, high energy efficiency, and low noise. Compared with air-cooled DCs, the total energy consumption of sprayed liquid-cooled DCs can be reduced by 25.8% (Kandasamy et al., 2022).

2.2 Application of Liquid Cooling Technology

Among the three liquid cooling methods, cold plate liquid cooling is the most widely used. In the cold plate liquid cooling system, the CDU plays a crucial role, not only by providing circulating coolant for the system but also by transporting heat from the cabinet cooling system to the outdoor cooling unit, and the temperature of the coolant can be flexibly regulated to meet different cooling requirements. Since CDU failure may lead to liquid cooling system paralysis, the equipment in CDU should be considered for redundant setup, and the circulating pump as the core component is generally used for one use and one standby. The current research on cold plate liquid cooling focuses on strengthening the heat transfer technology and designing efficient micro-channel heat sinks for heat-generating components (Kheirabadi and Groulx., 2016). There have been many application cases of cold plate liquid cooling. For example, IBM Power 575 and 775 supercomputers, using liquid-cooled cold plates connected directly to the processor and air-cooled auxiliary components, have achieved better energy-saving effect (Ellsworth et al., 2012). In addition, Beijing water-cooled supercomputing center uses a room temperature water cooling technology to solve the memory cooling problem of the DC, which reduces the DC energy consumption and makes it reach the highest energy-saving level (Wang et al., 2021). Furthermore, the all-liquid cooling solution from Huawei, which uses liquid technology, has better realized the high-density deployment of information technology (IT) equipment and improved the energy use efficiency of DCs (Wang et al., 2019), etc.

Immersion liquid cooling not only has high heat transfer efficiency but also avoids local hot spots. It is currently the most effective technical means to solve the problem of high-performance server heating, which can increase the power of a single cabinet to 100 kW or even more than 200 kW. Research on immersion systems is observed to be growing in the 21st century. In 2009, Green Revolution Cooling rebooted the concept of open bath immersion cooling by bringing commercial bath immersion systems to the high-performance computing industry. Moreover, the Open Compute Project officially embraced a new project under the Rack & Power as part of Advanced Cooling Solutions in 2018, while the first documented industry standard for immersion systems was presented at the Open Compute Project summit in San Jose in 2019. Midas Green Technologies designed and built the first immersive DC during the same year (Pambudi et al., 2022). In China, Sugon has launched an immersion cooling server, which can reduce the power usage effectiveness (PUE) of the DC room to 1.05 and reduce energy consumption by more than 30% compared to traditional air-cooled DC. In addition, Alibaba's "Kirin" server does not require air conditioning, fans, or other accessories, and it can be deployed anywhere on the ground, thereby saving more than 75% of space. In the research on cooling media, the U.S. company 3M has developed a coolant called Novec, which has a lower boiling point than pure water, fluorinated liquid, and mineral oil (Zhao et al., 2021).

Nozzle design is the key issue in the design of spray liquid cooling system, as the nozzle manufacturing process and nozzle structure affect the spray parameters and cooling performance (Chen et al., 2022). The heat transfer mechanism in the spray cooling process is more complex, while the theoretical basis of the research is relatively small and is still at the laboratory stage. Kandasamy et al. developed a lab-scale spray-cooled rack with PF5060 coolant using phase change heat transfer, which can make the temperature distribution on key components such as CPU and graphics processing unit more uniform compared with the cold plate liquid cooling method, and the total energy consumption of spray-cooled DCs is reduced by 25.8% compared with air-cooled DCs (Kandasamy et al., 2022). Due to the limited application scenarios of sprayed liquid cooling technology, only a small number of DCs have adopted this technology, such as the Shanghai Big Data Proving Ground, which uses modular containerized technology and is combined with sprayed liquid cooling technology to achieve an IT load of 284 kW and control the PUE of IT equipment within a stable range, which not only reduces the cost of building a DC but also improves the energy utilization efficiency of the DC. Spray cooling has great potential for application in DCs and thus merits further research to optimize its cooling performance for its application prospects (Wang et al., 2021).

3 OPPORTUNITIES AND CHALLENGES

At present, DC liquid cooling technology is still in the preliminary development stage, and it still faces many problems and challenges. The following points illustrate the development direction of future DC liquid cooling technology application research:

1) Because cold plate liquid cooling has lower requirements for the transformation and adaptation of traditional air-cooled servers, the technology is relatively mature and will represent the mainstream of liquid cooling development in the next few years. Immersion liquid cooling is currently only applicable to new DCs due to its special heat dissipation method, while spray liquid cooling systems are more complex and have the risk of coolant evaporating and escaping, and still need long-term research at the laboratory stage.
2) Liquid-cooled DCs use higher temperature coolants, which makes heat recovery possible for liquid-cooled systems. The coupling of liquid cooling technology and heat recovery will further improve the energy utilization efficiency of DCs, which can achieve broader energy saving and emission reduction by using waste heat for district heating, providing domestic hot water, etc.
3) In the cold plate liquid cooling system, there is often an uneven distribution of the flow of individual servers in a single cabinet, which may lead to local hot spots or wasted energy consumption of individual servers; thus, it is also crucial to study the flow characteristics and optimal design research of each parallel branch pipeline of servers.

4 CONCLUSION

The application of liquid cooling technology has greatly reduced the energy consumption of DCs, which is an important way to improve the energy efficiency of DCs and one of the future development trends. This study introduced the cooling methods and system components of three liquid cooling technologies and briefly analyzed their applications, pointing out the development direction of liquid cooling technology application research. In the future, the industry should actively pay attention to the changes in liquid cooling technology, actively promote its development, and lay the foundation for the realization of high-performance DC construction.

AUTHOR CONTRIBUTIONS

DL contributed to the conception of the study. HC wrote the first draft of the manuscript. All authors revised the manuscript and read and approved the submitted version.

FUNDING

This work was supported by the National Natural Science Foundation of China (No. 52006107) and the Natural Science Foundation of Jiangsu Province (BK20200720).

REFERENCES

Chen, H., Ruan, X.-h., Peng, Y.-h., Wang, Y.-l., and Yu, C.-k. (2022). Application Status and Prospect of Spray Cooling in Electronics and Energy Conversion Industries. *Sustain. Energy Technol. Assessments* 52. doi:10.1016/j.seta.2022.102181

Ellsworth, M. J., Goth, G. F., Zoodsma, R. J., Arvelo, A., Campbell, L. A., and Anderl, W. J. (2012). An Overview of the IBM Power 775 Supercomputer Water Cooling System. *J. Electron. Packag.* 134, 020906. doi:10.1115/1.4006140

Gong, Y., Zhou, F., Ma, G., and Liu, S. (2022). Advancements on Mechanically Driven Two-phase Cooling Loop Systems for Data Center Free Cooling. *Int. J. Refrig.* 138, 84–96. in press. doi:10.1016/j.ijrefrig.2022.03.007

Habibi Khalaj, A., and Halgamuge, S. K. (2017). A Review on Efficient Thermal Management of Air- and Liquid-Cooled Data Centers: From Chip to the Cooling System. *Appl. Energy* 205, 1165–1188. doi:10.1016/j.apenergy.2017.08.037

Kandasamy, R., Ho, J. Y., Liu, P., Wong, T. N., Toh, K. C., and Chua, S. J. (2022). Two-phase Spray Cooling for High Ambient Temperature Data Centers: Evaluation of System Performance. *Appl. Energy* 305, 117816. doi:10.1016/j.apenergy.2021.117816

Kheirabadi, A. C., and Groulx, D. (2016). Cooling of Server Electronics: A Design Review of Existing Technology. *Appl. Therm. Eng.* 105, 622–638. doi:10.1016/j.applthermaleng.2016.03.056

Pambudi, N. A., Sarifudin, A., Firdaus, R. A., Ulfa, D. K., Gandidi, I. M., and Romadhon, R. (2022). The Immersion Cooling Technology: Current and Future Development in Energy Saving. *Alexandria Eng. J.* 61 (12), 9509–9527. doi:10.1016/j.aej.2022.02.059

Sohel Murshed, S. M., and Nieto de Castro, C. A. (2017). A Critical Review of Traditional and Emerging Techniques and Fluids for Electronics Cooling. *Renew. Sustain. Energy Rev.* 78, 821–833. doi:10.1016/j.rser.2017.04.112

Wang, J. Y., Zhou, B. Y., Zhang, F., Shi, X., Zeng, N., and Liu, Z. Y. (2019). Data Center Energy Consumption Models and Energy Efficient Algorithms. *J. Comput. Res. Dev.* 56 (8), 1587–1603. doi:10.7544/issn1000-1239.2019.20180574

Wang, Y. S., Zhang, Q., Sun, C., Zhuang, Z. Y., Huang, Z. X., and Zhai, T. Y. (2021). Analysis on the Development of Liquid Cooling Data Center Technology. *Electr. Power Inf. Commun. Technol.* 19 (12), 69–74. doi:10.16543/j.2095-641x.electric.power.ict.2021.12.010

Xie, L. N., Xing, Y. P., and Lan, B. (2022). Investigation on Key Problems of Liquid Coolant of Immersion Liquid Cooling in Data Center. *Inf. Commun. Technol. Policy* 48 (3), 40–46. doi:10.12267/j.issn.2096-5931.2022.03.007

Zhang, H., Shao, S., Xu, H., Zou, H., and Tian, C. (2014). Free Cooling of Data Centers: A Review. *Renew. Sustain. Energy Rev.* 35, 171–182. doi:10.1016/j.rser.2014.04.017

Zhang, K., Zhang, Y., Liu, J., and Niu, X. (2018). Recent Advancements on Thermal Management and Evaluation for Data Centers. *Appl. Therm. Eng.* 142, 215–231. doi:10.1016/j.applthermaleng.2018.07.004

Zhao, T. T., Wang, L. Y., Zhang, X. Y., Sun, R. F., Xuan, C. B., Geng, W. G., et al. (2021). Research Progress of Immersion Phase-Change Cooling for Data Centers. *Huadian Technol.* 43 (10), 68–72. doi:10.3969/j.issn.1674-1951.2021.10.008

Zimmermann, S., Meijer, I., Tiwari, M. K., Paredes, S., Michel, B., and Poulikakos, D. (2012). Aquasar: A Hot Water Cooled Data Center with Direct Energy Reuse. *Energy* 43 (1), 237–245. doi:10.1016/j.energy.2012.04.037

Conflict of Interest: The authors declare that the research was conducted in the absence of any commercial or financial relationships that could be construed as a potential conflict of interest.

Publisher's Note: All claims expressed in this article are solely those of the authors and do not necessarily represent those of their affiliated organizations or those of the publisher, the editors, and the reviewers. Any product that may be evaluated in this article or claim that may be made by its manufacturer is not guaranteed or endorsed by the publisher.

frontiers | Frontiers in Energy Research

OPINION
published: 08 July 2022
doi: 10.3389/fenrg.2022.947453

Viewpoints on the Recent Advances of Micro-Oscillation Heat Pipes

*Hao Li and Lirong Li**

College of Electrical, Energy and Power Engineering, Yangzhou University, Yangzhou, China

Keywords: micro-oscillation heat pipes, hydrodynamic characteristics, thermal performance, heat transfer enhancement, application

INTRODUCTION

In recent years, with the integration and miniaturization of electronic equipment, the high-flux heat dissipation problem in confined space draws increasing attention. Available studies show that a sharp rise of operating temperature poses a serious threat to the stability and reliability of electronic equipment (Laguna et al., 2018; Li et al., 2022). Therefore, the efficient cooling technology has become the key issue for safe and steady operation of electronic equipment (Zhang et al., 2011; Zhang et al., 2019). Micro-oscillation heat pipe (MOHP), as a new cooling technology, is an attracting device for efficient electronic cooling due to its advantages of small size, simple structure, high thermal conductivity, and so on (Vasiliev, 2008; Liu et al., 2013). MOHPs commonly exhibit as the flat-plate structures with one serpentine micro-channel or several ones in them, which are usually fabricated by microelectromechanical systems (MEMS). The MOHPs are able to effectively improve the heat transfer performance in a confined space due to the good combination of internal sensible and latent heat transfer of vapor–liquid two-phase flow. Note that, owing to effects induced by more confined space in the micro-channel, the MOHPs exhibit different thermo-hydrodynamic characteristics when compared with the conventional oscillating heat pipes (OHPs) with minichannel. Recently, many researchers have made a series of progress in the field of MOHP, which is of great significance to develop its heat transfer enhancement methods and practical application in the future. Hence, the research progress of the MOHPs are briefly reviewed in this study, including the hydrodynamic characteristics, thermal performance, enhancement investigation on thermal performance, and the prospects in application field. Typical MOHPs and their characteristics involved in this paper are shown in **Figure 1**.

HYDRODYNAMIC CHARACTERISTICS IN THE MOHPS

The thermal performance of a heat pipe is largely determined by the internal flow motions of the working fluid, and thus it is of great significance to analyze the hydrodynamic characteristics in the MOHPs through visual thermal experimental studies. Therefore, researchers conducted a large number of visualization experiments on silicon-based MOHPs. It was found that due to influences in the micrometer-scale channels (e.g., large flow resistance and prominent interface tension), the operation of working fluid in the MOHPs has some different characteristics from that in the conventional OHPs. Especially, the complete fluid circulation under a relatively high-power inputs in the conventional OHPs was not observed in the MOHPs (Qu and Wu, 2011; Qu et al., 2012b; Liu et al., 2019). For example, Qu et al. (2012b) carried out simultaneous visualization and measurement study on MOHPs with trapezoidal cross section. Results show that for these MOHPs with hydraulic diameters of 251, 352, and 394 μm (numbered #1, #2, and #3, respectively), the characteristic bulk circulation can only be observed in #3 of the largest hydraulic diameter at high heat loads. Instead, a characteristic bulk circulation was observed at relatively high-power inputs (Qu and Wu, 2011; Qu

OPEN ACCESS

Edited by:
Chengbin Zhang,
Southeast University, China

Reviewed by:
Jinli Lu,
Anhui University of Technology, China

****Correspondence:***
Lirong Li
lirongli@yzu.edu.cn

Specialty section:
This article was submitted to Process and Energy Systems Engineering, a section of the journal Frontiers in Energy Research

Received: *18 May 2022*
Accepted: *27 May 2022*
Published: *08 July 2022*

Citation:
Li H and Li L (2022) Viewpoints on the Recent Advances of Micro-Oscillation Heat Pipes. Front. Energy Res. 10:947453. doi: 10.3389/fenrg.2022.947453

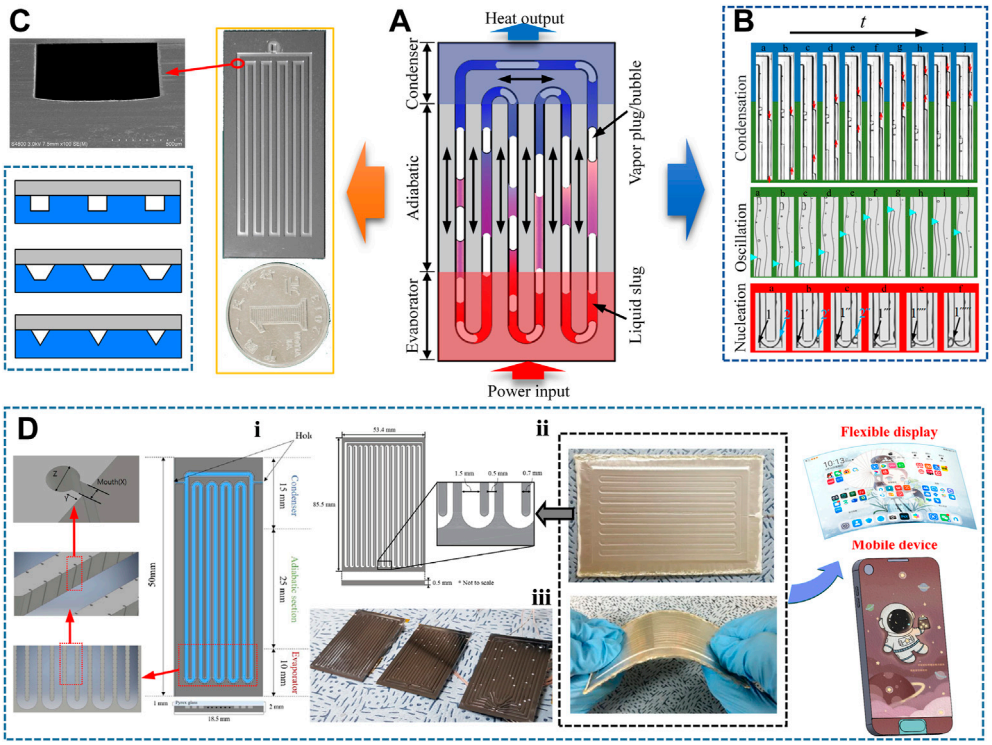

FIGURE 1 | Typical MOHPs and their characteristics: **(A)** operating principle of the MOHPs; **(B)** typical hydraulic characteristics in micro-channel; **(C)** photo of typical MOHPs and common section shapes of micro-channel; **(D)** developed MOHPs with practical value (Kim W. and Kim S. J., 2018)[i], (Lim and Kim, 2017; Lim and Kim, 2018; Jung et al., 2020)[ii], (Lim and Kim, 2017; Lim and Kim, 2018; Jung et al., 2020)[iii].

et al., 2012b). Under this fluid motion mode, the working fluid oscillates with a temporary and incomplete directional flow. Also, affected by the efficient heat conduction of the working fluid between the evaporator and condenser, the heat transfer performance of heat pipe was further enhanced in a characteristic bulk circulation state (Qu and Wu, 2011). On the other hand, more similar flow motions to the traditional OHPs were observed in the MOHPs. For example, in the experimental study conducted by Liu et al. (2019) on a MOHP with rectangular section having hydraulic diameter of 550 μm, the fluid flow mainly presented three motion modes including stop-over, small oscillation, and bulk oscillation. The oscillatory motions of the fluid in the MOHP are characterized by intermittent or individual appearance of these three modes.

Furthermore, MOHPs also have some flow patterns different from the conventional OHPs. Flow patterns commonly seen in conventional OHPs include semi-annular/annular flow, plug/slug flow, bubbly flow, and transitional flow between them (Xu et al., 2005; Liu et al., 2016). In addition to these flow patterns mentioned before, another flow pattern called injection flow was observed in the MOHPs (Qu and Wu, 2010; Qu et al., 2012b; Liu et al., 2019). Generally, under the condition of bulk oscillation, the vapor phase with thick liquid film continuously shrink and break up in the condensation process, forming the injection flow at the end of the annular flow. Accordingly, the bubbly-slug flow and the annular flows come out in the upper and lower parts of the injection flow, respectively. Moreover, nucleate boiling is also an important aspect in the studies on the MOHPs. Commonly, nucleation was hard to be observed during the boiling in the micrometer-scale channels. However, nucleate boiling was observed in MOHPs with larger diameter at the quasi-steady oscillation state (Qu and Wu, 2010; Qu et al., 2012b). This is because the intense film evaporation, instead of bubble's generation and expansion, drives the two-phase fluid oscillating in the MOHPs with small diameter.

THERMAL PERFORMANCE OF THE MOHPS

In addition to the hydrodynamic characteristics, many researches about the MOHPs were focused on the thermal performance, which is a most important issue for its practical application. The efficient heat transfer of MOHPs has been proved according to the rapid start-up and stable operation (Qu and Wu, 2011; Qu et al., 2012b; Liu et al., 2019). However, driven by the phase change process of the working fluid, the MOHPs are not able to operate before the heat input reaches a critical value. As the MOHPs start-up, the working fluid vaporizes rapidly and takes away a large amount of heat from the evaporator, resulting in the

decrease of evaporator temperature. Qu et al. (2012a) analyzed the thermal performance of the heat pipes in the experimental study and proposed that the MOHPs can effectively reduce the evaporator temperature, and the maximum temperature reduction can reach 42.1°C. Moreover, Qu and Wu (2011), Qu et al. (2012b), and Liu et al. (2019) also stated that the thermal performance was closely related to the fluid flow patterns in the micro-channels under the oscillating state of the MOHPs. The heat input into the evaporator of the MOHPs was transferred efficiently to the condenser by the bulk oscillation of the fluid, resulting in a smaller thermal resistance. Simultaneously, the injection flow, which was never observed in conventional OHPs, also facilitated the condensation heat transfer in the MOHPs (Sun et al., 2017). Thereafter, Liu et al. (2019) analyzed the oscillating wall temperature of the evaporator and the condenser of the MOHPs in detail and confirmed the relationship between thermal performance of the MOHPs and fluid flow motions in the micro-channels. Note that, when stop-over occurred, the evaporator temperature rose due to heat accumulation, while the condenser temperature dropped due to continuous cooling, which was shown as a series of corresponding peaks and valleys on the wall temperature oscillation at the evaporator and the condenser, respectively. In addition to the factors mentioned before, the thermal performance of the MOHPs was also related to the physical properties of working fluid, filling ratios, power inputs, inclination angles, channel sections, etc (Youn and Kim, 2012; Lee and Kim, 2017; Liu et al., 2019). Also, it needs to be emphasized that Lee and Kim (2017) pointed out that the heat transfer limit of the MOHPs is positively correlated with the cubic of the micro-channel hydraulic diameter regardless of the cross-sectional shape.

ENHANCEMENT OF MOHPS' THERMAL PERFORMANCE

As studies on the MOHPs continue, the complex heat and mass transfer characteristics had been gradually revealed. A new problem, heat transfer enhancement of the MOHPs, was increasingly noticed. In terms of the working fluid, considering the ultrahigh flow resistance in the micro-channels (Qu et al., 2014; Wang et al., 2018), the thermal physical property is a decisive factor in the selection of working fluid (Qu et al., 2016; Deng et al., 2022). Yang et al. (2015) experimentally proved that the high $(dP/dT)_{sat}$ of methanol contributes to the fluid oscillating and improved the thermal performance of the MOHPs. In addition, increasing number of researches concentrated on optimizing the structural design to improve the MOHPs' thermal performance (Chen et al., 2021). Sun et al. (2018) pointed out that micro-cavities embedded on the micro-channel wall can promote nucleation, thus enhancing the thermal performance of MOHPs. Thereafter, Kim W. and Kim S. J. (2018) confirmed that cavities of different sizes promote nucleation and reduce the start-up power of the MOHPs in different degrees. Also, the thermal resistance of the MOHPs with embedded cavities was reduced by up to 57%. Furthermore, in order to avoid the dry-out in evaporator, Kang and Huang (2002) and Hung and Seng (2011) successively proposed to modify the channel section into star-shaped, diamond-shaped, and other structures with sharp corners to enhance the capillary force, thus improving the rewetting of evaporator. Recently, Lee and Kim (2017) confirmed that, at the same hydraulic diameter, the maximum allowable heat flux of the MOHPs with square section was increased by 70% than that of the MOHPs with circular section. Moreover, from the perspective of channel optimization design, Kwon and Kim (2015) designed the MOHPs with a dual-diameter channel and proposed that the design with double-diameters reduces the flow resistance of the working fluid and promotes the formation of bulk oscillation, thus improving the thermal performance of the MOHPs. Huang et al. (2018), Xia et al. (2019), and Li et al. (2020) introduced curved structures into the micro-channels and proved that curved channels can effectively improve thermal performance of the micro-channels by promoting nucleation and destroying the heat transfer boundary layer. The curved micro-channel mentioned before with sinusoidal and triangular wavy sidewall gives new clues in terms of heat transfer enhancement methods for the MOHPs. In addition, Kim J. and Kim S. J. (2018) also studied the influence of condenser length on the thermal performance. The results indicate that there exists an optimal condenser length for the MOHPs of different designs.

PROSPECTS OF THE MOHPS' APPLICATIONS

Based on the broad prospects in aerospace, electronic, and other potential applications, various MOHPs with potential application value have been developed (Chen et al., 2022). Obviously, the application of the MOHPs in high-power heat dissipation is an important aspect. Luo et al. (2015) tested a silicon–aluminum MOHPs used for LED heat dissipation, results show that the MOHPs can effectively control the LED operating at a normal temperature. Previously, many researchers have carried out a lot of research on silicon-based MOHPs with integrated chips (Qu et al., 2012b; Kim W. and Kim S. J., 2018; Liu et al., 2019; Lim and Kim, 2021). Recently, with the development of flexible display technology, flexible MOHPs based on polymers is considered to be a solution to the heat dissipation due to its advantages of integration into flexible electronic packaging (Lim and Kim, 2018; Jung et al., 2020).

CONCLUSION

This study reviews the hydrodynamic characteristics, thermal performance, and its enhancement methods as well as prospects of the MOHPs' applications. The characteristic fluid motions and flow patterns during the operation of the MOHPs are introduced, and the related thermal performance is discussed. In addition, the on-going investigation of heat transfer enhancement methods for the MOHPs are also summarized and analyzed. Finally, the potential applications of the MOHPs are pointed out. It is believed these viewpoints on the recent advances of MOHPs could not only help the researchers to establish an overview of

studies on the MOHPs but also contribute to study and development of the MOHPs in future.

AUTHOR CONTRIBUTIONS

HL wrote the first draft of the manuscript. LL developed the concept of the study and revised the manuscript. All authors revised the manuscript and read and approved the submitted version.

FUNDING

This work was partially supported by the Natural Science Foundation of Jiangsu Province (No. BK20210819).

REFERENCES

Chen, X., Chen, S., Zhang, Z., Sun, D., and Liu, X. (2021). Heat Transfer Investigation of a Flat-Plate Oscillating Heat Pipe with Tandem Dual Channels under Nonuniform Heating. *Int. J. Heat Mass Transf.* 180, 121830. doi:10.1016/j.ijheatmasstransfer.2021.121830

Chen, X., Liu, X., Xu, D., and Chen, Y. (2022). Thermal Performance of a Tandem-Dual-Channel Flat-Plate Pulsating Heat Pipe Applicable to Hypergravity. *Int. J. Heat Mass Transf.* 189, 122656. doi:10.1016/j.ijheatmasstransfer.2022.122656

Deng, Z., Gao, S., Wang, H., Liu, X., and Zhang, C. (2022). Visualization Study on the Condensation Heat Transfer on Vertical Surfaces with a Wettability Gradient. *Int. J. Heat Mass Transf.* 184, 122331. doi:10.1016/j.ijheatmasstransfer.2021.122331

Huang, H., Wu, H., and Zhang, C. (2018). An Experimental Study on Flow Friction and Heat Transfer of Water in Sinusoidal Wavy Silicon Microchannels. *J. Micromech. Microeng.* 28 (5), 055003. doi:10.1088/1361-6439/aaad46

Hung, Y. M., and Seng, Q. b. (2011). Effects of Geometric Design on Thermal Performance of Star-Groove Micro-heat Pipes. *Int. J. Heat Mass Transf.* 54 (5-6), 1198–1209. doi:10.1016/j.ijheatmasstransfer.2010.09.070

Jung, C., Lim, J., and Kim, S. J. (2020). Fabrication and Evaluation of a High-Performance Flexible Pulsating Heat Pipe Hermetically Sealed with Metal. *Int. J. Heat Mass Transf.* 149, 119180. doi:10.1016/j.ijheatmasstransfer.2019.119180

Kang, S.-W., and Huang, D. (2002). Fabrication of Star Grooves and Rhombus Grooves Micro Heat Pipe. *J. Micromech. Microeng.* 12 (5), 525–531. doi:10.1088/0960-1317/12/5/303

Kim, J., and Kim, S. J. (2018a). Experimental Investigation on the Effect of the Condenser Length on the Thermal Performance of a Micro Pulsating Heat Pipe. *Appl. Therm. Eng.* 130, 439–448. doi:10.1016/j.applthermaleng.2017.11.009

Kim, W., and Kim, S. J. (2018b). Effect of Reentrant Cavities on the Thermal Performance of a Pulsating Heat Pipe. *Appl. Therm. Eng.* 133, 61–69. doi:10.1016/j.applthermaleng.2018.01.027

Kwon, G. H., and Kim, S. J. (2015). Experimental Investigation on the Thermal Performance of a Micro Pulsating Heat Pipe with a Dual-Diameter Channel. *Int. J. Heat Mass Transf.* 89, 817–828. doi:10.1016/j.ijheatmasstransfer.2015.05.091

Laguna, G., Vilarrubí, M., Ibañez, M., Betancourt, Y., Illa, J., Azarkish, H., et al. (2018). Numerical Parametric Study of a Hotspot-Targeted Microfluidic Cooling Array for Microelectronics. *Appl. Therm. Eng.* 144, 71–80. doi:10.1016/j.applthermaleng.2018.08.030

Lee, J., and Kim, S. J. (2017). Effect of Channel Geometry on the Operating Limit of Micro Pulsating Heat Pipes. *Int. J. Heat Mass Transf.* 107, 204–212. doi:10.1016/j.ijheatmasstransfer.2016.11.036

Li, W., Li, C., Wang, Z., and Chen, Y. (2022). Enhanced Flow Boiling in Microchannels Integrated with Supercapillary Pinfin Fences. *Int. J. Heat Mass Transf.* 183, 122185. doi:10.1016/j.ijheatmasstransfer.2021.122185

Li, Y. F., Xia, G. D., Ma, D. D., Yang, J. L., and Li, W. (2020). Experimental Investigation of Flow Boiling Characteristics in Microchannel with Triangular Cavities and Rectangular Fins. *Int. J. Heat Mass Transf.* 148, 119036. doi:10.1016/j.ijheatmasstransfer.2019.119036

Lim, J., and Kim, S. J. (2021). A Channel Layout of a Micro Pulsating Heat Pipe for an Excessively Localized Heating Condition. *Appl. Therm. Eng.* 196, 117266. doi:10.1016/j.applthermaleng.2021.117266

Lim, J., and Kim, S. J. (2017). "A Polymer-Based Pulsating Heat Pipe: Fabrication and Investigation of Thermal Performance," in 2017 16th IEEE Intersociety Conference on Thermal and Thermomechanical Phenomena in Electronic Systems (ITherm), Orlando, FL, USA, 30 May-2 June 2017. doi:10.1109/itherm.2017.7992542

Lim, J., and Kim, S. J. (2018). Fabrication and Experimental Evaluation of a Polymer-Based Flexible Pulsating Heat Pipe. *Energy Convers. Manag.* 156, 358–364. doi:10.1016/j.enconman.2017.11.022

Liu, X., Chen, Y., and Shi, M. (2013). Dynamic Performance Analysis on Start-Up of Closed-Loop Pulsating Heat Pipes (CLPHPs). *Int. J. Therm. Sci.* 65, 224–233. doi:10.1016/j.ijthermalsci.2012.10.012

Liu, X., Sun, Q., Zhang, C., and Wu, L. (2016). High-Speed Visual Analysis of Fluid Flow and Heat Transfer in Oscillating Heat Pipes with Different Diameters. *Appl. Sci.* 6 (11), 321. doi:10.3390/app6110321

Liu, X., Xu, L., Wang, C., and Han, X. (2019). Experimental Study on Thermo-Hydrodynamic Characteristics in a Micro Oscillating Heat Pipe. *Exp. Therm. Fluid Sci.* 109, 109871. doi:10.1016/j.expthermflusci.2019.109871

Luo, Y., Yu, B., Shan, Q., and Wang, X. (2015). "A Silicon-Aluminum Micro Heat Sink for Light Emitting Diode (LED) Chips," in 2015 16th International Conference on Electronic Packaging Technology (ICEPT), Changsha, China, 11-14 Aug. 2015, 526–529.

Qu, J., Wang, Q., Li, C., Han, X., and He, Z. (2014). A Simple Model for Taylor Flow Induced Contact Angle Hysteresis and Capillary Pressure inside Mini/micro-Scale Capillary Tubes. *Int. J. Heat Mass Transf.* 78, 1004–1007. doi:10.1016/j.ijheatmasstransfer.2014.07.048

Qu, J., Wang, Q., and Sun, Q. (2016). Lower Limit of Internal Diameter for Oscillating Heat Pipes: A Theoretical Model. *Int. J. Therm. Sci.* 110, 174–185. doi:10.1016/j.ijthermalsci.2016.07.002

Qu, J., Wu, H.-Y., and Wang, Q. (2012a). Experimental Investigation of Silicon-Based Micro-pulsating Heat Pipe for Cooling Electronics. *Nanoscale Microscale Thermophys. Eng.* 16 (1), 37–49. doi:10.1080/15567265.2011.645999

Qu, J., Wu, H., and Cheng, P. (2012b). Start-up, Heat Transfer and Flow Characteristics of Silicon-Based Micro Pulsating Heat Pipes. *Int. J. Heat Mass Transf.* 55 (21-22), 6109–6120. doi:10.1016/j.ijheatmasstransfer.2012.06.024

Qu, J., and Wu, H. (2010). Flow Visualization of Silicon-Based Micro Pulsating Heat Pipes. *Sci. China Technol. Sci.* 53 (4), 984–990. doi:10.1007/s11431-009-0391-y

Qu, J., and Wu, H. Y. (2011). Silicon-Based Micro Pulsating Heat Pipe for Cooling Electronics. *Amr* 403-408, 4260–4265. doi:10.4028/www.scientific.net/amr.403-408.4260

Sun, Q., Qu, J., Yuan, J., and Wang, H. (2018). Start-up Characteristics of MEMS-Based Micro Oscillating Heat Pipe with and without Bubble Nucleation. *Int. J. Heat Mass Transf.* 122, 515–528. doi:10.1016/j.ijheatmasstransfer.2018.02.003

Sun, Q., Qu, J., Yuan, J., and Wang, Q. (2017). Operational Characteristics of an MEMS-Based Micro Oscillating Heat Pipe. *Appl. Therm. Eng.* 124, 1269–1278. doi:10.1016/j.applthermaleng.2017.06.109

Vasiliev, L. L. (2008). Micro and Miniature Heat Pipes - Electronic Component Coolers. *Appl. Therm. Eng.* 28 (4), 266–273. doi:10.1016/j.applthermaleng.2006.02.023

Wang, J., Gao, W., Zhang, H., Zou, M., Chen, Y., and Zhao, Y. (2018). Programmable Wettability on Photocontrolled Graphene Film. *Sci. Adv.* 4 (9), eaat7392. doi:10.1126/sciadv.aat7392

Xia, G. D., Tang, Y. X., Zong, L. X., Ma, D. D., Jia, Y. T., and Rong, R. Z. (2019). Experimental Investigation of Flow Boiling Characteristics in Microchannels

with the Sinusoidal Wavy Sidewall. *Int. Commun. Heat Mass Transf.* 101, 89–102. doi:10.1016/j.icheatmasstransfer.2019.01.006

Xu, J. L., Li, Y. X., and Wong, T. N. (2005). High Speed Flow Visualization of a Closed Loop Pulsating Heat Pipe. *Int. J. Heat Mass Transf.* 48 (16), 3338–3351. doi:10.1016/j.ijheatmasstransfer.2005.02.034

Yang, K.-S., Cheng, Y.-C., Liu, M.-C., and Shyu, J.-C. (2015). Micro Pulsating Heat Pipes with Alternate Microchannel Widths. *Appl. Therm. Eng.* 83, 131–138. doi:10.1016/j.applthermaleng.2015.03.020

Youn, Y. J., and Kim, S. J. (2012). Fabrication and Evaluation of a Slicon-Based Micro Pulsating Heat Spreader. *Sensors Actuators A Phys.* 174, 189–197. doi:10.1016/j.sna.2011.12.006

Zhang, C., Chen, Y., Wu, R., and Shi, M. (2011). Flow Boiling in Constructal Tree-Shaped Minichannel Network. *Int. J. Heat Mass Transf.* 54 (1), 202–209. doi:10.1016/j.ijheatmasstransfer.2010.09.051

Zhang, C., Yu, F., Li, X., and Chen, Y. (2019). Gravity-capillary Evaporation Regimes in Microgrooves. *AIChE J.* 65, 1119–1125. doi:10.1002/aic.16484

Conflict of Interest: The authors declare that the research was conducted in the absence of any commercial or financial relationships that could be construed as a potential conflict of interest.

frontiers | Frontiers in Energy Research

TYPE Review
PUBLISHED 24 August 2022
DOI 10.3389/fenrg.2022.977925

OPEN ACCESS

EDITED BY
Xiangdong Liu,
Yangzhou University, China

REVIEWED BY
Yali Xue,
Tsinghua University, China
Yu Huang,
North China Electric Power University, China

*CORRESPONDENCE
Junli Zhang,
zjli@seu.edu.cn

SPECIALTY SECTION
This article was submitted to Process and Energy Systems Engineering, a section of the journal Frontiers in Energy Research

RECEIVED 25 June 2022
ACCEPTED 27 July 2022
PUBLISHED 24 August 2022

CITATION
Zhang J and Wei H (2022), A review on configuration optimization of hybrid energy system based on renewable energy.
Front. Energy Res. 10:977925.
doi: 10.3389/fenrg.2022.977925

A review on configuration optimization of hybrid energy system based on renewable energy

Junli Zhang* and Huashuai Wei

National Engineering Research Center of Power Generation Control and Safety, School of Energy and Environment, Southeast University, Nanjing, China

Hybrid energy system based on renewable energy is an important way to solve current energy and environmental problems. However, its achievable benefits need to be realized through an integrated optimization that considers optimization objectives, optimization models, and optimization algorithms. In this paper, the integrated structure and configuration optimization techniques of the hybrid energy system based on renewable energy (RE-HES) is summarized. The performance indicators, system characteristics, model construction, and solutions of RE-HES optimized configuration are comprehensively reviewed. Current review highlights the diversification of performance evaluation index, consideration of uncertainty and dynamic properties, superstructure approaches and intelligent algorithms.

KEYWORDS

hybrid energy system (HES), configuration optimization, renewable energy, dynamic, uncertainty, integrated structure

1 Introduction

The hybrid energy system based on renewable energy (RE-HES) has advantages of high efficiency, economy and low carbon emission, and is considered to be one of the effective ways to solve problems of energy shortage, environmental pollution and greenhouse gas emissions (Abba and Chee, 2019; Yi et al., 2021). RE-HES has high degree of flexibility and diversity, it provides a good platform for the comprehensive utilization of various energy sources (Mala and Rajeshwer, 2020), including the complementarity of continuous energy and intermittent energy (Merei et al., 2013), the complementarity of high-carbon energy and low-carbon energy (Yongpin et al., 2016; Junjie et al., 2022), the complementarity of electricity and gas (Merei et al., 2013), the complementarity of electricity and heat (Zeng et al., 2016), and so on.

RE-HES has many application scenarios, such as residential communities, office buildings, commercial areas, campuses, hospitals, and airports. Another potential application scenario is the data center (Pei et al., 2020). The data center consumes a large amount of energy (Caishan et al., 2021). RE-HES can provide efficient green energy for data centers to meet its power and cooling needs. At the same time, the

large amount of waste heat generated by the data center can also be combined with RE-HES to further improve the overall efficiency and economy of the system (Howard and Shengwei, 2019).

The performance of RE-HES in various application scenarios must first be guaranteed through configuration optimization. During the system configuration process, various energy sources are added as needed, the type and capacity of each device are selected, and its operation strategy is determined to make the final configured production system more economical, energy-efficient, and environmentally friendly (Seyed et al., 2022). RE-HES has numerous devices, diverse structures, and flexible operation strategies, which bring great challenges to the configuration optimization of the hybrid energy system. To this end, many literatures focus on the configuration optimization problem of RE-HES (Barun and Mahmudul, 2021; Lin et al., 2017).

Performance evaluation, model building, and model solving are the three main elements of a configuration optimization problem. In terms of performance evaluation, most researches are based on economic, energy saving, and environmental protection indexes (Liu et al., 2022), but in order to analyze system performance more comprehensively, many new evaluation indexes have also been developed in recent years (Ni et al., 2020) (Zhong et al., 2021). The construction of the model is closely related to the research object and research needs. In addition to the need to reasonably construct the objective function (mainly based on the research results of evaluation indexes), it is more important to reasonably describe the constraints (Wei et al., 2017; Cao et al., 2018). The constraints here include not only the internal constraints of the system and the physical interaction constraints between the system and the outside world, but also various non-physical constraints, such as economic constraints, human preference settings, etc. (Ahmad, 2021). The solution of the model also deserves attention. The configuration optimization model of the hybrid energy system is usually complex, which brings many challenges to the research of the solution algorithm. Many solving algorithms have been proposed, including classical algorithms (Yunfei et al., 2020), intelligent algorithms (Paliwal et al., 2014) and hybrid algorithms (Askarzadeh, 2013).

This paper aims to address the issues related to configuration optimization of RE-HES with a detailed review of performance evaluation, model building and model solving and other aspects of configuration optimization. The paper is structured as follows: Section 2 presents the integrated structure of RE-HES; Section 3 summarizes performance evaluation indexes of RE-HES; Subsequently, uncertainty and dynamics characteristic are concern in Section 4; Section 5 presents configuration optimization techniques used for RE-HES. Finally, conclusions are made.

2 Integrated structure of RE-HES

According to the current literature, the most basic integration methods of hybrid energy systems can be divided into two categories. One is series integration, the other is parallel integration. In the series integration type, the two energy sources do not work independently, but are strongly coupled in the same device and work together. As shown in Figure 1, based on gas steam combined cycle, solar collector is used to heat the outlet water of high-pressure economizer. In this system, the solar collector plays a role like the steam drum of the heat recovery steam generator in the gas steam combined cycle. The two energies converge at the inlet of the superheater of the heat recovery steam generator, and then jointly drive the steam turbine to do work (Antonanzas et al., 2014). In the parallel integration type, the various energy sources are less coupled during the energy conversion process, but only converge before being supplied to the user, as shown in Figure 2. The integration structure of the former is more complicated with stronger coupling, so the current research mainly focuses on the integration mechanism and performance analysis. Although the integration structure of the latter is relatively simple, it has many types of units and complex combinations, which makes the integration optimization more difficult and becomes the focus of current research.

2.1 Series integration

In hybrid energy systems, the integration of solar energy and natural gas is the most common. In addition to the integrated form shown in Figure 1, Solar energy is also used for the synthesis and decarbonization of gaseous fuels (Wei et al., 2011). In this system, natural gas reacts with water vapor under the high temperature heating of solar energy to generate H_2 and CO_2, and the H_2-rich fuel can be obtained by removing CO_2. According to the literature, not only 92% CO_2 can be removed, but also the power generation efficiency of the gas turbine reaches 39.2%, which is 7.9% higher than the reference system. Similarly, (Augusto et al., 2013) also uses solar energy for the synthesis of gaseous fuel, and then the synthesis gas is mixed with natural gas and then enters the gas turbine to be burned and do work. This study shows that when all syngas is used as fuel, about 20% of natural gas can be saved, which is quite close to the study by Wei et al. (2011) Solar and gas turbines are more closely integrated in Felsmann et al. (2015). Part of the air at the outlet of the compressor is heated by solar energy, mixed with the high-temperature flue gas at the outlet of the combustion chamber, and then enters the turbine to do work. In another proposed scheme, the solar collector directly replaced the function of the combustion chamber. All air at the compressor outlet is heated by solar energy to high temperature air and then goes directly to the turbine to do work. This scheme actually goes beyond the

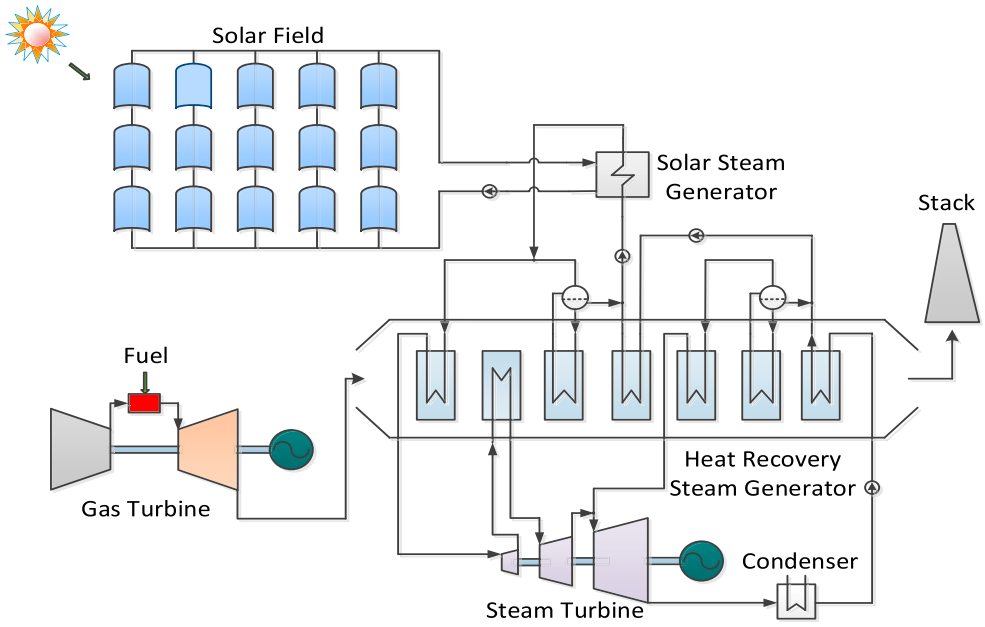

FIGURE 1
Series-integrated multi-energy complementary system.

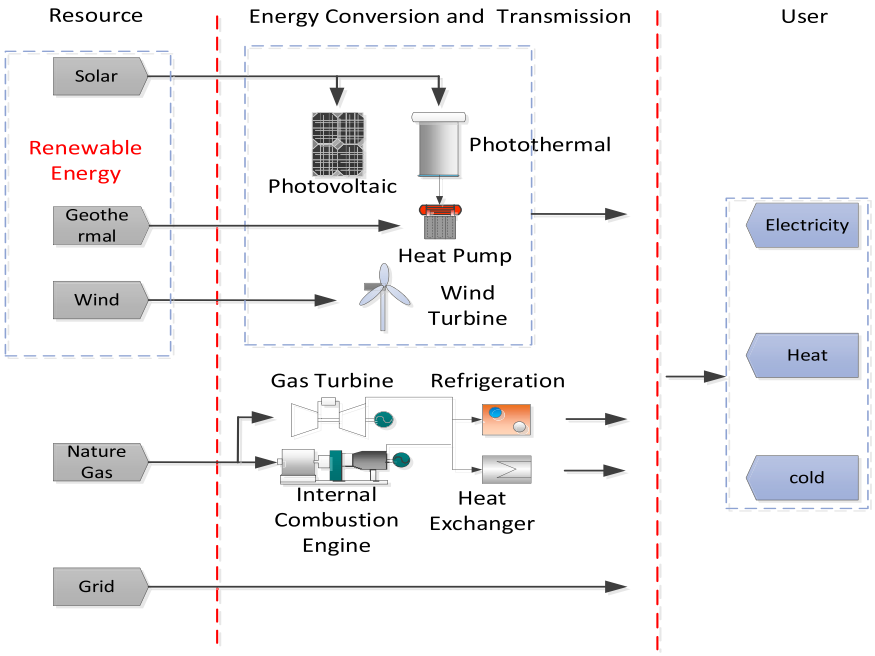

FIGURE 2
Parallel-integrated multi-energy complementary system.

combination of solar energy and natural gas and can be classified as a pure Solar System. Another way of integrating solar energy into gas turbines is given in Soltani et al. (2014). Part of the air at the outlet of the regenerator is heated by the solar collector and then enters the combustion chamber, and the solar collector plays the role of secondary heating of the air here. In addition to pure power generation systems, solar energy is also often introduced into cogeneration or combined cooling, heating and power systems. For example, Yagoub et al. (2006) studies the system performance of solar energy integrated with a gas boiler and turbine type cogeneration unit. In this study, solar energy was used to heat the exhaust flue gas of the boiler, and then combined with the high temperature flue gas from the combustion chamber to enter the boiler to heat the working fluid.

It can be seen from the above research that the series integration of solar and natural gas distributed energy systems is very diverse. Solar energy can penetrate from the fuel end of the natural gas distributed energy system to the waste heat recovery end. In contrast, the series integration of wind energy, geothermal energy, etc. with the natural gas distributed energy system is much less, and its integration is mainly at the waste heat recovery end. Parallel integration is a relatively common way to realize the complementary utilization of these energies.

2.2 Parallel integration

Compared with the series integration method, the parallel integration method is much more flexible. Through parallel integration, Multiple energy sources can work together on the same platform to meet the user's cooling, heating and power load needs. Kalantar and Mousavi G (2010) integrates 195 kW wind turbine, 85 kW solar power generation, 230 kW micro gas turbine and 2.14 kAh lead-acid battery and realizes the capacity optimization and operation control of the system. A similar study was conducted in Mousavi G (2012). In this study, a 315 kW wind turbine, a 175 kW tidal turbine, a 290 kW microturbine, and a 3.27 kAh lead-acid battery are operated together, and the capacity optimization and operation control methods of the system are studied. The introduction of renewable energy can significantly reduce greenhouse gas emissions from natural gas energy systems. This is fully reflected in the research in Braslavsky et al. (2015). In this study, DER-CAM tool was used to establish an economic optimization model for the integrated system, which includes natural gas combined cooling, heating and power plant, photovoltaic power generation, solar collectors, etc., and the minimum cost and minimum CO_2 emissions are used as the objective function. The results show that the combined natural gas supply system alone can reduce CO_2 emissions by 8.5% and 29.6% per year, respectively. After integrating solar energy, although the overall energy cost increases, the CO_2 emission reduction rate can reach 72%.

In addition to the above classification, it can also be classified according to the form of energy contained in the hybrid energy system. Such as solar-coal hybrid energy system (Yongpin et al., 2016; Yinghong et al., 2008), PV-wind-Battery hybrid energy system (Garima et al., 2017), PV-Wind-Diesel-Battery hybrid system (Mohammad et al., 2017), wind-diesel system with compressed air storage (Ibrahim et al., 2011). In the comprehensive utilization of multiple energy sources, it can be further subdivided according to whether each energy source is equal or has priority. Such as the solar-assisted coal-fired power generation system based on coal-fired power generation (Yongpin et al., 2016), solar thermal integration in combined cycle gas turbines (Antonanzas et al., 2014), and hybrid energy system with natural gas as main fuel (Hossein et al., 2017).

3 Configuration optimization architecture of HE-RES

The optimal configuration of a system means that the system has the best combination of equipment and capacity, which can optimize the overall performance of the system by optimizing operation under the expected load demand. Therefore, the configuration optimization of the hybrid energy system needs to solve two problems at the same time: one is the configuration problem, i.e., to determine the type and capacity of each device in the system; the other is the operation problem, i.e., to determine the optimal operation strategy of the system under the expected load demand. These two issues are not independent but affect each other (Ryohei et al., 2015). According to the way to deal with these two problems, the existing literature can be divided into two architecture: centralized architecture and layered architecture.

3.1 Centralized architecture

The centralized architecture refers to the unified construction and solution of the model to obtain the equipment type and size and the optimal operation strategy, as shown in Figure 3

Based on the centralized architecture, many studies have been carried out on hybrid energy systems. Yi et al. (2022) proposed a mixed integer nonlinear programming (MINLP) model and solved it using GAMS/DICOPT to obtain the optimal configuration of a solar-assisted natural gas distributed energy system with energy storage. Jianli et al. (2021) established a mixed integer programming model for a gas-wind-light-hydrogen integrated energy system with the goal of minimizing the total annual cost and carbon emissions, etc. The advantage of the centralized architecture is that he construction of the model can be closer to the original appearance of the problem, and there is no need to worry

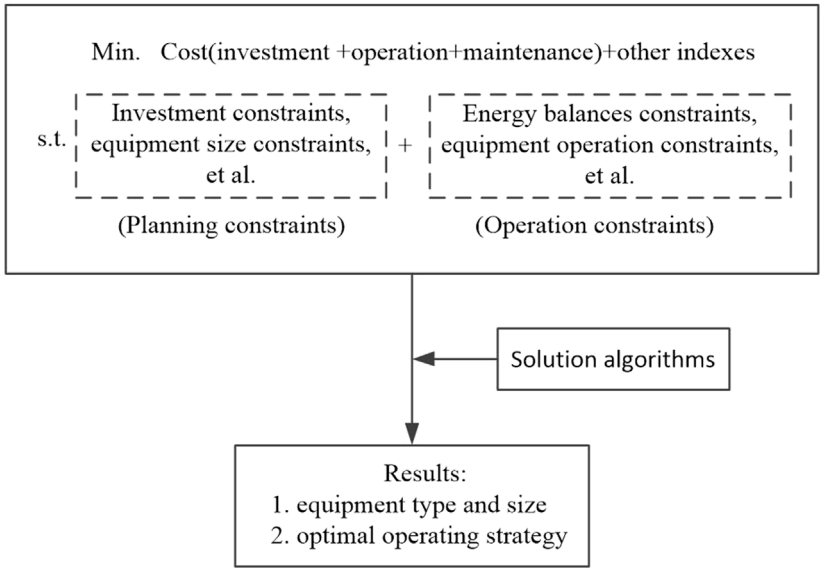

FIGURE 3
Load response curves under two different equipment capacity configurations at system level (Yuxuan et al., 2022)

about the loss of information that may be caused by the separation of the planning optimization model and the operation optimization model in the layered architecture. Therefore, with the support of efficient solving algorithms, the Centralized architecture is more likely to obtain theoretical optimal values than the layered architecture. However, as the complexity of the problem increases, the shortcomings of the overall architecture will become more and more obvious. The model obtained based on this method may be difficult to solve, and the accuracy of the model description and the solution efficiency are not easy to balance, which eventually leads to the problem of the quality of the optimization results.

3.2 Layered architecture

The layered architecture refers to dividing the configuration optimization problem into multiple problems to model and solve separately, as shown in Figure 4

In the layered architecture, the configuration problem is divided into the planning problem layer and the operation problem layer. These two layers can be modeled and solved separately, but the coupling problem between the two layers needs to be properly handled. The layered architecture has greater flexibility than the centralized architecture, and the choice of modeling and solution methods can be more free and targeted. Therefore, many researches have been carried out based on this architecture in recent years. Aiming at an isolated grid energy system composed of hydropower stations, hydrogen production equipment, hydrogen storage devices and fuel cells, a configuration optimization model based on a two-layer structure is designed in Huang et al. (2021), in which the upper layer aims to minimize the investment cost, and the lower layer aim for minimal operating costs. The Asynchronous Advantage Actor-Critic (A3C) reinforcement learning algorithm and Gurobi are used to solve the model. To solve the problem of optimal configuration of park integrated energy system under the influence of uncertainty, Min et al. (2022) proposes a two-stage robust optimization model based on a dynamic programming strategy. Wang et al. (2019a) presents a two-stage optimal configuration method. The first stage determines the capacity size, equipment selection and the number of units; the second stage considers the operation constraints, verifies and compares the reliability and economy of the configuration scheme, so as to obtain the optimal capacity configuration scheme.

For multi-objective optimization, more layers can be used. Since multi-objective optimization problems are often handled with a two-layer structure (Xu et al., 2020a), in the first layer, the multi-objective optimization results are obtained; in the second layer, the weight coefficients of each objective are determined. Therefore, if the multi-objective optimization results are computed in the first layer using the layered architecture, the entire optimization problem actually adopts a three-layer structure. Problems at different levels can be solved by different algorithms, which provides more possibilities for the combination of more algorithms to solve the problem. It is worth

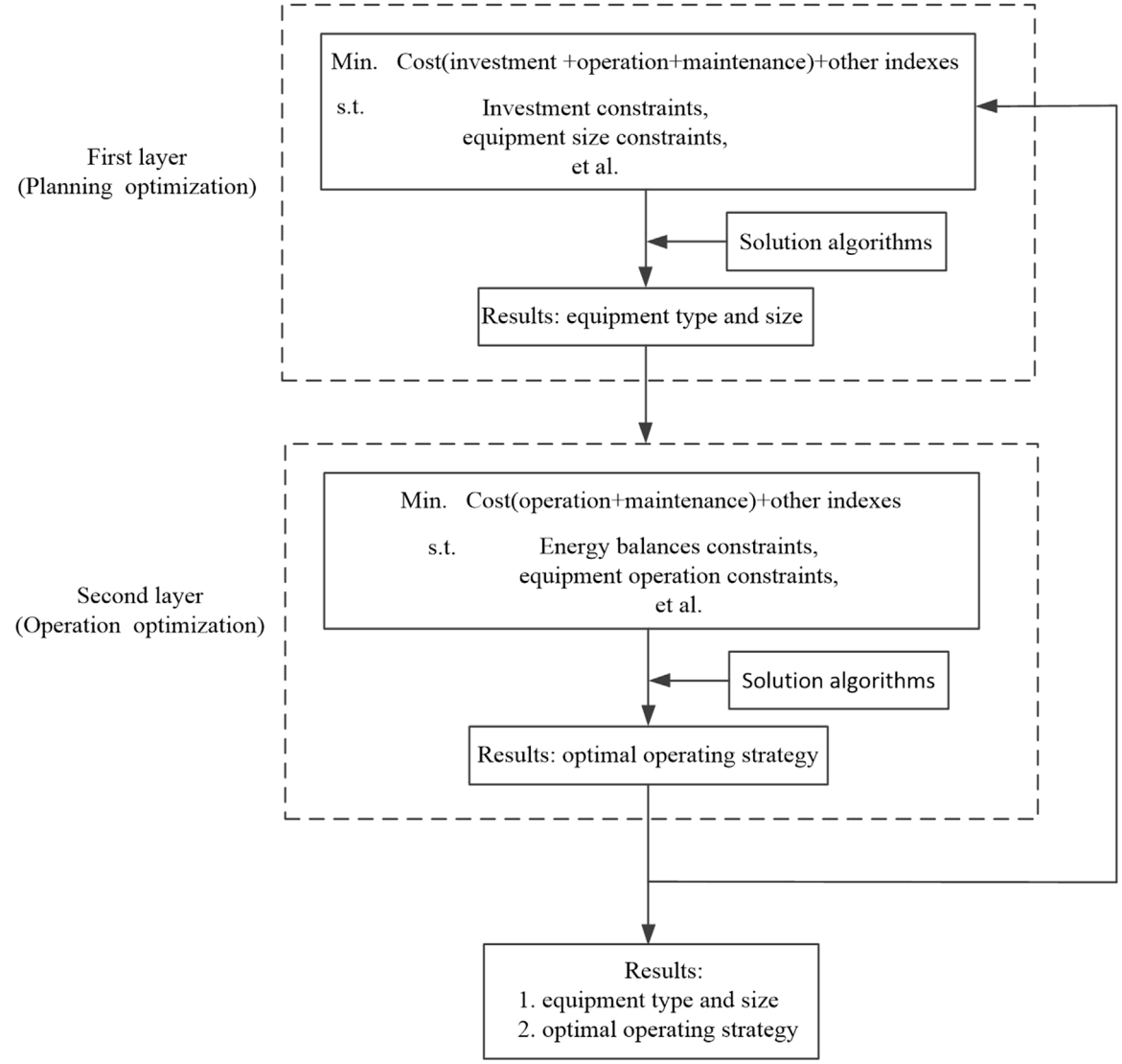

FIGURE 4
Centralized architecture for RE-HES configuration optimization.

noting that the more layers are divided, the easier the optimization problem may be to solve, but the more difficult it is to obtain the theoretical optimal value.

4 Model description and construction of RE-HES

4.1 Model construction method

The construction of an optimization model is one of the keys whether a centralized architecture or a layered architecture is adopted. In the process of model establishment, in addition to accurately describing various influencing factors of the system, the logic of model expression and the convenience of solution should also be considered. There are many structural forms of the hybrid energy system, and the operation strategy is also very flexible, especially in the case of the coupling of multiple energy flows, the system configuration optimization results have many possibilities. This brings great difficulties to the efficient construction of the model.

An efficient solution is to use a superstructure-based method (Tetsuya and Ryohei, 2014), where all possible or mainly possible structures are put into an overall structure, resulting in more structural forms than are required for the actual system. Then describe the characteristics of each device, the logic between each

device, the relationship between each energy flow, etc., so as to construct models such as mixed integer nonlinear programming (Juan et al., 2016; Zheng et al., 2022) and mixed integer linear programming (Yun et al., 2015a). The advantage of this method is that it can make the logical description of the optimization model clearer and reduce the impact of meaningless structures. Based on this method, Yun et al. (2015b) establishes a mixed-integer linear programming model of the coupled system of distributed energy and energy distribution network and realizes the optimal annual total cost of the system. It should be noted that when the system is more complex, the scale of the superstructure should be properly defined (Philip et al., 2012). The size of the scale affects the optimization results and efficiency of the solution. When the scale is small, it is easier to solve, but the optimal value may have been excluded from the structure. When the scale is large, although the chance of obtaining the optimal solution is greater, it may also introduce many meaningless structures, making the model difficult to solve.

4.2 Performance evaluation indexes of RE-HES

The performance evaluation index of the hybrid energy system is the basis for constructing the configuration optimization objective function, which has a significant impact on the configuration optimization results. Among the existing index, the three most commonly used indexes are economic, energy and environment related indexes and their combination. In recent years, with the increase in the proportion of renewable energy in the system, it is important to improve the reliability and flexibility of the system, and the related performance evaluation index has therefore received more attention.

4.2.1 Economic, energy, and environment related indexes

4.2.1.1 Economic

In most configuration optimization studies, the influence of economic index is considered when constructing the objective function. For example, Askarzadeh (2013) established a configuration optimization model for photovoltaic, wind, and battery hybrid energy systems with the annual total cost as the optimization goal. Ryohei et al. (2015) optimizes the number of photovoltaic panels and wind turbines in the wind-solar hybrid system with the lowest cost as the optimization goal. Yi et al. (2022) takes the minimum annual cost as the optimization goal optimizes and optimizes the configuration of a solar-assisted natural gas distributed energy system (DES) with energy storage. In these literatures, it can be found that the economic evaluation of the system is basically carried out with the lowest total annual cost. This index mainly includes two parts, one is fixed cost, such as equipment investment cost. The other is variable cost, such as fuel cost. Since the fuel cost of photovoltaic, wind power and other renewable energy utilization devices is basically negligible (except for biomass), and the investment cost of the equipment has been decreasing in these years, the configuration optimization results of RE-HES based on economic index tend to increase the proportion of the renewable energy consumption.

4.2.1.2 Energy

Energy-related indexes can be divided into two categories, one based on the first law of thermodynamics and the other based on the second law of thermodynamics.

1) Based on the first law of thermodynamics

The performance evaluation index based on the first law of thermodynamics mainly considers how much energy is lost in the process of energy utilization. In order to solve the problem that the traditional system cycle thermal efficiency and other evaluation indexes are difficult to scientifically evaluate the performance of the hybrid energy system, Yawen et al. (2014) puts forward the relative efficiency evaluation index of solar complementary power generation, which provides a new idea for the integrated design and optimization of solar complementary power generation. Yixun et al. (2017) considers the multi-energy flow characteristics of the integrated energy system and the influence of renewable energy access, and proposes a comprehensive energy utilization index suitable for multi-energy collaborative remote energy efficiency evaluation, which reflects the utilization level of renewable energy and non-renewable energy in the park. Like energy efficiency, primary energy consumption is often used as a performance evaluation index for configuration optimization (Xiaomin et al., 2017). No matter which index form is adopted, the index based on the first law of thermodynamics fails to take into account the difference in energy quality, which may lead to insufficient improvement of the performance of the system.

2) Based on the second law of thermodynamics

Compared with the single-energy energy system, the energy conversion structure of RE-HES is more complicated and the energy form of RE-HES is more diversified, which means, not only the amount of energy but also the energy grade needs to be considered. Therefore, many scholars have conducted research based on the second law of thermodynamics. Baghernejad and Yaghoubi (2010) studies the integrated system of solar energy and gas-steam combined cycle with exergy analysis method and obtains the main exergy loss components of the research object. Another paper further established the exergy economic optimization model of this type of system (Baghernejad and Yaghoubi, 2011), and used genetic algorithm to optimize it, which reduced the power generation cost of steam turbine and gas turbine by 7.1% and 1.17%, respectively. Calderón et al. (2011), Sayem and Ibrahim (2014) both apply the exergy

analysis method to the wind-solar hybrid power generation system. In addition to the necessary exergy analysis, the latter literature also conducts research from the perspective of energy and exergy economics to more fully demonstrate the performance of such systems. Integrating renewable energy with conventional coal-fired systems is a type of system that has received a lot of attention in recent years (Yinghong et al., 2008; Xuemin et al., 2015; Rongrong et al., 2016). For a more comprehensive analysis of the performance of the hybrid energy systems, (Suresh et al., 2010) even discusses the technical and economic feasibility of such systems from the perspective of 4E (Energy, Exergy, Environment, and Economy).

4.2.1.3 Environment

Environmental indexes have received great attention in recent years. Many studies have proved that the hybrid energy system has advantages in increasing the penetration rate of renewable energy and reducing carbon emissions in the social production process. Xue et al. (2017) proposes a comprehensive energy utilization index by adding the energy non-renewable coefficient to the evaluation index of the multi-park hybrid energy system, which can reflect the impact of renewable energy in primary energy, and through case calculation and comparative analysis, It verifies the consistency between the comprehensive energy utilization index and the economic index, and can improve the penetration rate of renewable energy in the hybrid energy system. In order to improve the renewable energy penetration rate of the system, in addition to directly establishing the optimization index considering the non-renewable coefficient of energy, many scholars try to add carbon trading mechanism to the hybrid energy system. Wei et al. (2016) proposed to introduce a carbon trading mechanism into the hybrid energy system of electricity-gas interconnection, taking the minimum sum of carbon trading cost and power generation energy cost as the objective function of the system, and combining the carbon trading mechanism with the collection of carbon taxes and other factors. Mechanisms were compared, and it was verified that the carbon trading mechanism can reduce the cost of power generation more effectively and has a good development prospect. Qu et al. (2018) verifies the feasibility of the carbon trading mechanism in the multi-regional hybrid energy system and establishes the optimization goal of the multi-regional hybrid energy system considering the carbon transaction cost. The results show that under the background of low coal prices in my country, the multi-regional hybrid energy system can make each regional energy system actively use low-emission technologies such as cogeneration and other clean energy through the carbon trading mechanism game. Wang et al. (2019b) further considers the impact of the combination of LCA energy chain and carbon trading mechanism on the optimization of the hybrid energy system, and solves the difficulty in calculating the total carbon emissions caused by the mutual conversion of various energy sources in the hybrid energy system. This ensures the effective operation of the carbon trading mechanism. In addition, studies have also considered the impact of carbon taxes (Wang et al., 2021) and renewable energy subsidies (Liu et al., 2021) on hybrid energy systems. Shebaz et al. (2021) conducts a study on the optimal configuration of solar and wind hybrid renewable energy systems with and without energy storage for environmental and social criteria.

4.2.2 Reliability and flexibility

System reliability and flexibility become important due to the presence of large amounts of renewable energy.

4.2.2.1 Reliability

In the practical application of the hybrid energy system, not only its environmental protection performance needs to be better than that of the traditional energy system, but also its reliability must be guaranteed. This is one of the keys to the large-scale commercial application of hybrid energy systems. By establishing the reliability evaluation index of the hybrid energy system to evaluate the reliability of each equipment, it is helpful to find the deficiencies of the system and improve them effectively (Li et al., 2021). Some studies do not consider the influence of randomness and quantify the influence of the failure of each device on the reliability of the hybrid energy system by establishing the fault correlation matrix of each device (Zhao et al., 2022). However, affected by the characteristics of renewable energy, the operating state of each device has a certain randomness. Therefore, some scholars have carried out reliability assessment based on probabilistic operating state modeling for hybrid energy systems. Usually, the Monte Carlo method is applied to reliability evaluation, and a new reliability evaluation index is proposed (Cao et al., 2022; Fang et al., 2022). Optimizing based on reliability alone may result in system redundancy. Therefore, the reliability index needs to be used together with other indexes such as economics. Yin et al. (2021) proposed a two-layer optimization method based on the reliability objective and the economic objective. The minimum outage capacity is converted into the minimum outage penalty cost, which is the reliability cost. The reliability cost and the economic cost are integrated to a new optimization target to realize the comprehensive optimization of the system reliability and economy.

4.2.2.2 Flexibility

Due to the stochastic of renewable energy, the hybrid energy system needs to have higher flexibility than the traditional energy system to ensure the energy supply and demand balance of the system. The higher the flexibility of a hybrid energy system, the greater its ability to utilize renewable energy (Liu et al., 2019). Wang et al. (2022a) combines the power grid with the hydrogen grid by adding electricity-to-hydrogen equipment in the hybrid energy system and improve the flexibility of the system, helping the grid to absorb the uncertainty of renewable energy generation,

smoothing the output power of renewable energy. Cui et al. (2022) cited the flexibility index of air source heat pump with waste heat recovery considering dynamic characteristics in integrated energy system. Hao et al. (2022) further studies the impact of energy storage devices on the flexibility of the hybrid energy system. In addition to the influence of equipment characteristics in the hybrid energy system on the flexibility index, the variability of the load side also has an impact on the flexibility index of the hybrid energy system. Chen et al. (2021), Zhang et al. (2021) respectively study the flexibility of hybrid energy systems from the perspective of load elasticity and load excitation response. The former's flexibility takes into account the maximum variation range of the load and is a definite value. The latter's flexibility is based on the value obtained from the game of incentives and market transaction mechanisms.

4.2.3 Multiple indexes

The configuration and development of hybrid energy systems are affected by various factors such as technology, cost, and policy. Therefore, the performance index of the hybrid energy system usually adopts the index based on thermodynamics, economy, environmental protection and so on (Wang et al., 2022b). In Xinjie et al. (2021) research, the synthesis of three indicators of energy efficiency, cost rate and emissions are considered for a novel hybrid solid oxide fuel cell (SOFC)-solar hybrid CCHP residential system. Arnette and Zobel (2012) considers both greenhouse gas emissions and annual operating costs. The minimum outage capacity in Yin et al. (2021) is converted into the minimum outage penalty cost, which is a combination of reliability indexes and economic indexes. The low-carbon indexes in Wei et al. (2016) are also represented by carbon transaction costs, which are ultimately reflected in economic goals. Zhong et al. (2021) builds a model that includes six evaluation indexes: energy saving rate, energy loss, new energy proportion, new energy consumption rate, and operation and maintenance cost. The system can be more comprehensively evaluated and optimized through multiple indexes, but how to reasonably determine the weight of each index is still one of the basic challenges of current multi-objective configuration optimization.

4.3 Considering uncertainty and dynamic characteristics in optimization

The system characterization has a significant impact on the configuration optimization model and its optimization results. Most of the existing configuration optimization studies ignore the uncertainty and dynamic characteristics of the system when describing the system. For hybrid systems that do not contain renewable energy, this treatment may not have a noticeable effect on the results. However, for systems with renewable energy sources, ignoring uncertainties and dynamics may lead to large deviations in system configuration results. This section is mainly divided into two aspects: considering uncertainty and considering dynamic characteristics.

4.3.1 Considering uncertainty

For the treatment of uncertainty, the commonly methods used are stochastic optimization methods and robust optimization methods.

4.3.1.1 Stochastic optimization methods

The main idea of the stochastic optimization method can be summarized as: based on a large amount of historical data, typical scenes are obtained by clustering, then the probability of occurrence of each scene is calculated, and finally the mathematical expectation model is solved. Stochastic optimization is mainly based on the probability prediction information of uncertain variables. The uncertain variables usually obey a certain probability density distribution, such as the wind speed obeys the Weibull distribution (Villanueva et al., 2011), and the forecast errors of wind power and photovoltaic output obey the normal distribution (Lange, 2005, Abedi et al., 2011). Using stochastic optimization method, (Yi et al., 2022) established an optimization model for the hybrid energy system and the uncertainty of cooling, heating and power load and the stochastic of renewable energy are described by Monte Carlo simulation method. Amirhossein et al. (2017) established a two-stage stochastic programming model for hybrid energy system configuration based on typical scenarios obtained by Monte Carlo sampling and K-Means clustering.

4.3.1.2 Robust optimization methods

Unlike stochastic optimization methods, which have higher requirements on historical data, robust optimization methods have much lower requirements on it. The method only needs to determine a reasonable fluctuation range of random variables to ensure the feasibility of configuring results within this range (Cao et al., 2018, Zugno and Conejo, 2015). Robust optimization methods can be summarized as traditional robust optimization methods and distributed robust optimization methods.

1) Traditional robust optimization method

The traditional robust optimization method is mainly to find the worst scenario in the uncertainty interval and calculate the optimal solution in this scenario. According to this idea, (Chen et al., 2019) established a robust optimization model considering the uncertainty factors of load demand and used the Benders algorithm to solve it. The optimization results obtained in the worst case are very conservative. To reduce the conservativeness of the method, a two-stage robust model is proposed. Based on two-stage robust method, Zeng and Zhao (2013) proposes a column-and-constraint generation (C&CG) algorithm based on the Benders decomposition method. By continuously

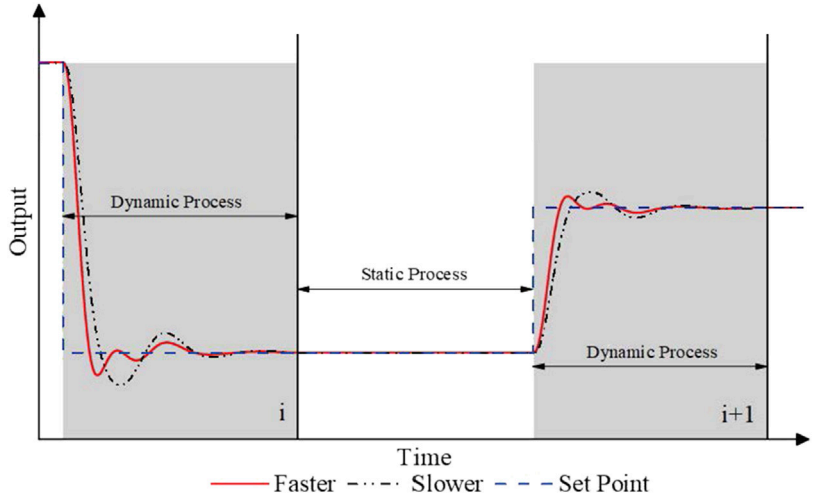

FIGURE 5
Layered architecture for RE-HES configuration optimization.

introducing optimal cut sets and feasible constraints in the loop, it can quickly solve two-stage robust optimization problems. To further improve the robustness, Yan et al. (2021) uses box uncertainty sets, ellipsoid uncertainty sets, and convex uncertainty sets to describe the distribution of uncertain factors and establishes a two-stage robust optimal configuration model.

2) Distribution robust optimization method

To achieve the balance of performance such as economy and conservatism, distributed robust optimization methods have been proposed and developed in recent years. The distribution-robust optimization (DRO) method is mainly to find the decision results under the worst probability distribution of uncertain parameters (Wang et al., 2018). It is mainly divided into two methods: probability density and distance information. DRO methods based on probability density mainly include three forms: multi-discrete scene (He et al., 2019), Wasserstein distance (Zhu et al., 2019) and KL divergence (Chen et al., 2018). DRO methods based on range information mainly include two forms: deterministic range (Chen et al., 2016) and indeterminate range (Alvarado et al., 2019; Lu et al., 2018a). The mathematical description of the DRO method based on distance information is more accurate, but the conversion and solution process are complicated. The DRO method based on probability density has the advantages of simple mathematical logic and easy solution, so it is currently used more in hybrid energy systems.

4.3.2 Considering dynamic characteristics

To cope with the uncertain influence of load demand and renewable energy output, the dynamic tracking performance of the system needs to be improved (Chen and Pan, 2021). Existing studies are mainly based on the steady-state characteristics of the system, and the improvement of system dynamic tracking performance by advanced control methods is limited (Blaud et al., 2020). Different device configurations result in different dynamic tracking performance, as shown in Figure 5. Therefore, ignoring the dynamic tracking performance in the capacity configuration may result in the inability of the hybrid energy system to track the load demand in time.

For scheduling optimization problems, some studies have considered the influence of dynamic characteristics, mainly the influence of thermal network and thermal inertia of buildings (Wei et al., 2017; Yang et al., 2020). However, the impact of considering dynamic properties in configuration optimization has only recently received attention. Existing studies have shown that the system exhibits more advantageous performance after adopting an optimized configuration that considers the dynamic characteristics (Yuxuan et al., 2022; Bingle and Xiao, 2022). With the increasing proportion of renewable energy in the system and the in-depth understanding of the dynamic characteristics of the hybrid energy system, considering the dynamic characteristics in the configuration and scheduling optimization are expected to bring more benefits to the system.

5 Model solution algorithms for RE-HES's configuration

The model solution algorithm plays an important role in the configuration optimization of the hybrid energy system. At present, a variety of solution algorithms have been developed, which can be mainly divided into two basic categories: classical optimization

algorithms and intelligent optimization algorithms. There are also some studies using commercial solver to solve optimization models. Such Gurobi (Jiang et al., 2022) and CPLEX (Zhou et al., 2022), which are widely used due to their superior performance. Some other solvers such as MOSEK (Zhang et al., 2018), XPRESS (Andrychowicz and Olek, 2016), LINGO (Xu et al., 2020b), INTLINPROG (Ibrahimi et al., 2019) are also commonly found in the literature. However, the core algorithms of these solvers are also based on classical algorithms or intelligent algorithms or hybrid algorithms of classic and intelligent. This paper mainly focuses on these two basic algorithms.

5.1 Classical optimization algorithms

The configuration optimization problem of RE-HES is essentially a nonlinear programming problem. When considering the discrete characteristics of the problem, such as discontinuity of equipment size, start-stop logic of equipment, etc., the problem becomes a nonlinear mixed integer programming problem. In practical applications, for the convenience of solving, nonlinear programming (or mixed integer nonlinear programming) problems are often transformed into linear programming (Peng et al., 2016) [or mixed integer linear programming (Jiang et al., 2022; Mazaheri et al., 2021)] problems through simplification or linearization. When using traditional solving methods, different solving algorithms are used for different models. For example, sequential quadratic programming methods can be used to solve nonlinear programming problems (Ahmad, 2021; Lu et al., 2018b); branch and bound methods and cutting plane methods can be used to solve mixed integer programming problems (Yi et al., 2022), etc.

Different from the generality pursued by some intelligent methods, traditional methods are generally more targeted to the problem, and the algorithm can often be improved according to the characteristics of the problem (Ryohei et al., 2015). For example, Lahdelma and Hakonen (2003) establishes a linear programming model for the cogeneration problem and proposes an improved simplex method according to the characteristics of the model, which achieves good results. Then, a TCS algorithm suitable for solving the linear programming model of the trigeneration system is proposed Rong and Lahdelma (2005). The enumeration method may also be an effective method when the model complexity is low or the value range of the decision variable is small (Shaneb et al., 2012; Sanaye et al., 2008).

5.2 Intelligent optimization techniques

The rapid development of intelligent optimization techniques in recent years has been clearly reflected in the comprehensive optimization of hybrid energy systems. Various novel and hybrid algorithms are selected and proposed to solve complex integrated optimization problems of hybrid energy systems. Paliwal et al. (2014) applies particle swarm optimization (PSO) to the study of capacity allocation optimization of wind-solar-diesel-storage hybrid energy systems. Mei et al. (2022) uses a multi-objective particle swarm algorithm to optimize the regional hybrid energy system. Arabli et al. (2013) studies the integrated optimization problem of the heating ventilation system (HVAC) powered by wind-solar storage and uses the genetic algorithm (GA)-based two-point estimation method to optimize the model. Chen et al. (2020) established an exergy analysis model for the hybrid energy system using an adaptive genetic algorithm and verified the validity of the model for the Bali hybrid energy system model. There are also some other new algorithms that can also be used to solve the configuration optimization problem of hybrid energy systems, such as ant colony algorithm (Abdolvahhab and Ehsan, 2015), big bang–big crunch algorithm (Saeedeh and Shirzad, 2016) and bee swarm algorithm (Akbar and Alireza, 2014). Due to the limitations of a single algorithm, some studies use a combination of multiple algorithms to improve the optimization performance. Shilaja (2021) combines the chaotic particle swarm optimizer and the gravitational search algorithm to deal with the power flow calculation problem in the hybrid energy system. Askarzadeh (2013) combines chaos search (CS), harmony search (HS) and simulated annealing (SA), and proposes a new discrete chaotic harmony-based simulated annealing method (DCHSSA) to solve the configuration optimization model of hybrid energy systems.

At present, the effective combination of intelligent algorithms and configuration optimization models is still insufficient. This is a general problem that deserves attention. Compared with the traditional method, the intelligent method does have better generality, but the excessive pursuit of generality will inevitably lead to the difficulty of improving the algorithm in combination with the specific characteristics of the model. To solve this problem, in addition to improving the intelligent algorithm itself, it is also an effective method to combine the intelligent algorithm with the traditional method. How to find a balance between the generality and individuality of the algorithm and realize the fast and high-quality solution of the configuration optimization model is a topic worthy of continuous discussion.

6 Conclusion

The integration of RE-HES can be summarized into two structures, series and parallel, among which the parallel structure is the focus of attention at present. A lot of research has been carried out on performance evaluation, optimization model construction and optimization algorithm application under parallel structure. Based on the configuration optimization problem processing framework, existing optimization techniques can be divided into holistic frameworks and hierarchical frameworks. The performance evaluation index is the basis for the construction of the optimization objective function. In addition to common indexes such as economy,

energy consumption, and environmental protection, related indexes such as reliability, flexibility and dynamic characteristics also received attention. The construction of the optimization model is closely related to the system and operational requirements. Due to the introduction of renewable energy, uncertainty and dynamic characteristics cannot be ignored in configuration optimization. Optimizing the dynamic characteristics of the system in the capacity allocation stage may effectively improve the system's ability to cope with renewable energy and load uncertainty. But this also brings new challenges to the solution of the optimization model. According to the way to deal with these two problems, the existing literature can be divided into two architecture: centralized architecture and layered architecture. Based on these two architectures, a lot of work has been carried on model building and model solving, and technologies such as superstructure methods and intelligent algorithms have been effectively applied in RE-HES.

Author contributions

JZ: Conceptualization, Methodology, Literature arrangement and review, Writing original draft. HW: literature arrangement and review.

Funding

This work was supported by National Natural Science Foundation of China under Grant 51936003 and National Key R&D Program of China under Grant 2018YFB1502900 and the Fundamental Research Funds for the Central Universities 2242021k10010.

Conflict of interest

The authors declare that the research was conducted in the absence of any commercial or financial relationships that could be construed as a potential conflict of interest.

Publisher's note

References

Abba, L. B., and Chee, W. T. (2019). A review on stand-alone photovoltaic-wind energy system with fuel cell: System optimization and energy management strategy. *J. Clean. Prod.* 221, 73–88. doi:10.1016/j.jclepro.2019.02.228

Abdolvahhab, F., and Ehsan, K. (2015). Size optimization for hybrid photovoltaic–wind energy system using ant colony optimization for continuous domains based integer programming. *Appl. Soft Comput.* 31, 196–209. doi:10.1016/j.asoc.2015.02.047

Abedi, S., Riahy, G. H., Hosseinian, S. H., and Alimardani, A. (2011). Risk-Constrained unit commitment of power system incorporating PV and wind farms. *Isrn Renew. Energy* 2011 (1)–8. doi:10.5402/2011/309496

Ahmad, R. J. (2021). Economic dispatch in grid-connected and heat network-connected CHP microgrids with storage systems and responsive loads considering reliability and uncertainties. *Sustain. Cities Soc.* 73, 103101. doi:10.1016/j.scs.2021.103101

Akbar, M., and Alireza, A. (2014). Artificial bee swarm optimization for optimum sizing of a stand-alone PV/WT/FC hybrid system considering LPSP concept[J]. *Sol. Energy* 107, 227–235. doi:10.1016/j.solener.2014.05.016

Alvarado, D., Moreira, A., Moreno, R., and Strbac, G. (2019). Transmission network investment with distributed energy resources and distributionally robust security. *IEEE Trans. Power Syst.* 34 (6), 5157–5168. doi:10.1109/tpwrs.2018.2867226

Amirhossein, D., Behnam, M., Mehdi, A., and Sajjad, T. (2017). Optimal stochastic design of wind integrated energy hub[J]. *IEEE Trans. Industrial Inf.* 13 (5), 2379–2388. doi:10.1109/TII.2017.2664101

Andrychowicz, M., and Olek, B. (2016). "Optimal structure of the RES in distribution systems," in International Conference on the European Energy Market, EEM 13th International Conference on the European Energy Market, Portugal, June 6-9, 2016 (IEEE). doi:10.1109/EEM.2016.752133

Antonanzas, J., Jimenez, E., Blanco, J., and Antonanzas-Torres, F. (2014). Potential solar thermal integration in Spanish combined cycle gas turbines. *Renew. Sustain. Energy Rev.* 37, 36–46. doi:10.1016/j.rser.2014.05.006

Arabli, S., Ghofrani, M., Etezadi-Amoli, M., Fadali, S., and Baghzouz, Y. (2013). Genetic-algorithm-based optimization approach for energy management. *IEEE Trans. Power Deliv.* 28, 162–170. doi:10.1109/TPWRD.2012.2219598

Arnette, A., and Zobel, C. W. (2012). An optimization model for regional renewable energy development. *Renew. Sustain. Energy Rev.* 16 (7), 4606–4615. doi:10.1016/j.rser.2012.04.014

Askarzadeh, A. (2013). A discrete chaotic harmony search-based simulated annealing algorithm for optimum design of PV/wind hybrid system. *Sol. Energy* 97, 93–101. doi:10.1016/j.solener.2013.08.014

Augusto, B., Marco, P., and Cesare, S. (2013). Solar steam reforming of natural gas integrated with a gas turbine power plant. *Sol. energy* 96, 46–55. doi:10.1016/j.solener.2013.06.030

Baghernejad, A., and Yaghoubi, M. (2011). Exergoeconomic analysis and optimization of an integrated solar combined cycle system (ISCCS) using genetic algorithm. *Energy Convers. Manag.* 52 (5), 2193–2203. doi:10.1016/j.enconman.2010.12.019

Baghernejad, A., and Yaghoubi, M. (2010). Exergy analysis of an integrated solar combined cycle system. *Renew. Energy* 35 (10), 2157–2164. doi:10.1016/j.renene.2010.02.021

Barun, K. D., and Mahmudul, H. (2021). Optimal sizing of a stand-alone hybrid system for electric and thermal loads using excess energy and waste heat. *Energy* 214, 119036. doi:10.1016/j.energy.2020.119036

Bingle, Z., and Xiao, W. (2022). Integrated capacity configuration and control optimization of off-grid multiple energy system for transient performance improvement. *Appl. Energy* 311, 118638. doi:10.1016/j.apenergy.2022.118638

Blaud, P. C., Haurant, P., Claveau, F., Lacarrière, B., Chevrel, P., and Mouraud, A. (2020). Modelling and control of multi-energy systems through multi-prosumer node and economic model predictive control. *Int. J. Electr. Power & Energy Syst.* 118, 105778. doi:10.1016/j.ijepes.2019.105778

Braslavsky, J. H., Wall, J. R., and Reedman, L. J. (2015). Optimal distributed energy resources and the cost of reduced greenhouse gas emissions in a large retail shopping centre. *Appl. Energy* 155, 120–130. doi:10.1016/j.apenergy.2015.05.085

Caishan, G., Fengji, L., Zexiang, C., Zhao, Y. D., and Rui, Z. (2021). Integrated planning of internet data centers and battery energy storage systems in smart grids. *Appl. Energy* 281, 116093. doi:10.1016/j.apenergy.2020.116093

Calderón, M., Calderón, A. J., Ramiro, A., Gonzalez, J. F., and Gonzalez, I. (2011). Evaluation of a hybrid photovoltaic-wind system with hydrogen storage

performance using exergy analysis. *Int. J. Hydrogen Energy* 36 (10), 5751–5762. doi:10.1016/j.ijhydene.2011.02.055

Cao, M., Shao, C., Hu, B., Xie, K., Li, W., Peng, L., et al. (2022). Reliability assessment of integrated energy systems considering emergency dispatch based on dynamic optimal energy flow. *IEEE Trans. Sustain. Energy* 13 (1), 290–301. doi:10.1109/TSTE.2021.3109468

Cao, Y., Wei, W., Wang, J., Mei, S., Shafie-khah, M., and Catalao, J. P. S. (2018). Capacity planning of energy hub in multi-carrier energy networks: A data-driven robust stochastic programming approach. *IEEE Trans. Sustain. Energy* 11 (1), 3–14. doi:10.1109/TSTE.2018.2878230

Chen, C., Shen, X., Guo, Q., and Sun, H. (2019). Robust planning-operation co-optimization of energy hub considering precise model of batteries' economic efficiency. *Energy Procedia* 158, 6496–6501. doi:10.1016/j.egypro.2019.01.111

Chen, H., Chen, S., Li, M., and Chen, J. (2020). Optimal operation of integrated energy system based on exergy analysis and adaptive genetic algorithm. *IEEE Access* 8, 158752–158764. doi:10.1109/ACCESS.2020.3018587

Chen, K., Chen, W., Lin, C., Zhang, S., Yu, D., Yang, Y., et al. (2021). "Integrated energy system day-ahead dispatch considering supply-side and demand-side flexibility," in 5th IEEE Conference on Energy Internet and Energy System Integration: Energy Internet for Carbon Neutrality, EI2 2021 5th IEEE Conference on Energy Internet and Energy System Integration, Taiyuan, China, October 22, 2021 (IEEE). EI2 2021. doi:10.1109/EI252483.2021.9713552

Chen, K., and Pan, M. (2021). Operation optimization of combined cooling, heating, and power superstructure system for satisfying demand fluctuation. *Energy* 237, 121599. doi:10.1016/j.energy.2021.121599

Chen, Y., Guo, Q., Sun, H., Li, Z., Wu, W., and Li, Z. (2018). A distributionally robust optimization model for unit commitment based on kullback–leibler divergence. *IEEE Trans. Power Syst.* 33 (5), 5147–5160. doi:10.1109/tpwrs.2018.2797069

Chen, Y., Wei, W., Liu, F., and Mei, S. (2016). Distributionally robust hydro-thermal-wind economic dispatch. *Appl. Energy* 173 (1), 511–519. doi:10.1016/j.apenergy.2016.04.060

Cui, Y., Guo, F., Fu, X., Zhao, Y., and Han, C. (2022). Source-load coordinated optimal dispatch of integrated energy system based on conversion of energy supply and use to promote wind power accommodation. *Dianwang Jishu/Power Syst. Technol.* 46 (4), 1437–1446. doi:10.13335/j.1000-3673.pst.2021.0625

Fang, L., Xu, X.-Y., Xia, J., and Tarasiuk, T. (2022). Reliability assessment of the port power system based on integrated energy hybrid system. *Bull. Pol. Acad. Sci. Tech. Sci.* 70 (2). doi:10.24425/bpasts.2022.140372

Fatih, O. H., Ömer, N. G., and Mehmet, K. (2009). A novel hybrid (wind–photovoltaic) system sizing procedure[J]. *Sol. Energy* 83, 2019–2028. doi:10.1016/j.solener.2009.07.010

Felsmann, C., Heide, S., Gampe, U., and Freimark, M. (2015). Modeling and simulation of the dynamic operating behavior of a high solar share gas turbine system. *J. Eng. Gas Turbines Power* 137, 1–9. doi:10.1115/1.4028445

Garima, S., Prashant, B., Anand, S., and Kurup, D. (2017). Optimal sizing and location of PV, wind and battery storage for electrification to an island A case study of Kavaratti, Lakshadweep. *J. Energy Storage* 12, 78–86. doi:10.1016/j.est.2017.04.003

Hao, J., Gou, X., Wang, S., Chen, Q., and Gao, K. (2022). Dynamic modeling and flexibility analysis of an integrated electrical and thermal energy system with the heat PumpThermal storage. *Front. Energy Res.* 10. doi:10.3389/fenrg.2022.817503

He, S., Gao, H., Liu, J., Liu, Y., Wang, J., and Xiang, Y. (2019). Distributionally robust optimal DG allocation model considering flexible adjustment of demand response [J]. *Proc. CSEE* 39 (8), 2253–2264. doi:10.1109/PESGM40551.2019.8973569

Hossein, Y., Mohammad, H. G., and Alibakhsh, K. (2017). Multi-objective optimal component sizing of a hybrid ICE + PV-T driven CCHP microgrid. *Appl. Therm. Eng.* 122, 126–138. doi:10.1016/j.applthermaleng.2017.05.017

Howard, C., and Shengwei, W. (2019). Optimal design of data center cooling systems concerning multi-chiller system configuration and component selection for energy-efficient operation and maximized free-cooling. *Renew. Energy* 143, 1717–1731. doi:10.1016/j.renene.2019.05.127

Huang, Y., Shi, M., Wang, W., and Lin, H. (2021). A two-stage planning and optimization model for water - hydrogen integrated energy system with isolated grid. *J. Clean. Prod.* 313, 127889. doi:10.1016/j.jclepro.2021.127889

Ibrahim, H., Younes, R., Basbous, T., Ilinca, A., and Dimitrova, M. (2011). Optimization of diesel engine performances for a hybrid wind–diesel system with compressed air energy storage. *Energy* 36 (5), 3079–3091. doi:10.1016/j.energy.2011.02.053

Ibrahimi, A. M., Howlader, H. O. R., Danish, M. S. S., Shigenobu, R., Sediqi, M. M., and Senjyu, T. (2019). Optimal unit commitment with concentrated solar power and thermal energy storage in Afghanistan electrical system. *Int. J. Emerg. Electr. Power Syst.* 20 (3), 0264. doi:10.1515/ijeeps-2018-0264

Jiang, H., Zhou, H., Xie, X.-P., Yang, D.-S., and Zhao, Y. (2022). Optimal control of integrated energy system considering temperature comfort and carbon trade. *Kongzhi Lilun Yu Yingyong/Control Theory Appl.* 39 (3), 519–526. doi:10.7641/CTA.2021.10665

Jianli, Z., Yunna, W., Zhiming, Z., Chuanbo, X., Yiming, K., and Jianwei, G. (2021). Modeling and configuration optimization of the natural gas-wind-photovoltaic-hydrogen integrated energy system: A novel deviation satisfaction strategy. *Energy Convers. Manag.* 243, 114340. doi:10.1016/j.enconman.2021.114340

Juan, I. M., Ana, M. A., Nicolás, J. S., Miguel, C. M., and Sergio, F. M. (2016). A discrete and continuous mathematical model for the optimal synthesis and design of dual pressure heat recovery steam generators coupled to two steam turbines. *Energy* 103, 807–823. doi:10.1016/j.energy.2016.02.129

Junjie, X., Yonghui, S., Jianxi, W., Zhipeng, L., Zhou, X., and Zhai, S. (2022). Multi-stage equipment optimal configuration of park-level integrated energy system considering flexible loads. *Int. J. Electr. Power & Energy Syst.* 140, 108050. doi:10.1016/j.ijepes.2022.108050

Kalantar, M., and Mousavi G, S. M. (2010). Dynamic behavior of a stand-alone hybrid power generation system of wind turbine microturbine, solar array and battery storage. *Appl. Energy* 87 (10), 3051–3064. doi:10.1016/j.apenergy.2010.02.019

Lahdelma, R., and Hakonen, H. (2003). An efficient linear programming algorithm for combined heat and power production. *Eur. J. Oper. Res., Eur. J. Operation Res.* 148, 141–151. doi:10.1016/s0377-2217(02)00460-5

Lange, M. (2005). On the uncertainty of wind power predictions—analysis of the forecast accuracy and statistical distribution of errors. *J. Sol. Energy Eng.* 127 (2), 177–184. doi:10.1115/1.1862266

Li, Z., Wang, Z., Fu, Y., and Zhao, N. (2021). Energy supply reliability assessment of the integrated energy system considering complementary and optimal operation during failure. *IET Gener. Transm. Distrib.* 15 (13), gtd2.12143–1907. doi:10.1049/gtd2.12143

Lin, G., Zetao, J., and Zongshun, T. (2017). Optimal diameter sizing based on centralized quality-quantity regulation and economic analysis of IES piping network. *Electr. Power Autom. Equip.* 37 (6), 75–83. (In Chinese).

Liu, T., Lu, J., He, C., and Xie, Y. (2019). Day-ahead economic dispatch of multi-energy parks considering integrated thermo-electric demand response and high penetration of renewable energy. *Electr. Power Autom. Equip.* (08), 261–268. doi:10.16081/j.epae.201908039

Liu, X., Li, N., Liu, F., Mu, H., Li, L., and Liu, X. (2021). Optimal design on fossil-to-renewable energy transition of regional integrated energy systems under co2 emission abatement control: A case study in dalian, China. *Energies* 14 (10), 2879. doi:10.3390/en14102879

Liu, X., Liu, F., Li, N., Mu, H., and Li, L. (2022). Hierarchical multi-objective design of regional integrated energy system under heterogeneous low-carbon policies. *Sustain. Prod. Consum.* 32, 357–377. doi:10.1016/j.spc.2022.04.027

Liuchen, L., Guomin, C., Jiaxing, C., Xiaohuang, H., and Di, L. (2022). Two-stage superstructure model for optimization of distributed energy systems (DES) part I: Model development and verification. *Energy* 245, 123227. doi:10.1016/j.energy.2022.123227

Lu, S., Li, Y., and Xia, H. (2018). Study on the configuration and operation optimization of CCHP coupling multiple energy system. *Energy Convers. Manag.* 177, 773–791. doi:10.1016/j.enconman.2018.10.006

Lu, X., Chan, K. W., Xia, S., Zhou, B., and Luo, X. (2018). Security-Constrained multiperiod economic dispatch with renewable energy utilizing distributionally robust optimization. *IEEE Trans. Sustain. Energy* 10 (2), 768–779. doi:10.1109/tste.2018.2847419

Mala, R., and Rajeshwer, P. S. (2020). Dispatch strategies based performance analysis of a hybrid renewable energy system for a remote rural area in India. *J. Clean. Prod.* 259, 120697. doi:10.1016/j.jclepro.2020.120697

Mazaheri, H., Abbaspour, A., Fotuhi-Firuzabad, M., Moeini-Aghtaie, M., Farzin, H., Wang, F., et al. (2021). An online method for MILP co-planning model of large-scale transmission expansion planning and energy storage systems considering N-1 criterion. *IET Gener. Transm. Distrib.* 15 (4), 664–677. doi:10.1049/gtd2.12050

Mei, A., Liu, P., Lu, C., Wei, J., and Zhang, K. (2022). "Hierarchical optimal scheduling of regional integrated energy power system based on multi-objective particle swarm optimization algorithm," in Proceedings - 2022 14th International Conference on Measuring Technology and Mechatronics Automation, ICMTMA 2022 14th International Conference on Measuring Technology and Mechatronics Automation, Changsha, China (Changsha, China: IEEE), 2022–January 15-16, 2022.2022, 110–115. doi:10.1109/ICMTMA54903.2022.00029

Merei, G., Berger, C., and Sauer, D. U. (2013). Optimization of an off-grid hybrid PV–Wind–Diesel system with different battery technologies using genetic algorithm. *Sol. Energy* 97, 460–473. doi:10.1016/j.solener.2013.08.016

Min, W., Jiazhu, X., Linjun, Z., Chang, L., Yuxing, L., Yuqin, Y., et al. (2022). Two-stage robust optimization model for park integrated energy system based on dynamic programming. *Appl. Energy* 308, 118249. doi:10.1016/j.apenergy.2021.118249

Mohammad, J. K., Amit, K. Y., and Lini, M. (2017). Techno economic feasibility analysis of different combinations of PV-Wind-Diesel-Battery hybrid system for telecommunication applications in different cities of Punjab, India. *Renew. Sustain. Energy Rev.* 76, 577–607. doi:10.1016/j.rser.2017.03.076

Mousavi G, S. M. (2012). An autonomous hybrid energy system of wind-tidal-microturbine-battery storage. *Int. J. Electr. Power & Energy Syst.* 43 (1), 1144–1154. doi:10.1016/j.ijepes.2012.05.060

Ni, W., Lu, L., Xiang, Y., Liu, J., Huang, Y., and Wang, P. (2020). Reliability evaluation of integrated energy system based on markov process Monte Carlo method. *Dianwang Jishu/Power Syst. Technol.* 44 (1), 150–158. (In Chinese). doi:10.13335/j.1000-3673.pst.2019.0047

Paliwal, P., Patidar, N. P., and Nema, R. K. (2014). Determination of reliability constrained optimal resource mix for an autonomous hybrid power system using Particle Swarm Optimization. *Renew. Energy* 63, 194–204. doi:10.1016/j.renene.2013.09.003

Pei, H., Benedetta, C., Xingxing, Z., Jingchun, S., Isabelle, L., Mats, R., et al. (2020). A review of data centers as prosumers in district energy systems: Renewable energy integration and waste heat reuse for district heating. *Appl. Energy* 258, 114109. doi:10.1016/j.apenergy.2019.114109

Peng, Z., Fu, C., Zhu, K., Zhang, Q., Ni, D., and Yang, S. (2016). An improved LP model for energy optimization of the integrated iron and steel plant with a cogeneration system in China. *J. Syst. Sci. Syst. Eng.* 25 (4), 515–534. doi:10.1007/s11518-015-5293-x

Philip, V., Matthias, L., Gregor, W., and André, B. (2012). Superstructure-free synthesis and optimization of distributed industrial energy supply systems. *Energy* 845, 424–435. doi:10.1016/j.energy.2012.01.041

Qu, K., Huang, L., Yu, T., and Zhang, X. (2018). Decentralized dispatch of multi-area integrated energy systems with carbon trading. *Proc. CSEE* 38 (03), 697–707. (In Chinese). doi:10.13334/j.0258-8013.pcsee.170602

Rong, A., and Lahdelma, R. (2005). An efficient linear programming model and optimization algorithm for trigeneration. *Appl. Energy* 82, 40–63. doi:10.1016/j.apenergy.2004.07.013

Rongrong, Z., Hongtao, L., Chao, L., Miaomiao, Z., and Yongpin, Y. (2016). Analysis of a solar-aided coal-fired power generation system based on thermo-economic structure theory. *Energy* 102, 375–387. doi:10.1016/j.energy.2016.02.086

Ryohei, Y., Yuji, S., Syusuke, T., Masashi, O., and Tetsuya, W. (2015). Optimization of energy supply systems by MILP branch and bound method in consideration of hierarchical relationship between design and operation. *Energy Convers. Manag.* 92, 92–104. doi:10.1016/j.enconman.2014.12.020

Saeedeh, A., and Shirzad, A. (2016). Application of the Hybrid Big Bang–Big Crunch algorithm for optimal sizing of a stand-alone hybrid PV wind battery system[J]. *Sol. Energy* 134, 366–374. doi:10.1016/j.solener.2016.05.019

Sanaye, S., Meybodi, M. A., and Shokrollahi, S. (2008). Selecting the prime movers and nominal powers in combined heat and power systems. *Appl. Therm. Eng.* 28 (10), 1177–1188. doi:10.1016/j.applthermaleng.2007.08.003

Sayem, Z., and Ibrahim, D. (2014). Energy, exergy and exergoeconomic analyses of a combined renewable energy system for residential applications. *Energy Build.* 71, 68–79. doi:10.1016/j.enbuild.2013.12.006

Seyed, M. H., Arezoo, H., Miadreza, S., Mohamed, L., and João, P. S. C. (2022). Optimal sizing of renewable energy systems in a Microgrid considering electricity market interaction and reliability analysis. *Electr. Power Syst. Res.* 203, 107678. doi:10.1016/j.epsr.2021.107678

Shaneb, O. A., Taylor, P. C., and Coates, G. (2012). Optimal online operation of residential μCHP systems using linear programming. *Energy Build. Energy Build.* 44, 17–25. doi:10.1016/j.enbuild.2011.10.003

Shebaz, A. M., Darshit, S. U., and Rajesh, N. P. (2021). Optimal configuration of solar and wind-based hybrid renewable energy system with and without energy storage including environmental and social criteria: A case study. *J. Energy Storage* 44, 103446. doi:10.1016/j.est.2021.103446

Shilaja, C. (2021). "Perspective of combining chaotic particle swarm optimizer and gravitational search algorithm based on optimal power flow in wind renewable energy," in 3rd International Conference on Computing and Communication, IC3 2020, India, March 20-21, 2020 (Rangpo: Springer Science and Business Media Deutschland GmbH). 2020. doi:10.1007/978-981-15-7394-1_44

Soltani, R., Mohammadzadeh Keleshtery, P., Vahdati, M., Khoshgoftarmanesh, M. H., Rosen, M. A., and Amidpour, M. (2014). Multi-objective optimization of a solar-hybrid cogeneration cycle: Application to CGAM problem. *Energy Convers. Manag.* 81, 60–71. doi:10.1016/j.enconman.2014.02.013

Suresh, M. V. J. J., Reddy, K. S., and Kolar, A. K. (2010). 4-E (Energy, Exergy, Environment, and Economic) analysis of solar thermal aided coal-fired power plants. *Energy Sustain. Dev.* 14, 267–279. doi:10.1016/j.esd.2010.09.002

Tetsuya, W., and Ryohei, Y. (2014). Optimal structural design of residential cogeneration systems in consideration of their operating restrictions. *Energy* 64, 719–733. doi:10.1016/j.energy.2013.10.002

Villanueva, D., Pazos, J. L., and Feijoo, A. (2011). Probabilistic load flow including wind power generation. *IEEE Trans. Power Syst.* 26 (3), 1659–1667. doi:10.1109/tpwrs.2010.2096436

Wang, C., Gao, R., Wei, W., Shafie-khah, M., Bi, T., and Catalao, J. P. S. (2018). Risk-based distributionally robust optimal gas-power flow with Wasserstein distance. *IEEE Trans. Power Syst.* 34 (3), 2190–2204. doi:10.1109/tpwrs.2018.2889942

Wang, J., Zeng, P., Li, Y., and Liu, J. (2022). Optimal capacity planning of power to hydrogen in integrated ElectricityHydrogenGas energy systems considering flexibility and hydrogen injection. *Front. Energy Res.* 10. doi:10.3389/fenrg.2022.845637

Wang, M., Yu, H., Yang, Y., Lin, X., Guo, H., Li, C., et al. (2021). Unlocking emerging impacts of carbon tax on integrated energy systems through supply and demand co-optimization. *Appl. Energy* 302, 117579. doi:10.1016/j.apenergy.2021.117579

Wang, S., Zhao, C., Liu, H., Gao, R., Liu, S., and Su, X. (2022). Comprehensive evaluation method and index system for electric-hydrogen-storage integrated energy network. In (Vol. 119, pp. 128–137). *Springer Sci. Bus. Media Deutschl. GmbH*. doi:10.1007/978-3-030-97064-2_13

Wang, Y., Wang, Y., Huang, Y., Li, F., Zeng, M., Li, J., et al. (2019). Planning and operation method of the regional integrated energy system considering economy and environment. *Energy* 171 (15), 731–750. doi:10.1016/j.energy.2019.01.036

Wang, Z., Shi, Y., Tang, Y., Men, X., Cao, J., and Wang, H. (2019). Low carbon economy operation and energy efficiency analysis of integrated energy systems considering LCA energy chain and carbon trading mechanism. *Proc. CSEE* 39 (06), 1614–1626+1858. (In Chinese). doi:10.13334/j.0258-8013.pcsee.180754

Wei, G., Jun, W., Shuai, L., Zhao, L., and Chenyu, W. (2017). Optimal operation for integrated energy system considering thermal inertia of district heating network and buildings. *Appl. Energy* 199, 234–246. doi:10.1016/j.apenergy.2017.05.004

Wei, H., Hongguang, J., and Rumou, L. (2011). A novel multifunctional energy system for CO2 removal by solar reforming of natural gas. *J. Sol. energy Eng.* 133, 1–8. doi:10.1115/1.4004034

Wei, Z., Zhang, S., Sun, G., Xu, X., Chen, S., and Chen, S. (2016). Carbon trading based low-carbon economic operation for integrated electricity and natural gas energy system. *Electr. Power Autom. Equip.* 40 (15), 9–16. (In Chinese). doi:10.1002/ese3.967

Xiaomin, L., Lei, C., Fei, X., Zeheng, L., Xiaohai, W., Youhua, H., et al. (2017). Optimal energy-source capacity ratios of integrated electictiy-heat energy system of west Inner Mongolia power grid. *Electr. Power Autom. Equip.* 37 (6), 132–138. (In Chinese). doi:10.16081/j.issn.1006-6047.2017.06.018

Xinjie, Y., Yuanchang, L., and Richard, B. (2021). *Optimised MOPSO with the grey relationship analysis for the multi-criteria objective energy dispatch of a novel SOFC-solar hybrid CCHP residential system in the UK*. UK: Energy Conversion and Management, 114406.

Xu, C., Ke, Y., Li, Y., Chu, H., and Wu, Y. (2020). Data-driven configuration optimization of an offgrid wind/PV/hydrogen system based on modified NSGA-II and CRITIC-TOPSIS. *Energy Convers. Manag.* 215, 112892. doi:10.1016/j.enconman.2020.112892

Xu, Z., Sun, Y., Xie, D., Wang, J., and Zhong, Y. (2020). Optimal configuration of energy storage for integrated region energy system considering power/thermal flexible load. *Dianli Xit. Zidonghua/Automation Electr. Power Syst.* 44 (2), 53–59. doi:10.7500/AEPS20190620005

Xue, Y., Guo, Q., Sun, H., Shen, X., and Tang, L. (2017). Comprehensive energy utilization rate for park-level integrated energy system. *Electr. Power Autom. Equip.* 37 (06), 117–123. (In Chinese). doi:10.16081/j.issn.1006-6047.2017.06.016

Xuemin, Y., Jia, W., and Chunxi, L. (2015). Energy conservation and emission reduction potentials of renewable energy integrated with coal-fired power generation system. *ACTA Energyiae Solaris Sinca* 36 (7), 717–1723. (In Chinese).

Yagoub, W., Doherty, P., and Riffat, S. B. (2006). Solar energy-gas driven micro-CHP system for an office building. *Appl. Therm. Eng.* 26 (14-15), 1604–1610. doi:10.1016/j.applthermaleng.2005.11.021

Yan, R., Wang, J., Lu, S., Ma, Z., Zhou, Y., Zhang, L., et al. (2021). Multi-objective two-stage adaptive robust planning method for an integrated energy system considering load uncertainty. *Energy Build.* 235 (2), 110741. doi:10.1016/j.enbuild.2021.110741

Yang, L., Chunling, W., Guoqing, L., Jinlong, W., Dongbo, Z., and Chen, C. (2020). Improving operational flexibility of integrated energy system with uncertain renewable generations considering thermal inertia of buildings. *Energy Convers. Manag.* 207, 112526. doi:10.1016/j.enconman.2020.112526

Yawen, Z., Hui, H., and HongGuang, J. (2014). Relative Efficiency improvement of solar-coal hybrid power. *plant J. Eng. Thermophys.* 35 (10), 1895–1900. (In Chinese).

Yi, G., Jitian, H., Qingzhao, M., and Jiahui, F. (2022). Optimal configuration and operation analysis of solar-assisted natural gas distributed energy system with energy storage. *Energy* 246, 123429. doi:10.1016/j.energy.2022.123429

Yi, Z., Chuntian, C., Cao, R., Gang, L., Jianjian, S., and Xinyu, W. (2021). Multivariate probabilistic forecasting and its performance's impacts on long-term dispatch of hydro-wind hybrid systems. *Appl. Energy* 283, 116243. doi:10.1016/j.apenergy.2020.116243

Yin, B., Li, Y., Miao, S., Lin, Y., and Zhao, H. (2021). An economy and reliability co-optimization planning method of adiabatic compressed air energy storage for urban integrated energy system. *J. Energy Storage* 40, 102691. doi:10.1016/j.est.2021.102691

Yinghong, C., Yongping YZhiping, Y., Hongjuan, H., and Xiyan, G. (2008). Coupling mechanism of solar supported coal-fired electric generation system. *Proc. CSEE* 28 (29), 99–104. (In Chinese). doi:10.13334/j.0258-8013.pcsee.2008.29.019

Yixun, X., Qinglai, G., Hongbin, S., Xinwei, S., and Lei, T. (2017). Comprehensive energy utilization rate for park-level integrated energy system. *Electr. Power Autom. Equip.* 37 (6), 117–122. (In Chinese. doi:10.16081/j.issn.1006-6047.2017.06.016

Yongpin, Y., Yong, Z., and Rongrong, Z. (2016). Study on solar contribution of solar tower aided coal-fired power generation system. *J. North China Electr. Power Univ.* 43 (3), 56–63. (In Chinese). doi:10.3969/j.ISSN.1007-2691.2016.03.09

Yun, Y., Shijie, Z., and Yunhan, X. (2015). An MILP (mixed integer linear programming) model for optimal design of district-scale distributed energy resource systems. *Energy* 90, 1901–1915. doi:10.1016/j.energy.2015.07.013

Yun, Y., Shijie, Z., and Yunhan, X. (2015). Optimal design of distributed energy resource systems coupled with energy distribution networks. *Energy* 85, 433–448. doi:10.1016/j.energy.2015.03.101

Yunfei, M., Wanqing, C., Xiaodan, Y., Hongjie, J., Kai, H., Congshan, W., et al. (2020). A double-layer planning method for integrated community energy systems with varying energy conversion efficiencies. *Appl. Energy* 279, 115700. doi:10.1016/j.apenergy.2020.115700

Yuxuan, L., Junli, Z., Xiao, W., Jiong, S., and Kwang, Y. L. (2022). Optimal design of combined cooling, heating and power multi-energy system based on load tracking performance evaluation of adjustable equipment. *Appl. Therm. Eng.* 211, 118423. doi:10.1016/j.applthermaleng.2022.118423

Zeng, B., and Zhao, L. (2013). Solving two-stage robust optimization problems using a column-and-constraint generation method. *OPERATIONS Res. Lett.* 41 (5), 457–461. doi:10.1016/j.orl.2013.05.003

Zeng, R., Li, H., Jiang, R., Liu, L., and Zhang, G. (2016). A novel multi-objective optimization method for CCHP–GSHP coupling systems. *Energy Build.* 112, 149–158. doi:10.1016/j.enbuild.2015.11.072

Zhang, B., Sun, Y., Zhong, Y., and Shen, M. (2018). "Optimal energy flow of electricity-gas integrated energy system using second-order cone Program," in Proceedings of the 30th Chinese Control and Decision Conference, CCDC 2018 30th Chinese Control and Decision Conference, June 9, 2018Shenyang, China (CCDC).

Zhang, P., Lu, X., and Li, K. (2021). Achievable energy flexibility forecasting of buildings equipped with integrated energy management system. *IEEE Access* 9, 122589–122599. doi:10.1109/ACCESS.2021.3110657

Zhao, J., Xiong, J., Yu, H., Bu, Y., Zhao, K., Yan, J., et al. (2022). Reliability evaluation of community integrated energy systems based on fault incidence matrix. *Sustain. Cities Soc.* 80, 103769. doi:10.1016/j.scs.2022.103769

Zheng, L., Yingzong, L., Xianglong, L., Jianyong, C., Zhi, Y., Chao, W., et al. (2022). Superstructure-based mixed-integer nonlinear programming framework for hybrid heat sources driven organic Rankine cycle optimization. *Appl. Energy* 307, 118277. doi:10.1016/j.apenergy.2021.118277

Zhong, Y., Hu, B., Lin, L., Zhang, W., Li, Y., and Qi, Y. (2021). "Comprehensive evaluation strategy of optimal operation mode of integrated energy system based on analytic hierarchy process," in 5th IEEE Conference on Energy Internet and Energy System Integration: Energy Internet for Carbon Neutrality, EI2 2021 5th IEEE Conference on Energy Internet and Energy System Integration, Taiyuan, China, October 22, 2021 (IEEE). EI2 2021. doi:10.1109/EI252483.2021.9713176

Zhou, B., Xia, H., and Zang, T. (2022). Station and network coordinated planning of park integrated energy system considering energy cascade utilization. *Dianli Zidonghua Shebei/Electric Power Autom. Equip.* 42 (1), 20–27. doi:10.16081/j.epae.202109038

Zhu, R., Wei, H., and Bai, X. (2019). Wasserstein metric based distributionally robust approximate framework for unit commitment. *IEEE Trans. Power Syst.* 34 (4), 2991–3001. doi:10.1109/tpwrs.2019.2893296

Zugno, M., and Conejo, A. J. (2015). A robust optimization approach to energy and reserve dispatch in electricity markets. *Eur. J. Operational Res.* 247 (2), 659–671. doi:10.1016/j.ejor.2015.05.081

frontiers | Frontiers in Energy Research

TYPE Opinion
PUBLISHED 10 January 2023
DOI 10.3389/fenrg.2022.977140

OPEN ACCESS

EDITED BY
Chengbin Zhang,
Southeast University, China

REVIEWED BY
Huilin Lai,
Fujian Normal University, China

*CORRESPONDENCE
Weiwei Yan,
yanww@cjlu.edu.cn

SPECIALTY SECTION
This article was submitted to Process and Energy Systems Engineering, a section of the journal Frontiers in Energy Research

RECEIVED 24 June 2022
ACCEPTED 08 July 2022
PUBLISHED 10 January 2023

CITATION
Wan G, Yan W, Wu C, Xiao Y, Lin J and Zhang S (2023), Research progress and challenges of the gas turbine flowmeter in energy measurement.
Front. Energy Res. 10:977140.
doi: 10.3389/fenrg.2022.977140

Research progress and challenges of the gas turbine flowmeter in energy measurement

Guanjun Wan[1], Weiwei Yan[1]*, Chenbing Wu[1], Yungong Xiao[2], Jingdian Lin[2] and Shengyi Zhang[2]

[1]College of Metrology and Measurement Engineering, China Jiliang University, Hangzhou, China, [2]Zhejiang Cangnan Instrument Group Co Ltd, Wenzhou, China

KEYWORDS

energy measurement, data center, flow rate measurement, gas turbine flowmeter, artificial intelligence

Introduction

During the strategic deployment of bridging the gap between eastern and western regions in computing resources, the data center is evolving from high-speed to high-quality development. An extremely significant part is to reduce energy consumption during operation and improve energy efficiency. As a gist for evaluating energy efficiency and a means of implementing energy-saving supervision, energy measurement is a powerful support and guarantee for achieving carbon peak and carbon neutrality goals (Zhao et al., 2021) and promoting the development of green energy (Wan, 2022). Fluid energy accounts for a large proportion in the energy structure, such as natural gas, steam, and crude oil. Among them, the proportion of natural gas in the primary energy structure continues to rise (Chang, 2019) in recent years. According to the "Statistical Review of World Energy", in 2021, the natural gas demand exceeds four trillion m^3 in the whole world, with a growth rate per annum of 4.8% and an average annual growth rate of 2.2% in the past decade (BP Group, 2022). Especially, Chinese natural gas supply and demand gap reached 167.3 billion m^3, and its foreign dependence reached 44.9%. It is a challenge to ensure the accuracy of natural gas measurement and the smooth progress of the natural gas trade. The gas turbine flowmeter has obtained a broad development space and economic benefits in the international natural gas trading market (Xiang and Ceng, 2020) because of its high precision, good repeatability, high range ratio, and convenient maintenance. But researchers still found that there are some questions in the development of the gas turbine flowmeter. First, the flow parameters of natural gas are dynamic and diverse (Zhang et al., 2021), which increases the difficulty of tracing the flow measurement value. Second, the complex structure of gas turbine flowmeter's performance is difficult to optimize. Furthermore, how to improve the measurement accuracy of small flow has always been a research difficulty. Finally, people often misunderstand the internal flow field because the numerical simulation flow–structure interaction of the gas turbine flowmeter is not accurate enough. This study mainly clarifies the aforementioned problems and puts forward some perspectives on the research of gas turbine flowmeters.

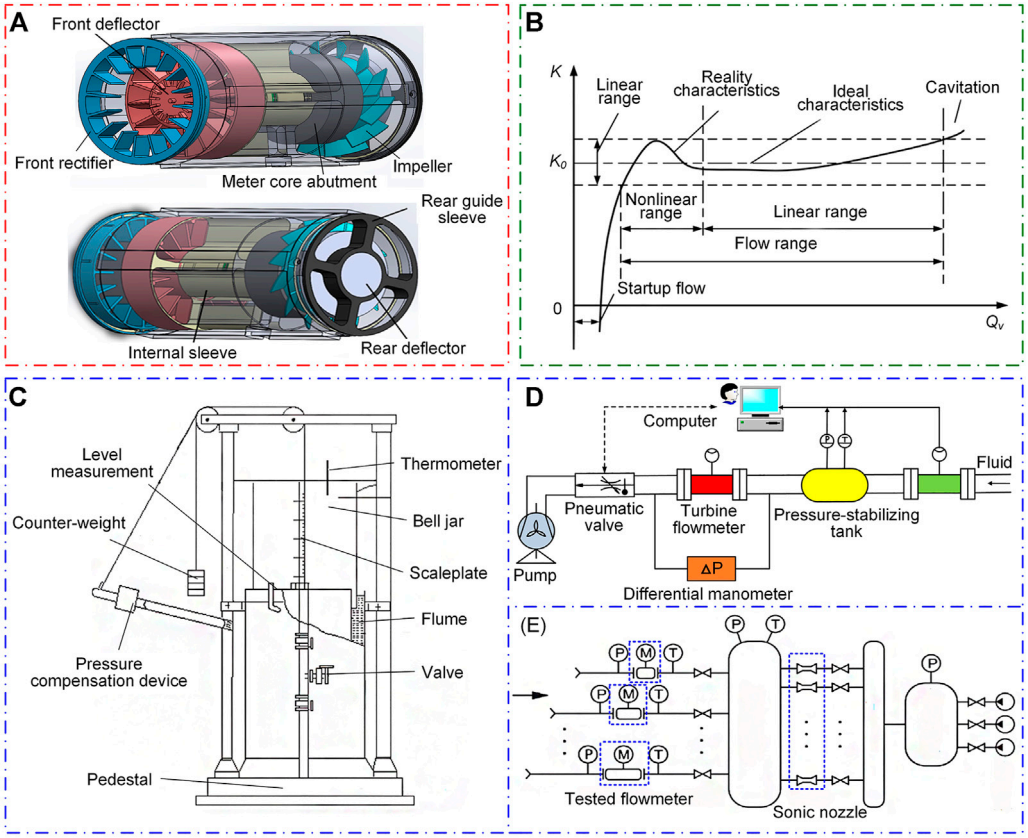

FIGURE 1
Flow rate measurement of gas turbine flowmeter: **(A)** Physical model of a gas turbine flowmeter, **(B)** K-Q curve of the gas turbine flowmeter, **(C)** bell jar–type gas flow standard device, **(D)** standard meter method flow standard device, and **(E)** sonic nozzle method gas flow standard devices.

Flowrate measurement of gas turbine flowmeter

The structure of a gas turbine flowmeter mainly consists of a front rectifier, impeller, rear deflector, flow totalizer, and so on, which is illustrated in Figure 1A. During the measurement process, the natural gas pushes the impeller blades to rotate, and the rotation of the impeller will periodically change the magnetoresistance value of the magneto electric converter and generate an electric pulse signal. The signal will converse an analog current to obtain the instantaneous flow value and then the pulse signal is sent to the flow integrator to obtain the cumulative flow value. In the aforementioned processes, the gas turbine flowmeter must overcome many resistances, such as impeller resistance torque, shaft friction torque, and magnetic resistance torque (Thompson and Grey, 1970). Especially, the influence of these resistances is obvious when measuring a small flow (Nie et al., 2018) that will make errors, as shown in Figure 1B. Moreover, the measurement effect of the gas turbine flowmeter will also be affected by the fluid motion state and velocity distribution (Huang, et al., 2016). Therefore, people usually use the flow standard device to achieve the magnitude calibration to verify the measurement of the gas turbine flowmeter under various working conditions.

The commonly used flow standard devices (Figure 1C–E) include the sonic nozzle method gas flow standard device (Jiang, et al., 2021), bell jar–type gas flow standard device (Yang and Peng, 2021), and standard meter method flow standard device (Yu and Jian, 2022). The working principle of the first two flow standard devices is different from the gas turbine flowmeter, which cannot reflect the dynamic parameters of natural gas truly. As for the standard meter method flow standard device, the accuracy demand of the standard flowmeter is high in the verification of a high-precision gas turbine flowmeter, which increases the difficulty of the device assembly. For tracing the dynamic value of state and physical parameters of natural gas under actual operating conditions, the actual flow calibration (Gao, et al., 2014) is much account of. To be specific, the high-pressure piston prover (HPPP) method can trace the measurement value to the national length and time benchmark (Yan, et al., 2019); the mass–time (MT) method (Li, et al., 2014) can trace the measurement value to the national

quality and time benchmark; and the p.V.T.t method (Wang, et al., 2021) can calculate the gas mass flow according to the pressure, volume, temperature, and time and complete the traceability of quantity value. Nevertheless, this research was carried out late in China due to technology, process, and other factors. It is important to transfer the quantity value to the standard device by using the gas turbine flowmeter in the future.

Relationship between performance and structure of the gas turbine flowmeter

In the current study, the performance of the gas turbine flowmeter is mainly assessed by linearity error, repeatability error, and pressure loss (Li et al., 2008). The linearity error and repeatability error can be calculated by the instrument coefficient. Both the instrument coefficient and pressure loss are significantly affected by the physical structure of the gas turbine flowmeter. Therefore, many researchers focus on optimizing the structure of a gas turbine flowmeter to reduce the pressure loss and make the instrument coefficient more stable.

The structure optimization of the gas turbine flowmeter mainly focuses on the front rectifier, impeller, and rear deflector. Research shows that in the part of the front rectifier, increasing its length can effectively improve flow field uniformity, reduce the linear error, repeatability error, and pressure loss, and shorten the front rectifier blade can improve the performance furthermore (Sun, et al., 2016). Moreover, the linearity error of the instrument coefficient will be reduced by changing the inflow angle, axial width, and coincidence degree of the blade (Sun, et al., 2022). As for the rear deflector, prolonging the length and position of the rear deflector vane can smooth the flow channel shape, to achieve the effect that the fluid decelerated and pressurized first and then diverted and significantly improved the stability of the instrument coefficient (Shao, et al., 2022).

To sum up, scholars have studied various structures of gas turbine flowmeters, but they only conducted qualitative research on structural design. As for how to obtain the optimal solution on the structural data, there is, no one can give a quantitative answer. With the development and popularization of machine learning algorithms, artificial intelligence can help people find the optimal structural design scheme, which will be the research focus in the design of gas turbine flowmeters in the future.

Simulation of a gas turbine flowmeter

For saving experimental resources and working time, people often predict the start-up flow and pressure loss by using the numerical simulation method (Liu and Yan, 2016). The commonly used numerical simulation module is the moving reference frame module (MRF), which is often used for CFD simulation of translation and rotation equipment. However, with the progress of the times, the accuracy of MRF cannot meet the requirements of our people, and the numerical simulation of fluid-structure in a passive mesh is becoming more popular (Pei, 2015). In fact, the passive mesh is difficult to converge and takes a long time in practical applications, people often optimized the grid generation technology, such as moving mesh generation technology, overlapping mesh generation technology, and adaptive mesh generation technology (Meng, et al., 2022) (Hong, et al., 2020) for fear of waste of times. The complex grid generation method needs to consume vast computing resources. Therefore, scholars have designed and implemented an Open Source Field Operation and Manipulation (OpenFOAM) grid generation server for a cloud computing environment to improve the efficiency of grid computing (Gao et al., 2022).

After mesh generation, the fluid motion is theoretically described by the Naiver–Stokes equation, but the analytical solution of the equation can be obtained only in a few cases for the non-linear conditions caused by the flow term (Tong, et al., 2016). Recently, a new research paradigm of fluid mechanics emerged with the development of artificial intelligence, which can select the grid input features or design the grid architecture based on the laws of fluid physics, called the physics-inspired deep learning method (Jin, et al., 2021). Scholars have found that this method can solve difficult problems in complex flows. For examples, the hydraulic simulation model of verification station constructed based on a BP neural network can better simulate the real flow state of the station while ensuring the calculation speed (Wen et al., 2021). The subgrid-scale (SGS) stress in large Eddy simulation (LES) is improved by artificial neural network-based non-linear algebraic models and obtains a high accuracy (Xie, Yuan, et al., 2020). Nevertheless, this method has not been widely used in the research of gas turbine flowmeters. In future research, applying the physics-inspired deep learning method to the gas turbine flowmeter and combining a gas turbine flowmeter with multidisciplinary will become a great challenge for contemporary scholars.

Challenges

From before, the development of the Chinese gas turbine flowmeter has faced the following main challenges:

1) Improving the ability of China's natural gas measurement traceability and the sound measurement standard system by developing the gas turbine flowmeter as the working level standard device for the transfer of the value of the function.

2) There is still a lot of space for the development of gas turbine flowmeter structure optimization, such as using deep learning methods to better determine the optimal structure optimization scheme.
3) Keeping the instrument coefficient stable in the small flow range is still a big problem, maybe can find a solution from each moment of resistance.
4) It is difficult to improve the accuracy of the numerical simulation results of gas turbine flowmeter and develop new algorithms for computational fluid dynamics. For example, how to use neural networks to incorporate the non-linear terms in the fluid motion process into the numerical simulation still needs people to research.

Conclusion

As the mainstream device of natural gas measurement, the gas turbine flowmeter plays a significant role in the field of energy measurement. Recently, the research on gas turbine flowmeters mainly through the methods of experiment and simulation to improve the metering performance of gas turbine flowmeters. As for the experimentation, people continuously improve the original standard device of measurement to reach the quantity traceability of natural gas. In the aspect of simulation, the traditional stand-alone numerical simulation is changed into the 'cloud + end' platform mode to improve the simulation efficiency, and the algorithm formula is optimized through the deep learning method to improve the simulation accuracy. The structure of the gas turbine flowmeter is analyzed and optimized to improve its performance by combining the experiment and simulation. A more perfect measurement standard system needs to be established in the future to guarantee a reasonable, fair, and just natural gas measurement. In addition, the machine learning algorithm is used to improve the structure of the gas turbine flowmeter, optimize the formula of the numerical simulation algorithm, and combine the traditional methods with the era of big data to improve the performance of the gas turbine flowmeter furthermore.

Author contributions

GW: investigation, data curation, and writing—original draft preparation. WY: conceptualization, methodology, and writing—reviewing and editing. CW: reviewing, editing, and supervision. YX: supervision, methodology, and validation. JL: supervision, methodology, and validation. SZ: supervision, methodology, and validation.

Conflict of interest

Authors YX, JL and SZ were employed by Zhejiang Cangnan Instrument Group Co., Ltd.

The remaining authors declare that the research was conducted in the absence of any commercial or financial relationships that could be construed as a potential conflict of interest.

Publisher's note

References

BP Group. (2022). Statistical Review of world energy. Available at: https://www.bp.com/en/global/corporate/energy-economics/statistical-review-of-world-energy/oil-gas-and-coal-trade.html.

Chang, J. C. (2019). Status and development trend on domestic and abroad natural gas flow metering technology. *Res. Discuss.* 2, 36–38.

Gao, R. C., Huaiet, X. Y., Zhang, Z. D., and Li, B. W. (2022). OpenFOAM mesh generation service foe cloud computing environment. *Comput. Technol. Its Appl.* 48 (4), 71–75. doi:10.16157/j.issn.0258-7998.211506

Gao, Z. G., Zhu, R. M., Wu, J., and Wang, M. Y. (2014). Design and research on actual flow calibration primary standard device of natural gas. *Automation Petro-Chemical Industry* 50, 13–16.

Hong, Z. C., Zong, Z., Wang, Y. G., Zhao, M. J., Liu, L., and Liang, G. J. (2020). Research on uncertainty of overset mesh technology based on orthogonal experiment method. *J. Ship Mech.* 24 (7), 865–873. doi:10.3969/j.issn.1007-7294.2020.07.003

Huang, C. H., Su, M. G., Kao, H. J., Jhong, J. H., Weng, S. L., and Lee, T. Y. (2016). UbiSite: Incorporating two-layered machine learning method with substrate motifs to predict ubiquitin-conjugation site on lysines. *BMC Syst. Biol.* 40, 6. doi:10.1186/s12918-015-0246-z

Jiang, H. C., Guo, G., and Tou, W. M. (2021). Online calibration of sonic nozzle gas flow standard device. *Process Autom. Instrum.* 42, 4. doi:10.16086/j.cnki.issn1000-0380.2020040034

Jin, X. W., Laima, S., and Li, H. (2021). Physics-enhanced deep learning methods foe modelling and simulating flow fields. *Chin. J. Theor. Appl. Mech.* 53 (10), 2616–2629. doi:10.6052/0459-1879-21-373

Li, X., Wang, Y. T., Li, C. J., Miao, Y. S., Yin, X. J., Sun, X. D., et al. (2008). *Verification regulation of turbine flowmeter*. Beijing: Inspection and Quarantine of the People's Republic of China.

Li, D. J., Zhang, M. Z., Li, S. X., and Ji, W. F. (2014). MT method for gas flow primary standard device. *Meas. Equip. Appl.* 24, 4. doi:10.13228/j.boyuan.issn1002-1183.2014.04.013

Liu, M. J., and Yan, B. (2016). Simulation and performance analysis on inner flow field of rotating part in the turbine flowmeters. *Mech. Eng.* 2, 42–45.

Meng, X. Q., Liu, Z. W., Liu, T. R., and Chen, J. J. (2022). Auto-generation algorithm of surface meshes on dirty geometries. *Acta Aerodyn. Sin.* 40, 1–8. doi:10.7638/kqdlxxb-2021.0400

Nie, Q., et al. (2018). Application of boundary flow in gas full - wheel flowmeter selection. *Ind. Meas.* 28, 1. doi:10.13228/j.boyuan.issn1002-1183.2016.0305

Pei, J. H. (2014). *Study on the optimal design of CNIM-TM series gas turbine flowmeter*. Hangzhou: China Jiliang University.

Shao, J. C., Yan, W. W., Lin, J. D., and Zhang, S. Y. (2022). Structure optimization design of rear deflector for gas turbine flowmeter. *Chin. J. Sci. Instrum.* 43 (1), 46–53. doi:10.19650/j.cnki.cjsi.2108364

Sun, H. J., Feng, Y., and Wang, B. (2016). Numerical simulation and optimal design of front diversion body in gas turbine flowmeter. *J. Electron. Meas. Instrum.* 30 (4), 550–557. doi:10.13382/j.jemi.2016.04.007

Sun, P. F., Xu, H. P, Li, T., Li, D. H., Li, B. T., and Hong, J. (2022). Structural optimization design of turbine flowmeter for tests of high-thrust liquid rocket engine. *J. Xi'an Jiaot. Univ.* 56 (5), 74–84. doi:10.7652/xjtuxb202205008

Thompson, R. E., and Grey, J. (1970). Turbine flowmeter performance model. *J. Fluids Eng.* 4, 712–722. doi:10.1115/1.3425117

Tong, N. G., Yu, Y. L., and Wang, Z. H. (2016). Some remarks on theoretical modelling approach in applied fluid mechanics and analysis of flow physics. *Phys. Gases* 1 (5), 1–8. doi:10.19527/j.cnki.2096-1642.2016.05.001

Wan, Y. Y. (2022). Green economy development, clean energy consumption and carbon dioxide emissions. *Ecol. Econ.* 38 (5), 40–46.

Wang, P., Zhang, Y. S., and Zhang, Y. T. (2021). Gas flow calibration facility by p. V. T. t technique. *Meas. Tech.* 41 (2), 159–166. doi:10.11823/j.issn.1674-5795.2021.02.24

Wen, K., et al. (2021). Neural network based intelligent control system of natural gas flowmeter verification process. *Nat. Gas. Ind.* 41 (7), 124–133. doi:10.1109/ITC.2010.47

Xiang, W. J., and Ceng, L. (2020). Application of turbine flowmeter in natural gas metering. *Metrology Meas. Tech.* 47 (2), 54–56. doi:10.15988/j.cnki.1004-6941.2020.2.017

Xie, C., Yuan, Z., and Wang, J. (2020). Artificial neural network-based nonlinear algebraic models for large eddy simulation of turbulence. *Phys. Fluids (1994).* 32, 115101. doi:10.1063/5.0025138

Yan, W. C., Xu, M., and Lu, Y. C. (2019). Uncertainty evaluation of sonic nozzle verification device by HPPP. *Ind. Meas.* 30, 2. doi:10.13228/j.boyuan.issn1002-1183.20619.0206

Yang, Y. T., and Peng, L. (2021). Research on the metrological traceability for bell prover. *Metrology Sci. Technol.* 65, 7. doi:10.12338/j.issn.2096-9015.2020.0291

Yu, Z. Y., and Jian, X. Z. (2022). Software design for calibration of gas flow standard facility with master meter method. *Electron. Sci. Technol.* 35, 10. doi:10.16180/j.cnki.issn1007-7820.2022.10.005

Zhang, H. Z., Cheng, Z. T., Jia, R., Zhou, C. W., and Li, M. Y. (2021). Economic optimization of electric-gas integrated energy system considering dynamic characteristics of natural gas. *Power Syst. Technol.* 45, 4. doi:10.13335/j.1000-3673.pst.2020.1997

Zhao, G. T., Qian, G. M., and Wang, S. (2021). Analysis on green and low-carbon development path for power industry to realize carbon peak and carbon neutrality. *Huadian Technol.* 43 (6), 11–20. doi:10.3969/j.issn.1674-1951.2021.06.002

frontiers | Frontiers in Energy Research

METHODS
published: 12 January 2023
doi: 10.3389/fenrg.2022.953387

Combustion Optimization Under Deep Peak Shaving Based on DYNA-A3C With Dynamic Weight

Tang Wei-Jie, Wang Hai-Tao, Liu Ping-Ji and Qian Feng-Lei*

China Energy Engineering Group Jiangsu Power Design Institute Co., Ltd., Nanjing, China

The combustion process of boilers under deep peak shaving is a multivariate process which has complex characteristics such as super multivariability, being nonlinear, and large delay. It is difficult to handle complex data and calculate appropriate distributed results. To this end, this study applies the A3C method based on the dynamic weight Dyna structure to the boiler combustion system. This method trains and optimizes the boiler combustion system by establishing a data center and designing appropriate states and reward values, and the simulation results show that this method can be used to optimize the boiler combustion system. It can effectively reduce NO_X emissions and improve the boiler combustion efficiency.

Keywords: data center, deep reinforcement learning, deep peak shaving, the combustion system, A3C

OPEN ACCESS

Edited by:
Xiangdong Liu,
Yangzhou University, China

Reviewed by:
Jianhong Lv,
Southeast University, China
Yi Zhang,
North China Electric Power University, China

****Correspondence:***
Tang Wei-Jie
tangweijie@jspdi.com.cn

Specialty section:
This article was submitted to Process and Energy Systems Engineering, a section of the journal Frontiers in Energy Research

Received: *26 May 2022*
Accepted: *09 June 2022*
Published: *12 January 2023*

Citation:
Wei-Jie T, Hai-Tao W, Ping-Ji L and Feng-Lei Q (2023) Combustion Optimization Under Deep Peak Shaving Based on DYNA-A3C With Dynamic Weight. Front. Energy Res. 10:953387. doi: 10.3389/fenrg.2022.953387

INTRODUCTION

In order to accelerate the completion of China's carbon emission and carbon neutrality goals and obtain digital transformation through data center in the energy industry, the National Energy Administration proposed the implement linkage of three reforms of a coal-fired power unit. The main technical difficulty is how to make the large-capacity coal-fired power unit perform deep peak shaving to the ultra-low load more digitally.

Using the data center to train the combustion system can effectively obtain the maximum amount of information. The boiler combustion process is a complex process with multi-variables, nonlinearity, and large delay. In particular, under deep peak shaving operation, the decrease in the load may lead to instability of boiler combustion, ineffective operation of the denitrification system, over-temperature of the tube wall of the boiler (Shi et al., 2019), etc. How to effectively ensure boiler efficiency and NOx emissions is an important research issue for combustion optimization under deep peak shaving.

The current research on the data application is mainly divided into two aspects. On the one hand, the boiler combustion process is optimized based on optimization algorithms, and the optimization is carried out with the goal of boiler combustion efficiency and environmental protection parameters, such as genetic algorithm (Dal Secco et al., 2015; Pan et al., 2018), particle swarm algorithm (Fang et al., 2012; Sanaye and Hajabdollahi, 2015; Xu et al., 2019), ant colony algorithms (Xu et al., 2008). But the speed of optimization is slow and easy to fall into local optimum. Particularly in deep peak shaving, the boiler combustion situation is more complicated. On the other hand, it is optimized by training neural networks, according to Li and Niu (2016) and Han et al. (2022), in which deep reinforcement learning in the data center has become the focus which has the ability of generalization and decision-making. Bouhamed et al. (2020) and Zou et al. (2020) proposed a deep deterministic policy gradient (DDPG) algorithm based on the actor-critic (AC) framework, which was used to update the policy when solving the DRL problem. Ye et al. (2021) suggested an asynchronous dominant actor-critic

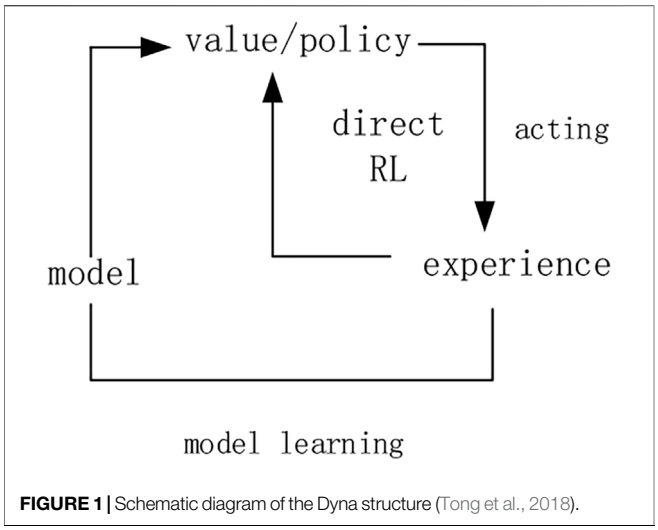

FIGURE 1 | Schematic diagram of the Dyna structure (Tong et al., 2018).

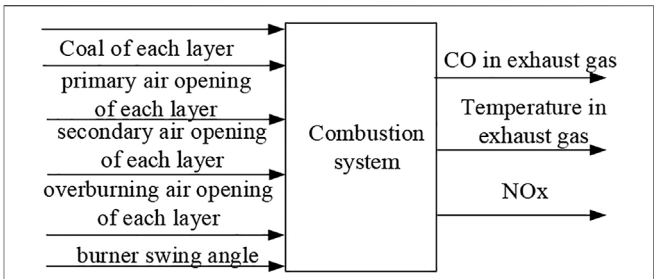

FIGURE 2 | Input and output variables of the boiler combustion system.

algorithm (AC), which used the multi-threading function of CPU to construct multiple agents in parallel and asynchronously for training at the same time. Therefore, at any time, due to the different states experienced by the parallel agents, the purpose of reducing the correlation between samples in the training process was achieved.

However, sometimes learning through environmental feedback from the data center may cause low learning efficiency, the Dyna structure (as shown in **Figure 1**) can enable agents to act in a virtual environment and generate virtual samples for learning, and combine them with learning experience in the actual environment to improve learning efficiency. So this study improved the asynchronous deep reinforcement learning algorithm (A3C) based on the Dyna structure as an optimization method to find the optimal boiler efficiency and NOx emission, so as to achieve the optimal control target. The simulation results show that the boiler combustion control optimization method based on DW-DYNA-A3C is an effective optimization method.

ESTABLISHMENT OF THE DW-DYNA-A3C METHOD

DW-Dyna-A3C Method

The learning efficiency of deep reinforcement learning is the main factor affecting the application effect. For this reason, this study considers the use of asynchronous methods to improve the learning efficiency. The asynchronous method refers to constructing different environment instances in multiple threads, and using multiple agents in parallel to interact with the environment. The asynchronous method enables the independent exploration in each agent of the thread, and multiple agents will share the acquired experience after joint exploration and parallel computing, and A3C is one such approach.

θ_a is the network parameter of critics shared globally, θ_v is the network parameter of the actors, $\theta_a^{'}$ and $\theta_v^{'}$ are the network parameter of critics and actors of a single thread, and then the gradient accumulation formula of the actors is:

$$d\theta_a \leftarrow d\theta_a + \nabla_{\theta_a^{'}} \log \pi\left(a_i \middle| s_i; \theta_a^{'}\right)\left(R - V\left(s_i; \theta_v^{'}\right)\right), \tag{1}$$

where π is the strategy which refers to the state-to-action mapping, a_i is the action determined by the current strategy (π), and R is the cumulative reward. The critic network cumulative gradient is.

$$d\theta_v \leftarrow d\theta_v + \partial\left(R - V\left(s_i; \theta_v^{'}\right)\right)^2 \Big/ \partial\theta_v^{'}. \tag{2}$$

Although the asynchronous strategy can improve the training speed, the learning process is still very slow if the number of samples obtained is insufficient. Therefore, consider putting the agent in a virtual environment, generating virtual samples for learning, and combining it with the learning experience in the actual environment (Liu et al., 2021). Therefore, it is proposed to add a Dyna structure to each thread in A3C to reduce the interaction with the real environment as well as improve the utilization of the virtual environment.

However, since there is a certain gap between the virtual environment model and real environment, if the learning results in the virtual environment are always dominant, it may cause wrong learning results. Therefore, the dynamic weight method is used to tackle the problem. When meeting the higher cumulative reward of the agent interacting with the real environment or the larger number of global updates, the learning result of the agent in the virtual environment will have less impact.

When updating the network parameters of actors and critics, dynamic weights μ is introduced to the virtual environment model in addition to its own learning rate, which is expressed as

$$\theta_a^{'} \leftarrow \theta_a^{'} + \mu\varepsilon_a d\theta_a^{'}, \theta_v^{'} \leftarrow \theta_v^{'} + \mu\varepsilon_v d\theta_v^{'}, \tag{3}$$

$$\mu = \left(1 - \frac{T}{T_{\max}}\right) e^{-\frac{R_m}{(j+1)r_{\max}}}. \tag{4}$$

In **formula (4)**, R_{m} is the cumulative reward in the virtual environment model. When R_{m}<0, R_{m} is set to zero to prevent the cumulative reward from being less than zero, which will cause the weight to be overlarge and fail to converge. r_{m} is the maximum reward given by the virtual environment for each step. j is the number of repeated executions in the virtual environment. μ decreases with the increase of global parameter updates' number and the cumulative reward. T is the global shared count.

METHOD FLOW

The improved algorithm is as follows:

The improved algorithm is as follows:

Repeat (for each episode)

1 Repeat (for each step of each episode)

2 Obtain the action (a_t)according to the strategy($\pi(a_t|s_t;\theta'_a)$)

3 Obtain reward (r_t) and new state (s_{t+1}) according to action(a_t)

4 Initialize states and actions: $s_m \leftarrow s_t$, $a_m \leftarrow a_t$

5 Reset parameters: $d\theta'_a = 0, d\theta'_v = 0$

6 Repeat n times in the model, j=0,…,n-1

7 Update the state and obtain a reward: $< s_{m,j+1}, r_{m,j+1} > \leftarrow MODEL < s_{m,j}, a_{m,j} >$

8 Obtain action $a_{m,j+1}$ according to strategy $\pi(a_{m,j+1}|s_{m,j+1};\theta'_a)$

9 Update cumulative reward: $R_m \leftarrow r_{m,j} + \gamma_m$

10 Update cumulative gradient of actor's network in a thread $d\theta'_a \leftarrow d\theta'_a + \nabla log\pi(a_{m,j}|s_{m,j};\theta'_a)(R_m - V(s_{m,j};\theta'_v))$

11 Update cumulative gradient of the critic's network $d\theta'_v \leftarrow d\theta'_v + \partial(R_m - V(s_{m,j};\theta'_v))^2 / \partial\theta'_v$

12 Calculate the weight μ according to formula (4)

13 Update parameters in a thread: $\theta'_a \leftarrow \theta'_a + \mu\varepsilon_a d\theta'_a$, $\theta'_v \leftarrow \theta'_v + \mu\varepsilon_v d\theta'_v$

14 Stop when the terminal state is obtained or the number of execution steps reaches the maximum

15 execute when $i \in \{t-1, \ldots, t_{start}\}$

16 Update cumulative rewards: $R \leftarrow r_i + \gamma R$

17 Calculate the cumulative gradient of the actor's network: $d\theta_a \leftarrow d\theta_a + \nabla_{\theta'} \log \pi(a_i | s_i;\theta'_a)(R - V(s_i;\theta'_v))$

18 Calculate the cumulative gradient of the critic's network: $d\theta_v \leftarrow d\theta_v + \partial(R - V(s_i;\theta'_v))^2 / \partial\theta'_v$

19 If $R > \bar{R}$, update the global parameter, $\theta_a \leftarrow \theta_a + \varepsilon_a d\theta_a$, $\theta_v \leftarrow \theta_v + \varepsilon_v d\theta_v$

20 until s achieves the termination state

21 until $T > T_{max}$

ε_a and ε_v are the learning rates of the actor and critic networks, R is the cumulative reward, T is the number of global updates, and the subscript m is the parameters of the algorithm in the virtual model.

The DW-Dyna-A3C algorithm adds an evaluation mechanism for the results of each thread on the basis of the original push mechanism in order to avoid pushing the results of poor operation in a thread to the global and thus affecting the speed and accuracy of convergence. If the cumulative reward of thread running is lower than the average of the cumulative reward of other threads in the last running, this update is only copied from the global parameters to the thread, and the update is not pushed to the global.

DESIGN OF THE COMBUSTION OPTIMIZATION SYSTEM BASED ON DW-DYNA-A3C

Analysis of the Combustion System

In the process of load lifting and lowering, the coordinated control system can calculate the total amount of coal and air required under different loads, after that, it was distributed to the burners and the air of each layer. The distribution method will directly affect the combustion efficiency of the boiler and the emission of NOx in the gas (Wang et al., 2018). At present, the coal of burners in each layer is usually distributed equally, and the air is allocated empirically, which is obviously not the optimal solution.

The boiler efficiency is generally calculated by the reverse balance method (Cheng et al., 2018), in which q_2 is expressed as exhaust heat loss, %. In addition, it is the largest in boiler heat loss and is closely related to temperature of exhaust gas (T_e). q_3 is the loss of the inadequacy burning, %, which is observed on-site by measuring the CO concentration in the exhaust gas while none of the other losses can be measured in real-time (Adams et al., 2021), Therefore, the boiler efficiency is mainly represented by the exhaust gas temperature and the CO concentration in the exhaust gas in this study.

Under deep peak shaving, the wall temperature of the heating surface is the key factor restricting the adjustment. Due to the reduction of the working fluid, the heat transfer of the hydrodynamic cycle is deteriorated, resulting in the over-temperature.

The main objectives of the boiler combustion optimization control system are to (as shown in **Figure 2**): 1) reduce the amount of CO in the exhaust gas (CO); 2)reduce the NOx content at the SCR inlet(NO_x); 3) ensure that temperature of waterwall (Tp) is not overheated; 4) minimize q2.

State Design

The state of the agent can best reflect the optimization goal and the optimization system. Therefore, the state quantity of the combustion optimization system should be composed of the target set value, the actual value, the adjustment value, and the deviation. The set values include the amount of carbon monoxide CO_{sp}, the exhaust gas temperature $T_{e,sp}$, and the set value of NOx concentration $NO_{x,sp}$. The total amount of air D_{AIR}, i-th layer primary air opening $V_{s,j}$, j-th layer secondary air opening $V_{s,j}$, k-layer overburning air opening $V_{c,k}$, and burner swing angle A_f;

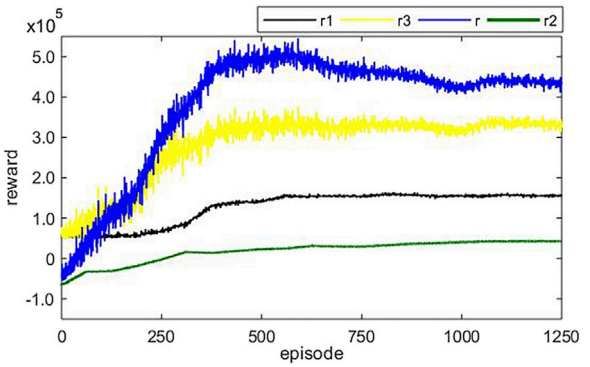

FIGURE 3 | Input and output variables of the boiler combustion system.

e_{Cx}, e_{Te}, e_{NOx} are CO deviation, T_e deviation, and NO_x deviation, respectively. In the optimization process, considering the safety and economy of boiler, the safety margin ΔT_P between the actual maximum wall of T_P and the over-temperature value should be added to the state (Dzikuć et al., 2020). Therefore, the system at time t has a state S_t.

$$S_t = \{T_{e,sp}, NO_{x,sp}, CO_{sp}, D_{AIR}, D_{B,n}, V_{f,i}, V_{s,j} V_{c,k}, A_f, CO, Te, NOx, e_{co}, e_{Te}, e_{NOx}, \Delta T_p\}. \quad (5)$$

Reward Design

Rewards should be able to promote deep reinforcement learning to the optimal strategy. In the reward design, the agent should continue to be rewarded when it learns the optimal strategy, and at the same time, the agent should meet various constraints of the system, such as the rapidity of adjustment, the stability, and the rate of change of the control quantity, so the reward design for the coordinated control system is divided into the following aspects.

Continuing Reward Items

The continuous reward should ensure that the reward increases with the decrease of the deviation in the optimization process, and the reward value reaches the maximum and remains unchanged when the system reaches the optimal value. Since there are three optimization objectives of the combustion optimization system, it is necessary to carry out weighted processing for the deviation of each optimized variable.

$$e_t = [|e_{Te}|, |e_{NOx}|, |e_{co}|] \begin{bmatrix} \lambda_1 \\ \lambda_2 \\ \lambda_3 \end{bmatrix}. \quad (6)$$

In **Formula (6)**, $[\lambda_1, \lambda_2, \lambda_3]^T$ is the deviation weight matrix, whose proportion can be modified according to the regulating target of the combustion system. Take the weighted deviation e_t at time t as an important reference for the continuous reward.

TABLE 1 | Parameters of the actor network and critic network.

Description	Value
Maximum number of global updates	1200
Maximum number of updates for a thread	8000
Actor network learning rate	0.00001
Critic network learning rate	0.00001
Virtual environment model repeats	100
Thread rewards update discount factor	0.99
Global update frequency	5

$$r_1 = \frac{10}{e_t^2 + 1}. \quad (7)$$

Limit Term of the Change Rate of the Control Quantity

In the optimization process, considering that the fast change rate of pipe wall temperature will produce thermal stress and reduce its service life and the adjustment rate of each actuator also has certain limits, it is necessary to limit the change rate of control quantity. The output of the actor network is the increment of each regulation quantity, so it only needs to judge the upper and lower limits of the actor network output, and then reward and punish the reward value.

Suppose that the sampling period of the algorithm is T_s, and the output of the actor network at time t is $\Delta D_{AIR}, \Delta V_{f,i}, \Delta V_{s,j}, \Delta V_{c,k}, \Delta A_f$, so the limiting term of the control variable rate of change is

$$r2 = \begin{cases} 0, & if \begin{cases} \Delta D_{AIR}/T_s \in [d_{AIR\min}, d_{AIR\max}], \\ \Delta V_{f,i}/T_s \in [v_{f\min}, v_{f\max}], \\ \Delta V_{s,j}/T_s \in [v_{s\min}, v_{s\max}], \\ \Delta V_{c,k}/T_s \in [v_{c\min}, v_{c\max}], \\ \Delta A_f/T_s \in [a_{f\min}, a_{f\max}]. \end{cases} \\ -20, & else \end{cases} \quad (8)$$

In **Formula (8)**, $d_{\mathrm{AIRmin}}, d_{\mathrm{AIRmax}}, d_{AIR\min} and d_{AIR\max}$ are the lower limit and upper limit of the coal quantity adjustment rate; $v_{\mathrm{smin}}, v_{\mathrm{smax}}$, $v_{\mathrm{fmin}}, v_{\mathrm{fmax}}$, $v_{\mathrm{cmin}}, and v_{\mathrm{cmax}}$ are the lower limit and upper limit of the adjusting rate of primary damper opening, secondary damper opening, and burnt out damper opening; $a_{fmin} and a_{fmax}$ are the lower limit and upper limit of the burner swing angle adjustment rate, when the three conditions are met at the same time, no punishment is given.

Auxiliary Tasks

The ultimate goal of combustion system optimization should improve boiler operation efficiency as much as possible and meet environmental protection requirements. Because combustion system optimization is a complex problem of multi-objective optimization, auxiliary tasks are added through weighted deviations, and when the optimization structure begins to gradually become better, and continuously increases the reward value. At the same time, when the maximum value of the boiler inner wall temperature is close to the over-temperature value, that is, when the safety margin ΔT_P is small, a penalty should be given to avoid this situation as much as possible, so the auxiliary task reward is

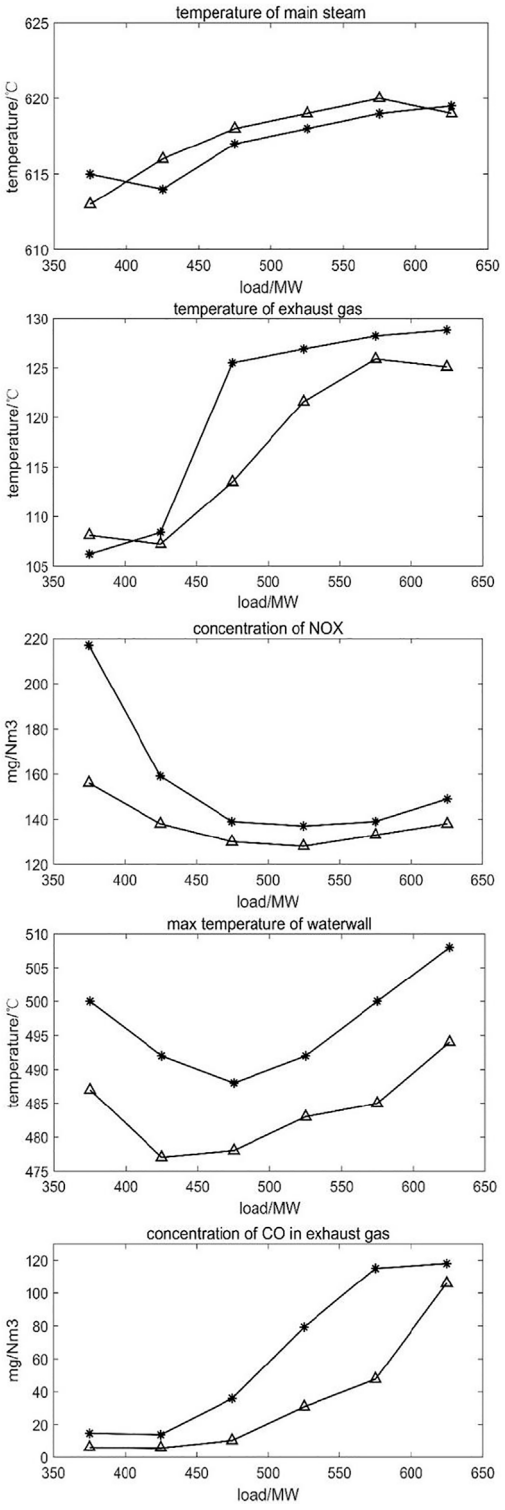

FIGURE 4 | Change in optimized variables from 350 to 650 MW ("*" represents effects before applying the method; "Δ" represents effects after applying the method.).

TABLE 2 | Comparison of the boiler efficiency before and after optimization.

Power range/MW	Boiler efficiency (before)	Boiler efficiency (after) (%)
300–400	91.55	91.89
400–500	92.32	92.44
500–600	92.45	92.76
600–700	92.88	92.92
700–800	93.12	93.22
800–1000	93.56	93.67

$$r3 = \begin{cases} 50, & if\ (|e_t| < 5), \\ \dfrac{5}{e_t^2 + 1}, & if\ (|e_t| < 10), \\ -10, & if\left(\Delta T_p < 5\right), \\ 0, & else. \end{cases} \tag{9}$$

So the final reward value for the boiler combustion system is.

$$r = r_1 + r_2 + r_3. \tag{10}$$

Simulation Experiment Research

Training Process

Taking the model of a 1000 MW boiler combustion system as an example, there are six layers of burners, six layers of primary air, 24 layers of secondary air, and eight layers of exhaust air, so n = 6, i = 6, j = 24, and k = 8, the rest of the set value and the range of the adjustment amount are set according to the boiler design manual. In the neural network structure, both the actor network and the critic network in the algorithm are designed as a 9-layer fully connected neural network structure. A total of 120 nodes were present, the output layer contains 1 node, the input layer of the actor network contains state information, and the output of the critic network, a total of 17 nodes were present, the middle hidden layer is the same as the critic network, the output layer has five nodes, and the output control amount is incremented. The rest of the relevant training parameters are shown in the **Table 1**.

Figure 3 shows the changing trend of the algorithm learning total reward value and each sub-item reward value, where r_1 is the continuous reward item, r_2 is the control amount change rate limit item, and r_3 is the auxiliary task item. As the number of learning increases, the total reward value of the system begins to increase rapidly after 200 episodes, and the algorithm basically converges around 600 episodes.

Simulation Experiment Under Deep Peak Shaving Conditions

After the training is completed, the trained algorithm is used to simulate the model under the condition of deep peak regulation. The load variation range is 350–650 MW, and the steady-state values of various indicators before and after training are observed.

As shown in **Figure 4** that after the optimization, the exhaust gas temperature of the boiler has decreased, and

the main steam temperature has increased compared with that before the optimization, which indicates that the boiler efficiency has been improved throughout the load range of the simulation experiment, mainly because the adjustment after optimization, the air distribution method reduces the temperature of the inner wall of the furnace, which is about 15K lower than the maximum value of the optimized front wall temperature, leaving a sufficient safety margin for increasing the temperature of the main steam. The ratio of heat absorption is more reasonable. At the same time, the concentrations of CO and NOx have also decreased, indicating that the combustion in the furnace is more sufficient after optimization (Yang et al., 2019), and the NOx concentration is reduced by means of staged air distribution and oxygen-enriched combustion, which not only improves the economy of the boiler combustion system, but also improves the environmental performance.

As presented in **Table 2**, obviously the boiler efficiency after optimization is larger than before. Considering the pollutant emission constraints, the average efficiency of boiler is increased by increasing the temperature of main steam and reheat steam by improving the combustion quality.

CONCLUSION

This article studies the combustion optimization system under deep peak shaving. Because the boiler combustion system has complex characteristics such as nonlinearity and multi-variables, this study proposed the DW-Dyna-A3C method to study, train, and simulate the combustion system. The DW-Dyna-A3C method is a reward evaluation system that takes into account both the control and the controlled state so that it can meet the requirements of multivariable nonlinear system control.

The simulation results show that this method can effectively improve the boiler efficiency, reduce pollutant emissions, and obtain a better ratio effect under the working conditions of deep peak regulation.

DATA AVAILABILITY STATEMENT

The raw data supporting the conclusion of this article will be made available by the authors, without undue reservation.

AUTHOR CONTRIBUTIONS

TW-J studied the method and wrote three sections of the manuscript. WH-T provided a simulation platform. LP-J wrote one section of the manuscript. QF-L provided running data.

FUNDING

This work is supported by China Energy Engineering Group Jiangsu Power Design Institute Co., Ltd. its project number is 32-JK-2022-020.

REFERENCES

Adams, D., Oh, D.-H., Kim, D.-W., Lee, C.-H., and Oh, M. (2021). Deep Reinforcement Learning Optimization Framework for a Power Generation Plant Considering Performance and Environmental Issues. *J. Clean. Prod.* 291, 125915. doi:10.1016/j.jclepro.2021.125915

Bouhamed, O., Ghazzai, H., Besbes, H., and Massoud, Y. (2020). "Autonomous UAV Navigation: A DDPG-Based Deep Reinforcement Learning Approach," in Proceeding of the 2020 IEEE International Symposium on Circuits and Systems (ISCAS) (IEEE), 1–5. doi:10.1109/iscas45731.2020.9181245

Cheng, Y., Huang, Y., Pang, B., and Zhang, W. (2018). ThermalNet: A Deep Reinforcement Learning-Based Combustion Optimization System for Coal-Fired Boiler. *Eng. Appl. Artif. Intell.* 74, 303–311. doi:10.1016/j.engappai.2018.07.003

Dal Secco, S., Juan, O., Louis-Louisy, M., Lucas, J.-Y., Plion, P., and Porcheron, L. (2015). Using a Genetic Algorithm and CFD to Identify Low NOx Configurations in an Industrial Boiler. *Fuel* 158, 672–683. doi:10.1016/j.fuel.2015.06.021

Dzikuć, M., Kuryło, P., Dudziak, R., Szufa, S., Dzikuć, M., and Godzisz, K. (2020). Selected Aspects of Combustion Optimization of Coal in Power Plants. *Energies* 13 (9), 2208. doi:10.3390/en13092208

Fang, Y., Qin, X., and Fang, Y. (2012). "Optimization of Power Station Boiler Coal Mill Output Based on the Particle Swarm Algorithm," in Proceeding of the 2012 IEEE International Conference on Industrial Engineering and Engineering Management(IEEE), 612–616. doi:10.1109/ieem.2012.6837812

Han, Z., Li, J., Hossain, M. M., Qi, Q., Zhang, B., and Xu, C. (2022). An Ensemble Deep Learning Model for Exhaust Emissions Prediction of Heavy Oil-Fired Boiler Combustion. *Fuel* 308, 121975. doi:10.1016/j.fuel.2021.121975

Li, G., and Niu, P. (2016). Combustion Optimization of a Coal-Fired Boiler with Double Linear Fast Learning Network. *Soft Comput.* 20 (1), 149–156. doi:10.1007/s00500-014-1486-3

Liu, X., Zhang, H., Long, K., Nallanathan, A., and Leung, V. C. (2021). Deep Dyna-Reinforcement Learning Based on Random Access Control in LEO Satellite IoT Networks. *IEEE Internet Things J* 103, 312–327. doi:10.1109/jiot.2021.3112907

Pan, H., Zhong, W., Wang, Z., and Wang, G. (2018). Optimization of Industrial Boiler Combustion Control System Based on Genetic Algorithm. *Comput. Electr. Eng.* 70, 987–997. doi:10.1016/j.compeleceng.2018.03.003

Sanaye, S., and Hajabdollahi, H. (2015). Thermo-economic Optimization of Solar CCHP Using Both Genetic and Particle Swarm Algorithms. *J. Sol. Energy Eng.* 137 (1). doi:10.1115/1.4027932

Shi, Y., Zhong, W., Chen, X., Yu, A. B., and Li, J. (2019). Combustion Optimization of Ultra Supercritical Boiler Based on Artificial Intelligence. *Energy* 170, 804–817. doi:10.1016/j.energy.2018.12.172

Tong, C., Niu, W., Xiang, Y., Bai, X., and Gang, L. (2019). Gradient band-based adversarial training for generalized attack immunity of A3C path finding. arXiv e-prints 1807, 6752. doi:10.48550/arXiv.1807.06752

Wang, C., Liu, Y., Zheng, S., and Jiang, A. (2018). Optimizing Combustion of Coal Fired Boilers for Reducing NOx Emission Using Gaussian Process. *Energy* 153, 149–158. doi:10.1016/j.energy.2018.01.003

Xu, Q., Yang, J., and Yang, Y. (2008). "Identification and Control of Boiler Combustion System Based on Neural Networks and Ant Colony Optimization Algorithm," in Proceeding of the 2008 7th World Congress on Intelligent Control and Automation (IEEE), 765–768. doi:10.1109/wcica.2008.4593018

Xu, X., Chen, Q., Ren, M., Cheng, L., and Xie, J. (2019). Combustion Optimization for Coal Fired Power Plant Boilers Based on Improved Distributed ELM and Distributed PSO. *Energies* 12 (6), 1036. doi:10.3390/en12061036

Yang, W., Wang, B., Lei, S., Wang, K., Chen, T., Song, Z., et al. (2019). Combustion Optimization and NOx Reduction of a 600 MWe Down-Fired Boiler by Rearrangement of Swirl Burner and Introduction of Separated Over-fire Air. *J. Clean. Prod.* 210, 1120–1130. doi:10.1016/j.jclepro.2018.11.077

Ye, Z., Zhang, D., Wu, Z. G., and Yan, H. (2021). A3C-based Intelligent Event-Triggering Control of Networked Nonlinear Unmanned Marine Vehicles Subject to Hybrid Attacks. *IEEE Trans. Intelligent Transp. Syst.* 75, 165–178. doi:10.1109/tits.2021.3118648

Zou, J., Hao, T., Yu, C., and Jin, H. (2020). A3C-Do: A Regional Resource Scheduling Framework Based on Deep Reinforcement Learning in Edge Scenario. *IEEE Trans. Comput.* 70 (2), 228–239. doi:10.1109/TC.2020.2987567

Conflict of Interest: TW-J, WH-T, LP-J, and QF-L were employed by the company China Energy Engineering Group Jiangsu Power Design Institute Co., Ltd.

Frontiers in Energy Research

Advances and innovation in sustainable, reliable and affordable energy

Explores sustainable and environmental developments in energy. It focuses on technological advances supporting Sustainable Development Goal 7: access to affordable, reliable, sustainable and modern energy for all.

Discover the latest Research Topics

See more →

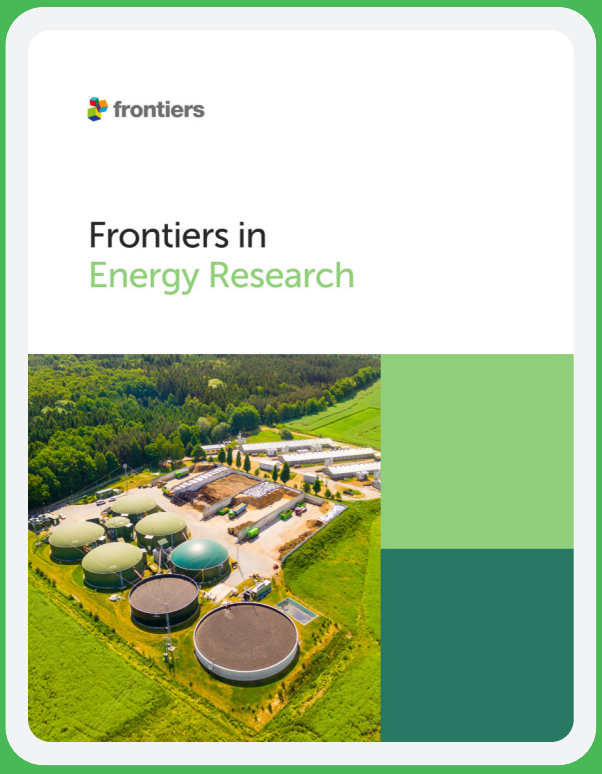

Frontiers

Avenue du Tribunal-Fédéral 34
1005 Lausanne, Switzerland
frontiersin.org

Contact us

+41 (0)21 510 17 00
frontiersin.org/about/contact